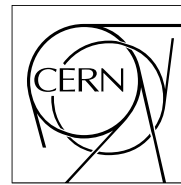


The Compact Muon Solenoid Experiment Analysis Note

The content of this note is intended for CMS internal use and distribution only



16 May 2013 (v12, 17 September 2013)

Search for the standard model Higgs boson produced in association with top quarks and decaying to leptons

Cristina Botta, Andrew Brinkerhoff, Patrick Janot, Kevin Lannon, Anne-Catherine Le Bihan, Charlie Mueller, Giovanni Petrucciani, Jason Slaunwhite, and Anna Woodard

Abstract

A search for the standard model Higgs boson produced in association with a top quark pair is presented, using 19.6 fb^{-1} of 8 TeV pp collision data collected by the CMS experiment at the LHC. Final states with a Higgs boson that decays to either ZZ^* , WW^* , or $\tau\tau$ are required to have a top quark pair that decays to either lepton plus jets ($t\bar{t} \rightarrow \ell\nu jj b\bar{b}$) or dileptons ($t\bar{t} \rightarrow \ell\nu\ell\nu b\bar{b}$), where ℓ represents an electron or a muon. The following signatures are selected: two isolated same-sign leptons (electrons or muons) plus b-tagged jets, three isolated leptons plus b-tagged jets, or four isolated leptons plus b-tagged jets. The expected 95% confidence level upper limit on the Higgs boson production cross section for a Higgs boson mass of 125.7 GeV/c² is 2.4 times the standard model expectation, to be compared to an observed limit of 6.6. The signal strength μ , relative to the expectation for the standard model Higgs boson, is measured to be $\mu = 3.7^{+1.6}_{-1.4}$.

This box is only visible in draft mode. Please make sure the values below make sense.

PDFAuthor: The TTH Leptonic group
PDFTitle: Search for Higgs Produced in Association with a Top Quark Pair and Decaying to Leptons
PDFSubject: CMS
PDFKeywords: CMS, physics, higgs, top

Please also verify that the abstract does not use any user defined symbols

DRAFT

1 Introduction

2 The newly-discovered Higgs boson [1, 2] provides a gateway for exploring physics beyond
 3 the standard model. The properties of the Higgs boson are well-predicted by the standard
 4 model, given a precise mass value. The CMS measurement of the new particle mass has already
 5 reached good precision, 125.7 ± 0.3 (stat.) ± 0.3 (syst.) GeV [3]. This precise mass result has
 6 created an opportunity to test the predictions of the standard model by measuring the other
 7 properties of the Higgs boson. Any deviation from expectation could be a sign of new physics.
 8 So far, the analyses studying some of the Higgs boson properties have confirmed that this
 9 particle is compatible with the standard model [3]. These analyses are not exhaustive and there
 10 is room for new studies to expand on the work they began.

11 It is of particular interest to measure the coupling of the Higgs boson to the top quark because of
 12 its large mass. The mass of the top quark may be a clue that it plays a special role in the context
 13 of electroweak symmetry breaking. The Higgs boson does not decay to top quarks; however,
 14 the $t\bar{t}H$ interaction vertex is present in a rare production mechanism where the Higgs boson is
 15 produced in association with a top quark-antiquark pair. We can use this process to directly
 16 probe the top-Higgs coupling at tree level. The process is expected to have a cross section of
 17 130 fb at next-to-leading order (NLO) [4] in 8 TeV pp collisions. Since direct standard model
 18 Higgs boson production at the LHC is dominated by a top loop, we already have an indirect
 19 measurement of the coupling between the top quark and the Higgs boson, assuming there are
 20 no contributions beyond the standard model. Our goal is to probe the coupling without a
 21 strong assumption about new physics, which makes the associated channel a better option.

22 The first searches for $t\bar{t}H$ production were performed at the CDF and D \oslash experiments. The
 23 searches looked for $b\bar{b}$ decays of the Higgs boson and set 95% confidence level (CL) upper
 24 limits on the $t\bar{t}H$ production cross section times $BR(H \rightarrow b\bar{b})$ at values more than 10 times the
 25 standard model prediction [5, 6]. More sensitive searches for $t\bar{t}H$ in the same decay mode have
 26 been performed by ATLAS [7] and CMS [8]. The ATLAS result uses 5 fb^{-1} of 7 TeV data and
 27 the CMS result uses 5 fb^{-1} of 7 TeV data in addition to 5 fb^{-1} of 8 TeV data, setting an upper
 28 limit of 5.8 times the standard model on $t\bar{t}H$ production. CMS also performed the search for $t\bar{t}H$
 29 production in events where the Higgs boson decays to $\gamma\gamma$ using 19.6 fb^{-1} of 8 TeV data [9]. This
 30 is currently the most sensitive result, setting an upper limit of 5.4 times $\sigma_{t\bar{t}H} \times BR(H \rightarrow \gamma\gamma)$.

31 We investigate for the first time the production of $t\bar{t}H$ where the Higgs boson decays into ZZ^* ,
 32 WW^* , or $\tau\tau$, requiring at least one Z , W or τ to decay leptonically. Example Feynman diagrams
 33 for $t\bar{t}H$, together with the decays of the top quark and the Higgs boson that lead to the signa-
 34 tures described above are shown in Fig. 1. Despite the low branching ratios of these
 35 decay channels, the presence of one or two additional leptons from the top quark pair decays
 36 leads to the following clean experimental signatures:

- 37 • two same-sign leptons (electrons or muons) plus two b-tagged jets
- 38 • three leptons plus two b-tagged jets
- 39 • four leptons plus two b-tagged jets

40 In Table 1 the expected signal events within each of the three final states considered in this
 41 measurement are reported after basic requirements on the physics objects which emulate the
 42 CMS detector acceptance.

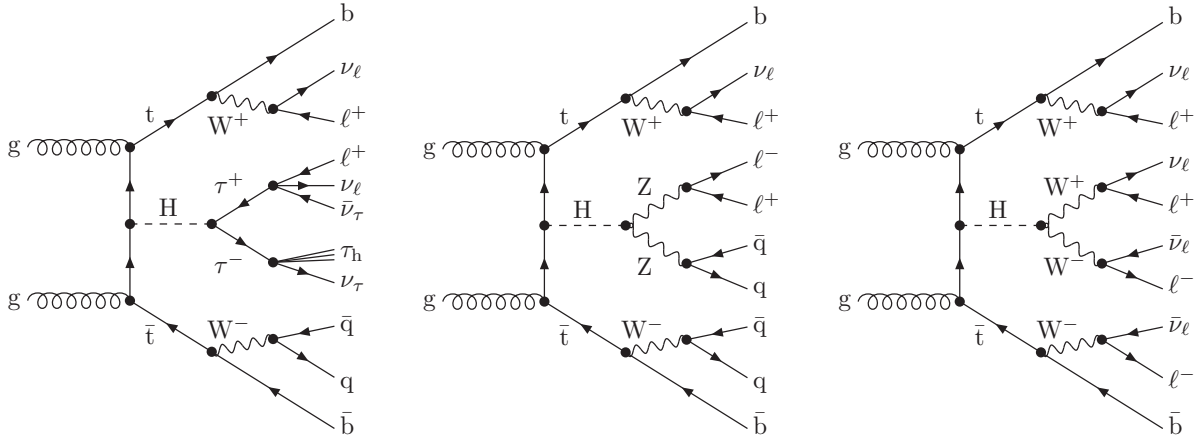


Figure 1: Example leading order Feynman diagrams for $t\bar{t}H$ production at pp colliders, with the Higgs boson decaying to $\tau\tau$, ZZ^* and WW^* (from left to right). The first, second, and third diagrams are examples of the two same-sign lepton signature, the three lepton signature, and the four lepton signature, respectively.

Table 1: Expected signal events for the three experimental signatures within detector acceptances for an integrated luminosity of 19.6 fb^{-1} . Muon acceptance: $p_T > 5 \text{ GeV}$, $|\eta| < 2.4$; electron acceptance: $p_T > 7 \text{ GeV}$, $|\eta| < 2.5$; b-jets acceptance: $p_T > 25 \text{ GeV}$, $|\eta| < 2.5$. To simulate the trigger acceptance we require two leptons with p_T above the double-lepton trigger thresholds: (20, 10) GeV.

Final state	$H \rightarrow WW^*$	$H \rightarrow \tau\tau$	$H \rightarrow ZZ^*$	Total
2 same-sign 1 (μ, e)	49.9	16.3	3.8	70.4
3 1 (μ, e)	22.3	8.3	3.7	34.7
4 1 (μ, e)	1.5	0.6	1.0	3.2
2 same-sign 1 (μ, e) + 2b	36.3	11.4	2.9	51.0
3 1 (μ, e) + 2b	16.0	6.0	2.8	25.0
4 1 (μ, e) + 2b	1.09	0.4	0.7	2.2

43 2 Data and MC Samples

44 2.1 Data Samples

45 The results presented here are based on the full $\sim 19.6 \text{ fb}^{-1}$ of the 2012 CMS dataset. Table 2 lists
46 the datasets used for this analysis, based on the triggers used to collect the data (see Sect. 3.1
47 for more details). The Run2012D-16Jan2013 datasets replace the stated runs in the Run2012D-
48 PromptReco datasets, which had a pixel movement problem. Luminosities are quoted from the
49 HF luminosity calculation and have a 4.4% uncertainty [10].

50 2.2 Signal Samples

51 The $t\bar{t}H$ signal is modeled using the PYTHIA Monte Carlo generator. The samples and associated cross sections used are listed in Table 3.

53 2.3 Background Samples

54 To model the backgrounds, this analysis primarily uses Monte Carlo (MC) samples from the
55 “Summer12” MC campaign. Most of the samples are generated either with the MADGRAPH
56 tree-level matrix element generator matched to PYTHIA for the parton shower, or with the

Dataset	Run Range	Integrated Luminosity
/DoubleMu/Run2012A-13Jul2012-v1/AOD	190456–193621	0.81 fb ⁻¹
/DoubleMu/Run2012A-recover-06Aug2012-v1/AOD	190782–190949	0.08 fb ⁻¹
/DoubleMu/Run2012B-13Jul2012-v4/AOD	193834–196531	4.40 fb ⁻¹
/DoubleMu/Run2012C-24Aug2012-v1/AOD	198022–198523	0.50 fb ⁻¹
/DoubleMu/Run2012C-PromptReco-v2/AOD	198941–203746	6.40 fb ⁻¹
/DoubleMu/Run2012D-PromptReco-v1/AOD	203768–208686	7.27 fb ⁻¹
/DoubleMu/Run2012D-16Jan2013-v2/AOD	207883–208319	0.63 fb ⁻¹
Total DoubleMu	190645–208686	19.5 pb⁻¹
/DoubleElectron/Run2012A-13Jul2012-v1/AOD	190456–193621	0.81 fb ⁻¹
/DoubleElectron/Run2012A-recover-06Aug2012-v1/AOD	190782–190949	0.08 fb ⁻¹
/DoubleElectron/Run2012B-13Jul2012-v1/AOD	193834–196531	4.40 fb ⁻¹
/DoubleElectron/Run2012C-24Aug2012-v1/AOD	198022–198523	0.50 fb ⁻¹
/DoubleElectron/Run2012C-PromptReco-v2/AOD	198941–203746	6.40 fb ⁻¹
/DoubleElectron/Run2012D-PromptReco-v1/AOD	203768–208686	7.27 fb ⁻¹
/DoubleElectron/Run2012D-16Jan2013-v1/AOD	207883–208319	0.63 fb ⁻¹
Total DoubleElectron	190645–208686	19.5 fb⁻¹
/MuEG/Run2012A-13Jul2012-v1/AOD	190456–193621	0.81 fb ⁻¹
/MuEG/Run2012A-recover-06Aug2012-v1/AOD	190782–190949	0.08 fb ⁻¹
/MuEG/Run2012B-13Jul2012-v1/AOD	193834–196531	4.40 fb ⁻¹
/MuEG/Run2012C-24Aug2012-v1/AOD	198022–198523	0.50 fb ⁻¹
/MuEG/Run2012C-PromptReco-v2/AOD	198941–203746	6.40 fb ⁻¹
/MuEG/Run2012D-PromptReco-v1/AOD	203768–208686	7.27 fb ⁻¹
/MuEG/Run2012D-16Jan2013-v2/AOD	207883–208319	0.63 fb ⁻¹
Total MuEG	190645–208686	19.5 fb⁻¹

Table 2: The datasets analyzed for this analysis.

Mass	Higgs Decay	Dataset	Cross Sect.
110 GeV/c ²	$H \rightarrow$ all	/TTH_Inclusive_M110_8TeV_pythia6/Summer12_DR53X-PU_S10_START53_V7Av1/AODSIM	0.1887 pb
115 GeV/c ²	$H \rightarrow$ all	/TTH_Inclusive_M115_8TeV_pythia6/Summer12_DR53X-PU_S10_START53_V7Av1/AODSIM	0.1663 pb
120 GeV/c ²	$H \rightarrow$ all	/TTH_Inclusive_M120_8TeV_pythia6/Summer12_DR53X-PU_S10_START53_V7Av1/AODSIM	0.1470 pb
122.5 GeV/c ²	$H \rightarrow$ all	/TTH_Inclusive_M122_5.8TeV_pythia6/Summer12_DR53X-PU_S10_START53_V7Av1/AODSIM	0.1383 pb
125 GeV/c ²	$H \rightarrow$ all	/TTH_Inclusive_M125_8TeV_pythia6/Summer12_DR53X-PU_S10_START53_V7Av1/AODSIM	0.1302 pb
127.5 GeV/c ²	$H \rightarrow$ all	/TTH_Inclusive_M127_5.8TeV_pythia6/Summer12_DR53X-PU_S10_START53_V7Av1/AODSIM	0.1227 pb
130 GeV/c ²	$H \rightarrow$ all	/TTH_Inclusive_M130_8TeV_pythia6/Summer12_DR53X-PU_S10_START53_V7Av1/AODSIM	0.1157 pb
135 GeV/c ²	$H \rightarrow$ all	/TTH_Inclusive_M135_8TeV_pythia6/Summer12_DR53X-PU_S10_START53_V7Av1/AODSIM	0.1031 pb
140 GeV/c ²	$H \rightarrow$ all	/TTH_Inclusive_M140_8TeV_pythia6/Summer12_DR53X-PU_S10_START53_V7Av1/AODSIM	0.09207 pb

Table 3: List of signal MC datasets and cross sections used to determine the SM expectation.

NLO generator POWHEG combined with PYTHIA. These samples are reconstructed with the same CMSSW version as the data samples listed above. The pileup distribution in all MC samples is reweighted, using the procedure listed below so that the MC pileup distribution matches the one expected for data. Table 4 lists the background MC samples and associated cross sections.

2.4 MC pileup reweighting

During the 2012 data taking period, the LHC provided increasingly large instantaneous luminosities to the experiments. As a result, the average number of overlapping events per time interval has also increased. These overlapping pileup events that occur along with the physics events of interest can affect everything from lepton isolation to jet reconstruction. Therefore, it is important that our simulated events have the same distribution of pileup events as data.

When the simulation events were generated, the average amount of pileup that we would see in 2012 was unknown. Therefore, the pileup distribution in the simulation needs to be reweighted to match the data. For the simulation, it is known how many additional interactions were added to every generated event. For the data, the number of pileup interactions for each unit of time depends on the instantaneous luminosity for each bunch pair and the total inelastic cross section, $\sigma_{inelastic}$. Empirically, we found that $\sigma_{inelastic} = 69.4$ mb described the data well, and we used values that varied by $\pm 7\%$ for our systematic uncertainty.

As a measure of how well the pileup in simulation matches the data, we can look at the number of reconstructed vertices. Figure 2 shows the number of reconstructed vertices for data and for the $t\bar{t} + \text{jets}$ MC sample, both before and after pileup reweighting. After reweighting, the data and MC distributions agree very well, indicating that the pileup reweighting is working as expected.

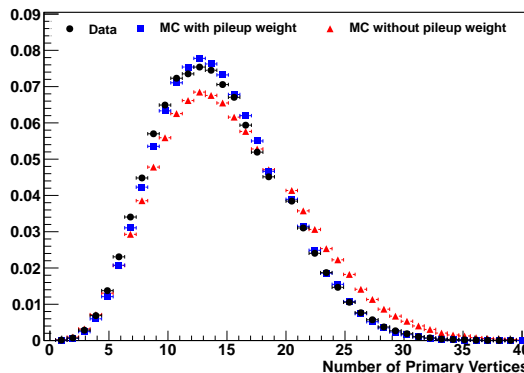


Figure 2: Comparison of number of reconstructed vertices for data (black) and the $t\bar{t} + \text{jets}$ MC sample before (red) and after (blue) pileup reweighting. After pileup reweighting, the MC matches the data well.

3 Event reconstruction and object identification

3.1 Triggers

We select events recorded with either double- or triple-lepton triggers. Table 5 lists the triggers we use. Events recorded with the triple-lepton triggers are only used in the 3ℓ and 4ℓ final states.

Sample	Dataset	Cross Sect.
$t\bar{t}$ jets	/TTJets_MassiveBinDECAY_TuneZ2star_8TeVmadgraph-tauola/Summer12_DR53XPU_S10_START53_V7Av1/AODSIM	225.197 pb
$t\bar{t} \rightarrow$ all	/TTJets_MassiveBinDECAY_TuneZ2star_8TeVmadgraph-tauola/Summer12_DR53XPU_S10_START53_V7Av2/AODSIM	
$t\bar{t} \rightarrow$ jets	/TTJets_HadronicMGDecays_8TeVmadgraph/Summer12_DR53XPU_S10_START53_V7A_extv1/AODSIM	106.94 pb
$t\bar{t} \rightarrow \ell\nu + 4$ jets	/TTJets_SemiLeptMGDecays_8TeVmadgraph/Summer12_DR53XPU_S10_START53_V7A_extv1/AODSIM	102.49 pb
$t\bar{t} \rightarrow \ell\nu\ell\nu + 2$ jets	/TTJets_FullLeptMGDecays_8TeVmadgraph/Summer12_DR53XPU_S10_START53_V7Av2/AODSIM	24.57 pb
$t\bar{t} + W$	/TTWJets_8TeVmadgraph/Summer12_DR53XPU_S10_START53_V7Av1/AODSIM	0.249 pb
$t\bar{t} + Z$	/TTZJets_8TeVmadgraph_v2/Summer12_DR53XPU_S10_START53_V7Av1/AODSIM	0.208 pb
W + jets	/WJetsToLNu_TuneZ2Star_8TeVmadgraphtarball/Summer12_PU_S7_START52_V9v1/AODSIM	36257.2 pb
W + 1 jet	/W1JetsToLNu_TuneZ2Star_8TeVmadgraph/Summer12_DR53XPU_S10_START53_V7Av1/AODSIM	6440.4 pb
W + 2 jets	/W2JetsToLNu_TuneZ2Star_8TeVmadgraph/Summer12_DR53XPU_S10_START53_V7Av1/AODSIM	2087.2 pb
W + 3 jets	/W3JetsToLNu_TuneZ2Star_8TeVmadgraph/Summer12_DR53XPU_S10_START53_V7Av1/AODSIM	619.0 pb
W + 4 jets	/W4JetsToLNu_TuneZ2Star_8TeVmadgraph/Summer12_DR53XPU_S10_START53_V7Av1/AODSIM	255.2 pb
$Z/\gamma^* +$ jets $10 \text{ GeV}/c^2 < M_{\ell\ell} < 50 \text{ GeV}/c^2$	/DYJetsToLL_M-10To50_TuneZ2Star_8TeV-madgraph/Summer12_DR53XPU_S10_START53_V7A-v1/AODSIM	14702 pb
$M_{\ell\ell} > 50 \text{ GeV}/c^2$	/DYJetsToLL_M-50_TuneZ2Star_8TeV-madgraph-tarball/Summer12_DR53XPU_S10_START53_V7A-v1/AODSIM	3505.7 pb
$Z/\gamma^* + 1$ jet	/DY1JetsToLL_M-50_TuneZ2Star_8TeV-madgraph/Summer12_DR53XPU_S10_START53_V7A-v1/AODSIM	666.7 pb
$Z/\gamma^* + 2$ jets	/DY2JetsToLL_M-50_TuneZ2Star_8TeV-madgraph/Summer12_DR53XPU_S10_START53_V7A-v1/AODSIM	215.1 pb
$Z/\gamma^* + 3$ jets	/DY3JetsToLL_M-50_TuneZ2Star_8TeV-madgraph/Summer12_DR53XPU_S10_START53_V7A-v1/AODSIM	66.07 pb
$Z/\gamma^* + 4$ jets	/DY4JetsToLL_M-50_TuneZ2Star_8TeV-madgraph/Summer12_DR53XPU_S10_START53_V7A-v1/AODSIM	27.38 pb
Single t s-channel	/T_s-channel_TuneZ2star_8TeV-powheg-tauola/Summer12_DR53XPU_S10_START53_V7A-v1/AODSIM	3.79 pb
t -channel	/T_t-channel_TuneZ2star_8TeV-powheg-tauola/Summer12_DR53XPU_S10_START53_V7A-v1/AODSIM	56.4 pb
tW	/T_tW-channel-DR_TuneZ2star_8TeV-powheg-tauola/Summer12_DR53XPU_S10_START53_V7A-v1/AODSIM	11.1 pb
Single \bar{t} s-channel	/Tbar_s-channel_TuneZ2star_8TeV-powheg-tauola/Summer12_DR53XPU_S10_START53_V7A-v1/AODSIM	1.76 pb
t -channel	/Tbar_t-channel_TuneZ2star_8TeV-powheg-tauola/Summer12_DR53XPU_S10_START53_V7A-v1/AODSIM	30.7 pb
tW	/Tbar_tW-channel-DR_TuneZ2star_8TeV-powheg-tauola/Summer12_DR53XPU_S10_START53_V7A-v1/AODSIM	11.1 pb
WW	/WW_TuneZ2star_8TeV_pythia6_tauola/Summer12_DR53XPU_S10_START53_V7A-v1/AODSIM	54.8 pb
WZ	/WZ_TuneZ2star_8TeV_pythia6_tauola/Summer12_DR53XPU_S10_START53_V7A-v1/AODSIM	32.3 pb
ZZ	/ZZ_TuneZ2star_8TeV_pythia6_tauola/Summer12_DR53XPU_S10_START53_V7A-v1/AODSIM	7.7 pb

Table 4: List of background MC datasets and cross sections used for normalization.

- We use these trigger requirements to select events in both data and simulation. In general, the trigger efficiencies in the data and the simulation agree well. For 3ℓ and 4ℓ events we do not apply a correction factor to the simulation. We apply an uncertainty of $XX\%$ to all processes modeled with simulation in these two channels that is large enough to accommodate any differences in performance. For two-lepton events, we do apply a correction factor to the simulation that corrects for small differences in performance compared to the data.
- The correction factor for 2ℓ events is the ratio of the efficiency in data to the efficiency in simulation. We use correction factor values measured with the procedure described in reference [11]. The same procedure was used to produce correction factors in the $t\bar{t}H$, $H \rightarrow b\bar{b}$ analysis [12]. Measuring the efficiency in simulated events is straightforward because there is no trigger bias with generated events. To measure the efficiency in data one must first select a set of events that were recorded on a trigger that is uncorrelated with the trigger of interest. This procedure uses events recorded on a MET trigger as a unbiased sample. It then looks for candidate events with exactly two good leptons. Then it measures the efficiency for the candidate events to pass the trigger.
- The correction factor values were derived using a different lepton identification criteria than we use in our analysis. We assume that the differences in the correction factors are small and covered by the uncertainty on the correction factor. Specifically, the correction factors were derived for the lepton selection in $t\bar{t}H$, $H \rightarrow b\bar{b}$ [12] with some additional cuts designed to reject leptons with mismeasured charge.

Dataset	Trigger Name
DoubleMu	HLT_Mu17_Mu8_v*
DoubleMu	HLT_Mu17_TkMu8_v*
DoubleEle	HLT_Ele17_CaloIdT_CaloIsoVL_TrkIdVL_TrkIsoVL_Ele8_CaloIdT_CaloIsoVL_TrkIdVL_TrkIsoVL_v*
DoubleEle	HLT_Ele15_Ele8_Ele5_CaloIdL_TrkIdVL_v*
MuEG	HLT_Mu17_Ele8_CaloIdT_CaloIsoVL_TrkIdVL_TrkIsoVL_v*
MuEG	HLT_Mu8_Ele17_CaloIdT_CaloIsoVL_TrkIdVL_TrkIsoVL_v*

Table 5: List of triggers and their corresponding datasets.

3.2 Jets and B-tagging

- A complete reconstruction of the individual particles emerging from each collision event is obtained via a particle-flow (PF) technique. The technique uses the information from all CMS sub-detectors to identify and reconstruct individual particles in the collision event [13, 14]. The particles are classified into mutually exclusive categories: charged hadrons, neutral hadrons, photons, muons, and electrons.
- Jets are reconstructed by clustering PF candidates using the anti- k_T algorithm with distance parameter $\Delta R = 0.5$, as implemented in the FASTJET package [15, 16]. The charged hadrons not coming from the primary vertices are subtracted from the PF candidates considered in the clustering. The primary vertex is chosen as the vertex with the highest sum of p_T^2 of its constituent tracks. Jet energy corrections are applied as a function of the jet E_T and η [17]. In addition, a multivariate discriminator is applied to distinguish between jets coming from the primary vertex and jets coming from pile-up vertices. The discrimination is based on the differences in the jet shapes, in the relative multiplicity of charged and neutral components, and in the different fraction of transverse momentum which is carried by the hardest components. Within the tracker acceptance the jet tracks are also required to be compatible with the primary vertex. Jets are only considered if they have a transverse energy above 25 GeV and $|\eta| < 2.4$. In addition, they have to be separated from any lepton candidates by requiring $\Delta R = \sqrt{(\eta^\ell - \eta^{jet})^2 + (\phi^\ell - \phi^{jet})^2} > 0.5$.

The CSV b-tagging algorithm [18] is used to identify jets that are likely to originate from the hadronization of bottom quarks. This algorithm combines both secondary vertex information and track impact parameter information together in a likelihood discriminant. The discriminant output value ranges from zero to one. It distinguishes between b -jets and jets originating from light quarks, gluons and charm quarks. The efficiency to tag b -jets and the rate of misidentification of non- b jets depend on the operating point chosen. Both the efficiency and the fake rate are parameterised as a function of the transverse momentum and pseudorapidity of the jets. These performance measurements are obtained directly from data in samples that can be enriched in b jets, such as $t\bar{t}$ and multijet events where a muon can be found inside the one of jets. Two working points for the CSV output discriminant are used in the analysis. The *loose* one ($\text{CSV} > 0.244$) has approximately 85% efficiency to tag jets with b quarks and a 10% chance to tag jets with only light quarks or gluons. The *medium* working point ($\text{CSV} > 0.679$) has approximately 70% efficiency for tagging jets with b quarks and 1.5% efficiency to tag jets with only light quarks or gluons [18, 19]. Corrections that take into account the different performances of the CSV tagging in data and simulation are applied to the MC samples used in the analysis.

3.3 Missing Energy

The missing transverse energy vector is calculated offline as the negative of the vector sum of transverse momenta of all PF candidates identified in the event. The magnitude of this vector is referred to as E_T^{miss} . In order to recover from the degradation of performances of the missing transverse energy due to the pile-up interactions, we consider also the H_T^{miss} variable computed in the same way as the E_T^{miss} , but using only the selected jets and leptons (the lepton selection will be described in the following paragraphs). The H_T^{miss} variable has worse resolution than E_T^{miss} but it is more robust as it does not rely on the soft part of the event. In this analysis the event selection makes use of a linear discriminator based on the two variables, $E_T^{\text{miss}} \text{LD}$, exploiting the fact that E_T^{miss} and H_T^{miss} are less correlated in events with instrumental missing energy with respect to events with real missing energy. The $E_T^{\text{miss}} \text{LD}$ is defined as

$$E_T^{\text{miss}} \text{LD} = E_T^{\text{miss}} * 0.00397 + H_T^{\text{miss}} * 0.00265 \quad (1)$$

and the working point used is $E_T^{\text{miss}} \text{LD} > 0.2$. Fig. 3 shows the correlation between H_T^{miss} and E_T^{miss} in signal events and DY+jets events and the comparison between the performances of the two variables and the linear discriminator.

3.4 Lepton Preselection

We pre-select electron and muon objects requiring lepton identification and isolation criteria similar to those used in the $H \rightarrow ZZ^* \rightarrow 4l$ analysis. These requirements are *loose* criteria with very high efficiency on *signal leptons* and moderate *fake lepton* rejection. More details can be found in [20, 21].

Throughout this note we will call fake leptons those coming from b -hadrons decays, from the misidentification of light jets, and from photon conversions. We consider as signal leptons the isolated leptons coming from W , Z , and τ decays.

152

3.4.1 Muons Reconstruction and Identification

The muon objects considered in this analysis are reconstructed within the geometrical acceptance $|\eta^\mu| < 2.4$ and with transverse momentum $p_T^\mu > 5 \text{ GeV}$. The reconstruction combines the information from both the silicon tracker and the muon spectrometer. The matching between

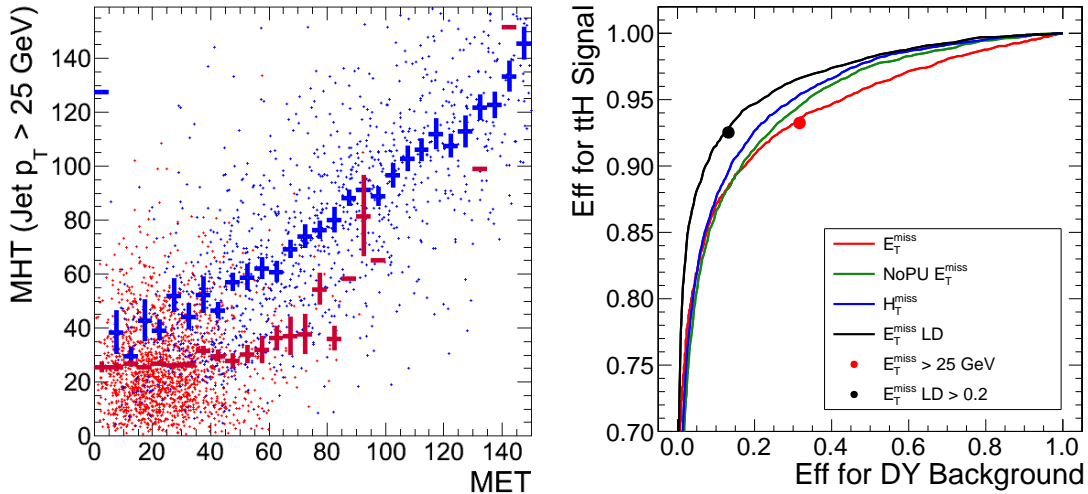


Figure 3: The figure on the left shows the correlation between the H_T^{miss} and E_T^{miss} variables in signal events (blue) and DY+jets events (red). The figure on the right shows the ROC curve for the two variables H_T^{miss} and E_T^{miss} and the linear discriminator $E_T^{\text{miss}} \text{LD}$, as well as the LD working point used in the analysis.

the inner and outer tracks is initiated either "outside-in", starting from a track in the muon system, or "inside-out", starting from a track in the silicon tracker.

In particular muon tracks are first reconstructed independently in the inner tracker (*tracker track*) and in the muon system (*standalone-muon track*). Based on these objects, two reconstruction approaches are used: *Global Muon* (outside-in) reconstruction and *Tracker Muon* (inside-out) reconstruction [22].

The Tracker Muon reconstruction is more efficient than the Global Muon reconstruction at low momenta, $p \lesssim 5 \text{ GeV}/c$, because it requires only a single muon segment in the muon system, whereas Global Muon reconstruction is designed to have high efficiency for muons penetrating through more than one muon station and typically requires segments in at least two muon stations. Thanks to the high tracker-track efficiency [23] and a very high efficiency of reconstructing segments in the muon system, about 99% of muons produced in pp collisions and having sufficiently high momentum are reconstructed either as a Global Muon or a Tracker Muon, and very often as both. Candidates found both by the Global Muon and the Tracker Muon approaches that share the same tracker track are merged into a single candidate. Muons reconstructed only as standalone-muon tracks have worse momentum resolution and less favourable collision muon to cosmic-ray muon ratio than the Global and Tracker Muons and are usually not used in physics analyses.

The combination of different algorithms provides a robust and efficient muon reconstruction. A given physics analysis can achieve the desired balance between identification efficiency and purity by applying a selection based on various muon identification variables. For the lepton preselection we choose the *Loose Muon selection*, which accepts all the particle-flow muon candidates (PF Muons) without additional quality criteria. The PF Muons are selected among the reconstructed muon track candidates by applying minimal requirements on the track components in the muon system and taking into account a matching with small energy deposits in the calorimeters. More details of the particle-flow muon selection are described in Ref. [24]. We additionally require a very loose selection on the distance of the muon track from the primary vertex in order to reject badly reconstructed tracks or tracks from pileup vertices. In particular we request the significance of the impact parameter to the event vertex, $SIP_{3D} = |\frac{\text{IP}}{\sigma_{\text{IP}}}|$,

186 to be less than 10, and the distances in the transverse plane, d_{xy} , and along the z axis, d_z , to be
 187 less than 0.5 cm and 1 cm respectively.

188 In this analysis, momentum scale calibrations are applied to muons both in data and in simu-
 189 lations, derived from the $1/p_T$ distributions of muons from Z decays [25]. The corrections are
 190 designed to calibrate the overall momentum scale and to remove any dependency of the scale
 191 on the p_T , η , ϕ and charge of the muon, thereby improving also the momentum resolution. In
 192 addition, on simulation a smearing of the momentum measurement is applied to better match
 193 the momentum resolution in data.

194 3.4.2 Electron Reconstruction and Identification

195 The electron objects considered in this analysis are reconstructed within the geometrical accep-
 196 tance $|\eta^e| < 2.5$ and with transverse momentum $p_T^e > 7\text{ GeV}$. Instead of starting from the PF
 197 electron candidate collections, reconstructed candidates are first obtained in an inclusive way
 198 to gain efficiency.

199 The reconstruction combines the information from clusters of energy deposits in the ECAL
 200 and the trajectory in the inner tracker [26–29]. The track-cluster matching is initiated either
 201 “outside-in” from energy cluster measurements, or “inside-out” from track reconstruction. The
 202 energy deposited in the electromagnetic calorimeter (ECAL) is measured in clusters of clusters
 203 (superclusters) which collect Bremsstrahlung photons emitted in the tracker volume. Super-
 204 clusters are used to search for hits in the innermost tracker layers which are used to seed elec-
 205 tron tracks. This procedure is complemented by a tracker-driven approach which improves the
 206 reconstruction efficiency at low p_T . Trajectories in the tracker volume are reconstructed using
 207 a dedicated modeling of the electron energy loss and fitted with a Gaussian sum filter (GSF
 208 tracks). A cleaning is performed to resolve ambiguous cases where several tracks are recon-
 209 structed due to the conversion of radiated photons in the tracker material. Electron candidates
 210 are preselected using loose cuts on track-cluster matching observables to preserve the highest
 211 possible efficiency while removing part of the QCD background.

212

213 The identification of electrons relies on a Boosted Decision Tree (BDT) multivariate technique [30]
 214 that combines observables sensitive to the amount of bremsstrahlung along the electron trajec-
 215 tory, the geometrical and momentum matching between the electron trajectory and associated
 216 clusters, as well as shower-shape observables. The multivariate identification was trained us-
 217 ing a Higgs boson Monte Carlo (MC) sample for the signal and a $W + 1\text{-fake}$ electron data
 218 sample for background. The working point was optimized using a $Z + 1\text{-fake}$ electron data
 219 sample. More details can be found in [20].

220 The cut values on the BDT output resulting from the optimization procedure are summarized
 221 below:

- 222 • $5 < p_T < 10\text{ GeV}$:
 - 223 • $|\eta| < 0.8 : \text{BDT} > 0.47$
 - 224 • $0.8 < |\eta| < 1.479 : \text{BDT} > 0.004$
 - 225 • $|\eta| > 1.479 : \text{BDT} > 0.295$
- 226 • $p_T > 10\text{ GeV}$
 - 227 • $|\eta| < 0.8 : \text{BDT} > 0.5$
 - 228 • $0.8 < |\eta| < 1.479 : \text{BDT} > 0.12$
 - 229 • $|\eta| > 1.479 : \text{BDT} > 0.6$

We additionally require a very loose selection on the distance of the electron track from the primary vertex in order to reject badly reconstructed tracks or tracks from pile-up vertices. In particular we request the significance of the impact parameter to the event vertex, $SIP_{3D} = |\frac{IP}{\sigma_{IP}}|$, to be less than 10, and the distances in the transverse plane, d_{xy} , and along the z axis, d_z , to be less than 0.5 cm and 1 cm respectively. Finally the number of missing hits in the innermost tracker layer must be less than two.

The four-momenta for an electron is obtained by taking angles from the associated GSF track, and the energy from a combination of tracker and ECAL information [31]. The information from the track is measured at the distance-of-closest approach to the beam spot position in the transverse plane. Electron tracks are not re-fitted to the common primary vertex.

The electron momentum scale and resolution can be controlled using Z boson (and J/Ψ) decays to electrons. Some discrepancies with respect to simulation are still present, especially in the low p_T part of the electron spectrum and in the endcaps. Based on $Z \rightarrow ee$ data and simulated events, these discrepancies are dealt with by correcting the energy scale in data and by then determining the smearing needed to apply to the simulated samples so as to have the best match between data and simulation. More detail on the procedure and on its performances can be found in [20, 21].

3.4.3 Lepton Isolation

The isolation of individual e or μ leptons is measured relative to their transverse momentum p_T^ℓ , by summing over charged and neutral particles in a cone $\Delta R = \sqrt{(\eta^\ell - \eta^i)^2 + (\phi^\ell - \phi^i)^2} < 0.4$ around the lepton direction at the interaction vertex:

$$R_{\text{Iso}}^\ell \equiv \left(\sum_{\text{charged}} p_T + \text{MAX} \left[0, \sum_{\text{neutral}} p_T + \sum_{\gamma} p_T - 0.5 \sum_{\text{charged,PU}} p_T \right] \right) / p_T^\ell, \quad (2)$$

where $\sum_{\text{charged}} p_T$, $\sum_{\text{neutral}} p_T$, and $\sum_{\gamma} p_T$ are respectively the scalar sums of the transverse momenta of charged particles from the primary vertex, neutral hadrons, and photons located in the lepton cone. The contribution of pileup photons and neutral hadrons is estimated from the scalar sum of the transverse momenta of charged hadrons from pileup vertices in the cone, $\sum_{\text{charged,PU}} p_T$. This quantity is multiplied by a factor of 0.5, which corresponds approximately to the ratio of neutral to charged hadron production in the hadronization process of pileup interactions, as estimated from simulation. Possible double counting in the isolation evaluation, caused by small differences between reconstructed electron candidates and those identified from the PF algorithm, is avoided by applying specific vetoes [21]. The electrons or muons are considered isolated if $R_{\text{Iso}}^\ell < 0.4$.

3.4.4 Preselection Efficiency

The efficiency of the lepton preselection has been computed in data and in simulation with the tag-and-probe technique [32]. By using appropriate definitions for probes, the overall efficiency per lepton can be factorized in a series of terms, that can be measured independently:

$$\epsilon = \epsilon_{\text{RECO}|\text{trackORclustering}} \times \epsilon_{\text{ID}|\text{RECO}} \times \epsilon_{\text{ISO}|\text{ID}} \quad (3)$$

The details of the measurements are described in [21, 33]. In the following we just report the efficiency distributions for electrons and muons for the three separate contributions: reconstruction efficiency, identification efficiency, isolation efficiency (Fig. 4 5 6 7 8). From the measured values we have extracted data/simulation scale factors that we use in the analysis to correct the expected MC yields.

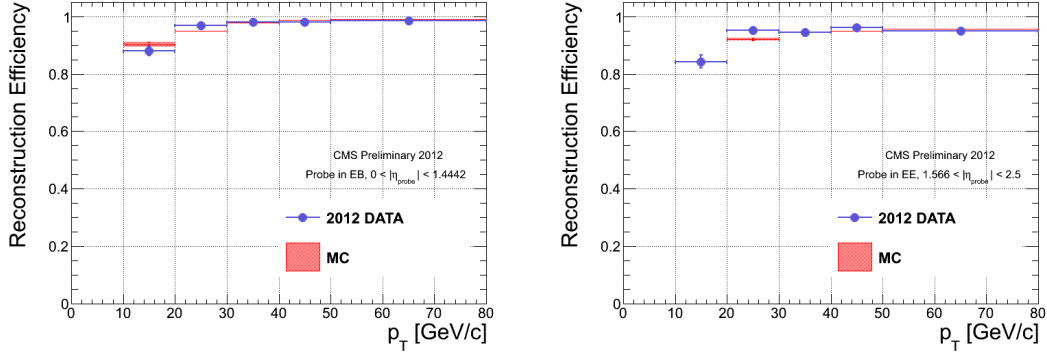


Figure 4: Efficiency to reconstruct a signal electron candidate (GSF track plus supercluster matching) for ECAL barrel, $|\eta| < 1.479$ (left), and ECAL endcaps, $|\eta| > 1.479$ (right), as a function of the electron p_T .

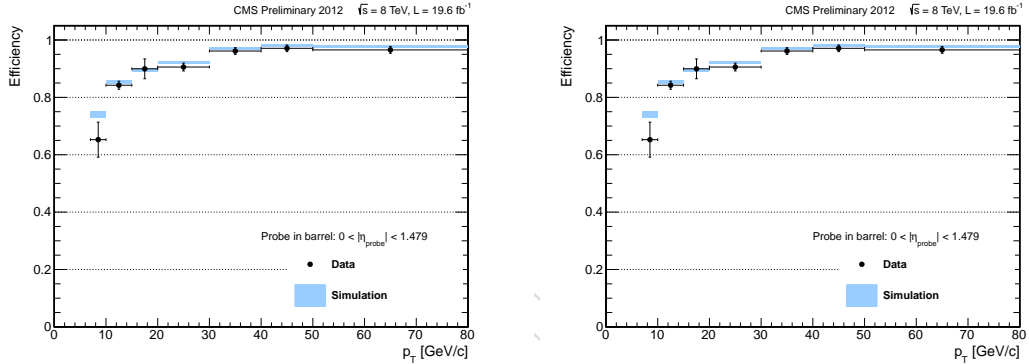


Figure 5: Efficiency of the identification and isolation criteria for a reconstructed signal electron for ECAL barrel, $|\eta| < 1.479$ (left), and ECAL endcaps, $|\eta| > 1.479$ (right), as a function of the electron p_T .

267 3.5 Lepton MVA Discriminator

268 We have then additional handles to tighten the lepton identification in order to suppress further
269 the reducible backgrounds from events with non-prompt leptons misidentified as prompt ones,
270 or opposite-sign dilepton events in which the charge of one of the leptons is mismeasured,
271 preserving high efficiency on signal leptons from W , Z , and τ decays.

272 In this analysis the most important source of misidentified leptons comes from the decay of
273 b-hadrons (from $t\bar{t}$ +jets, DY+jets, and W+jets events). We therefore developed a multivariate
274 discriminator based on boosted decision tree (BDT) techniques to distinguish signal leptons
275 (from W , Z , or τ decays) from background leptons (mostly from b-hadron decays). We refer
276 to it as the *lepton MVA discriminator* throughout this document. The multivariate discriminator
277 is trained using simulated signal leptons from the $t\bar{t}H$ MC sample and fake leptons from the
278 $t\bar{t}$ -jets MC sample, separately for muons and electrons and for several bins of p_T and η listed
279 in Table 6.

280 The input variables considered can be categorized into three groups: variables related to the
281 impact parameter of the lepton computed with respect to the primary vertex, variables related
282 to the isolation of the lepton considering separately the neutral and charged candidate deposits
283 in the lepton isolation cone, and variables related to the jet reconstructed in the event closest
284 to the lepton. For this last set of variables we use the PF jets reconstructed around the leptons,

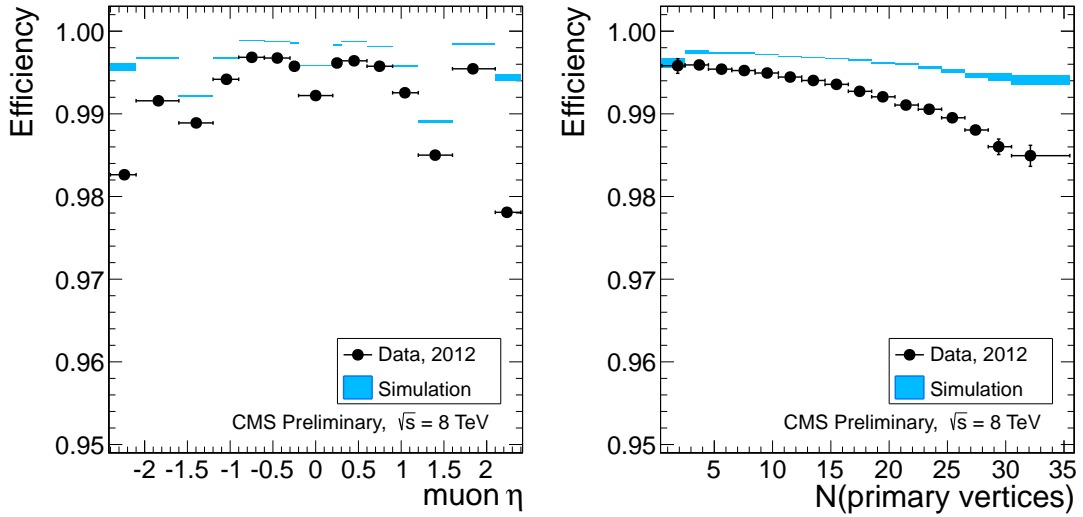


Figure 6: Efficiency to reconstruct the muon tracker track as a function of the $|\eta|$ of muon object reconstructed in the muon spectrometer (left), and as a function of the number of vertices reconstructed in the events (right).

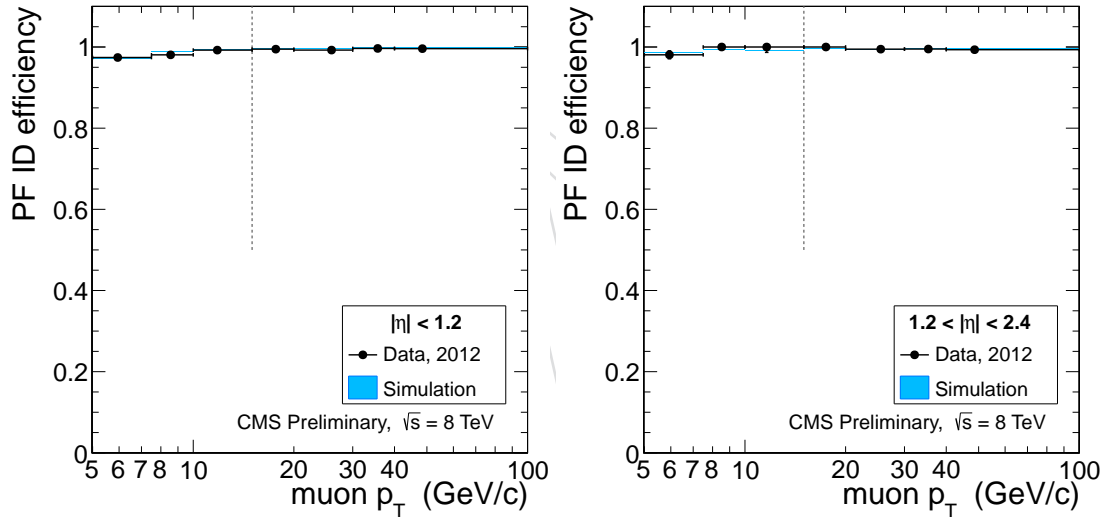


Figure 7: Efficiency of the muon identification criteria as a function of p_T of the muon tracker track for the muon system barrel region, $|\eta| < 1.2$ (left), and for the endcaps region $|\eta| > 1.2$ (right).

requiring $\Delta R = \sqrt{(\eta^\ell - \eta^{jet})^2 + (\phi^\ell - \phi^{jet})^2} < 0.5$; charged hadrons from pile-up primary vertices are not removed prior to the jet clustering. The three discriminating variables relying on jets are the ΔR distance between the lepton and the closest jet, the ratio between the p_T of the lepton and the p_T of the jet and the CSV b-tagging discriminator value of the jet.

In the case of electrons, the multivariate discriminator used for the preselection and the number of missing hits in the innermost tracker layer are also used as inputs, to suppress backgrounds from charged hadrons misidentified as electrons or from photon conversions.

The detailed list of variables used in the training is summarized below:

- For muons and electrons:
 - significance of the impact parameter with respect to the primary vertex,

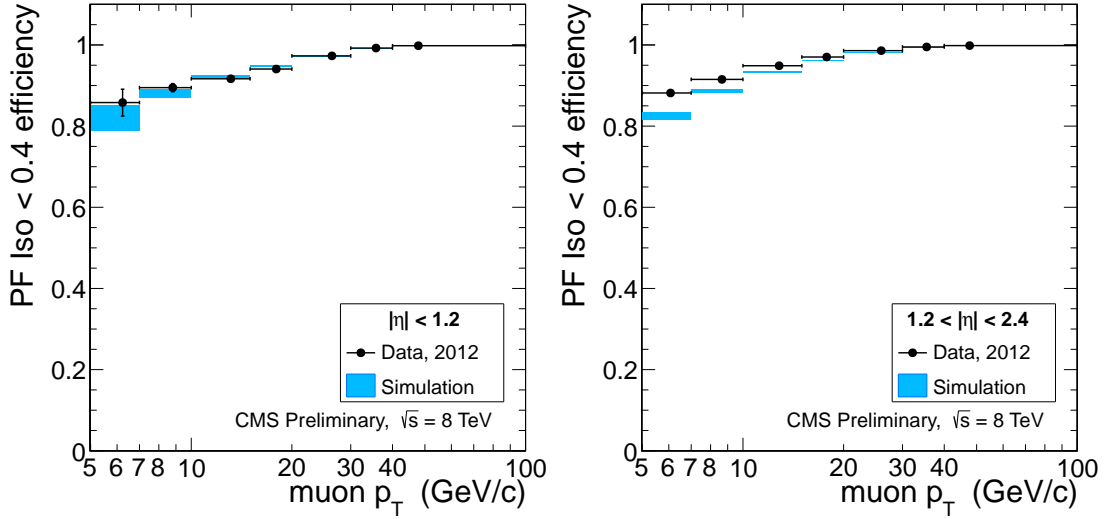


Figure 8: Efficiency of the muon isolation criteria as a function of p_T of the identified muon object for the muon system barrel region, $|\eta| < 1.2$ (left), and for the endcaps region $1.2 < |\eta| < 2.4$ (right).

Table 6: Transverse momentum and pseudorapidity regions used to trained separately the multivariable discriminator.

Electrons	$ \eta $	p_T
low-cb	0-0.8	<10
low-fb	0.8-1.479	<10
low-ec	1.479-2.5	<10
high-cb	0-0.8	>10
high-fb	0.8-1.479	>10
high-ec	1.479-2.5	>10

Muons	$ \eta $	p_T
low-b	<1.5	<15
low-e	>1.5	<15
high-b	<1.5	>15
high-c	>1.5	>15

$$295 \quad |SIP_{3D}| = \frac{|IP|}{\sigma_{IP}};$$

- $$296 \quad \bullet \text{ the contribution of the charged hadrons in the lepton isolation cone, } \sum_{\text{charged}} p_T;$$
- $$297 \quad \bullet \text{ the contribution of the neutral hadrons and photons in the lepton isolation cone, } \sum_{\text{neutral}} p_T + \sum_{\gamma} p_T;$$
- $$298 \quad \bullet \Delta R \text{ distance between the lepton and the closest jet;}$$
- $$299 \quad \bullet \text{ the ratio between the } p_T \text{ of the lepton and the } p_T \text{ of the closest jet;}$$
- $$300 \quad \bullet \text{ the CSV b-tagging discriminator value of the closest jet;}$$

- $$301 \quad \bullet \text{ For muons only:}$$

- $$302 \quad \bullet \text{ distance in the transverse place, } d_{xy}, \text{ with respect to the primary vertex;}$$
- $$303 \quad \bullet \text{ distance on the z axis, } d_z, \text{ with respect to the primary vertex;}$$

- $$304 \quad \bullet \text{ For electrons only:}$$

- $$305 \quad \bullet \text{ the multivariate discriminator used for the electron preselection;}$$

- 307 • number of missing hits in the innermost tracker layer.

308 Fig. 9 shows the correlations between the variables listed above for the signal and background
 309 samples used for training the multivariate discriminator. Fig. 10 shows the separation power
 310 of the BDT outputs. In both figures only a few bin categories are considered.

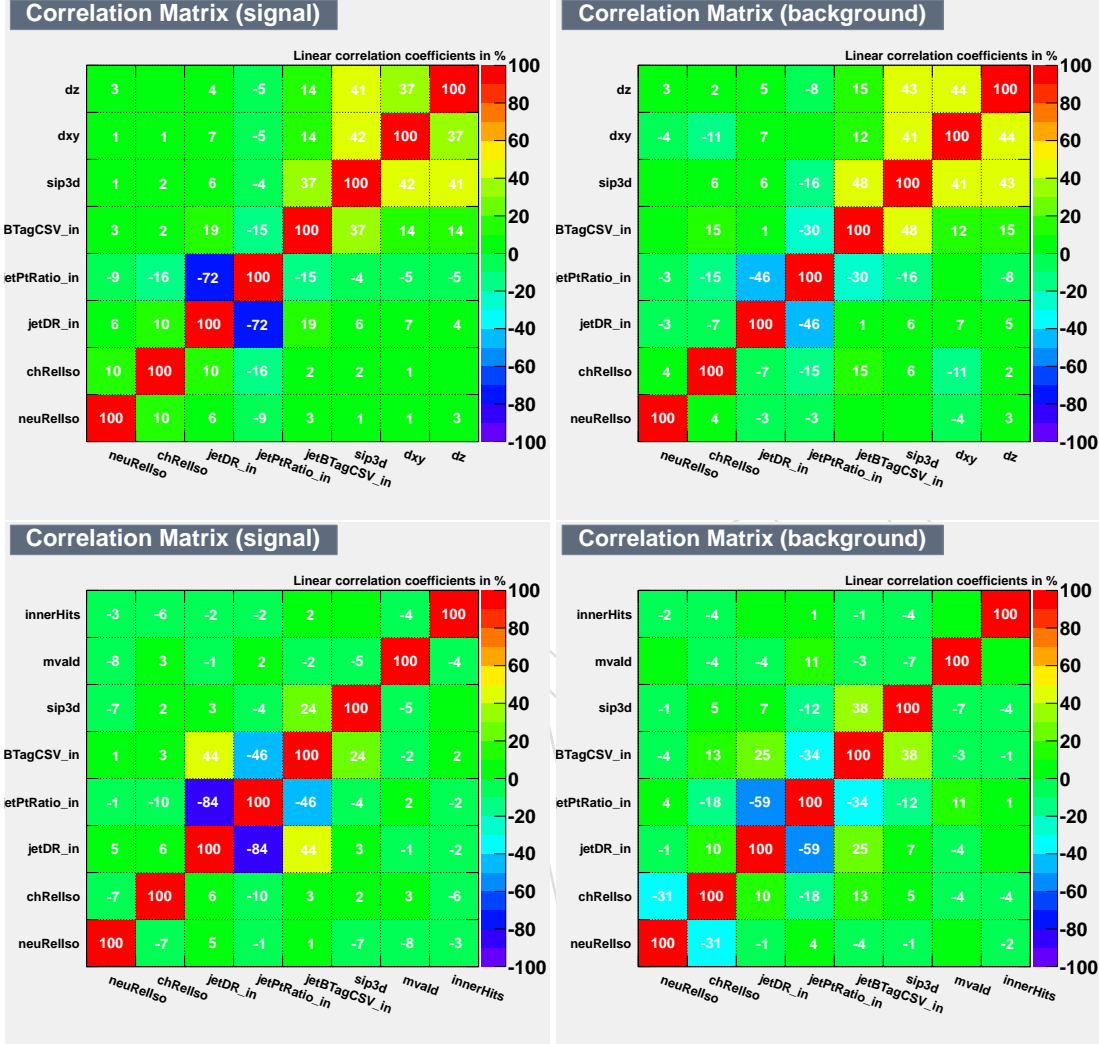


Figure 9: The correlations between the input variables of the lepton MVA discriminator. On the top row the correlations are shown for the high-e muon category and in the bottom row for the low-cb electron category.

311 The gain that we obtain in this analysis using the lepton MVA discriminator is shown in Fig. 11.
 312 In this figure there is one plot for each of the considered final states (two lepton same-sign $\mu\mu$,
 313 two lepton same-sign ee , two lepton same-sign $e\mu$, three leptons, four leptons); in each plot the
 314 ROC curve obtained by applying a lepton MVA cut is compared to the ROC curves that can
 315 be obtained simply applying a cut on the PF isolation variable or on the SIP_{3D} variable. Two
 316 working points of the lepton MVA discriminator are used in this analysis: a tight one (>0.7)
 317 used for the search in the dilepton and trilepton final states, and a loose one (>-0.3) used for the
 318 four-lepton final state. When using the tight working point, to further suppress background
 319 events with leptons arising from photon conversions we reject electrons with missing hits in
 320 the innermost layer or associated with a successfully reconstructed conversion vertex [34].
 321 These two working points are compared with the usual tight lepton selections (red markers

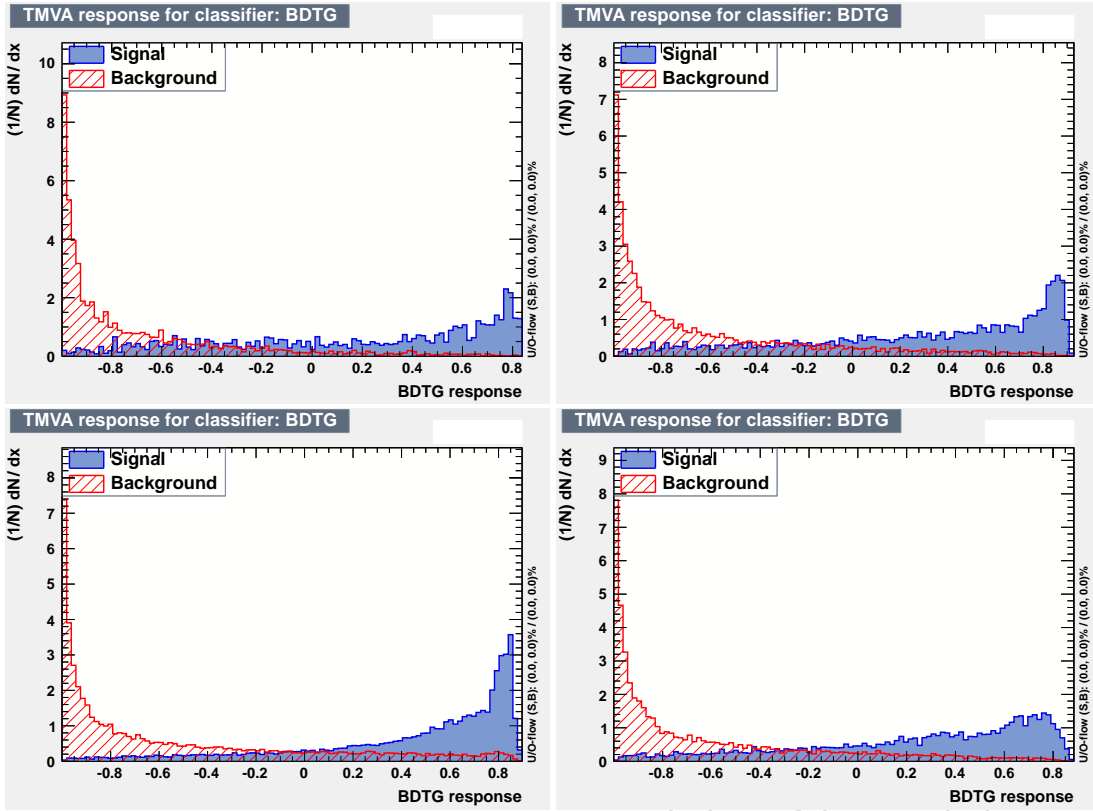


Figure 10: The BDT output of the lepton MVA discriminator. The comparison between the signal and background shapes is shown for few categories. From top right to bottom left: the muon low- e category, the muon low- b category, the electron high-fb category, the electron high-ec category.

in the plots) in which tighter cuts on the isolation variable, on the impact parameter variables and on the identification criteria are applied. The ROC curves are obtained using the $t\bar{t}H$ and $t\bar{t}+j$ -jets MC events that passed the selections described in section[ref], without the cut on the lepton MVA discriminator.

3.6 Validation with data

The agreement between data and simulation of the input variables and the final lepton multivariate discriminator is validated in dedicated control regions. For signal leptons we select control samples with high purity of $Z \rightarrow \mu^+\mu^-$, $Z \rightarrow e^+e^-$, $Z \rightarrow \tau^+\tau^-$; for background leptons we select samples enriched in leptons from b-hadron decay with $Z + \ell$ and $t\bar{t} + \ell$ control regions.

The detailed definitions of the control regions is described in the following:

- $Z \rightarrow \mu^+\mu^-$ and $Z \rightarrow e^+e^-$:
 - at least two preselected leptons with the highest p_T ones being of same flavour and opposite sign ($\mu^+\mu^-$, e^+e^-);
 - if there are additional leptons, the third one (ordered in p_T) must have $p_T < 10$ GeV;
 - $E_T^{miss} < 30$ GeV;
 - the invariant mass of the best Z ($m_{\ell^+\ell^-}$ with mass closest to the Z boson mass) must be within [60,120] GeV;

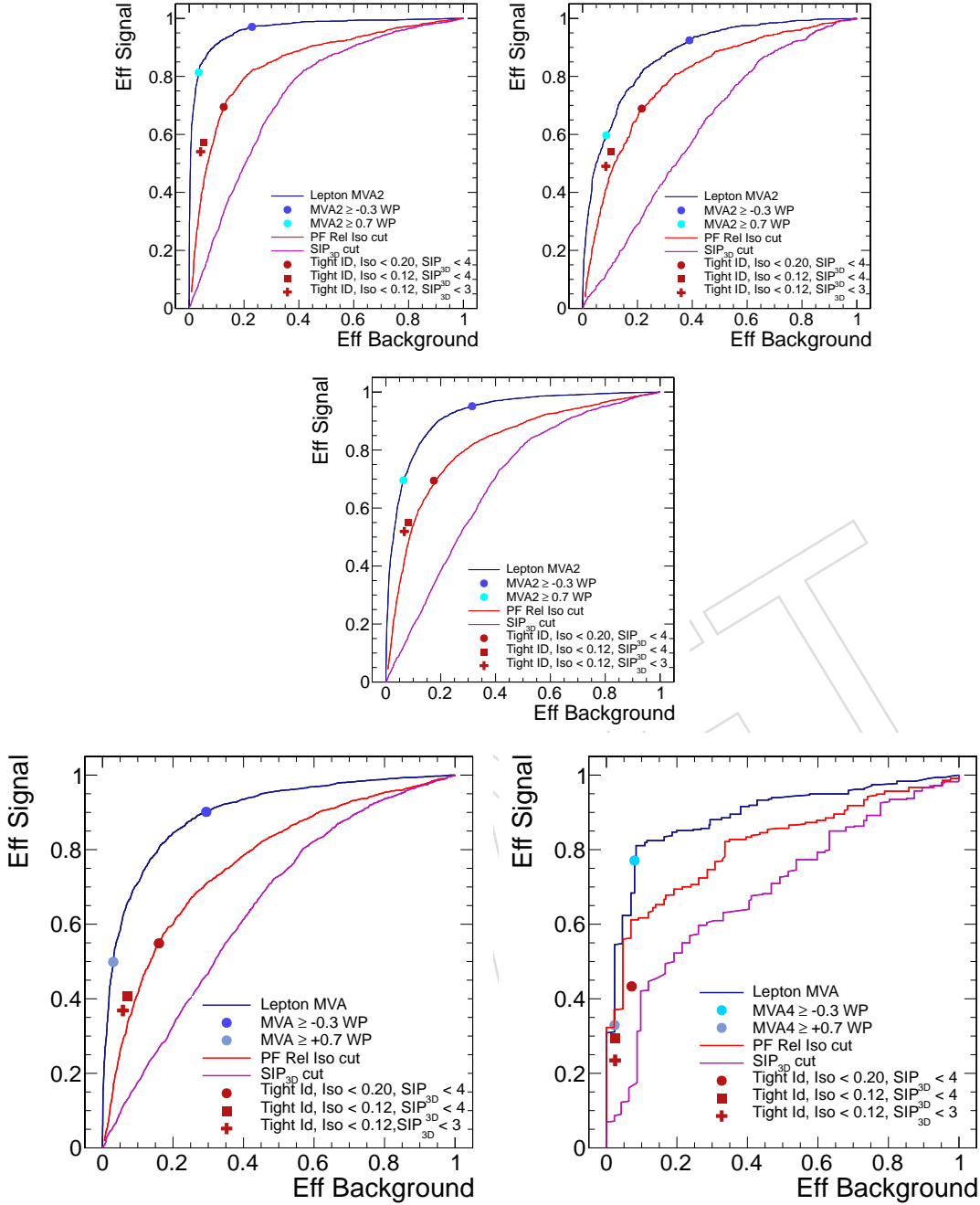


Figure 11: ROC curves to compare the performance of the lepton MVA discriminator with respect to the other usual tight lepton selections. From top left to bottom right: two lepton same-sign $\mu\mu$ channel, two lepton same-sign ee channel, two lepton same-sign $e\mu$ channel, three leptons channel, four leptons channel.

- 341 • tight cuts are applied on the leading lepton, $R_{\text{Iso}}^{\ell} < 0.2$ and $p_T > 25 \text{ GeV}$.
 342 These control regions are used to check the agreement between data and
 343 simulation of the input and output variables of the lepton MVA discrimi-
 344 nator for the second lepton.
- 345 • $Z \rightarrow \tau^+\tau^-$:
- 346 • at least two preselected leptons with the highest p_T ones being of opposite

- flavour and opposite sign (μ^+e^- , μ^-e^+);
- if there are additional leptons, the third one (ordered in p_T) must have $p_T < 10$ GeV;
 - $E_T^{miss} LD < 0.2$;
 - the di-lepton $p_T < 20$ GeV;
 - the minimum invariant mass of any $\ell\ell$ couples must be within [20,80] GeV;
 - tight cuts on the electron, $R_{Iso}^\ell < 0.1$, $p_T > 25$ GeV, $\eta < 1.479$, $SIP_{3D} < 1.5$. This control regions is used to check the agreement between data and simulation of the input and output variables of the lepton MVA discriminator for the muon from τ decay.
 - tight cuts on the muon, $R_{Iso}^\ell < 0.1$, $p_T > 25$ GeV, $\eta < 1.2$, $SIP_{3D} < 1.5$. This control regions is used to check the agreement between data and simulation of the input and output variables of the lepton MVA discriminator for the electron from τ decay.
- $Z + \ell$:
- three preselected leptons with the highest p_T ones being of same flavour and opposite sign ($\mu^+\mu^-$, e^+e^-) and the third one with $p_T < 30$ GeV;
 - tight working point of the lepton MVA discriminator applied on the two leading leptons;
 - the minimum invariant mass of any $\ell\ell$ couples must be > 12 GeV;
 - the invariant mass of the two leading leptons must be within 10 GeV from the nominal Z boson mass;
 - the transverse mass of the E_T^{miss} and the third lepton must be < 40 GeV;
 - $E_T^{miss} LD < 0.3$;
 - this control region is used to check the agreement between data and simulation of the input and output variables of the lepton MVA discriminator for a fake lepton (third lepton in this selection).
- $t\bar{t} + \ell$:
- at least three preselected leptons with the highest p_T ones being of opposite flavour and opposite sign (μ^+e^- , μ^-e^+);
 - tight working point of the lepton MVA discriminator applied on the two leading leptons;
 - the minimum invariant mass of any $\ell\ell$ couples must be > 12 GeV;
 - Z veto, the difference between the invariant mass of the best Z and the nominal Z mass must be > 15 GeV;
 - at least two central jets with $p_T > 25$ GeV;
 - at least one central jets with $p_T > 25$ GeV with medium CSV b-tagging;
 - this control region is used to check the agreement between data and simulation of the input and output variables of the lepton MVA discriminator for a fake lepton (third lepton in this selection).

Small corrections to better match the data distributions of the input variables are applied to the simulation before performing the training of the MVA discriminant, and also whenever the MVA is output is evaluated on simulated events.

391 Corrections for prompt leptons are derived for events in the $Z \rightarrow \ell\ell$ control region, as function
 392 of lepton type, p_T and η , for the impact parameter variables (SIP_{3D} , d_{xy} and d_z), the ΔR separation
 393 between lepton and jet and the ratio of the p_T of the lepton and the jet. These corrections
 394 are applied to all prompt leptons from simulations, including the ones from tau decays; the cor-
 395 rections to the impact parameter variables are also applied to simulated non-prompt leptons
 396 that do not originate from a b-jet, as they mostly have prompt-like impact parameter. Approximate
 397 correction for some of these variables are derived also for non-prompt leptons from b jets,
 398 from the $Z + \ell$ control region. A closure test of the corrections on leptons from $t\bar{t} \rightarrow e^\pm \mu^\mp$ is
 shown in Fig. 12.

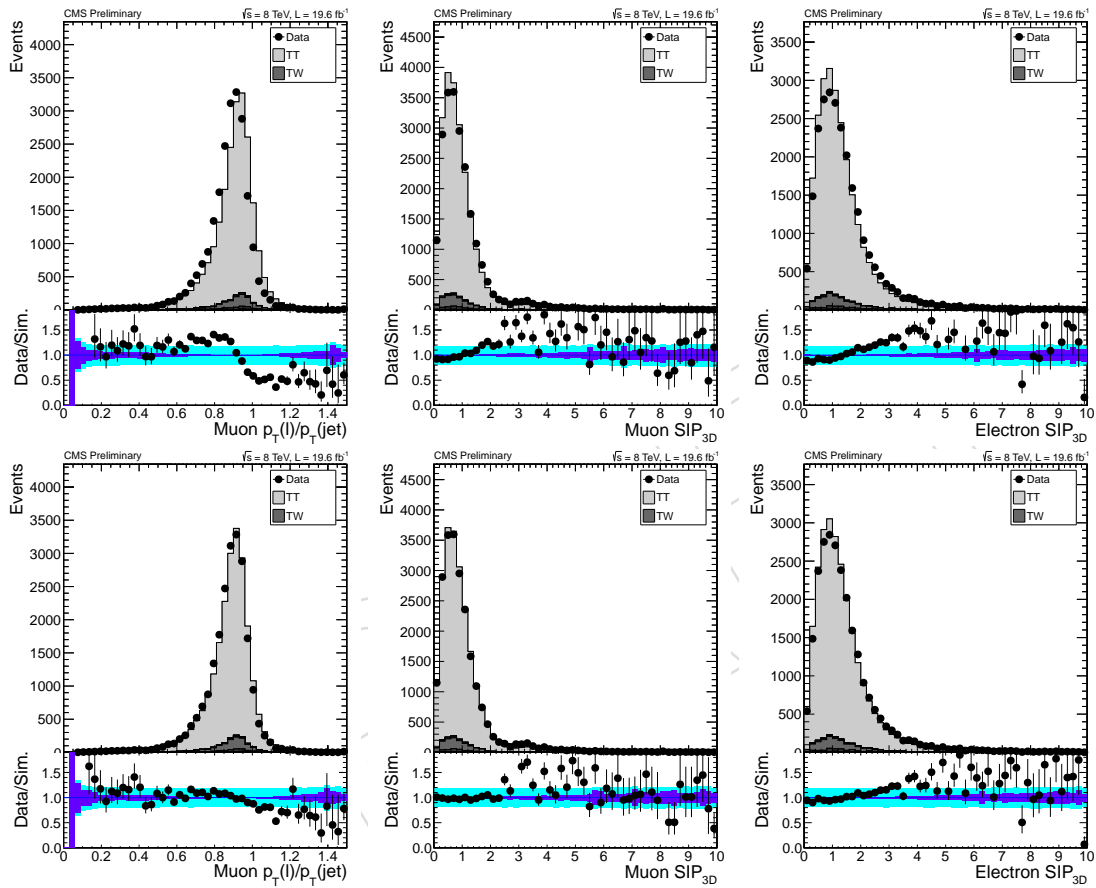


Figure 12: Data to simulation comparison for the shapes of some input variables to the lepton MVA discriminator in $t\bar{t} \rightarrow e^\pm \mu^\mp$ events before and after the corrections derived from $Z \rightarrow \ell\ell$ events. From left to right: the ratio of the lepton p_T to the jet p_T for muons, the SIP_{3D} for muons, and the SIP_{3D} for electrons. The plots in the top row are before the correction, the ones in the bottom row are after the correction.

399

400 Fig. 13 shows the data and simulation agreement after these corrections are applied, for some
 401 of the input variables to the lepton MVA discriminator in the $Z \rightarrow \mu^+\mu^-$ control region. Fig. 14,
 402 Fig. 15, Fig. 16, and Fig. 17 show the same for the $Z \rightarrow e^+e^-$, $Z \rightarrow \tau^+\tau^-$, $Z + \ell$, and $t\bar{t} + \ell$ control
 403 regions. The MC is normalized to the observed event yields in data; scale factors to take into
 404 account different efficiencies of lepton preselection, lepton MVA discriminator, b-tagging in
 405 data and simulation are not included in these plots. The agreement is fairly good.

406 In appendix C the agreement between data and simulation of the input variables is shown for
 407 events with high pile-up (we request at least 20 reconstructed vertices), using the $Z \rightarrow \mu^+\mu^-$,

408 $Z \rightarrow e^+e^-$ control samples.

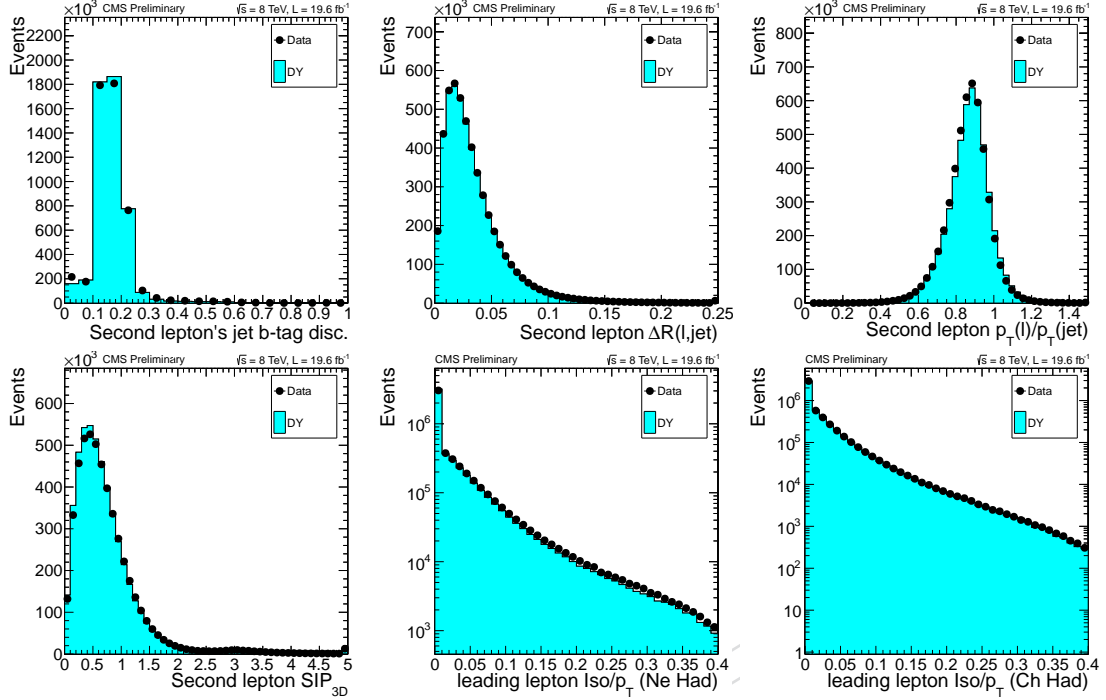


Figure 13: Data to simulation comparison for the shapes of the input variables to the lepton MVA discriminator in the $Z \rightarrow \mu^+\mu^-$ control region. From top left to bottom right the following variables for the signal muon are shown: the CSV b-tagging discriminator value of the closest jet, ΔR distance between the lepton and the closest jet, the ratio between the p_T of the lepton and the p_T of the closest jet, SIP_{3D} of the lepton, the neutral hadrons iso deposit, and the charged hadrons iso deposit.

409 Fig. 18 shows the data and simulation comparison for the BDT output of the lepton MVA dis-
 410 criminator for signal muons and electrons in different p_T and η regions, using the $Z \rightarrow \mu^+\mu^-$
 411 and the $Z \rightarrow e^+e^-$ control regions. The residual disagreement is taken into account in the
 412 analysis applying to the simulation data to MC scale factors extracted from the measured effi-
 413 ciencies of the lepton MVA discriminator working points. The measurement of the efficiencies
 414 is performed for signal leptons and it is described in the following section. Backgrounds with
 415 misidentified leptons are estimated directly from data, as described in section 7.

416 3.6.1 Lepton MVA Efficiency

417 With the usual tag-and-probe technique we have computed the efficiencies of the loose and
 418 tight working point of the lepton MVA discriminator for preselected signal leptons from $Z \rightarrow$
 419 $\ell^+\ell^-$ decays. The results are shown in Fig. 19 and Fig. 20. From these measurements we have
 420 extracted data to simulation scale factors in several lepton p_T and η bins, which are then used
 421 in the analysis to correct the simulated performances of the lepton MVA discriminator.

422 With the tight working point the efficiency to select signal muons in the $|\eta^\mu| < 1.5$ ($1.5 < |\eta^\mu| <$
 423 2.4) region is on the order of 60% (40%) for $p_T^\mu \sim 10$ GeV and reaches the plateau of 98% (95%)
 424 at $p_T^\mu \sim 45$ GeV; for signal electrons in ECAL barrel (ECAL endcap) it is on the order of 40%
 425 (20%) for $p_T^e \sim 10$ GeV and reaches the plateau of 90% (70%) at $p_T^e \sim 45$ GeV. The efficiency to
 426 select muons (electrons) from b-hadron decays is less than 5% (between 5-10%) averaging over
 427 the whole p_T and η ranges.

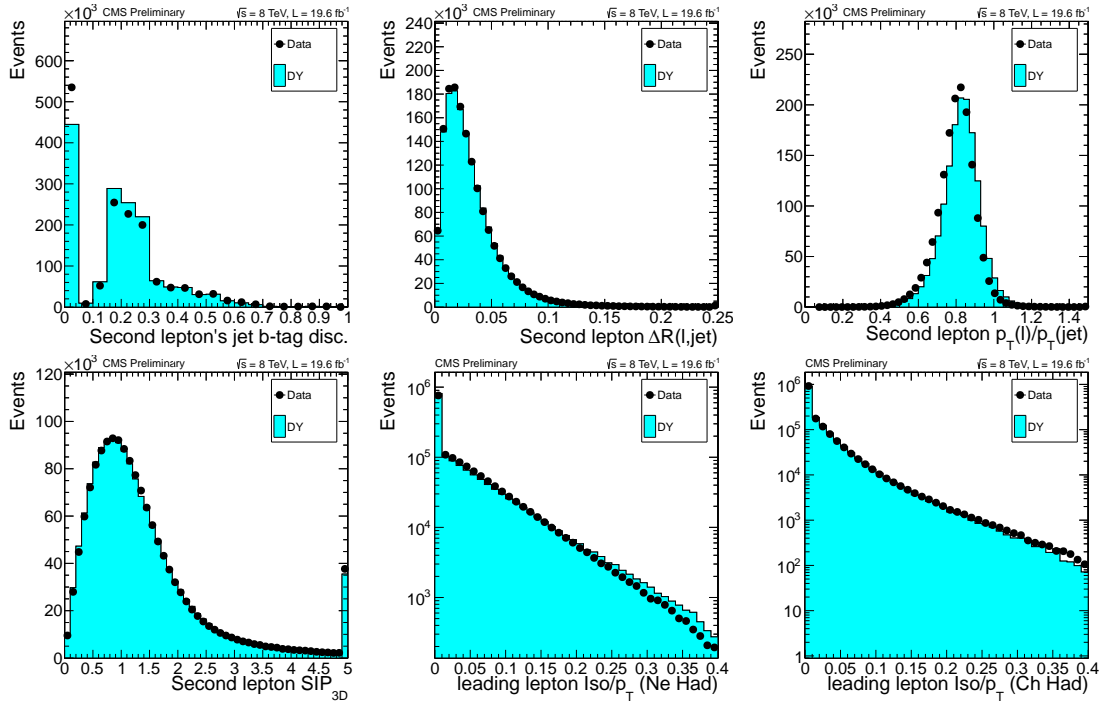


Figure 14: Data to simulation comparison for the shapes of the input variables to the lepton MVA discriminator in the $Z \rightarrow e^+e^-$ control region. From top left to bottom right the following variables for the signal electron are shown: the CSV b-tagging discriminator value of the closest jet, ΔR distance between the lepton and the closest jet, the ratio between the p_T of the lepton and the p_T of the closest jet, SIP_{3D} of the lepton, the neutral hadrons iso deposit, and the charged hadrons iso deposit.

428 3.7 Tight Charge

429 In the dilepton final state additional requirements on the quality of the charge assignment are
 430 applied to suppress opposite-sign events in which the charge of one of the leptons is mismeas-
 431 ured. For the electrons we require consistency between the independent measurements of the
 432 charge from the ECAL supercluster and the tracker, while for the muons we require the track
 433 transverse momentum to be well measured ($\Delta p_T / p_T < 0.2$). With the usual tag-and-probe
 434 technique we measured the efficiencies of this requirements in data and simulation to extract
 435 data to MC scale factors to be used in the analysis. The efficiencies of the tight charge require-
 436 ments are computed with respect to probe leptons that have passed the preselection and the
 437 MVA discriminator tight working point. The results are shown in Fig. 21.

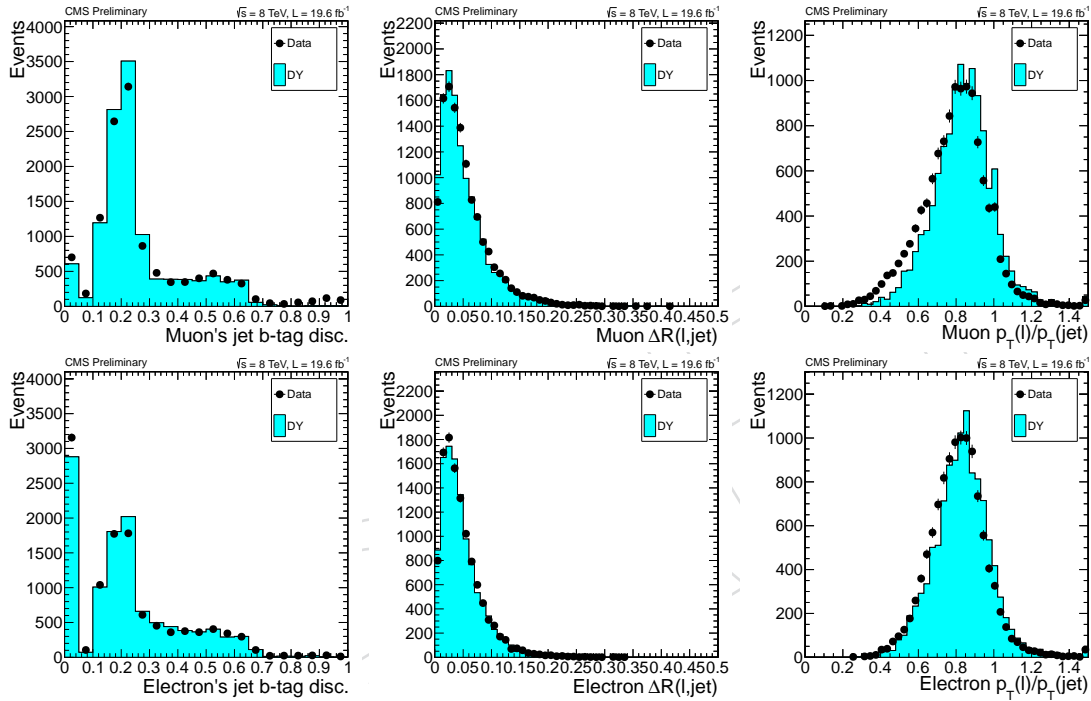


Figure 15: Data to simulation comparison for the shapes of the input variables to the lepton MVA discriminator in the $Z \rightarrow \tau^+ \tau^-$ control region. In the first row the following variables for the signal muon from τ decay are shown: the CSV b-tagging discriminator value of the closest jet, ΔR distance between the lepton and the closest jet, the ratio between the p_T of the lepton and the p_T of the closest jet. In the second row the same variables are shown for the signal electron from τ decay.

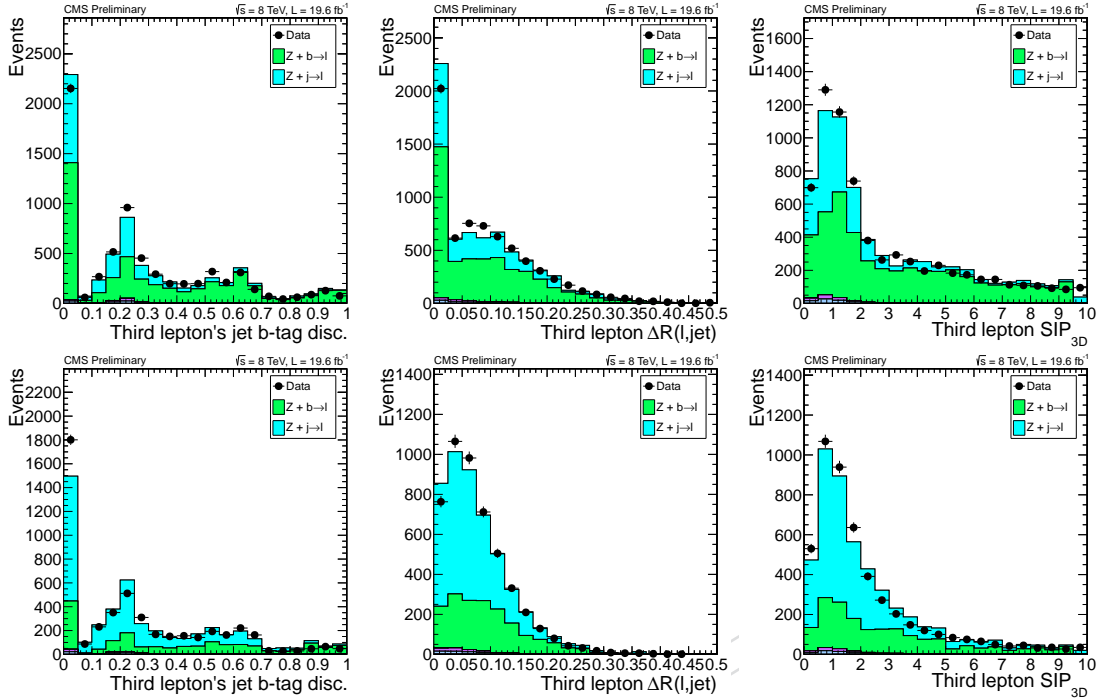


Figure 16: Data to simulation comparison for the shapes of the input variables to the lepton MVA discriminator in the $Z + \ell$ control region. In the first row the following variables for the fake muon (from b-hadrons decay, or from light jets) are shown: the CSV b-tagging discriminator value of the closest jet, ΔR distance between the lepton and the closest jet, SIP_{3D} of the lepton. In the second row the same variables are shown for the the fake electron (from b-hadrons decay, or from light jets)

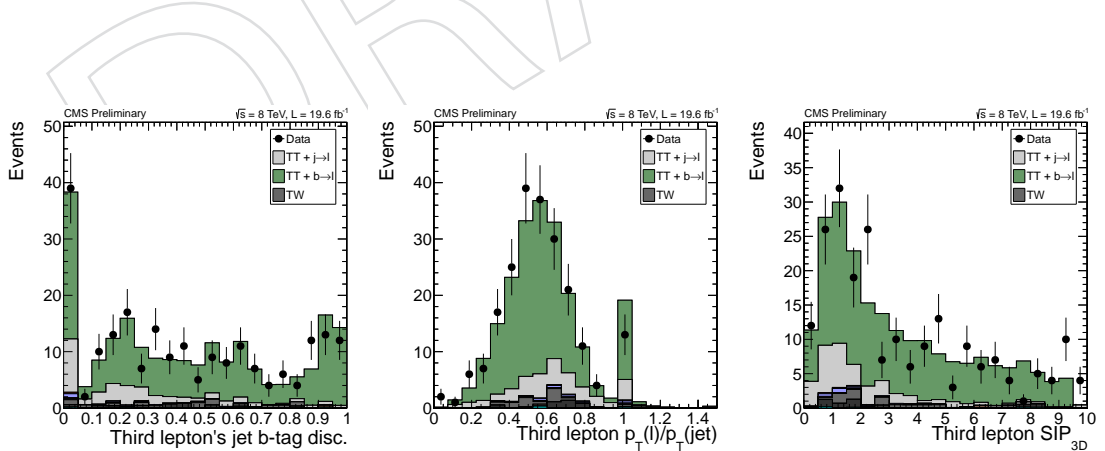


Figure 17: Data to simulation comparison for the shapes of the input variables to the lepton MVA discriminator in the $t\bar{t} + \ell$ control region. From left to write the following variables for the fake lepton (from b-hadrons decay, or from light jets) are shown: the CSV b-tagging discriminator value of the closest jet, ΔR distance between the lepton and the closest jet, SIP_{3D} of the lepton.

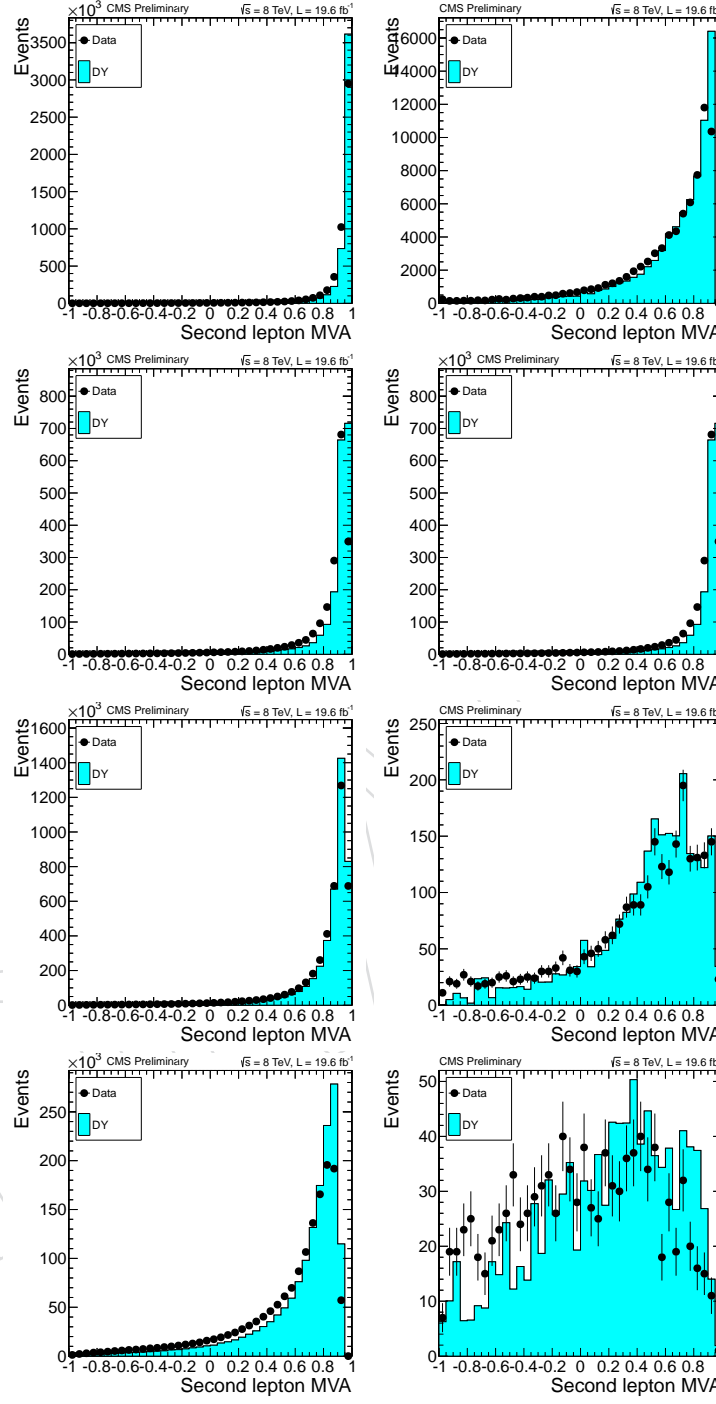


Figure 18: Data to simulation comparison for the BDT output of the lepton MVA discriminator in the $Z \rightarrow \mu^+ \mu^-$ and the $Z \rightarrow e^+ e^-$ control regions. From top left to bottom right the comparison is shown for: muons with $p_T > 15 \text{ GeV}$ and $|\eta| < 1.5$, $p_T < 15 \text{ GeV}$ and $|\eta| < 1.5$, $p_T > 15 \text{ GeV}$ and $|\eta| > 1.5$, $p_T < 15 \text{ GeV}$ and $|\eta| > 1.5$, electrons with $p_T > 10 \text{ GeV}$ and $|\eta| < 1.479$, $p_T < 10 \text{ GeV}$ and $|\eta| < 1.479$, electrons with $p_T > 10 \text{ GeV}$ and $|\eta| > 1.479$, $p_T < 10 \text{ GeV}$ and $|\eta| > 1.479$.

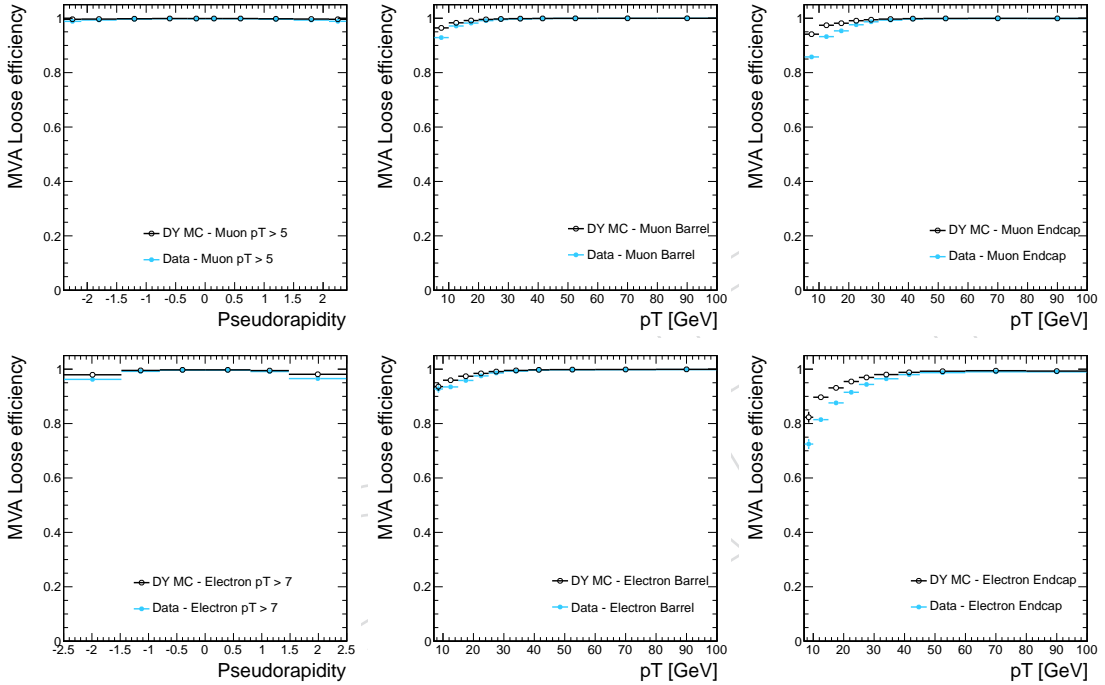


Figure 19: Efficiencies for the loose lepton MVA discriminator working point with respect to preselected muons and electrons from Z decays, extracted with the tag-and-probe technique on data and simulation. From top left to bottom right the efficiencies are shown with respect to the muon η , the muon p_T for $|\eta| < 1.5$, the muon p_T for $|\eta| > 1.5$, the electron η , the electron p_T for $|\eta| < 1.479$, and the electron p_T for $|\eta| > 1.479$.

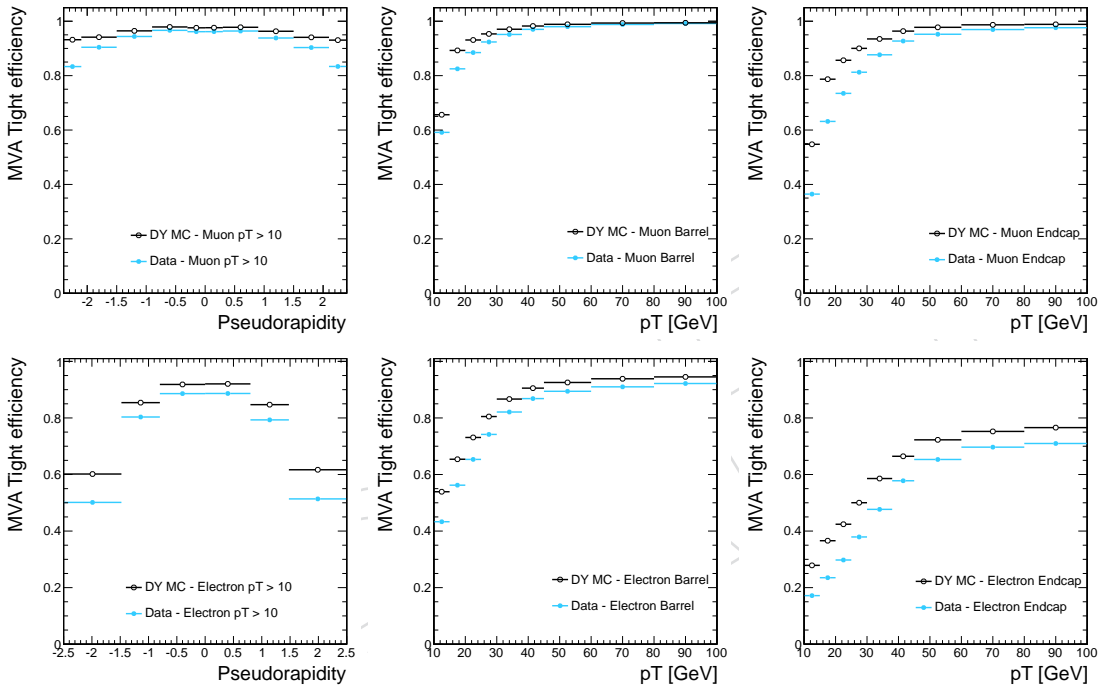


Figure 20: Efficiencies for the tight lepton MVA discriminator working point with respect to preselected muons and electrons from Z decays, extracted with the tag-and-probe technique on data and simulation. From top left to bottom right the efficiencies are shown with respect to the muon η , the muon p_T for $|\eta| < 1.5$, the muon p_T for $|\eta| > 1.5$, the electron η , the electron p_T for $|\eta| < 1.479$, and the electron p_T for $|\eta| > 1.479$.

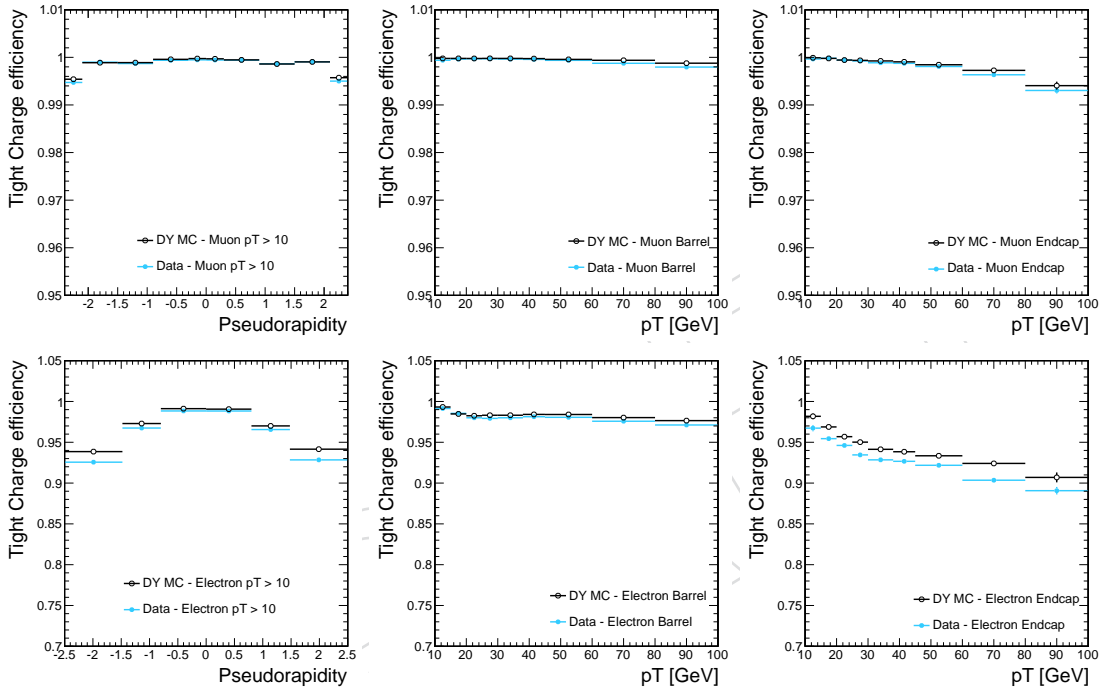


Figure 21: Efficiencies for the tight charge requirements with respect to preselected muons and electrons from Z decays which have passed the tight working point of the lepton MVA discriminator. The efficiencies are extracted with the tag-and-probe technique on data and simulation. From top left to bottom right the efficiencies are shown with respect to the muon η , the muon p_T for $|\eta| < 1.5$, the muon p_T for $|\eta| > 1.5$, the electron η , the electron p_T for $|\eta| < 1.479$, and the electron p_T for $|\eta| > 1.479$.

4 Event selection

We select candidate events that match our decay signatures by requiring combinations of reconstructed objects. There are three features that are common to all three of our decay signatures and motivate selection requirements that are applied to every category. First, all of our data is recorded on either double-lepton or triple-electron triggers. We require each event to have one lepton with transverse momentum greater than 20 GeV and another with transverse momentum greater than 10 GeV in order to be above the trigger selection thresholds. Second, our simulation does not model lepton pairs with very low invariant mass. We reject any event that has a pair of leptons with an invariant mass less than 12 GeV. Lastly, each of our events will have a pair of top quarks that decays to two b-jets. We therefore require each event to have at least two jets with $|\eta| < 2.4$, where both satisfy the loose working point of the CSV b-tagger, or at least one satisfies the medium working point of the same tagger. Besides these three requirements, the other selection components are specific to each channel.

We require same-sign dilepton events to have exactly two leptons with identical charge, and at least four hadronic jets. We ask for each lepton to pass the lepton preselection, the tight working point of the lepton MVA discriminant, and the charge-quality requirements. We apply two additional selections to reject pairs of electrons from Z boson decays with a mismeasured electron charge: the invariant mass of the electrons must be more than ± 10 GeV from the mass of the Z boson, and we require significant missing transverse momentum, $E_T^{\text{miss}} LD > 0.2$. In all three final states, to further suppress reducible backgrounds, especially not from $t\bar{t}$, we raise the threshold on the p_T of the second lepton to 20 GeV, and we require the scalar sum of the transverse momenta of the two lepton and of the E_T^{miss} to be above 100 GeV.

Our three-lepton candidate selection begins by requiring exactly three leptons that pass the lepton preselection and tight working point of the lepton MVA discriminant. The transverse momenta of two leptons is dictated by the trigger selection. The final lepton can have a transverse lepton as low as allowed by the preselection electron and muon requirements (7 and 5 GeV, respectively). We apply two additional selections to reject background processes with Z bosons. First, we require that no pair of same-flavor opposite-sign lepton masses fall within ± 10 GeV of the mass of the Z boson. We then add an $E_T^{\text{miss}} LD$ requirement, with a tighter threshold if the event has a pair of leptons with the same flavor and opposite sign. For events with large jet multiplicity (≥ 4 jets), where the contamination from the Z background is smaller, the requirement on $E_T^{\text{miss}} LD$ is not applied.

The four-lepton candidate selection asks for exactly four leptons that each pass the lepton preselection and the loose working point of the lepton MVA discriminant. The sum of the electrical charges of the four leptons is required to be zero. The transverse momenta of two leptons are fixed by the trigger selection. The transverse momenta of the other two leptons can be as low as allowed by the preselection. The background from ZZ is larger than our signal and can contain two on-shell Z bosons, while our signal contains at most one on-shell Z. We reject the ZZ background by removing events that have any pair of same-flavor opposite-sign leptons within ± 10 GeV of the mass of the Z boson.

The observed event yields in data for each final state and the expectations from the different physical processes are summarised in table 7. The details of the calculations of the signal and background yields will be discussed in the sections that follow.

Figure 22 shows the jet multiplicity distribution for events passing the 2ℓ selection with at least four jets.

Figure 23 shows the jet multiplicity distributions for events passing the 3ℓ and 4ℓ selections.

	$\mu\mu$	ee	$e\mu$	3ℓ	4ℓ
$t\bar{t}H, H \rightarrow WW$	2.0 ± 0.3	0.9 ± 0.1	2.7 ± 0.4	3.2 ± 0.6	0.28 ± 0.05
$t\bar{t}H, H \rightarrow ZZ$	0.1 ± 0.0	0.0 ± 0.0	0.1 ± 0.0	0.2 ± 0.0	0.09 ± 0.02
$t\bar{t}H, H \rightarrow \tau\tau$	0.6 ± 0.1	0.3 ± 0.0	0.9 ± 0.1	1.0 ± 0.2	0.15 ± 0.02
$t\bar{t}W$	8.2 ± 1.5	3.4 ± 0.6	13.0 ± 2.2	9.2 ± 1.9	-
$t\bar{t}Z/\gamma^*$	2.5 ± 0.5	1.6 ± 0.3	4.2 ± 0.9	7.9 ± 1.7	1.25 ± 0.88
$t\bar{t}WW$	0.2 ± 0.0	0.1 ± 0.0	0.3 ± 0.1	0.4 ± 0.1	0.04 ± 0.02
$t\bar{t}\gamma$	-	1.3 ± 0.3	1.9 ± 0.5	2.9 ± 0.8	-
WZ	0.8 ± 0.9	0.5 ± 0.5	1.2 ± 1.3	4.2 ± 0.9	-
ZZ	0.1 ± 0.1	0.0 ± 0.0	0.1 ± 0.1	0.4 ± 0.1	0.45 ± 0.09
rare SM bkg.	1.1 ± 0.0	0.4 ± 0.0	1.5 ± 0.0	0.8 ± 0.0	0.01 ± 0.00
non-prompt	10.8 ± 4.8	8.9 ± 4.5	21.2 ± 8.1	33.2 ± 12.3	0.53 ± 0.32
charge flip	-	1.9 ± 0.6	2.4 ± 0.8	-	-
all signals	2.7 ± 0.4	1.2 ± 0.2	3.7 ± 0.6	4.4 ± 0.8	0.52 ± 0.09
all backgrounds	23.7 ± 5.2	18.0 ± 4.7	45.9 ± 8.6	58.9 ± 12.7	2.28 ± 0.94
data	41	19	51	68	1

Table 7: Expected and observed yields after the selection in all five final states. The rare SM backgrounds include triboson production, $t\bar{t}Z$, $W^\pm W^\pm qq$, and WW produced in double-parton interactions.

484 Figure 24 shows the sum of lepton charges for events passing the $\mu\mu$, ee , $e\mu$, and 3ℓ selections.

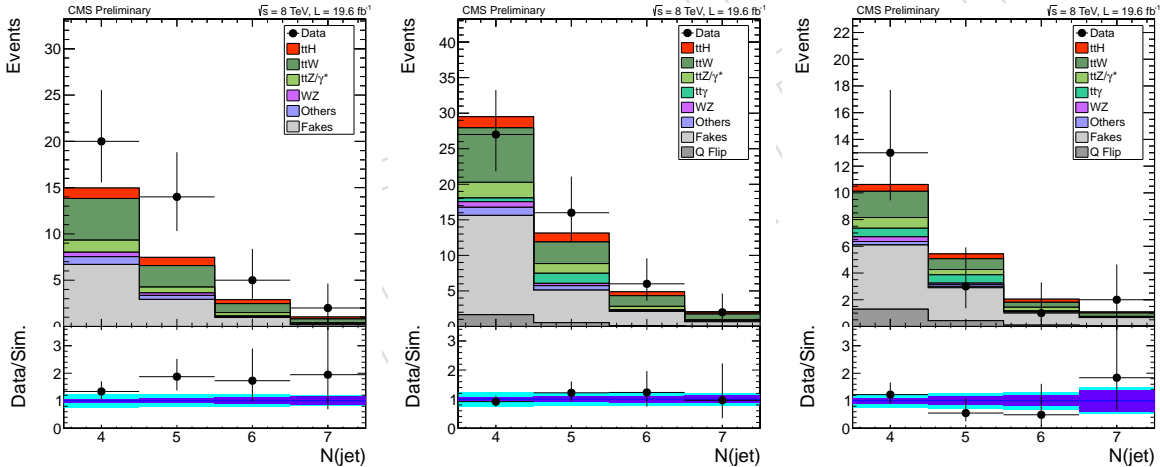
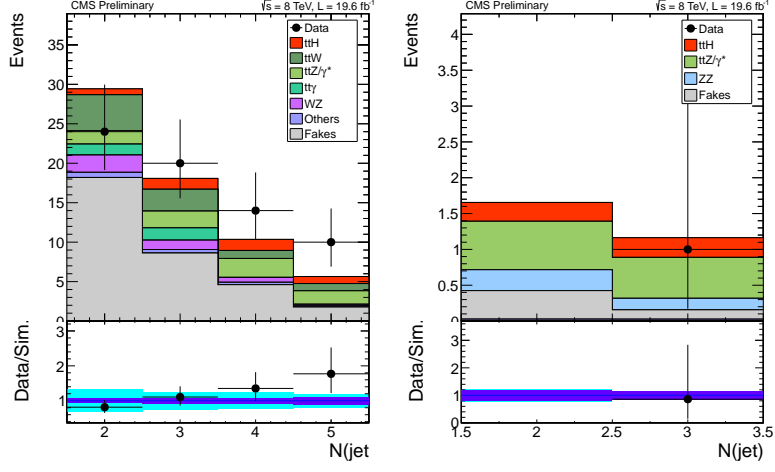
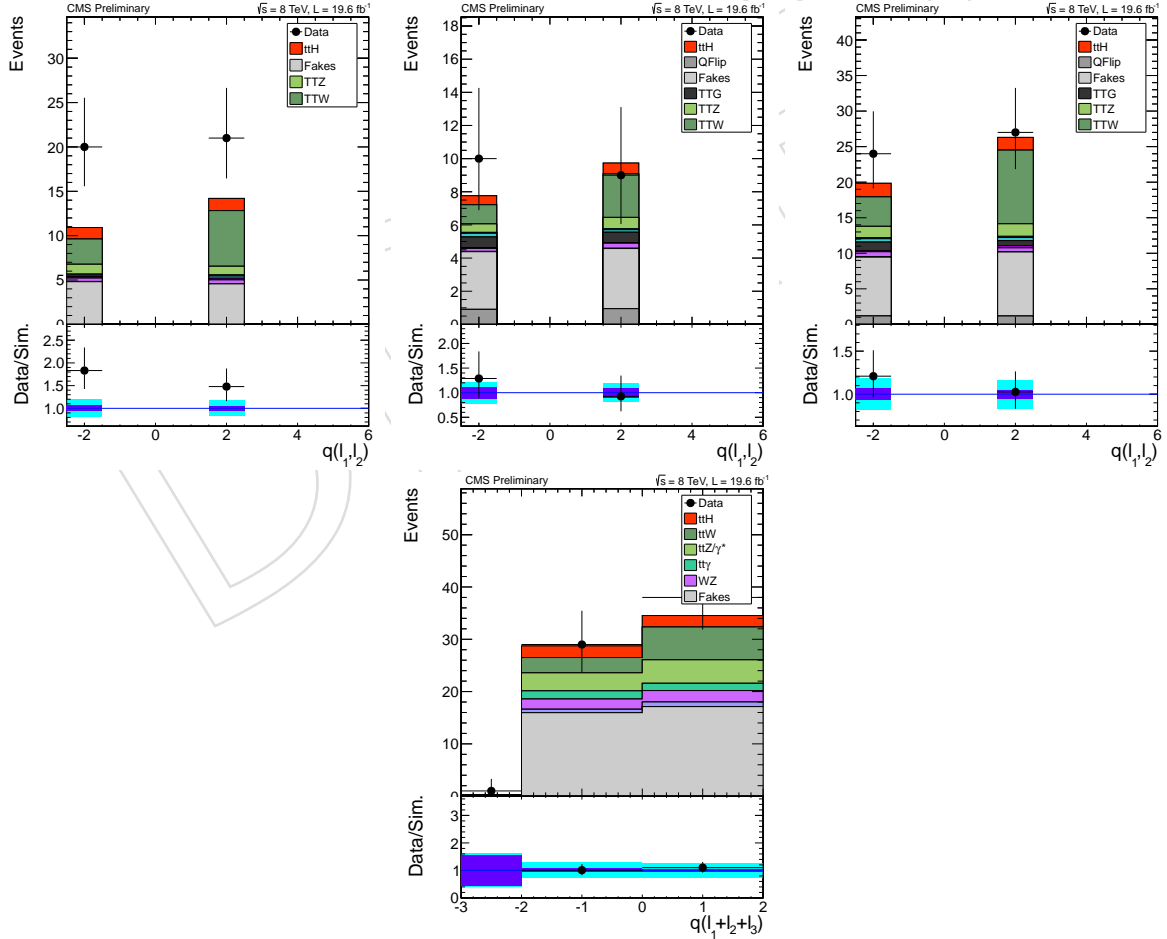


Figure 22: 2ℓ selection. Jet multiplicity distributions for events with at least 4 jets. Left: events with two muons. Middle: events with one electron and one muon. Right: events with two electrons.

Figure 23: 3ℓ (left) and 4ℓ (right) selections: jet multiplicity distribution.Figure 24: Sum of lepton charges for the $\mu\mu$, ee , $e\mu$, and 3ℓ selections.

485 5 Signal extraction

486 After the event selection described in the previous section, the overall yields are still domi-
 487 nated by background. It is not possible to infer the presence of a $t\bar{t}H$ signal on the basis of the
 488 yields alone. The strategy adopted in this search is to split the selected events into multiple
 489 exclusive categories, with different signal purities, and in each category extract the signal from
 490 the distribution of a suitable discriminating variable.

491 In the dilepton and trilepton final state, the events are separated according to the sum of the
 492 electrical charges of the leptons, to exploit the charge asymmetry present in several SM back-
 493 grounds in pp collisions ($t\bar{t}W$, WZ , t -channel single top, $W+jets$). The gain in sensitivity from
 494 categorizing the events is approximately 15%.

495 In the dilepton analysis, we use a boosted decision tree as discriminating variable. The BDT
 496 is trained using simulated $t\bar{t}H$ signal and $t\bar{t}$ background events, relying on six discriminating
 497 variables: the p_T and $|\eta|$ of the trailing lepton, the minimal angular separation between the
 498 trailing lepton and the closest selected jet, the transverse mass of the leading lepton and E_T^{miss} ,
 499 the scalar sum of the p_T of all leptons and jets H_T , and the modulus of the negative vector
 500 sum of the transverse momenta of all leptons and jets H_T^{miss} . Figures 25-27 compare data and
 501 simulation distributions for the input variables. We use the same training for the ee , $e\mu$ and $\mu\mu$
 502 final states, as the gain in performance from dedicated trainings in each final state is found to be
 503 negligible at this stage. Fig. 28 shows the mva output distributions for signal and background
 504 for merged charge categories.

DRAFT

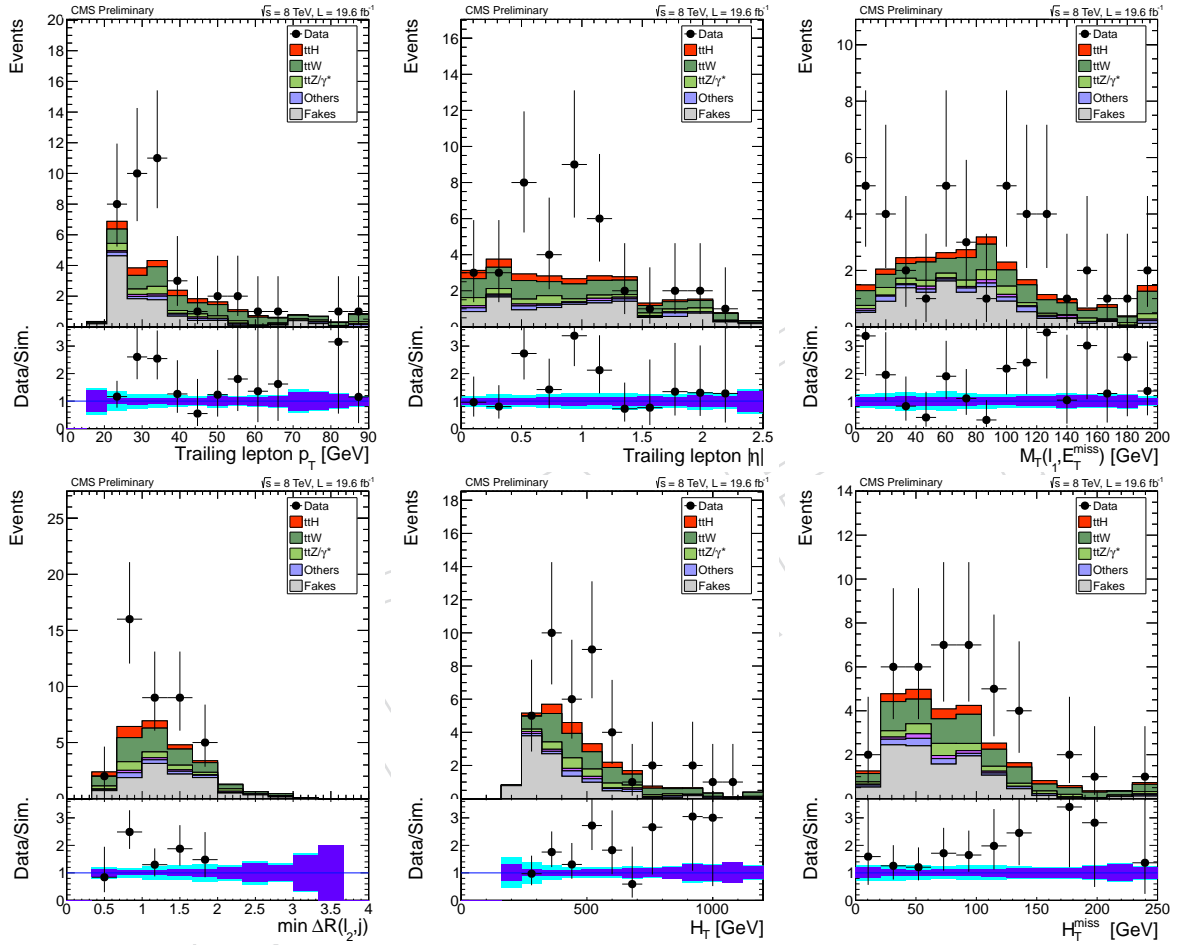


Figure 25: 2ℓ , two muon selection. MVA input variable distributions for events with at least four jets.

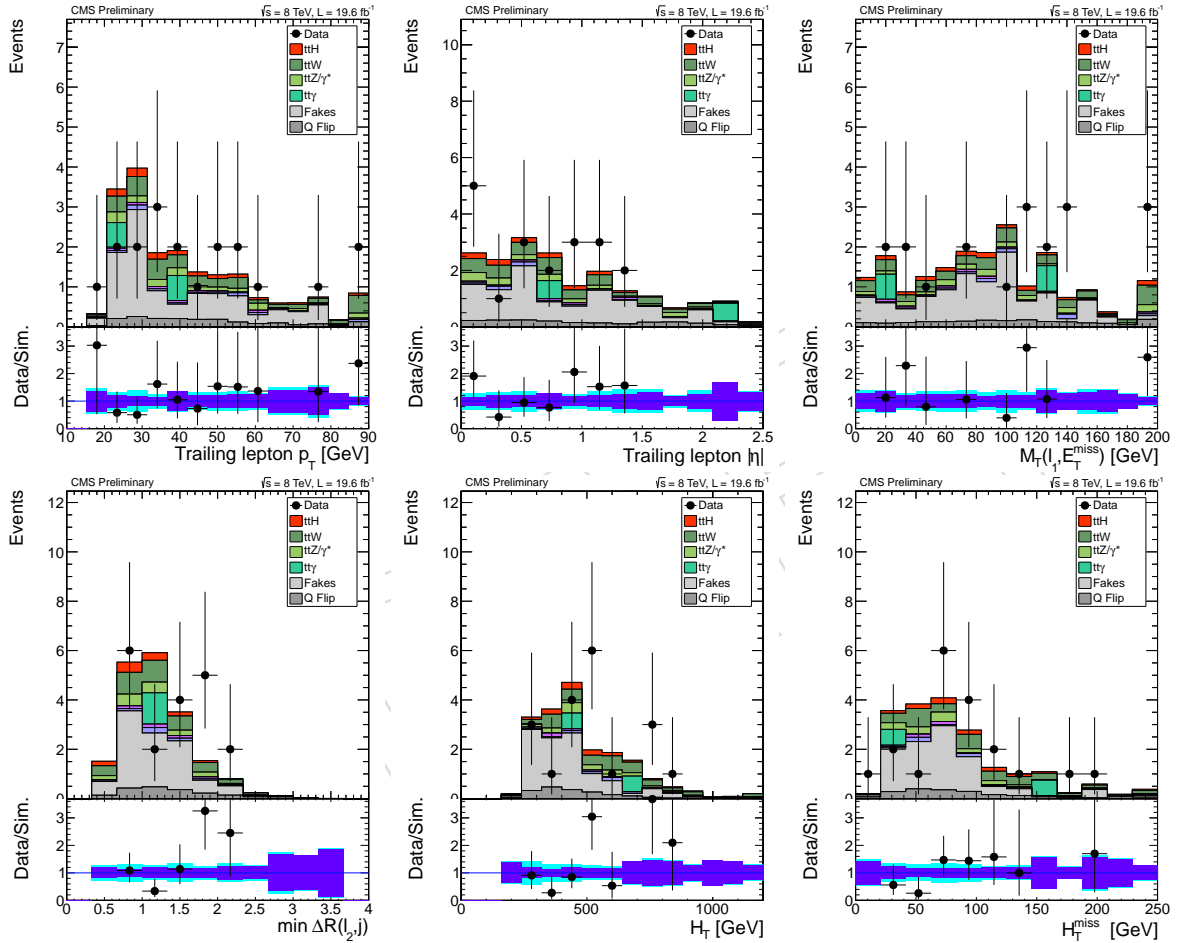


Figure 26: 2ℓ , two electron selection. MVA input variable distributions for events with at least 4 jets.

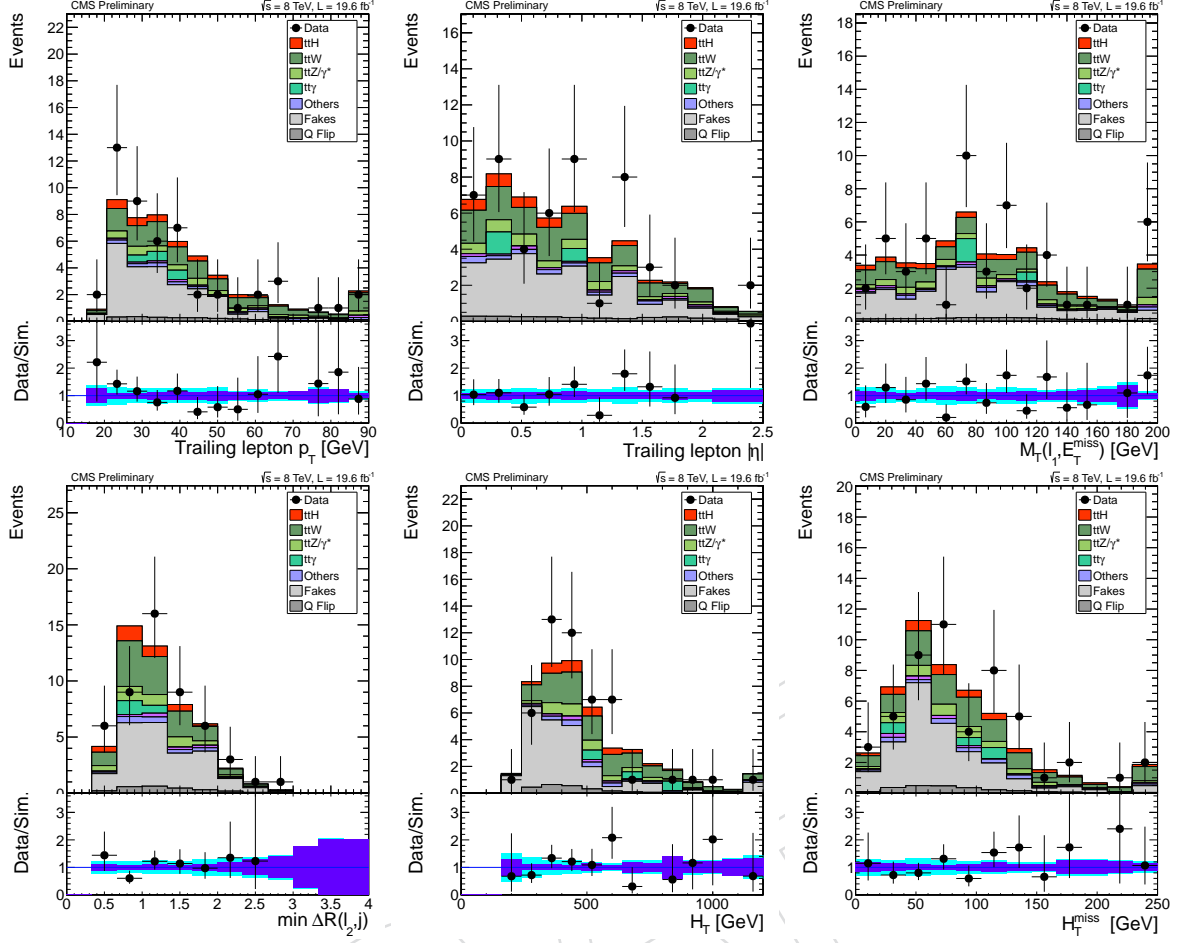


Figure 27: 2ℓ , one electron and one muon selection. MVA input variable distributions for events with at least 4 jets.

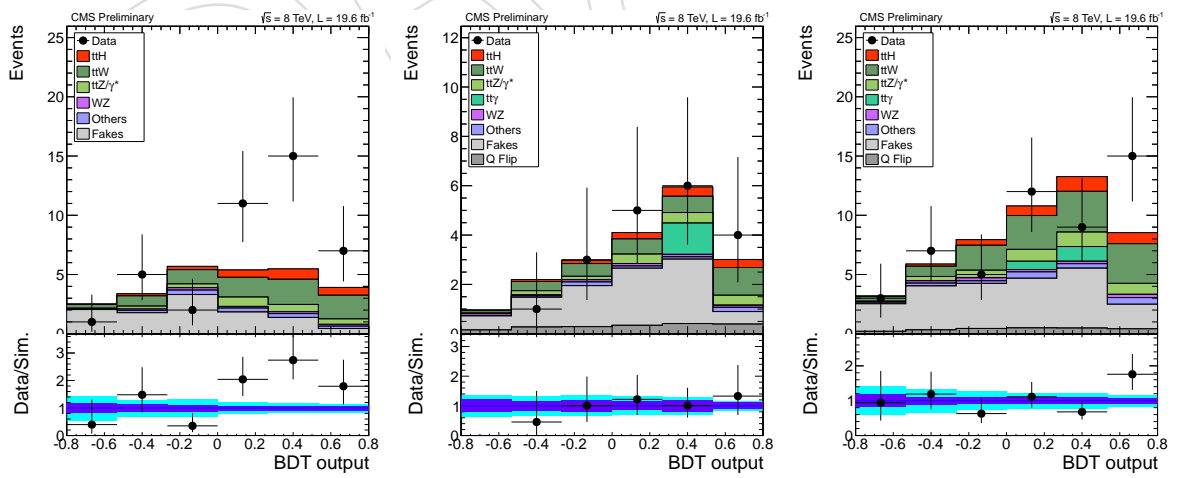


Figure 28: Distribution of the BDT discriminator for the same-sign dilepton search, for the final states $\mu\mu$ (left), ee (center), and $e\mu$ (right). Events with positive and negative charge are merged in these plots. The charge categories are used separately in the signal extraction. The bottom panel of each plot shows the ratio between the observed events and the expectation from simulation, with statistical (violet) and systematic (cyan) uncertainties.

505 In the trilepton analysis, we also use a BDT for the final discrimination. The BDT is trained us-
506 ing simulated $t\bar{t}H$ signal and a mix of $t\bar{t}$, $t\bar{t}W$ and $t\bar{t}Z$ background events, using seven discrim-
507 inating variables: the multiplicity of hadronic jets, the p_T of the jet with the highest b-tagging
508 discriminator, H_T , the fraction of H_T from jets and leptons within $|\eta| < 1.2$, the maximum of
509 the $|\eta|$ values of the three leptons, the minimal ΔR separation between any pair of opposite-
510 sign leptons, and the mass of the best candidate hadronically-decaying top quark reconstructed
511 from the jets in the event. The inputs to the mva are shown in Fig. 29. The expected and ob-
512 served BDT output distributions for the trilepton analysis are shown in Fig. 30.

513 As a cross-check in both the dilepton and the trilepton final states we also perform the analysis
514 using as discriminating variable the multiplicity of hadronic jets. The gain in sensitivity for the
515 multivariate analysis compared to this simpler cross-check is about 20%.

516 In the four lepton analysis, we simply use the multiplicity of hadronic jets: the sensitivity of
517 this channel is anyway limited by the very small branching ratio, and the estimation of the
518 kinematic distributions of the reducible backgrounds from data is also challenging due to the
519 low event yields.



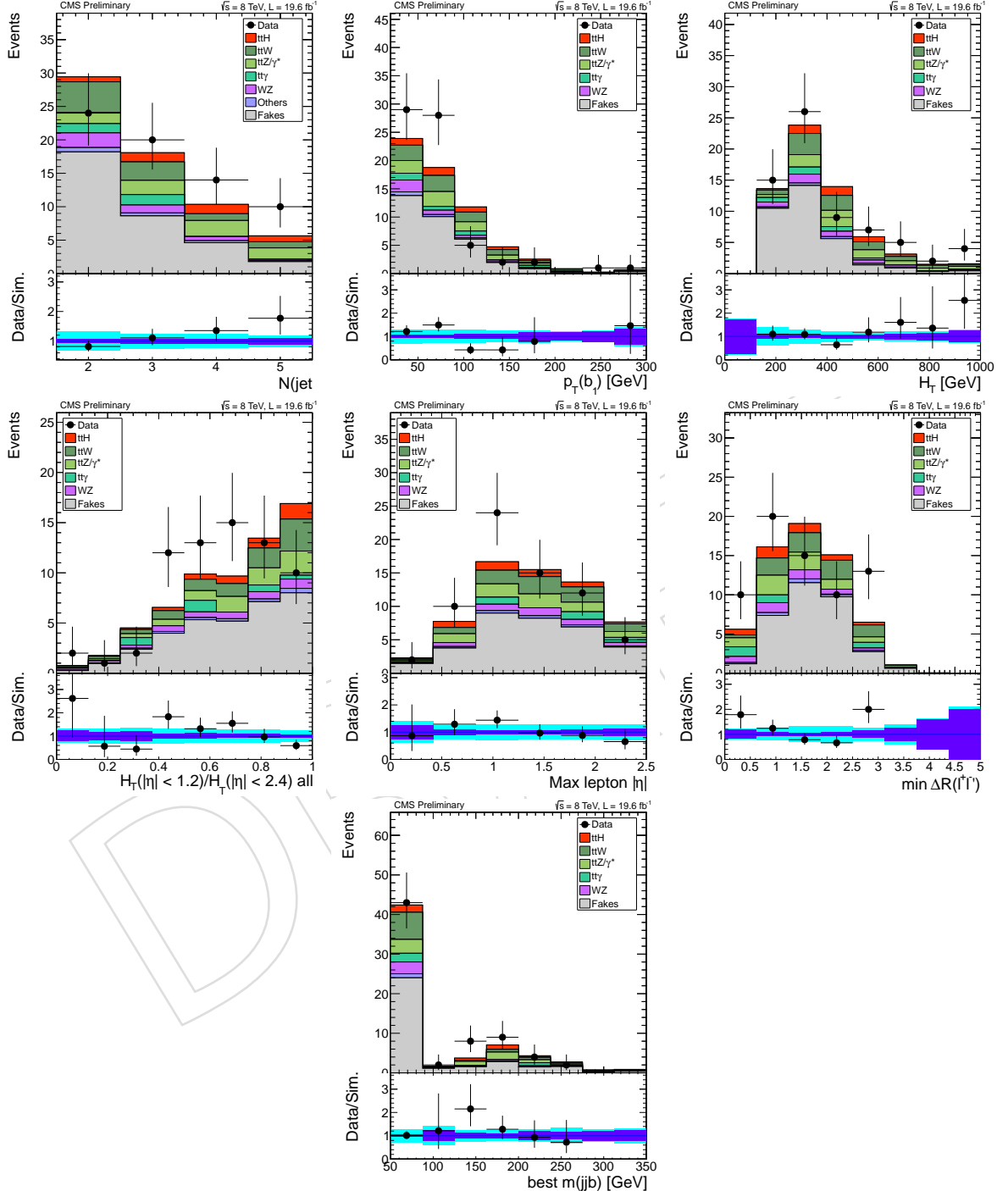


Figure 29: 3ℓ . Input variables to the MVA for 3ℓ leptons. Events with positive and negative charge are merged in these plots, but they are used separately in the signal extraction.

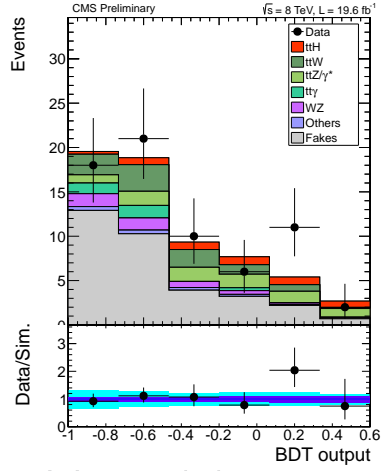


Figure 30: Distribution of the BDT discriminator for the trilepton search. Events with positive and negative charge are merged in these plots, but they are used separately in the signal extraction. The bottom panel shows the ratio between the observed events and the expectation from simulation, with statistic (violet) and systematic (cyan) uncertainties.

520 6 Signal modeling

521 The signal is modelled using simulated events. The simulation has two different sources of
 522 systematic uncertainty. The first source of uncertainty is correction factors applied to the simula-
 523 tion in order to better reproduce the detector conditions and performance in data. The second
 524 source is assumptions made in the theoretical models that were used to produce the simulation.
 525 We account for uncertainties from both sources.

526 6.1 Correction factors and experimental uncertainties

527 As discussed in Section 3, we use scale factors to correct for differences in lepton performance
 528 between data and simulation. The scale factors account for the differences in the trigger, lepton
 529 preselection, and lepton MVA discriminant. Each of these scale factors has an uncertainty
 530 associated with it. The average correction factors for the different final states range between
 531 7% and 15%, with associated systematic uncertainties of about 5% per lepton.

532 The corrections we apply to jet energies in simulation have uncertainties associated with them [17].
 533 The uncertainties are parameterised as a function of p_T , η , and flavor of the jets. We assess the
 534 impact of the uncertainties by shifting the jet energy correction factors for each jet up and down
 535 by $\pm 1\sigma$ and re-calculating all kinematic quantities.

536 We found that the uncertainty from the jet energy resolution plays a negligible role in this
 537 analysis.

538 The b -tagging efficiency and fake rate corrections each have an uncertainty associated with
 539 them [18, 19]. The uncertainties are parameterised as a function of p_T , η , and flavor of the jet.
 540 We assess their effect on the analysis by shifting the weight of each jet up and down by $\pm 1\sigma$ of
 541 the appropriate uncertainty and we recalculate the overall event weight.

542 In order to validate the modelling in the simulation for the $E_T^{\text{miss}}LD$ discriminator, and for the
 543 scalar sum of lepton transverse momenta and E_T^{miss} , we rely on $t\bar{t} \rightarrow e^\pm \mu^\mp$, inclusively or with
 544 the additional requirement of two hadronic jets, for which these variables have a spectrum sim-
 545 ilar to the $t\bar{t}H$ signal (Fig. 31). For this purpose, events are selected requiring a $e^\pm \mu^\mp$ pair satis-
 546 fying the tight lepton requirements, and two b -jets satisfying the CSV medium working point,
 547 with no requirement on the E_T^{miss} . In these control regions, we observe a very good agreement
 548 between data and simulations (Fig. 32). Quantitatively, the efficiencies of the selection require-
 549 ments $E_T^{\text{miss}}LD > 0.2$, $E_T^{\text{miss}}LD > 0.3$ are in agreement between data and simulation within
 550 0.3% or better, and the efficiency for the $H_T(\ell\ell E_T^{\text{miss}}) > 100\text{ GeV}$ is also reproduced within bet-
 551 ter than 0.6%. Within the sensitivity of our $t\bar{t}H$ analysis we can therefore neglect any correction
 552 or systematical uncertainty from the modelling of these variables in the signal simulation.

553 In order to validate the agreement between data and simulation after these corrections, the
 554 same physics objects and methods are used to select well known processes with larger cross
 555 sections in dedicated control regions: $t\bar{t} \rightarrow e^\pm \mu^\mp b\bar{b} \nu\bar{\nu}$, $WZ \rightarrow 3\ell$, $ZZ \rightarrow 4\ell$ and $Z \rightarrow 2\ell$. The
 556 overall event yields in the control regions are found to be in agreement with the predictions
 557 within the uncertainties.

558 6.2 Theoretical uncertainties

559 The theoretical uncertainties on the NLO prediction for the inclusive $t\bar{t}H$ production cross sec-
 560 tion amount to 6% from unknown higher orders in the perturbative series and 8% from the
 561 knowledge of the parton distribution functions (PDFs) [4].

562 Systematic uncertainties arising from the modelling of the process in PYTHIA are estimated by

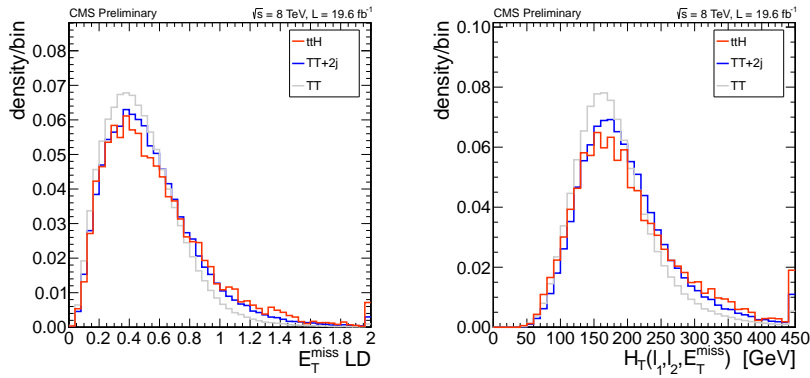


Figure 31: Comparison of the expected distributions for $E_T^{\text{miss}} \text{ LD}$ discriminator and for scalar sum of lepton transverse momenta and E_T^{miss} in inclusive $t\bar{t}$, $t\bar{t} + 2$ jets and $t\bar{t}H$ events, in the $e^\pm \mu^\mp$ final state. All distributions are normalised to the same area.

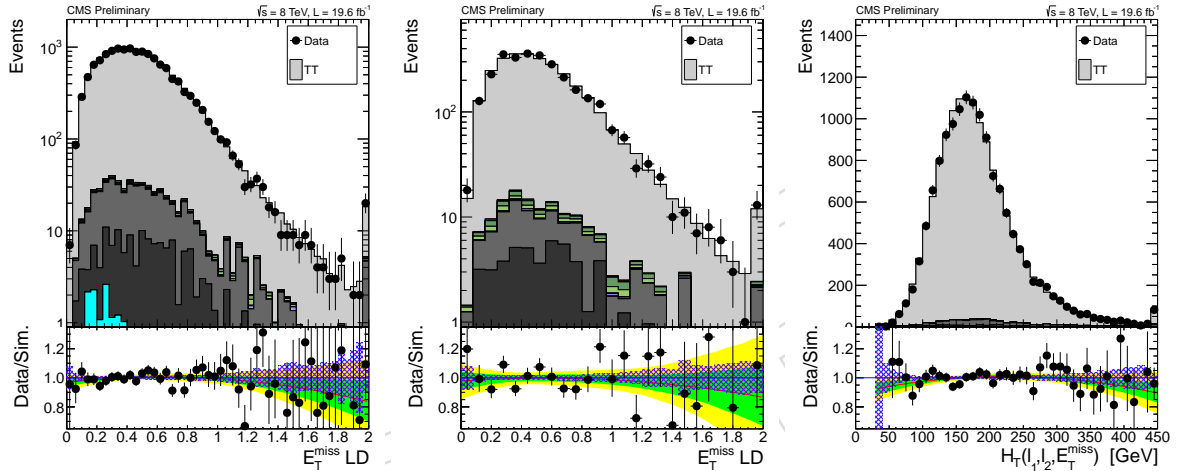


Figure 32: Validation of the E_T^{miss} modelling on $t\bar{t}$ events: $E_T^{\text{miss}} \text{ LD}$ discriminator in inclusive $t\bar{t}$ events (left) and in events with two additional hadronic jets (centre), and scalar sum of the E_T^{miss} and the lepton transverse momenta in inclusive $t\bar{t}$ events (right). The overall normalisation of the $t\bar{t}$ background is scaled to match the observed yield in data. The lower panel on each plot shows the ratio between data and simulation, with the result of a fit to the ratio with a second order polynomial (red line, $\pm 1\sigma$ and $\pm 2\sigma$ bands), and the statistical uncertainty on the simulation (hatched area).

563 comparing the predictions obtained with different tunes of the generator, affect the way extra
 564 radiation in modelled. The nominal prediction is taken from the Z2* tune, and an uncertainty
 565 band is obtained from the envelope of the predictions for the Z2*, Z2, PROFESSOR Q_0^2 and Pe-
 566 rugia '11 tunes [35], all normalised to the same inclusive cross section. The relative differences
 567 observed in variables related to hadronic jet activity are of about 10% in the well populated part
 568 of the distributions, while the uncertainties are smaller for variables related to leptons (Fig. 33).
 569 If we were to include also the older D6T tune, now disfavoured by LHC data, the uncertainty
 570 would not increase dramatically.

571 Uncertainties from the PDFs beyond the ones affecting the overall normalisation are estimated
 572 with the [36] prescriptions using the thee PDF sets [37], [38], [39]. The resulting uncertainties
 573 on the shapes of the discriminating variables used for signal extraction are in the 2 – 4% range.
 574

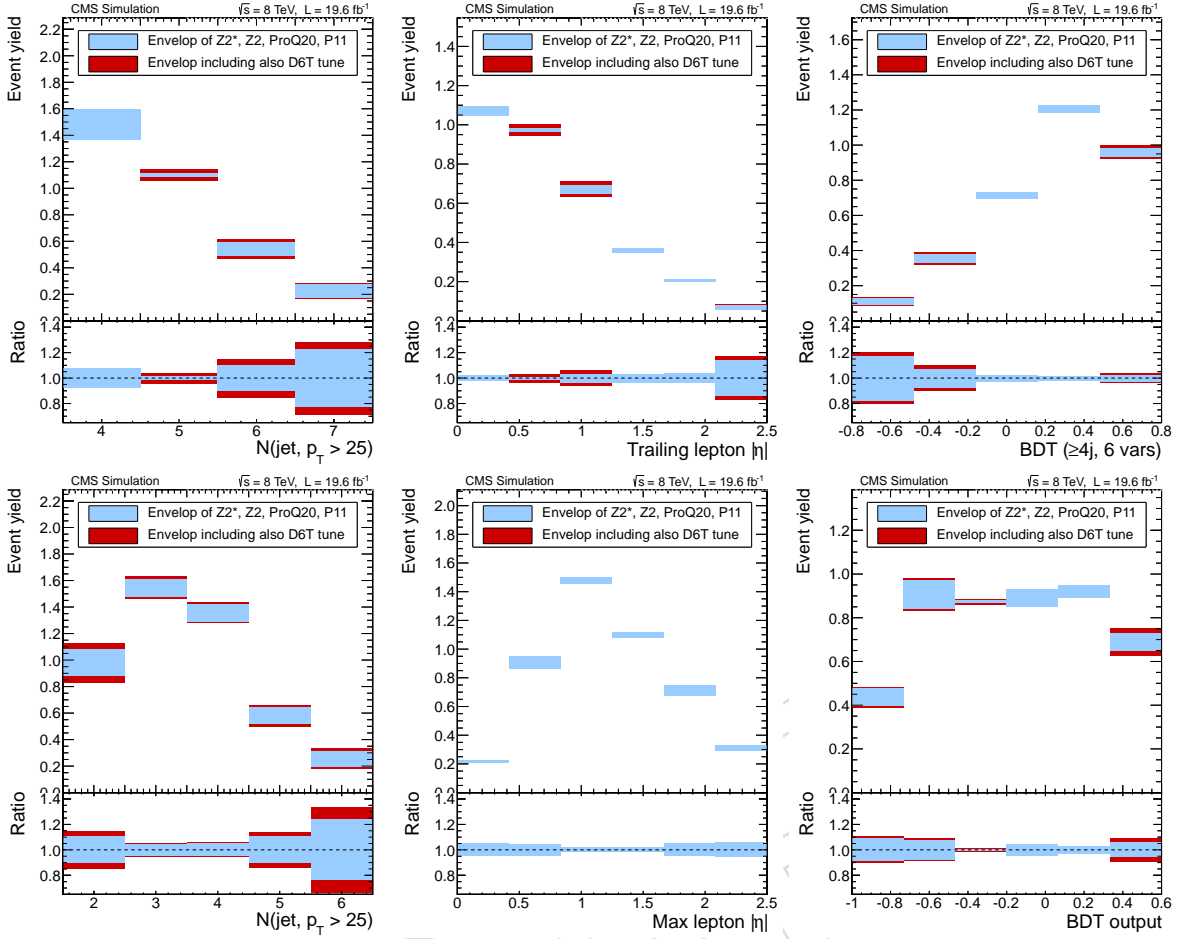


Figure 33: Shape uncertainties on the $t\bar{t}H$ signal from the MC modelling in PYTHIA: multiplicity of hadronic jets (left), lepton pseudorapidity (centre) and BDT used for signal extraction (right); the plots in the top row are for the $e^\pm \mu^\mp$ final state, the ones in the bottom row for the 3ℓ one.

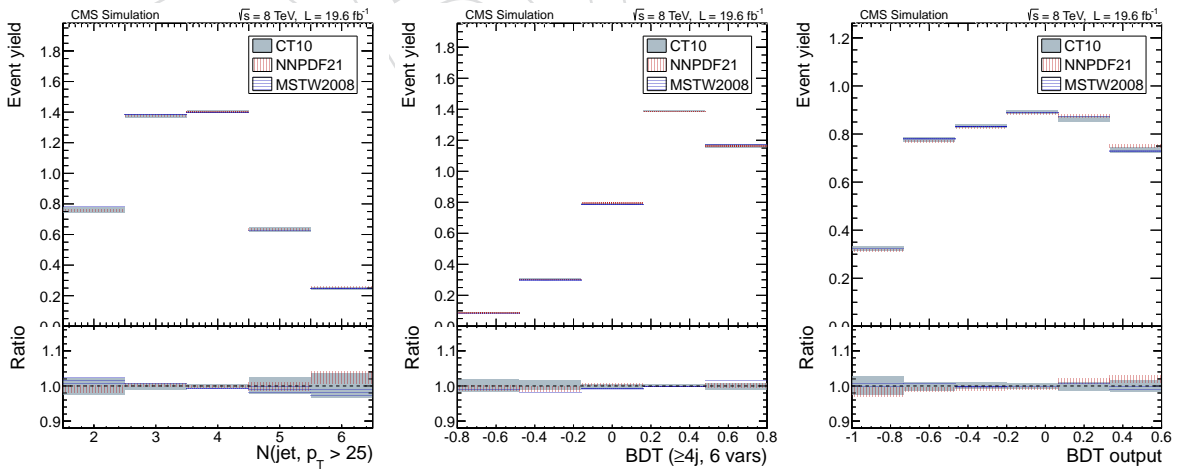


Figure 34: Shape uncertainties on the $t\bar{t}H$ signal from the PDFs: multiplicity of hadronic jets in the 3ℓ final state (left), and BDTS used for signal extraction in the $e^\pm \mu^\mp$ (centre) and 3ℓ (right) final states.

575 7 Background predictions

576 There are three categories of backgrounds in this search: irreducible backgrounds from as-
 577 sociated production of a $t\bar{t}$ pair and one or more electroweak bosons; electroweak diboson
 578 or multiboson production associated with multiple hadronic jets; and reducible backgrounds
 579 from events with non-prompt leptons misidentified as prompt ones, or opposite-sign dilep-
 580 ton events in which the charge of one of the leptons is mismeasured. These three classes of
 581 backgrounds are estimated separately with different methods, as described below. Additional
 582 minor backgrounds like triboson production are estimated directly from simulated events.

583 7.1 Irreducible backgrounds

584 Irreducible backgrounds from $t\bar{t}W$, $t\bar{t}Z$ and $t\bar{t}WW$, are estimated from simulated events. Just
 585 like for the signal, corrections are applied for the different performance the individual physics
 586 objects between data and simulation measured in control regions in data. In all the analysed
 587 final states, the contribution of the $t\bar{t}WW$ process is found to be at least an order of magnitude
 588 smaller than $t\bar{t}W$ and $t\bar{t}Z$.

589 The inclusive production cross sections for the $t\bar{t}W$ and $t\bar{t}Z$ processes are taken from the NLO
 590 computation in [1208.2665], with theoretical uncertainties from unknown higher orders of 10%
 591 and 11% respectively, and uncertainties from the knowledge of the parton density functions of
 592 7% and 9% respectively.

593 In addition to the overall normalisation, systematic uncertainties of theoretical origin on the
 594 distribution of the events in the final discriminating variables are considered, estimated con-
 595 ventionally by varying the normalisation and factorisation scales up and down by a factor two
 596 and matching threshold between matrix element and parton shower (Fig. 35).

597 Shape uncertainties from parton distribution functions are also considered, as per the PDF4LHC
 598 prescriptions using the PDF sets CT10, NNPDF21, MSTW2008 (Fig. 36). In addition, for the $t\bar{t}W$
 599 process it is also important to consider the uncertainty on the charge asymmetry: the predic-
 600 tions on the ratio between the yields in the mostly-positive and mostly-negative final states for
 601 the dilepton and trilepton final states are 2.33 ± 0.17 and 2.05 ± 0.15 and respectively. These
 602 uncertainties can be modelled as a $\pm 2.1\% / \pm 2.3\%$ relative uncertainty on the mostly-positive
 603 yields in the $2\ell/3\ell$ final state anti-correlated with relative uncertainties of $\pm 5.0\% / \pm 4.8\%$ on
 604 the mostly-negative yields.

605 Experimental uncertainties on the estimation are also considered, originating from the knowl-
 606 edge of the lepton selection efficiencies, b-tagging efficiencies, jet energy scales and jet energy
 607 resolutions. These uncertainties are estimated in the same way as for signal events, and in the
 608 statistical analysis they are assumed to be completely correlated across the different physics
 609 processes.

610 In order to validate the agreement between data and simulation after these corrections, the
 611 same physics objects and methods are used to select well known processes with larger cross
 612 sections in dedicated control regions: $t\bar{t} \rightarrow e^\pm \mu^\mp b\bar{b} \nu\bar{\nu}$, $WZ \rightarrow 3\ell$, $ZZ \rightarrow 4\ell$ and $Z \rightarrow 2\ell$. The
 613 overall event yields in the control regions are found to be in agreement with the predictions
 614 within the uncertainties.

615 The prediction for the $t\bar{t}Z$ process is also tested directly in a trilepton control region requiring
 616 two of the leptons to have the same flavour, opposite electrical charge and the invariant mass
 617 pair of the pair to be within 10 GeV of the nominal Z boson mass. Good agreement is observed
 618 in this control region, though in this case the precision of the test is dominated by the statistical

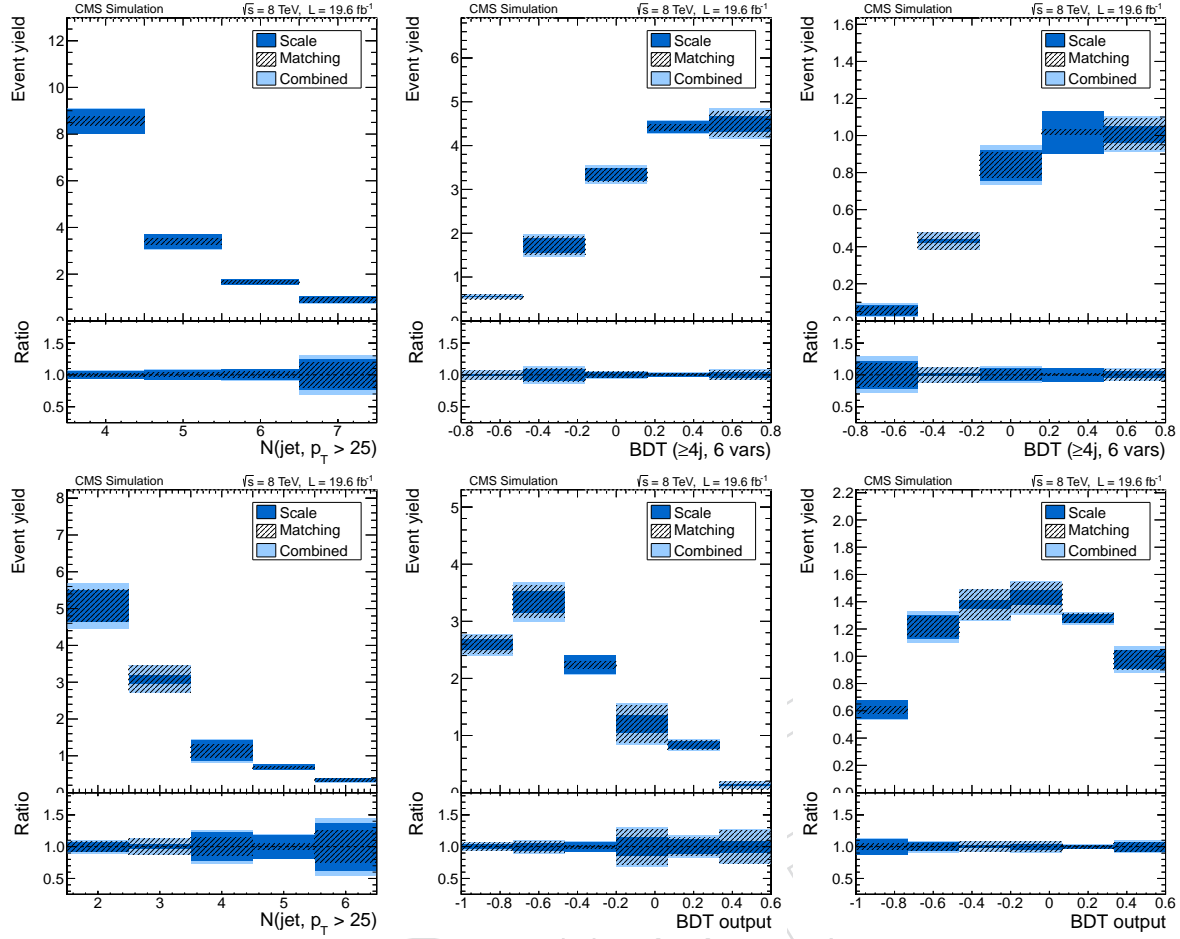


Figure 35: Shape uncertainties on the irreducible backgrounds from the MC modelling in MADGRAPH: multiplicity of hadronic jets in ttW (left), and BDT used for signal extraction in ttW (centre) and ttZ (right); the plots in the top row are for the $e^\pm \mu^\pm$ final state, the ones in the bottom row for the 3ℓ one.

uncertainty of about 35%.

7.2 $t\bar{t}\gamma^*$ and $t\bar{t}\gamma$ backgrounds

The cross section for the $t\bar{t}\gamma^*$ process with $\gamma^* \rightarrow \ell^+\ell^-$ process becomes large for decreasing virtuality of the γ^* , i.e. for small invariant masses of the dilepton pair. While in the analysis we reject events with low mass dileptons, the $t\bar{t}\gamma^*$ process can still contribute as a background when one of the two leptons is not reconstructed; this in particular can happen in kinematic configurations where the conversion is very asymmetric and one of the two leptons has transverse momentum below the acceptance.

Since the nominal ttZ MC sample is generated with the requirement $m_{\ell^+\ell^-} > 10 \text{ GeV}$, to estimate this background we rely on an additional $t\bar{t}\gamma^*$ MC sample generated in the remaining part of the phase space. This additional sample is generated with MADGRAPH 5, with dilepton masses down to the kinematic limit $m_{\ell^+\ell^-} = 2m_\ell$ for muon and tau pairs, and down to 100 MeV for electron pairs; lepton masses are taken into account in the event generation, and no p_T and η requirements are applied at the generation stage. The events are then processed with PYTHIA for soft radiation and hadronization effect, and through the CMS fast simulation and event reconstruction.

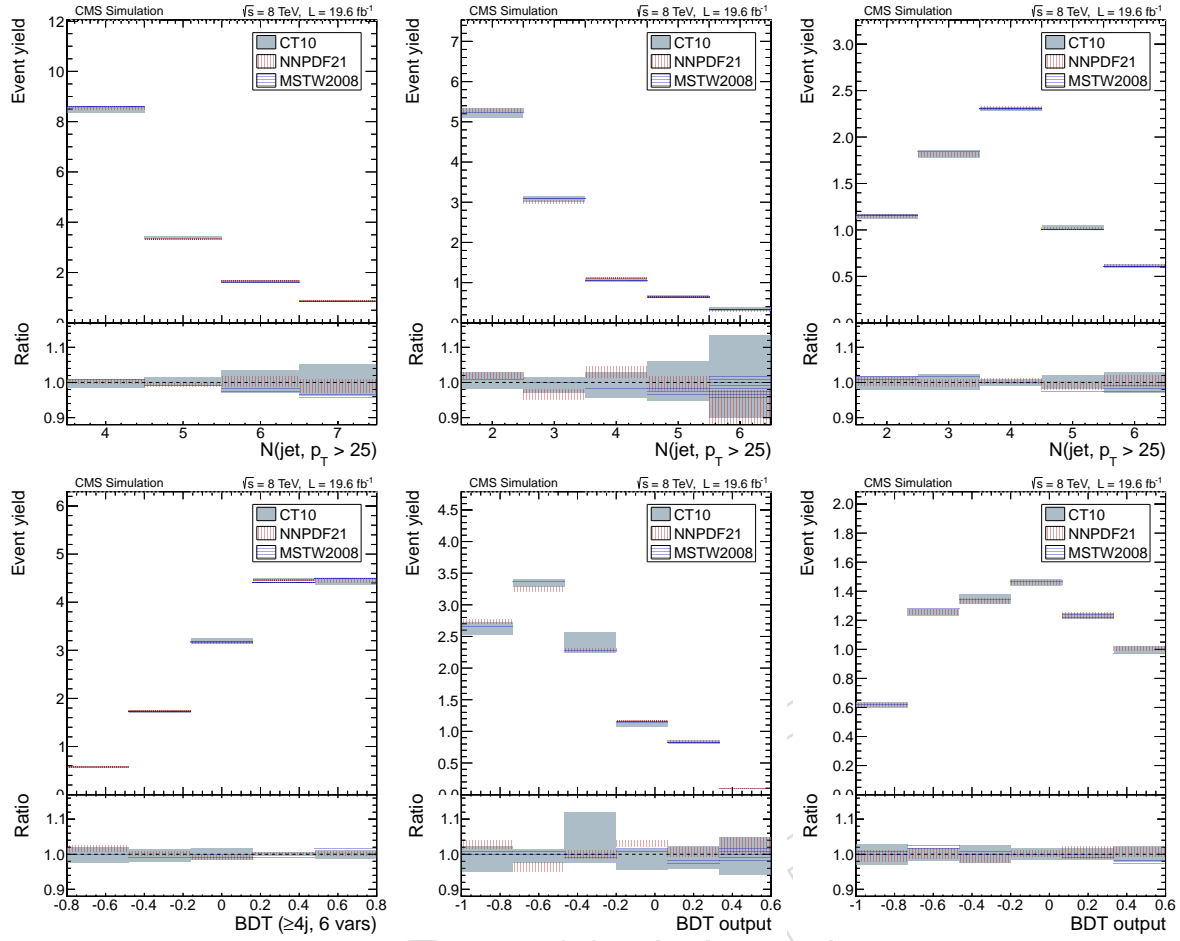


Figure 36: Shape uncertainties on the irreducible backgrounds from the PDFs: $t\bar{t}W$ events in the $e^\pm \mu^\pm$ final state (left); $t\bar{t}W$ (centre) and $t\bar{t}Z$ (right) in the 3ℓ final state. The plots in the top row are for the multiplicity of hadronic jets, the ones in the bottom row for the BDT used for signal extraction.

635 The event from this dedicated generation are then normalised by requiring the distribution
 636 of the invariant mass of dilepton pairs to match smoothly with the $t\bar{t}Z$ sample, which was
 637 normalised to the NLO prediction for the cross section (Fig. 37). This matching corresponds
 638 to applying a k-factor of approximately 1.5 to the LO prediction of the $t\bar{t}\gamma^*$ cross section from
 639 MADGRAPH, comparable with the ones computed for other similar processes.

640 In order to validate the event generation and the description of asymmetric low mass dilepton
 641 pairs in the fast simulation, we use the same setup to simulate the $pp \rightarrow (\ell^+\ell^-)(\ell^+\ell^-)$ process
 642 including both the Z and γ^* contributions for both dilepton pairs, and allowing for dilepton
 643 masses down to 100 MeV. We normalise this MC sample to the 4ℓ sample from POWHEG for
 644 $m_{\ell^+\ell^-} > 12 \text{ GeV}$, deriving a k-factor of about 1.3, and then validate on data the resonant pro-
 645 duction $pp \rightarrow Z \rightarrow \ell^+\ell^-\gamma^*$ where the dilepton pair from the γ^* is asymmetric and only one
 646 lepton is reconstructed. In this kinematic configuration, the invariant mass of the three recon-
 647 structed leptons peaks at the nominal Z boson mass, allowing the process to be well separated
 648 from the non-resonant background (Fig. 38). The background from WZ is reduced with the
 649 requirements $E_T^{\text{miss}} \text{LD} < 0.3$ and $m_T(\ell\nu) < 40 \text{ GeV}$, while the contribution from an off-shell Z
 650 plus a non-prompt lepton is suppressed requiring $m_{\ell^+\ell^-} < m_Z - 10 \text{ GeV}$.

651 We then test the prediction for the $t\bar{t}\gamma^*$ process in data in the $\ell^\pm \mu^+ \mu^-$ final state, for $m_{\mu^+ \mu^-} <$

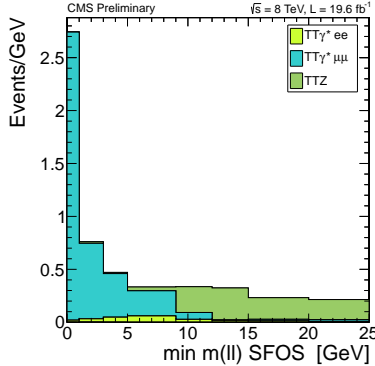


Figure 37: Distribution of the minimum invariant mass of reconstructed same-flavour opposite-sign lepton pairs in simulated $t\bar{t} + Z/\gamma^*$ in the trilepton final state. The samples labelled as $t\bar{t}Z$ and the $t\bar{t}\gamma^*$ processes correspond to event generation with $m_{\ell^+\ell^-}$ above and below 10 GeV respectively (both samples are generated including both the Z and γ^* contribution to the matrix element). The dielectron sample has negligible contribution at low $m_{\ell^+\ell^-}$ since the reconstruction in the ECAL becomes inefficient at small separation.

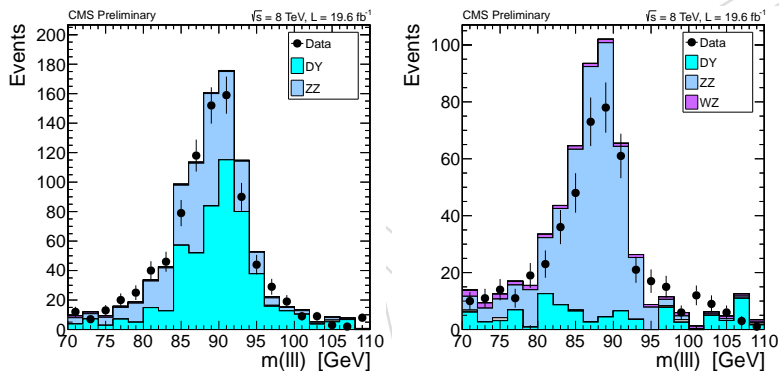


Figure 38: Invariant mass of the three leptons in $\ell^+\ell^-e^\pm$ (left) $\ell^+\ell^-e^\pm$ (right) events in data and predictions from simulations. The MC labelled as ZZ corresponds to $Z \rightarrow \ell^+\ell^-\gamma^*$ events where only one lepton from the γ^* asymmetric is reconstructed, while the one labelled as DY corresponds to off-shell $Z \rightarrow \ell^+\ell^-$ events with an additional non-prompt lepton; in the case of electrons, there is also a sizable contribution from $Z \rightarrow \ell^+\ell^-\gamma$ where the photon converts in the detector material and is misidentified as an electron.

652 15 GeV. Compared to the trilepton selection used for the extraction of the $t\bar{t}H$ signal, we relax
 653 the lepton selection using the loose MVA working point for the two muons instead of the tight
 654 one, and we require at least three hadronic jets (instead of 2). We impose no lower bound on
 655 the dimuon invariant mass, but we veto events within invariant masses within 0.2 GeV from
 656 the J/Ψ resonance or in the mass range dominated by the Y resonances [9, 11] GeV. We observe
 657 a satisfactory agreement between the data and the expectations from simulation (Fig. 39); in
 658 this context, also the reducible background is estimated from simulations, as the data-driven
 659 estimate that we use in the rest of the analysis is not appropriate for configurations with close-
 660 by leptons.

661 In the case of electrons, in addition to the $t\bar{t}\gamma^*$ background there is a similar topology of events
 662 from $t\bar{t}\gamma$ production where the photon converts early in the detector material, one conversion
 663 electron is not reconstructed and the remaining can then be misidentified as prompt electron¹.
 664 This background, despite being reducible, is not covered by the reducible background esti-

¹If both electrons are reconstructed, then the conversion veto applied in the electron selection will reject both.

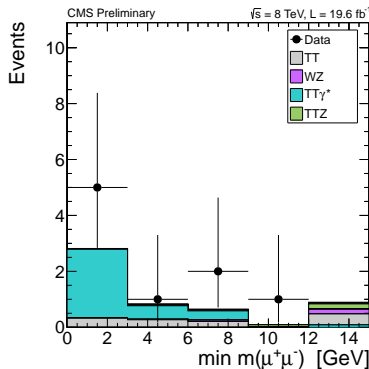


Figure 39: Distribution of the minimum dimuon invariant mass in $\ell^\pm \mu^+ \mu^-$ events with $m_{\mu^+ \mu^-} < 15$ GeV, compared to the predictions from simulation.

665 mation obtained extrapolating from leptons failing the MVA requirement, described later in
 666 section 7.4, since the electron arising from the converted photon will be isolated, unlike non-
 667 prompt electrons from hadron decays or misidentified charged hadrons. We therefore rely on
 668 simulations, supported by the good agreement seen in the $Z \rightarrow \ell^+ \ell^- \gamma^*$ final state (Fig. 38).
 669 In the lack of a NLO result for the $t\bar{t}\gamma$ cross section at 8 TeV, we take the LO result from MAD-
 670 GRAPH and scale it to the same k-factor of inclusive $t\bar{t}$ production (1.8), compatible with other
 671 estimates available in the literature [40–42].

672 The background predictions for $t\bar{t}Z/\gamma^*$ and $t\bar{t}\gamma$ in the dilepton and trilepton final states are
 673 summarised in table 8. In addition to the experimental uncertainties, we assign a systematical
 674 uncertainty of 30% to the overall normalization of $t\bar{t}\gamma$ and a systematical uncertainty of 50%
 on the overall normalization of $t\bar{t}\gamma^*$.

	$\mu\mu$	ee	$e\mu$	3ℓ
$t\bar{t}Z$	2.1	1.2	3.4	6.9
$t\bar{t}\gamma^*$	0.4	0.4	0.9	1.1
$t\bar{t}\gamma$	-	1.3	1.9	2.9

Table 8: Expected background from $t\bar{t}Z/\gamma^*$ and $t\bar{t}\gamma$ to the dilepton and trilepton final states from simulations. The $t\bar{t}Z$ and the $t\bar{t}\gamma^*$ entries correspond to event generation with $m_{\ell^+ \ell^-}$ above and below 10 GeV respectively; both samples are generated including both the Z and γ^* contribution to the matrix element.

675

676 7.3 Di-bosons backgrounds

677 WZ and ZZ production with the gauge bosons decaying to electrons, muons or taus can yield
 678 the same leptonic final states as the signal, considering also events where not all leptons are
 679 identified.

680 When not requiring additional hadronic jets in the final states, these processes are predicted
 681 theoretically at NLO accuracy, and the inclusive cross sections have been successfully mea-
 682 sured at the LHC. However these good agreement does not translate automatically to the signal
 683 regions used in this search, which always require the presence of at least one b-tagged jet.

684 Since dibosons are preferentially produced in association with jets from light quarks or gluons,
 685 it is possible to isolate a clean control region of WZ or ZZ plus hadronic jets by inverting the
 686 b-tagging requirements of the signal region, and also inverting the $Z \rightarrow \ell\ell$ veto. The approach
 687 chosen for estimating this background is therefore to use simulated events but normalising
 688 the overall event yield in control regions of WZ plus two not b-tagged jets and ZZ plus one not

689 b-tagged jet. This reduces the systematic uncertainty on the prediction, since the theoretical un-
 690 certainty on the ratio of event yields between signal region and control region is much smaller
 691 than the uncertainty on the production cross section of diboson plus multijet: the majority
 692 of events from this background in the signal region contain jets from gluons or light quarks
 693 mistagged as b-jets, for which the extrapolation is affected only by uncertainties of experimen-
 694 tal origin, and for the remainder the uncertainties from unknown higher orders in QCD partially
 695 cancel out in the ratio.

696 7.3.1 Measurement in data from events with no b-jets

697 Tables 9 and 10 show the number of expected and observed events in the WZ and ZZ control
 698 regions. The expected purities are for both control regions higher than 90%.

Table 9: Estimated and observed number of events in the WZ control region.

	ttH	WJets	DY	TTG	TW	TT	ZZ	WZ	WW	VVV	TTWW	TTZ	TTW	ALL BKG	DATA
3 tights leptons	7.26	1.00	571.51	2.06	3.97	41.43	383.55	2064	1.08	18.99	0.53	41.38	19.15	3148	4161
$Z \rightarrow ll$	1.14	0.00	394.89	0.35	0.37	6.07	207.98	1727	0.18	12.09	0.06	31.33	2.54	2383	2839
met LD	1.01	0.00	18.82	0.00	0.37	4.65	34.74	903.00	0.11	8.88	0.06	27.81	2.22	1000	1002
≥ 2 jets	0.97	0.00	7.85	0.00	0.00	2.41	5.84	159.07	0.05	5.65	0.05	26.64	1.80	209.37	249.00
b-jet veto	0.07	0.00	2.59	0.00	0.00	0.31	2.96	98.30	0.05	2.82	0.01	1.59	0.11	108.73	118.00

Table 10: Estimated and observed number of events in the ZZ control region.

	ttH	WJets	DY	TTG	TW	TT	ZZ	WZ	WW	VVV	TTWW	TTZ	TTW	ALL BKG	DATA
4 good leptons	1.07	0.00	3.51	0.00	0.00	0.59	292.62	2.87	0.05	2.21	0.06	8.20	0.13	310.25	416.00
$Z \rightarrow ll$	0.32	0.00	1.24	0.00	0.00	0.19	255.14	1.64	0.05	2.06	0.01	6.37	0.02	266.72	350.00
≥ 1 jet	0.31	0.00	0.57	0.00	0.00	0.19	79.31	0.75	0.00	1.16	0.01	6.25	0.02	88.26	111.00
b-jet veto	0.02	0.00	0.37	0.00	0.00	0.06	60.42	0.49	0.00	0.73	0.00	0.66	0.00	62.73	75.00

699 The extraction of the WZ yield in the control region is performed via a one dimensional nega-
 700 tive log likelihood fit of the shape of the transverse mass of the lepton not associated to the Z
 701 boson to the data. The shape and normalisation of the residual backgrounds are fixed to the ex-
 702 pectations from simulation. Similarly the ZZ yield is extracted performing a template fit of the
 703 reconstructed Z boson invariant mass to the data. Table 11 shows the number of fitted events.
 704 The first uncertainty is from the fit whereas the second one is obtained varying the residual
 705 background contributions by $\pm 100\%$.

Table 11: Fitted number of WZ and ZZ events in the respective control regions.

Number of fitted WZ events	Number of fitted ZZ events
$108 \pm 11 \pm 11$	$73 \pm 9 \pm 3$

706 Figures 40 to 43 show the good agreement observed in the WZ control region for following
 707 distributions :

- 708 • the transverse invariant mass of the lepton not associated to the reconstructed Z
 709 boson and the E_T^{miss}
- 710 • the $E_T^{miss} LD$ variable
- 711 • the selected jet multiplicity
- 712 • the sum of the selected lepton charges
- 713 • the vectorial sum of the transverse momenta of the selected leptons
- 714 • the invariant mass of the selected leptons

- 715 • the reconstructed Z boson invariant mass
 716 • the transverse momentum of the reconstructed Z boson

717 Similar agreement can be seen on Figures 44 to 47 for the ZZ control region.

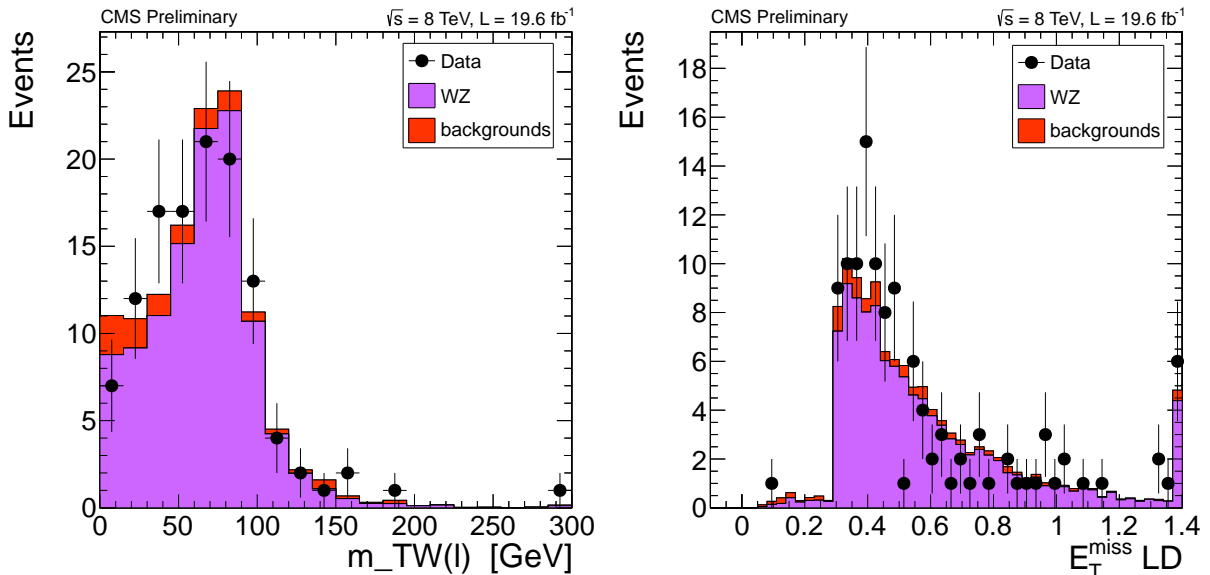


Figure 40: Distribution of the transverse invariant mass of the lepton not associated to the reconstructed Z boson, $m_T(l)$, (left) and $E_T^{\text{miss}} \text{LD}$ variable (right), after a fit of the WZ and background processes to the data.

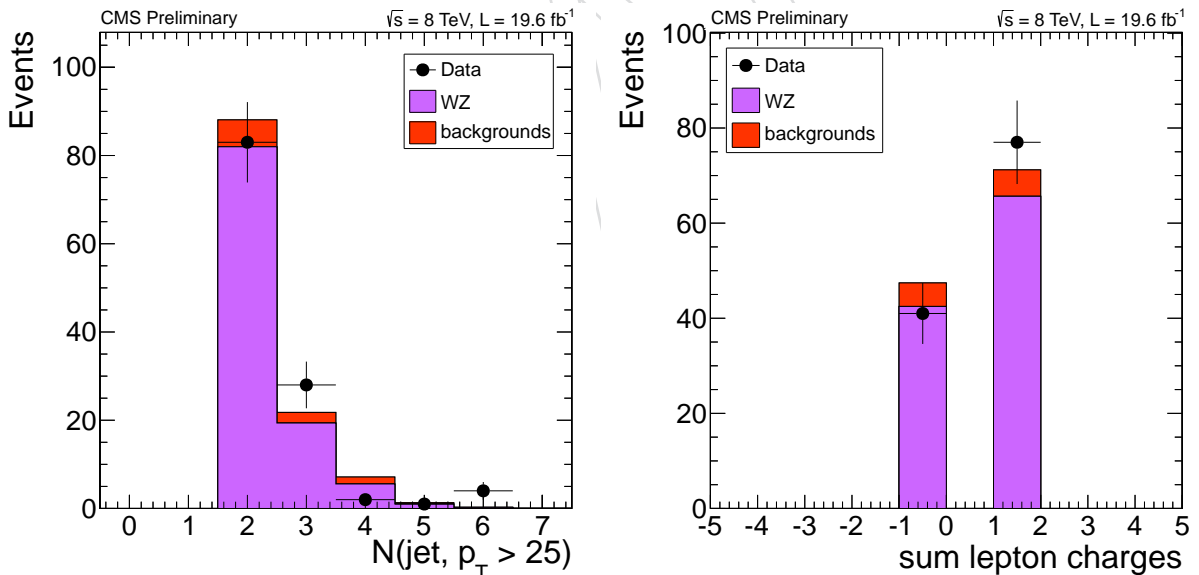


Figure 41: Distribution of the jet multiplicity (left) and sum of the lepton charges (right) after a fit of the WZ and background processes to the data.

718 7.3.2 Extrapolation to events with b-jets

- 719 The ratios of the event yields between signal region and control regions, WZbb/WZ2j0b and
 720 ZZb(b)/ZZ1j0b are measured in simulation.
 721 The main systematics are expected to come from the b-tagging scale factors since most of the
 722 WZ plus two b-jets events and ZZ plus one or two b-jets are due to mistags:

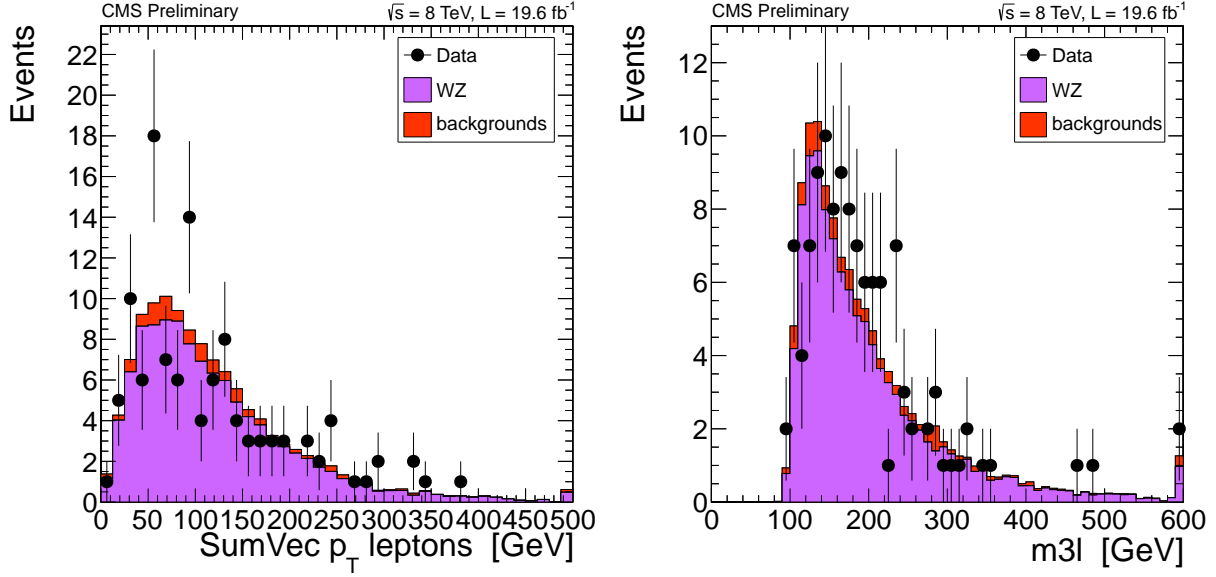


Figure 42: Distribution of the vectorial sum of the lepton transverse momenta (left) and invariant mass of the selected leptons (right) after a fit of the WZ and background processes to the data.

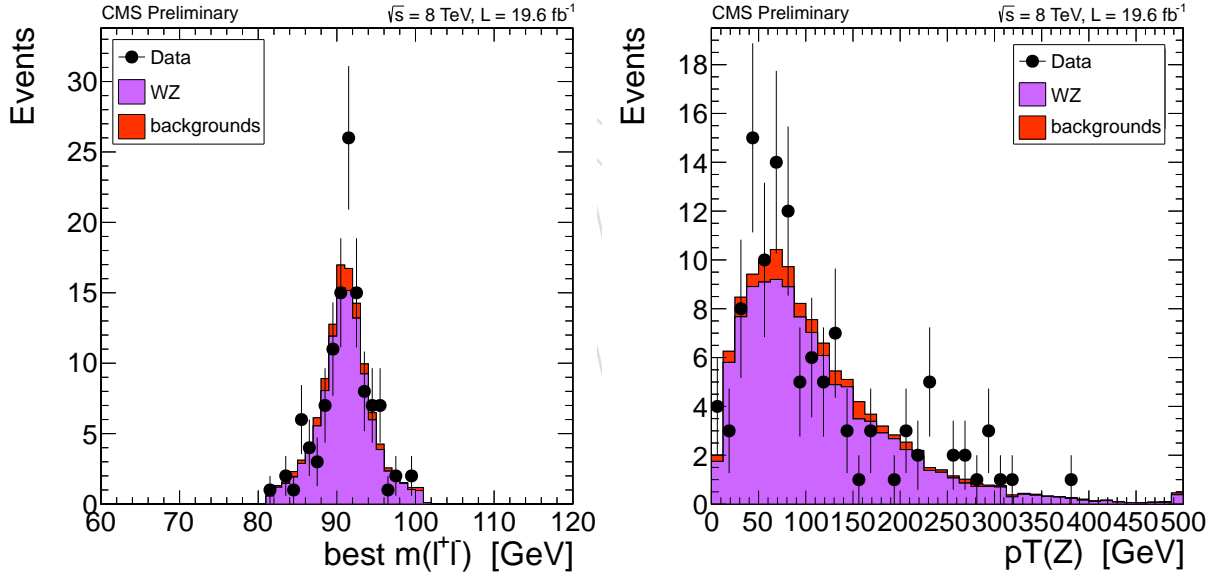


Figure 43: Distribution of the reconstructed Z boson invariant mass (left) and transverse momentum (right) after a fit of the WZ and background processes to the data.

$$^{723} \text{WZbb/WZ2j0b} = 0.021 \pm 0.003(SF_l) \pm 0.001(SF_b)$$

$$^{724} \text{ZZb(b)/ZZ1j0b} = 0.0096 \pm 0.0005(SF_l) \pm 0.0005(SF_b)$$

Theoretical uncertainties can arise from the modelling of the heavy flavour content of the jets in diboson plus multijet events. The expected flavour composition for WZ events satisfying the b-tagging selection used in the analysis is approximately 47% events with mistagged jets from gluons or u,d,s quarks, 38% events with at least a jet from a charm quark light jet (3% being WZ + cc>, the rest single-charm production), and the remaining 15% from events with at least one bottom quark or antiquark (3% from WZ + bb>). For ZZ the flavour composition is different: 40% mistags, 25% charm, and 35% bottom, about one third of which from ZZ + bb> and

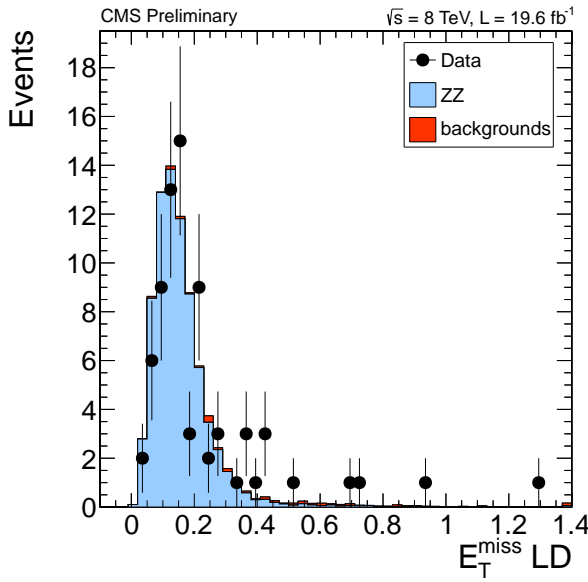


Figure 44: Distribution of the $E_T^{\text{miss}} \text{LD}$ variable (left) after a fit of the ZZ and background processes to the data.

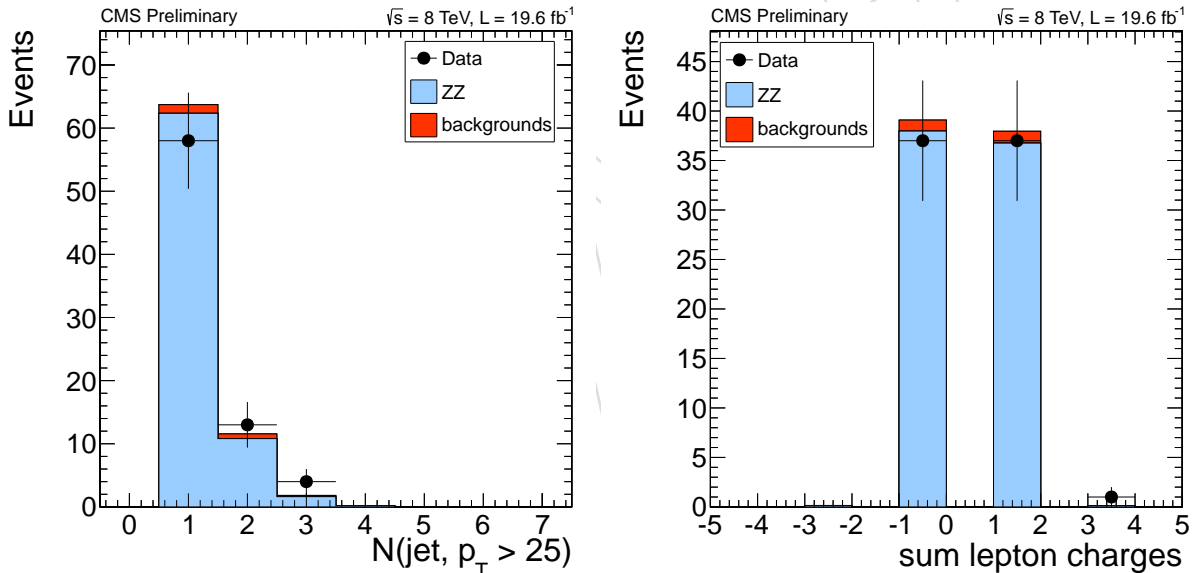


Figure 45: Distribution of the jet multiplicity (left) and sum of the lepton charges (right) after a fit of the ZZ and background processes to the data.

- 732 the rest from events with a single b-jet.
- 733 The uncertainties from unknown higher orders in QCD are estimated using MADGRAPH and
734 aMC@NLO. Computations are performed at parton level, applying to the jets the same p_T and
735 η cuts used in the analysis; no requirements instead are applied on the decay products of the
736 W and Z. When generating the ZZ process in MADGRAPH, we veto the Feynmann diagrams
737 with a Higgs boson exchanged in the s-channel.
- 738 For the WZ case, we focus the analysis on the dominant contribution from WZ plus a charm
739 quark or antiquark. We perform both a LO computation for diboson plus dijets using MAD-
740 GRAPH and an NLO computation for inclusive WZ plus charm or anti-charm using aMC@NLO.
741 We compare the cross sections computed for these processes with the ones inclusive in the jet

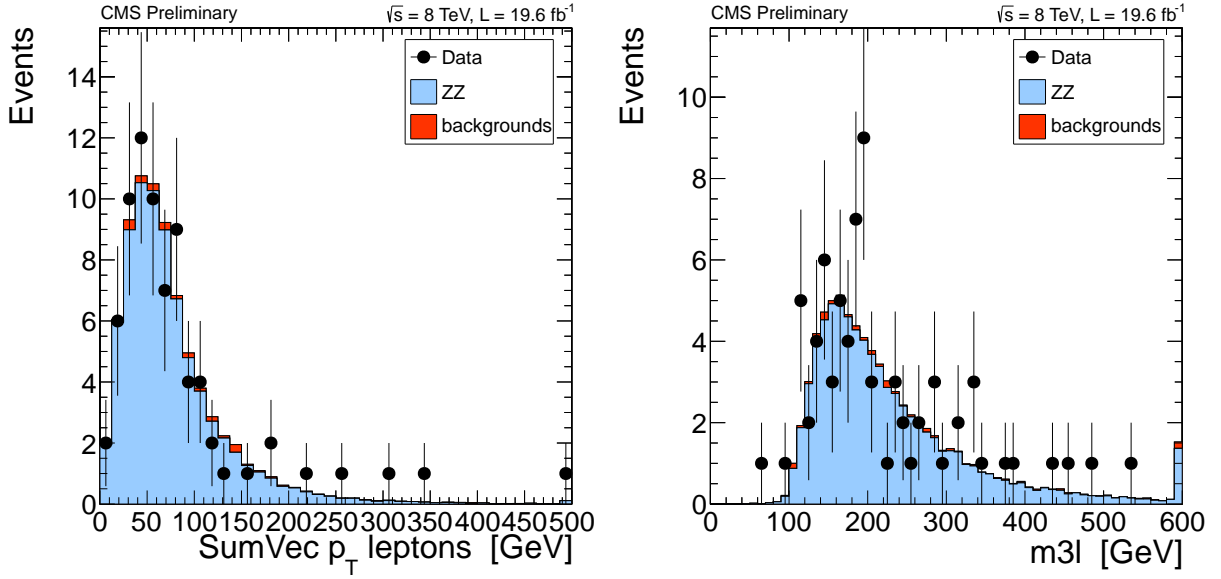


Figure 46: Distribution of the vectorial sum of the lepton transverse momenta (left) and invariant mass of the selected leptons (right) after a fit of the ZZ and background processes to the data.

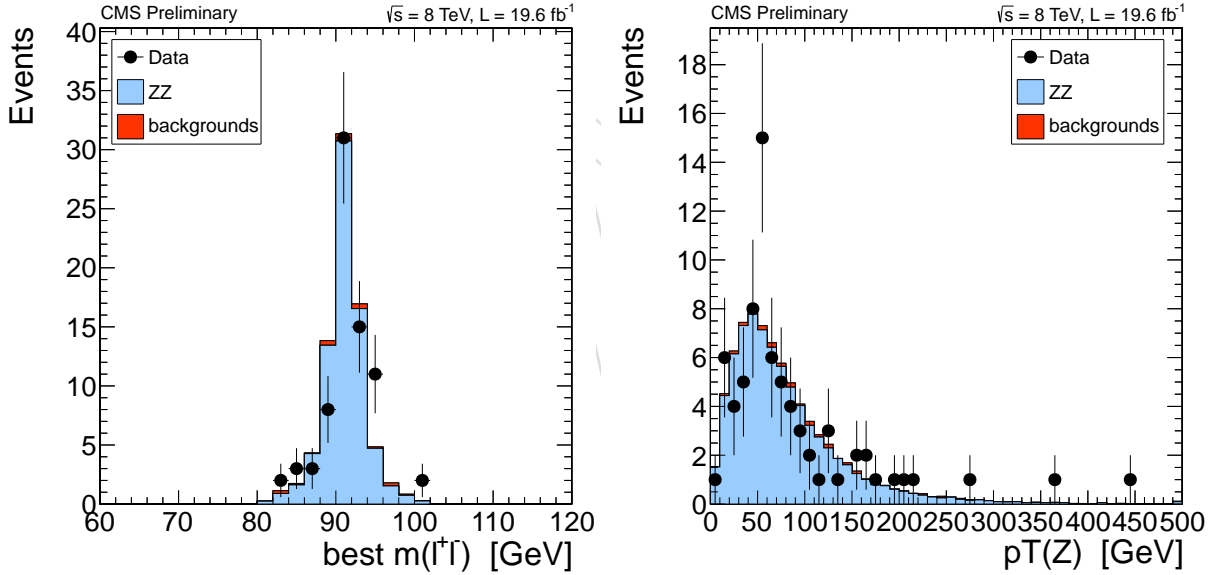


Figure 47: Distribution of the reconstructed Z boson invariant mass (left) and transverse momentum (right) after a fit of the ZZ and background processes to the data.

flavour, at NLO. The results are reported in Tab. 12. We observe little or no dependence of the fraction of charm flavour on the choice of the renormalization and factorization scale, while the variation of the overall cross section is about 30% at LO and 12% at NLO. We therefore estimate that the theoretical uncertainty on the flavour composition should be significantly smaller than the variation of the cross section. Since only half of the WZ events with b-jets is from heavy flavour, we assume that the overall theoretical uncertainty from missing higher orders in QCD on this background should be smaller than about 5%, and thus negligible compared to the other uncertainties.

In the case of ZZ, we extrapolate from one jet to two jets, so we expect the impact of missing

process	order	nominal	scale up	scale down
$\sigma(WZ+c+j)$	LO	0.44 pb	0.34 pb	0.58 pb
$\sigma(WZ+j+j)$	LO	5.47 pb	4.20 pb	7.35 pb
$\sigma(WZ+c)$	NLO	0.61 pb	0.56 pb	0.69 pb
$\sigma(WZ+j)$	NLO	8.10 pb	7.59 pb	8.64 pb

Table 12: Cross sections for WZ production in association with jets containing charm quarks or antiquarks (c) or any flavour of quarks except the bottom (j), for the nominal choice of the renormalization and factorization, for twice that value (scale up) and half of that value (scale down). LO cross sections are computed with MADGRAPH, while NLO ones are from aMC@NLO.

process	nominal	scale up	scale down
$\sigma(ZZ+j)$	1.729 pb	1.522 pb	1.971 pb
$\sigma(ZZ+j+j)$	0.629 pb	0.487 pb	0.830 pb

Table 13: Cross sections for ZZ production in association with one and two jets, for the nominal choice of the renormalization and factorization, for twice that value (scale up) and half of that value (scale down). Gluons and all quark flavours are included in the jet definition. All computations are performed at LO using MADGRAPH.

higher orders in QCD to be larger. We estimate this uncertainty by looking at the variation of the ratio between the production cross sections of ZZ associated with one or two jets when changing the renormalization and factorization scales up and down by a factor two in a correlated way across the two processes, which leads to a 12% systematic uncertainty (Tab. 13) between the two processes. In addition we also study the dependence of the flavour composition of ZZ plus dijet events, and as in the WZ case we observe only a very small dependency on the scale choice (Tab. 14).

Uncertainties on the extrapolation arising from parton distribution functions are estimated by simulated reweighting the events to different PDFs sets and all their associated eigenvectors or replicas, and combining them according to the PDF4LHC prescription.

The overall uncertainty on the normalisation of the WZ background is 22%: 10% from the statistical uncertainty in the control region, 10% from the residual backgrounds in the control region, 15% from the uncertainties on the b-tagging efficiencies, 4% from the parton distribution functions and below 5% from the theoretical uncertainties on the extrapolation.

The overall uncertainty on the normalisation of the ZZ background is 19%: 12% from the statistical uncertainty in the control region, 4% from the residual backgrounds in the control region, 7.5% from the uncertainties on the b-tagging efficiencies, 3% from the parton distribution

process	nominal	scale up	scale down
$\sigma(ZZ+j_l+j_l)$	0.544 pb	0.419 pb	0.723 pb
$\sigma(ZZ+c+j)$	0.022 pb	0.018 pb	0.028 pb
$\sigma(ZZ+b+j)$	0.025 pb	0.021 pb	0.030 pb
$\sigma(ZZ+b+b)$	0.038 pb	0.029 pb	0.049 pb

Table 14: Cross sections for ZZ production in association with jets containing only light quarks or gluons (j_l), charm quarks or antiquarks (c), bottom quarks or antiquarks (b) and flavour of quarks except the bottom (j). The results are given for the nominal choice of the renormalization and factorization, for twice that value (scale up) and half of that value (scale down). All computations are performed at LO using MADGRAPH.

functions and 12% from the theoretical uncertainties on the extrapolation (dominated by the uncertainty on the ratio between the theoretical predictions for $ZZ + 2\text{jets}$ and $ZZ + 1\text{jet}$).

For the WZ background in the trilepton final state, we evaluate also the PDF uncertainty on the charge asymmetry; this amounts to approximately a relative $\pm 5\%$ on the yields in the mostly-positive final state anti-correlated with a similar uncertainty on the mostly-negative final state².

7.4 Fake lepton backgrounds

The estimation of the reducible backgrounds arising from non-prompt leptons misidentified as prompt ones is based on the “fake rate” method: a control region dominated by reducible backgrounds is defined by selecting events with the same kinematics as the signal region but in which at least one of the leptons does not satisfy the lepton MVA requirements. The extrapolation from this control region to the signal region is then performed relying on the probability for a non-prompt lepton to satisfy the lepton MVA requirement (*fake rate*), measured in a second control region. In order to avoid confusion, the control region where the measurement of the probability is performed will be referred to as *measurement region* while the control region obtained from the signal region relaxing the lepton selection will be referred as *application region*.

The fake rate does not depend only on the type of lepton, muon or electron, or on the kinematics, but also on its origin: real leptons from semileptonic decays of B hadrons have a different fake rate with respect to charged hadrons misidentified as lepton or muons from decays in flight of light hadrons, since the discriminating variables used in the MVA will be distributed differently in the two cases. In order for this method to provide an unbiased estimate of the reducible background in the signal region, it is therefore necessary to define a measurement region in which fake rates reproduces well the fake rate in the application region. It is also necessary to control the contamination from prompt leptons in the measurement region, as they would otherwise result in an overestimation of the fake rate.

Studies with simulated events have been performed to determine a control region enriched in non-prompt leptons, and whose flavour composition and fake rate well reproduces the ones of the application region, which is expected to be dominated by $t\bar{t}$ and single-top events.

A suitable control region is found to be QCD $b\bar{b}$ events in which both b -jets contain a reconstructed lepton, allowing the events to be selected with the double muon and muon electron triggers, similar to what used in the signal region, and are not prescaled. Another good control region is QCD $b\bar{b}$ events where one jet satisfies the tight working point of the CSV b -tagger and the second contains a reconstructed lepton. In this case, we have to rely on single lepton triggers, which are all prescaled. For electrons, where the fake rate is less dependent on the sample composition, a third control region can be defined selecting events that contain a $Z \rightarrow \ell\ell$ candidate plus a third lepton; this control sample is not usable for muons, since it contains mostly leptons not originating from B hadron decays.

The measurement of the misidentification probabilities and the application to the events in the control region are performed separately for events with at most one jet satisfying the medium operating point of the CSV b tagger and for events with at least two, to account for the different flavour composition and kinematic of the two samples.

²The requirement of loosely b -tagged jets favours the production of WZ in association with c quarks from a Wcs vertex, so the WZ is not produced from annihilation of quarks from the proton, and there is no charge asymmetry.

809 **7.4.1 QCD dilepton control region**

810 Events in this control region are selected by requiring one lepton (*tag lepton*) to be identified as
 811 a muon from a B hadron decay, by having a large impact parameter significance ($S_{\text{IP3D}} > 7$)
 812 and being anti-isolated ($I_{\text{rel}} > 0.5$), while the second lepton (*probe lepton*) must satisfy the lepton
 813 preselection applied upstream to the MVA. When measuring the fake rate for the tight working
 814 point used in the two-lepton same-sign analysis, the extra requirements to suppress charge
 815 misidentification are also applied to the probe before the measurement.

While the requirements on the tag lepton strongly suppress events where the lepton is promptly produced, there is still a significant contamination from events with a prompt lepton, the probe, plus a b-jet, providing the tag. Additional requirements are then applied to reduce this contamination: (i) events are vetoed if additional leptons satisfying the preselection are found, to suppress Drell-Yan events; (ii) the tag and probe leptons are required to be in a back-to-back topology, $|\Delta\phi| > 2.5$ and not unbalanced in transverse momentum in favour of the probe:

$$\frac{p_T(\text{probe})}{p_T(\text{tag}) \cdot (1 + I_{\text{rel}}(\text{tag}))} < 1$$

816 In this condition, the tag momentum is corrected by the relative isolation since the tag lepton is
 817 by construction less isolated than the probe, and therefore otherwise carrying a smaller fraction
 818 of the b-jet momentum.

819 When measuring the fake rate for events with two b-tagged jets, some modifications to the
 820 control region are made: a b-jet is required, with $p_T > 25 \text{ GeV}$, satisfying the medium working
 821 point of the CSV tagger, and separated from the tag and from the probe by $\Delta R > 0.7$. The
 822 criteria to suppress the contamination from prompt leptons are also modified, since in this
 823 control region prompt leptons from semileptonic $t\bar{t}$ are more important. In addition to the
 824 veto for additional leptons, the following requirements are imposed: (i) events are vetoed if
 825 they have more than two hadronic jets with $p_T > 25 \text{ GeV}$, $|\eta| < 2.4$, or any hadronic jet with
 826 $p_T > 25 \text{ GeV}$, $2.4 < |\eta| < 4.7$; (ii) the tag and the b-tagged jet are required to be separated
 827 in pseudorapidity, $|\eta_{\text{tag}} - \eta_b| > 1.5 \cdot (p_{T,\text{probe}}/50 \text{ GeV})$, which suppresses $t\bar{t}$ compared to QCD
 828 (the p_T dependency of the cut introduced since the contamination from $t\bar{t}$ increases with p_T).
 829 To increase the acceptance, the requirements on the tag are relaxed slightly ($S_{\text{IP3D}} > 4$ and
 830 $I_{\text{rel}} > 0.4$).

831 **7.4.2 Corrections for prompt-lepton contamination**

832 Depending on the transverse momentum of the lepton, different approaches are used to con-
 833 trol the residual contamination from prompt leptons after this selection. For low transverse
 834 momentum $p_T < 10$, where the contamination is smaller, a tight requirement is applied on the
 835 missing transverse energy in the event, $E_T^{\text{miss}} < 15 \text{ GeV}$. This provides a satisfactory rejection
 836 of the events with prompt leptons: $W \rightarrow \ell\nu$, $Z \rightarrow \ell^+\ell^-$ with one lepton not reconstructed
 837 (and thus visible as E_T^{miss}), or $Z \rightarrow \tau^+\tau^-$ events with one tau decaying leptonically and one
 838 hadronically, or semileptonic $t\bar{t}$.

For higher transverse momenta, the fake rate is measured separately for events with small E_T^{miss}
 ([0, 20] GeV) and events with large E_T^{miss} ([45, 80] GeV). As the fake rate does not depend on the
 missing transverse energy, neither for prompt nor for non-prompt leptons, the measured fake
 rates in the two regions differ only because of the different relative fractions of prompt and
 non-prompt leptons. Relying on simulated events to estimate the relative yields of events with
 prompt leptons in the two E_T^{miss} regions, it is then possible to extract from the two measurement
 the fake rate for non-prompt leptons alone. Let f_{QCD} and f_P be the fake rates for non-prompt

and prompt leptons, and $f^S = N_{\text{pass}}^S / N_{\text{all}}^S$, $f^L = N_{\text{pass}}^L / N_{\text{all}}^L$, the measured fake rates in the regions with small and large E_T^{miss} :

$$\begin{aligned} f^{S,L} &= \frac{N_{\text{pass}}^{S,L}}{N_{\text{all}}^{S,L}} = \frac{N_{\text{QCD,pass}}^{S,L} + N_{\text{P,pass}}^{S,L}}{N_{\text{all}}^{S,L} + N_{\text{P,all}}^{S,L}} = f_{\text{QCD}} \cdot \frac{N_{\text{QCD,all}}^{S,L}}{N_{\text{all}}^{S,L}} + f_{\text{P}} \cdot \frac{N_{\text{P,all}}^{S,L}}{N_{\text{all}}^{S,L}} = \\ &= f_{\text{QCD}} \cdot \left(1 - \frac{N_{\text{P,all}}^{S,L}}{N_{\text{all}}^{S,L}}\right) + f_{\text{P}} \cdot \frac{N_{\text{P,all}}^{S,L}}{N_{\text{all}}^{S,L}} = f_{\text{QCD}} \cdot (1 - x_{\text{P}}^{S,L}) + f_{\text{P}} \cdot x_{\text{P}}^{S,L}, \end{aligned}$$

where $x_{\text{P}}^{S,L} := N_{\text{P,all}}^{S,L} / N_{\text{all}}^{S,L}$ is the contamination from prompt lepton in the two regions at denominator, i.e. before the application of the lepton MVA.

The ratio of the contaminations in the two control regions can be factorised:

$$r_{\text{P}}^{\text{SL}} := \frac{x_{\text{P}}^S}{x_{\text{P}}^L} = \frac{N_{\text{P,all}}^S / N_{\text{all}}^S}{N_{\text{P,all}}^L / N_{\text{all}}^L} = \left(\frac{N_{\text{P,all}}^S}{N_{\text{P,all}}^L}\right) \left(\frac{N_{\text{all}}^L}{N_{\text{all}}^S}\right),$$

where the first term is estimated from simulated events, while the second is a ratio of overall observed event yields in data. This leads to a set of two linear equations,

$$\begin{aligned} f^L &= f_{\text{QCD}} \cdot (1 - x_{\text{P}}^L) + f_{\text{P}} \cdot x_{\text{P}}^L = f_{\text{QCD}} + (f_{\text{P}} - f_{\text{QCD}}) \cdot x_{\text{P}}^L \\ f^S &= f_{\text{QCD}} + (f_{\text{P}} - f_{\text{QCD}}) \cdot x_{\text{P}}^S = f_{\text{QCD}} + (f_{\text{P}} - f_{\text{QCD}}) \cdot r_{\text{P}}^{\text{SL}} x_{\text{P}}^L \end{aligned}$$

with two unknowns f_{QCD} and $(f_{\text{P}} - f_{\text{QCD}}) \cdot x_{\text{P}}^S$, that can be solved directly:

$$f_{\text{QCD}} = \frac{f_S - r_{\text{P}}^{\text{SL}} f_L}{1 - r_{\text{P}}^{\text{SL}}}.$$

This approach is viable as long as r_{P}^{SL} is significantly smaller than unity.

7.4.3 QCD b-jet plus lepton control region

This control region is defined similarly to the QCD dilepton control region, but the role of the tag is taken by a b-tagged jet. The jet is required to have $p_T > 40$ GeV and pass the tight working point of the CSV b-tagger. As in the dilepton region, the jet is required to be back-to-back with the probe lepton, the p_T of the probe must not exceed the p_T of the tag, and events with more than one lepton satisfying the preselection requirement are vetoed.

Muon probes are selected using the inclusive non-isolated single muon triggers with thresholds of 5, 8, 12, 17, 24 and 40 GeV. As the triggers have different prescale factors, within each p_T bin only a single trigger is used, the one with the highest threshold among those whose threshold is lower than the low edge of the bin. For the lowest momentum bins, an additional trigger with a p_T threshold of 5 GeV and a very loose isolation criteria ($I_{\text{rel}} < 1.0$) is also used. To further increase the sample size at low momentum, events are also accepted if they are triggered by the inclusive non-isolated single muon trigger with p_T threshold of 40, not matched to the probe, and they do not otherwise qualify for the dilepton control region; typically these events contain a probe muon with p_T below the threshold for the double muon trigger, 8 GeV, and a high-momentum non-prompt muon within the tag jet that provides the trigger and fails the lepton preselection.

Electron probes are selected using the logical OR of the prescaled single electron triggers with p_T thresholds of 8 and 17 GeV, with tight calorimetric identification requirements, and very

861 loose requirements for the calorimetric isolation, track-based identification and track-based
 862 isolation, similarly to what requested in double-lepton triggers.

863 The approach used to subtract the contamination from prompt leptons in this control region is
 864 identical to the one used in the QCD dilepton control region.

865 When measuring the fake rate for events with two b-tagged jets, the control region is modified
 866 in the same way as the dilepton one, by requiring an additional b-jet other than the tag, and
 867 imposing $N(\text{jet})$ and $\Delta\eta$ criteria to suppress $t\bar{t}$. Similarly to that case, to increase the accep-
 868 tance the requirements on the tag are relaxed slightly: $p_T > 30 \text{ GeV}$ instead of 40 GeV , and the
 869 medium CSV working point is used instead of the tight one..

870 7.4.4 Z plus lepton control region

871 A control region that with small contamination from prompt leptons and easily accessible in
 872 terms of triggers is the one defined by the presence of a $Z \rightarrow \ell^+ \ell^-$ candidate plus a third lepton.
 873 This control region is not enriched in leptons from b hadron decays, but is nonetheless usable
 874 for measuring the fake rate of low p_T electron candidates, less dependent on the flavour; on
 875 simulated events, a good agreement is found between the fake rate extracted from leptons in
 876 this control region and the target fake rate from non-prompt leptons in $t\bar{t}$ events.

877 The $Z \rightarrow \ell^+ \ell^-$ candidate is selected requiring both leptons to pass the loose MVA require-
 878 ments, and the pair to be within 10 GeV from the nominal mass of the Z boson. The invariant
 879 mass of the two pairs containing a lepton from the Z and the probe lepton are both required to
 880 be larger than 12 GeV , to suppress events with $W/Z + \gamma^*$ events, or conversion electrons from
 881 final state radiation photons.

882 Additional requirements are needed to control the contaminations from WZ and ZZ production
 883 in data: events with $E_T^{\text{miss}} LD > 0.3$ are rejected, the transverse mass of the probe lepton and
 884 E_T^{miss} system is required to be below 40 GeV , and events are vetoed if more than three leptons
 885 are found.

886 The residual contamination from this selection is subtracted at numerator and denominator of
 887 the fake rate using simulated WZ and ZZ events, normalised using the integrated luminosity
 888 of the data sample. A systematic uncertainty of $\pm 50\%$ is assumed on this subtraction.

889 The measurement in this region is performed only for $p_T < 30$, beyond which the contamina-
 890 tion from prompt leptons becomes too large. No attempt is made to use this control region in
 891 events with two b-jets.

892 7.4.5 Results

893 The measured fake rates for each of the control regions are reported separately in appendix B.

894 In general, the fake rate expectation from simulated events of the control regions is compatible
 895 with the expectations from non-prompt leptons in simulated $t\bar{t}$ events within their statistic
 896 uncertainties and an additional systematic uncertainty of about $\pm 40\%$.

897 In all control regions, the fake rates measured from data are mostly in agreement with the
 898 expectations from simulation. However, the uncertainties on individual measurements are
 899 sizable.

900 In order to reduce the statistic fluctuations in the results, measurements from the different
 901 control regions in data are combined, with weights proportional to the inverse of the squares
 902 of the uncertainties on the individual measurements. The corresponding expectations from

903 simulated events are likewise combined, using the same weights as the data, so that the result
 904 remains comparable with the one from data even when the hierarchy of the uncertainties in
 905 simulation and data differ.

906 The combination is found to improve the agreement both between data and expectations from
 907 simulation and between control regions in simulation and $t\bar{t}$ events in simulation (Fig. 48,49,50).
 908 This is expected from the reduction of the statistic uncertainties, and there is potentially also a
 909 partial cancellations of possible systematic biases in the measurements if they affect the individual control regions differently.

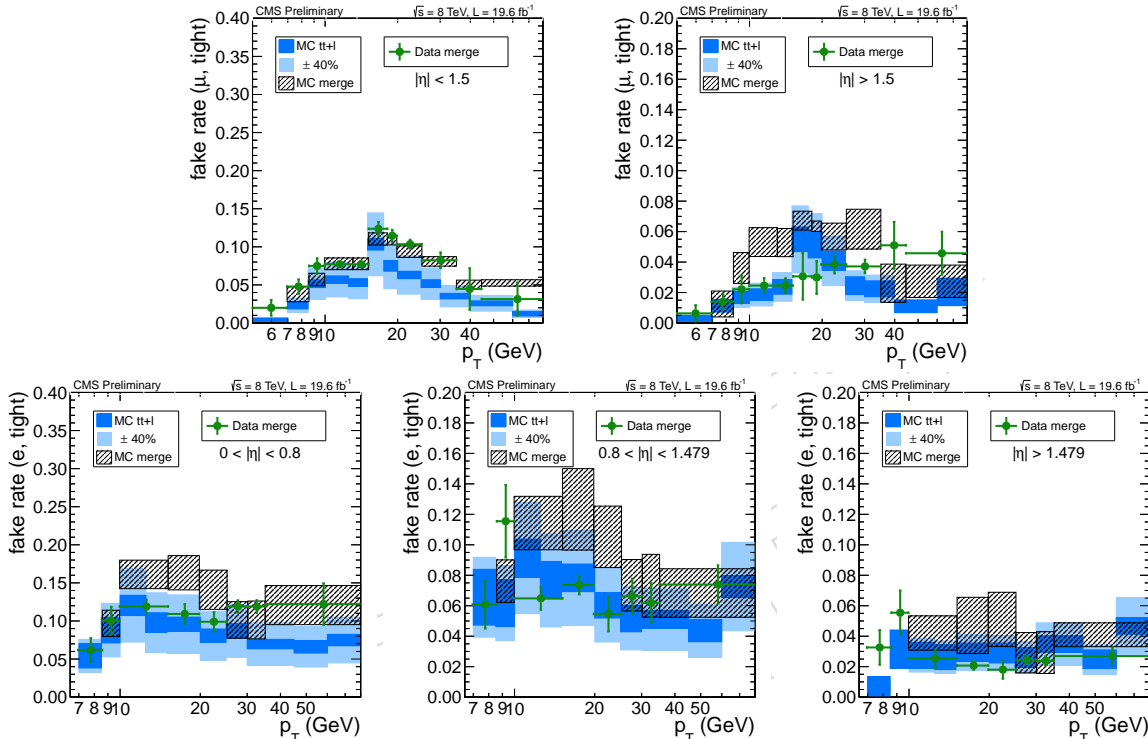


Figure 48: Measured fake rates for the tight MVA working point, combining the different control regions. Combined values from data (dots with error bars) are compared with the combination of the expectations simulated events in control regions (black hatched boxes) and $t\bar{t}$ events in the signal region (blue filled boxes). The results in the top row are for muons, the ones in the bottom for electrons; the results in the different columns corresponds to different $|\eta|$ ranges, increasing from left to right, as written in the plots. Data uncertainties for different p_T bins are not uncorrelated, and neither are the uncertainties on the values from control regions in simulations.

911 7.5 Fake rate application

912 The expected yields in an event with n leptons of which k pass the full selection and $(n - k)$
 913 fail that selection can be written in terms of the expected yields from processes with n leptons
 914 among prompt and non-prompt ones, and of the efficiencies and fake rates.

915 7.5.1 Two-lepton final state

Two lepton events can be separated according to whether both pass the selection N_{pp} , the first passes and the second fails N_{pf} or viceversa N_{fp} , or both fail N_{ff} . All four states can receive contributions from events in which both leptons are prompt (N_{11}), both are non-prompt (N_{00})

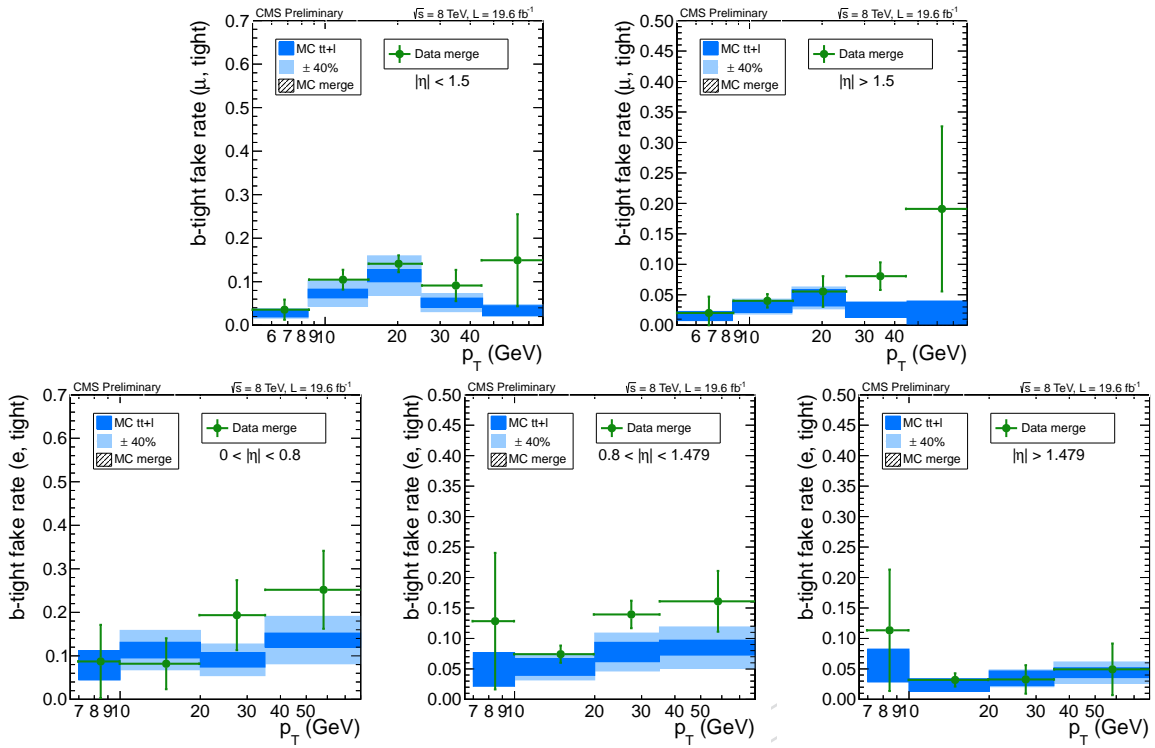


Figure 49: Measured fake rates for the tight MVA working point, combining the different control regions, for events with at least two jets satisfying the medium operation point of the CSV tagger. Combined values from data (dots with error bars) are compared with the expectations for $t\bar{t}$ events in the signal region (blue filled boxes). The results in the top row are for muons, the ones in the bottom for electrons; the results in the different columns corresponds to different $|\eta|$ ranges, increasing from left to right, as written in the plots. Data uncertainties for different p_T bins are not uncorrelated.

or one is prompt and the other isn't (N_{01}, N_{10}). If ϵ_i and f_i are the efficiency for prompt leptons and fake rate for non-prompt ones as function of the p_T, η of the i -th lepton, the yields can be expressed as

$$\begin{pmatrix} N_{pp} \\ N_{pf} \\ N_{fp} \\ N_{ff} \end{pmatrix} = \begin{pmatrix} \epsilon_1 \epsilon_2 & \epsilon_1 f_2 & f_1 \epsilon_2 & f_1 f_2 \\ \epsilon_1 (1 - \epsilon_2) & \epsilon_1 (1 - f_2) & f_1 (1 - \epsilon_2) & f_1 (1 - f_2) \\ (1 - \epsilon_1) \epsilon_2 & (1 - \epsilon_1) f_2 & (1 - f_1) \epsilon_2 & (1 - f_1) f_2 \\ (1 - \epsilon_1) (1 - \epsilon_2) & (1 - \epsilon_1) (1 - f_2) & (1 - f_1) (1 - \epsilon_2) & (1 - f_1) (1 - f_2) \end{pmatrix} \begin{pmatrix} N_{11} \\ N_{10} \\ N_{01} \\ N_{00} \end{pmatrix}$$

In principle, one can solve the linear system of equations to determine the expected contribution in the N_{pp} arising from the backgrounds (N_{10}, N_{01}, N_{00}) as function of the yields in the four regions and of the efficiency and fake rate. However, in practice in our case it is possible to simplify the equations significantly with an approximations: the contributions from prompt leptons failing the selection can be neglected with respect to the contributions of non-prompt leptons, e.g. $\epsilon_1 (1 - \epsilon_2) N_{11}$ can be neglected with respect to $\epsilon_1 (1 - f_2) N_{10}$, both because of the smaller prefactor $(1 - \epsilon_2) < (1 - f_2)$ and of the smaller yield $N_{11} < N_{10}$. Likewise, in the yields for events with exactly one passing lepton, the contributions from processes with exactly one prompt lepton are dominated by cases where the prompt lepton passes the selection and the non-prompt one fails it, and the case where the two are swapped can be neglected $\epsilon_1 (1 - f_2) N_{10} \gg (1 - \epsilon_1) f_2 N_{01}$ since the initial yields are of the same order but the coefficients

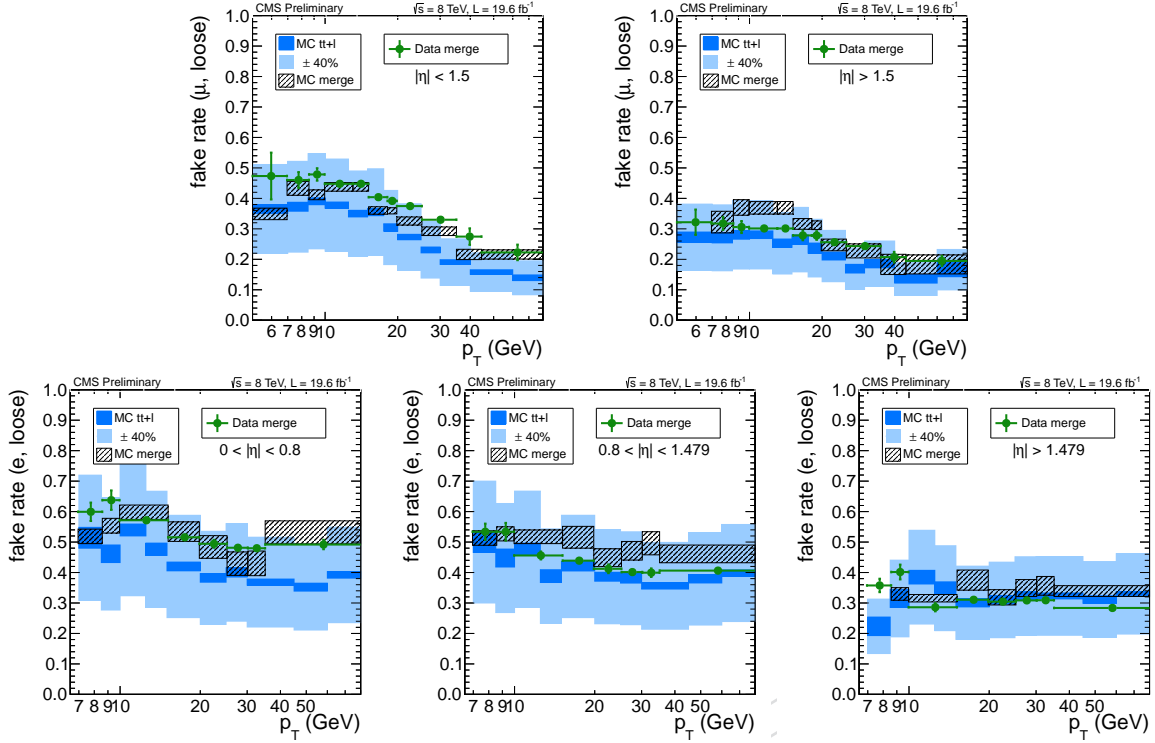


Figure 50: Measured fake rates for the loose MVA working point, combining the different control regions. Combined values from data (dots with error bars) are compared with the combination of the expectations simulated events in control regions (black hatched boxes) and $t\bar{t}$ events in the signal region (blue filled boxes). The results in the top row are for muons, the ones in the bottom for electrons; the results in the different columns corresponds to different $|\eta|$ ranges, increasing from left to right, as written in the plots. Data uncertainties for different p_T bins are not uncorrelated, and neither are the uncertainties on the values from control regions in simulations.

are not, $\epsilon(1-f) \gg (1-\epsilon)f$.

$$\begin{pmatrix} N_{pp} \\ N_{pf} \\ N_{fp} \\ N_{ff} \end{pmatrix} = \begin{pmatrix} \epsilon_1 \epsilon_2 & \epsilon_1 f_2 & f_1 \epsilon_2 & f_1 f_2 \\ 0 & \epsilon_1 (1-f_2) & 0 & f_1 (1-f_2) \\ 0 & 0 & (1-f_1) \epsilon_2 & (1-f_1) f_2 \\ 0 & 0 & 0 & (1-f_1)(1-f_2) \end{pmatrix} \begin{pmatrix} N_{11} \\ N_{10} \\ N_{01} \\ N_{00} \end{pmatrix}$$

With this approximation N_{00} can be derived directly from the last equation, and substituted in the two middle ones,

$$\begin{aligned} N_{pf} &= \epsilon_1 (1-f_2) N_{10} + f_1 (1-f_2) [N_{ff} / (1-f_1)(1-f_2)] \\ N_{fp} &= \epsilon_2 (1-f_1) N_{01} + f_2 (1-f_1) [N_{ff} / (1-f_1)(1-f_2)], \end{aligned}$$

which can be solved for N_{10} and N_{01} :

$$\begin{aligned} N_{10} &= \frac{N_{pf} - \frac{f_1}{1-f_1} N_{ff}}{\epsilon_1 (1-f_2)} \\ N_{01} &= \frac{N_{fp} - \frac{f_2}{1-f_2} N_{ff}}{\epsilon_2 (1-f_1)}, \end{aligned}$$

so that eventually the background contribution in the signal region is just

$$\begin{aligned} N_{pp}^{\text{bkg}} &= \epsilon_1 f_2 N_{10} + \epsilon_2 f_1 N_{01} + f_1 f_2 N_{00} = \\ &= \epsilon_1 f_2 \frac{N_{pf} - \frac{f_1}{1-f_1} N_{ff}}{\epsilon_1(1-f_2)} + \epsilon_2 f_1 \frac{N_{fp} - \frac{f_2}{1-f_2} N_{ff}}{\epsilon_2(1-f_1)} + f_1 f_2 \frac{N_{ff}}{(1-f_1)(1-f_2)} = \\ &= \frac{f_1}{1-f_1} N_{pf} + \frac{f_2}{1-f_2} N_{fp} - \frac{f_1 f_2}{(1-f_1)(1-f_2)} N_{ff}. \end{aligned}$$

- 916 Any prediction for the yield and distribution of background events after the full selection can
 917 thus be obtained from the events with one or both leptons failing the MVA weighted by fac-
 918 tors of $f/(1-f)$. This approximation is also convenient because it decouples the background
 919 prediction in the signal region from the event observed yield in that region.

920 7.5.2 Three-lepton final state

For the three-lepton final state the approach is similar. Working directly in the same approxi-
 mations as for the two-lepton final state the yields are given by

$$\begin{pmatrix} N_{ppp} \\ N_{ppf} \\ N_{pff} \\ N_{fff} \end{pmatrix} = \begin{pmatrix} \epsilon\epsilon\epsilon & \epsilon\epsilon f & \epsilon f f & f f f \\ 0 & \epsilon\epsilon(1-f) & \epsilon f(1-f) & f f(1-f) \\ 0 & 0 & \epsilon(1-f)(1-f) & f(1-f)(1-f) \\ 0 & 0 & 0 & (1-f)(1-f)(1-f) \end{pmatrix} \begin{pmatrix} N_3 \\ N_2 \\ N_1 \\ N_0 \end{pmatrix}$$

- 921 where all the permutations have not been written out explicitly, e.g. $\epsilon f f N_1$ is a shorthand for
 922 $\epsilon_1 f_2 f_3 N_{100} + f_1 \epsilon_2 f_3 N_{010} + f_1 f_2 \epsilon_3 N_{001}$.

As before, the equations can be solved starting from the sample with all failing leptons and progressing up; for N_{pff} the equation becomes

$$N_{pff} = \epsilon_1 (1-f_2) (1-f_3) N_{100} + \frac{f_1}{1-f_1} N_{fff},$$

and so

$$N_{100} = \frac{N_{pff} - \frac{f_1}{1-f_1} N_{fff}}{\epsilon_1 (1-f_2) (1-f_3)}.$$

Propagating one step back,

$$\begin{aligned} N_{ppf} &= \epsilon_1 \epsilon_2 (1-f_3) N_{110} + \epsilon_1 f_2 (1-f_3) N_{100} + f_1 \epsilon_2 (1-f_3) N_{010} + f_1 f_2 (1-f_3) N_{000} = \\ &= \epsilon_1 \epsilon_2 (1-f_3) N_{110} + \frac{f_2}{1-f_2} \left(N_{pff} - \frac{f_1}{1-f_1} N_{fff} \right) + \\ &\quad + \frac{f_1}{1-f_1} \left(N_{fpf} - \frac{f_2}{1-f_2} N_{fff} \right) + \frac{f_1 f_2}{(1-f_1)(1-f_2)} N_{fff} = \\ &= \epsilon_1 \epsilon_2 (1-f_3) N_{110} + \frac{f_2}{1-f_2} N_{pff} + \frac{f_1}{1-f_1} N_{fpf} - \frac{f_1 f_2}{(1-f_1)(1-f_2)} N_{fff}, \end{aligned}$$

so that

$$N_{110} = \frac{1}{\epsilon_1 \epsilon_2 (1-f_3)} \left(N_{ppf} - \frac{f_2}{1-f_2} N_{pff} - \frac{f_1}{1-f_1} N_{fpf} + \frac{f_1 f_2}{(1-f_1)(1-f_2)} N_{fff} \right).$$

Some care is needed to get the right combinatoric in the final result for N_{ppp}^{bkg} .

$$\begin{aligned} N_{ppp}^{\text{bkg}} = & \epsilon_1 \epsilon_2 f_3 N_{110} + \epsilon_1 f_2 \epsilon_3 N_{101} + f_1 \epsilon_2 \epsilon_3 N_{011} + \\ & + \epsilon_1 f_2 f_3 N_{100} + f_1 \epsilon_2 f_3 N_{010} + f_1 f_2 \epsilon_3 N_{001} + \\ & + f_1 f_2 f_3 N_{000} \end{aligned}$$

Substituting the expressions derived previously for N_{110} , N_{100} , N_{000} and their permutations, one gets

$$\begin{aligned} N_{ppp}^{\text{bkg}} = & \frac{f_3}{1-f_3} \left(N_{ppf} - \frac{f_2}{1-f_2} N_{pff} - \frac{f_1}{1-f_1} N_{fpf} + \frac{f_1 f_2}{(1-f_1)(1-f_2)} N_{fff} \right) + \\ & + \frac{f_2}{1-f_2} \left(N_{pf} - \frac{f_3}{1-f_3} N_{pff} - \frac{f_1}{1-f_1} N_{ffp} + \frac{f_1 f_3}{(1-f_1)(1-f_3)} N_{fff} \right) + \\ & + \frac{f_1}{1-f_1} \left(N_{fpp} - \frac{f_2}{1-f_2} N_{ffp} - \frac{f_3}{1-f_3} N_{fpf} + \frac{f_2 f_3}{(1-f_2)(1-f_3)} N_{fff} \right) + \\ & + \frac{f_2 f_3}{(1-f_2)(1-f_3)} \left(N_{pff} - \frac{f_1}{1-f_1} N_{fff} \right) + \\ & + \frac{f_1 f_3}{(1-f_1)(1-f_3)} \left(N_{fpf} - \frac{f_2}{1-f_2} N_{fff} \right) + \\ & + \frac{f_1 f_2}{(1-f_1)(1-f_2)} \left(N_{ffp} - \frac{f_3}{1-f_3} N_{fff} \right) + \\ & + \frac{f_1 f_2 f_3}{(1-f_1)(1-f_2)(1-f_3)} N_{fff}. \end{aligned}$$

Just as in the two-lepton case, the events with a single failing lepton enter the estimate weighted by $f/(1-f)$, and events with two failing leptons enter as with a negative weight $-f_i f_j / ((1-f_i)(1-f_j))$, evaluated on the two leptons failing the selection. In addition, events with all leptons failing the selection enter with a positive weight equal to the product of $f/(1-f)$ factors evaluated on the three leptons.

7.5.3 Four-lepton final state

In the four-lepton final state, studies on simulated events show that the background is mostly from $t\bar{t}$ events with two non-prompt leptons. This is understandable both in terms of the hierarchy of the cross sections between $t\bar{t}$ and $t\bar{t}V$ and of the looser MVA requirement used in this final state.

While the prediction based on the same math used for the three-lepton case is in principle correct also in this case, the contribution from these processes is affected by a very large statistical uncertainty since it's obtained from the subtraction between the events with a single failing lepton and the events with two failing leptons.

We therefore choose to adopt a different approach. Under the approximation that all background is from non-prompt leptons, this can be estimated both from the one-fail and the two-fail events according to

$$N_{4p}^{\text{bkg}} \approx \frac{1}{2} \sum_{3p1f} \frac{f}{1-f} \approx \sum_{2p2f} \frac{f_1 f_2}{(1-f_1)(1-f_2)} \quad (4)$$

937 and we can also combine the two to reduce the statistical uncertainty.

938 We compare the different predictions for the background in a relaxed signal region where we
 939 don't require the charges of the four leptons to add up to zero and we also allow events with
 940 a single hadronic jet provided it satisfies the medium operating point of the CSV b-tagger. In
 941 that region, the prediction using the same algorithm of the three-lepton final state is 2.2 ± 1.7
 942 events, while the predictions using only events with one failing lepton or only events with two
 943 failing leptons yield 1.6 ± 0.8 and 1.0 ± 0.6 events respectively. All predictions are compatible,
 944 and the combination of the last two yields 1.2 ± 0.5 events.

945 Since the event yields in data are small even for events failing the lepton MVA criteria, we
 946 can not rely on the fake rate method to predict the expected distributions of the reducible
 947 background nor the yields after the tight b-tagging criteria. We therefore choose to use the
 948 fake rate method to predict only the overall yield in the relaxed signal region described in the
 949 previous paragraph, and then use simulated $t\bar{t}$ event to extrapolate to the signal region proper
 950 and to predict the kinematic distributions of the background. To support this decision, we
 951 validate the MC description of the distributions in $t\bar{t}$ events with two additional non-prompt
 952 lepton by looking at events satisfying the same requirements of the relaxed signal region, but
 for which at least one lepton fails the MVA requirements (Fig. 51).

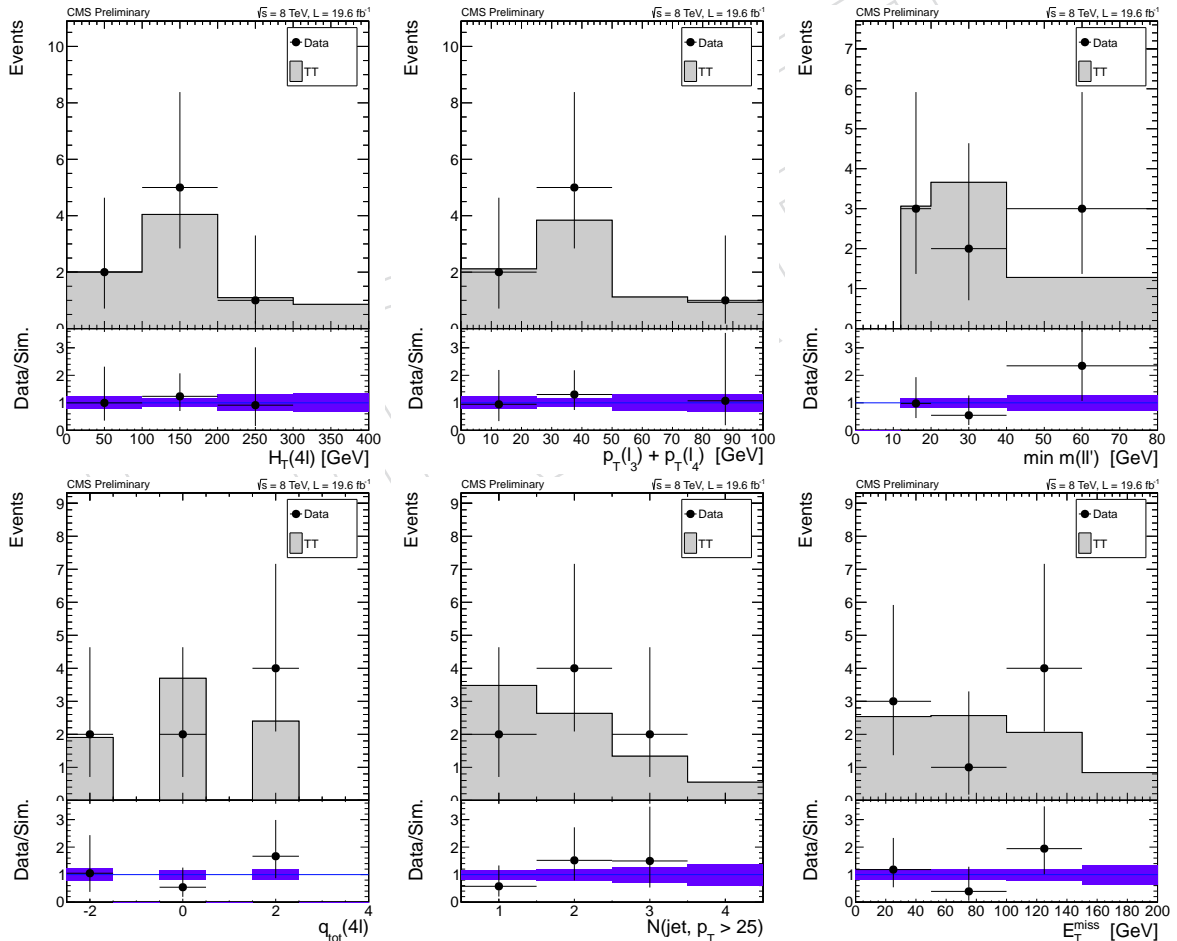


Figure 51: Observed four-lepton events in data and predictions from $t\bar{t}$ MC in a control region obtained from the relaxed signal region by requiring one or two leptons to fail the lepton MVA requirements. The $t\bar{t}$ MC is normalised to the yield in data.

954 **7.5.4 Systematical uncertainties on the predictions**

955 The measurement of the fake rate in the control region has an associated systematical uncer-
 956 tainty of about 40% for inclusive events and 60% for the events with at least two b-jets, esti-
 957 mated from the level of agreement achieved between the fake rate in control regions in simu-
 958 lation and the target fake rate for non-prompt leptons in $t\bar{t}$ MC.

959 To propagate this uncertainty to the background prediction in the signal region, we choose to
 960 separate the uncertainties affecting dominantly the overall normalization of the background
 961 from the ones affecting to the shape of its distribution.

962 In order to assign an uncertainty on the overall normalization of the background, we scale the
 963 overall fake rate by $\pm 40\%$ and derive the predictions accordingly. We assume this normaliza-
 964 tion uncertainty to be independent for electrons and muons, but otherwise correlated across
 965 the different final states and categories. However, since the trilepton final state also includes
 966 leptons with $p_T < 20 \text{ GeV}$, so there is also an uncorrelated component of the normalization
 967 between this final state and the dileptonic ones. We estimate by computing the difference in
 968 the predicted background normalization when varying the fake rate by $\pm 40\%$ only in the low
 969 p_T part, separately for electrons and muons; we obtain an uncertainty of approximately 11%
 970 for each of the two lepton flavours.

971 Systematic variations of the fake rate in different lepton kinematic ranges can also impact the
 972 shape of the reducible background distributions. To assess this effect, we introduce different
 973 variations in the fake rate dependent on p_T and η , and for each variation derive a new back-
 974 ground prediction; we normalize all these background predictions to the same yield, and then
 975 take the envelop of the variations as an uncertainty band for the shape of the reducible back-
 976 ground. The variations that we consider for the dilepton final states are: (i) shifting the fake
 977 rate by $\pm 40\%$ for leptons with $p_T > 30 \text{ GeV}$ and simultaneously by $\mp 40\%$ for leptons with
 978 $p_T \leq 30 \text{ GeV}$; (ii) shifting the fake rate by $\pm 40\%$ in the barrel and simultaneously by $\mp 40\%$ in
 979 the endcaps; (iii) for electrons only, shifting the fake rate by $\pm 40\%$ in the central part of the
 980 barrel ($|\eta| < 0.8$) and simultaneously by $\mp 40\%$ in the forward part of the barrel. In the trilep-
 981 ton final state we do the same variations, but the p_T threshold for the first variation is 20 GeV
 982 instead of 30 GeV, since the trilepton selection allows also lower momentum leptons. For this
 983 uncertainty on the shape of the distribution, we treat all as independent, but we still assume
 984 the effect to be correlated across the b-tagging and lepton charge categories. In the signal ex-
 985 traction, we account for the uncertainty band allowing for linear or quadratic deformations of
 986 the shape within the band, as described more in detail in section 8.

987 The results of the estimation are shown in Fig. 53 and 52 for electrons and muons respectively.
 988 As expected, the normalization uncertainties in the final states with a single lepton flavour, ee
 989 and $\mu\mu$, are approximately $\pm 40\%$; in the mixed final states the uncertainties reflect the different
 990 composition of the fakes, with the electrons contributing more especially at high p_T . In the
 991 core of the distribution, the shape uncertainties are much smaller than the normalization ones;
 992 shape uncertainties on the jet multiplicity are mostly smaller than the ones for the BDT since
 993 the latter relies directly on the lepton kinematic.

994 Another possible source of uncertainty arises from the difference in the fake rate between the
 995 loose and tight b-tagging categories. This systematic is still being evaluated.

996 **7.5.5 Closure tests on simulated events**

997 The reducible background estimation using the fake rate assumes that the fake rate can be
 998 parameterised in terms of only the lepton p_T and $|\eta|$, independently of the kinematic of the rest

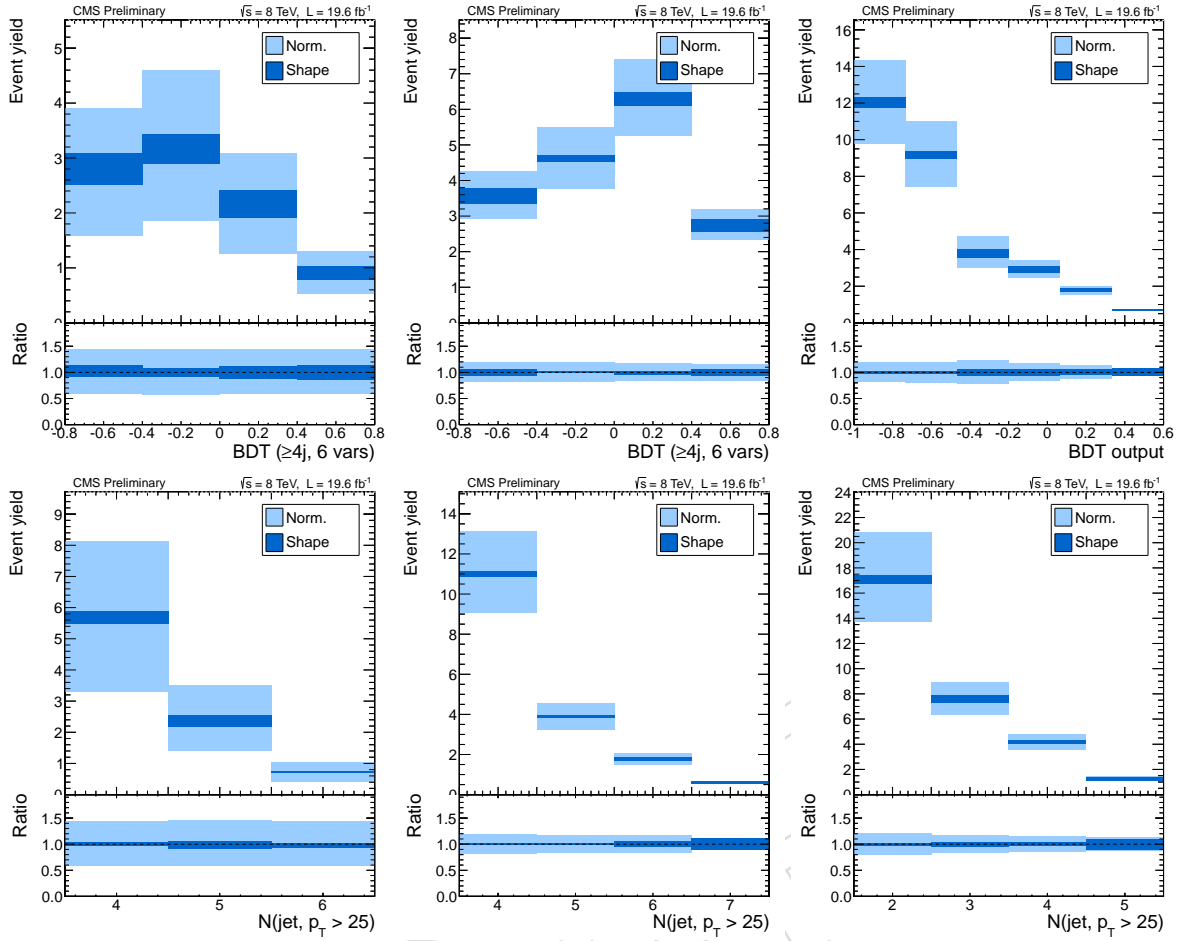


Figure 52: Systematical uncertainty on the normalization of the non-prompt background arising from the knowledge of the muon fake rate, in the $\mu\mu$, $e\mu$, and 3ℓ final states, from left to right. The predictions for the BDT output are shown in the top row, the ones for the jet multiplicity in the bottom row.

of the event. In order to test this assumption on simulated events, a closure test is performed. A fake rate extracted from non-prompt leptons in $t\bar{t}$ MC inclusively, and used to predict the yields and distributions of reducible background ($t\bar{t}$, single-top, Drell-Yan, and $W+jets$) in the signal region, with the same approach used in data. This prediction is then compared to what obtained directly by applying the lepton MVA requirement to the simulated events.

The results of the test are shown in Fig. 54 and 55 for the dilepton and trilepton final state respectively. The statistical accuracy of the test is limited by the size of the simulated samples, but in general a fair agreement is seen between the predicted and observed yields and distribution in simulation.

7.6 Charge misassignment

In the same-sign dilepton final state a non-negligible background contribution is expected from dileptonic $t\bar{t}$ events where the charge of one of the two leptons is misassigned. In this analysis, we estimate this background from data following a strategy similar to the one used for the background from non-prompt leptons: the background is estimated from opposite-sign dilepton events passing the full selection, weighted according to the probability of a charge misassignment to happen.

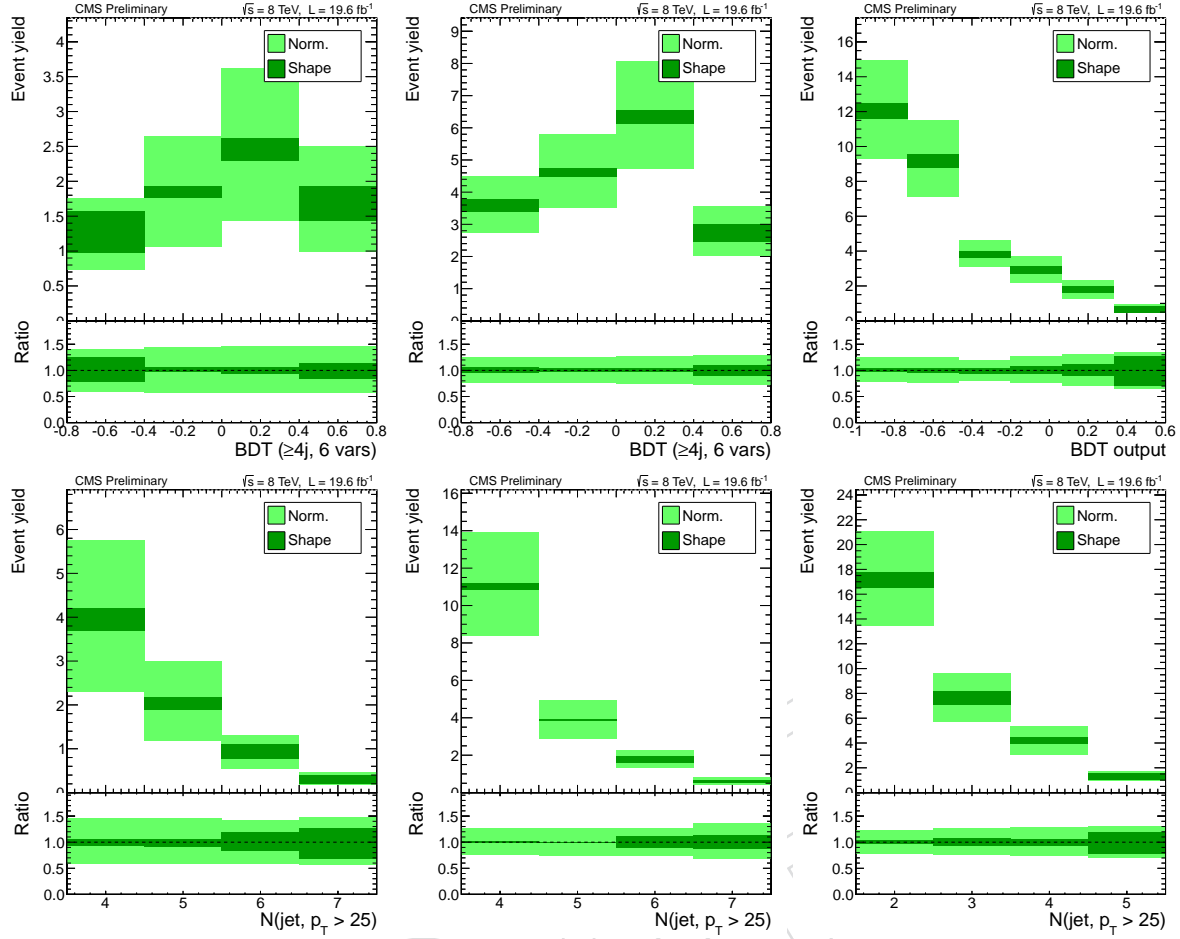


Figure 53: Systematical uncertainty on the normalization of the non-prompt background arising from the knowledge of the electron fake rate, in the ee , $e\mu$, and $3l$ final states, from left to right. The predictions for the BDT output are shown in the top row, the ones for the jet multiplicity in the bottom row.

7.6.1 Measurement of the charge misassignment probabilities

- For muons the probability of charge misassigned is found to be negligible in simulations, while the corresponding probability for electrons varies in the 0.03–0.3% range depending on the electron p_T and η . Since the momentum of high p_T electrons can be measured reliably even when the charge is misassigned, it is possible to measure the charge misassignment probability in data by selecting same-sign dielectron events with an invariant mass close to that of an on-shell Z .

The strategy adopted is to define 6 bins of electron p_T and η . The inclusive samples of $Z \rightarrow e^\pm e^\pm$ and $Z \rightarrow e^\pm e^\mp$ candidates in data can then be split into 6×6 dielectron bins according to the p_T and η of the leading and trailing electron. A combined fit for the the charge misassignment probabilities in each single-electron bins is then performed from all the non-empty dielectron bins³. If i, j denote single-electron bins, with associated charge misassignment probabilities $p(i)$ and $p(j)$, then in each dielectron bin (i, j) we have

$$N_{\pm\pm}(i, j) = [p(i) + p(j)] \times N_{\pm\mp}(i, j), \quad (5)$$

³Some bins are necessarily empty since the p_T of the leading electron is by definition larger than the p_T of the trailing electron.

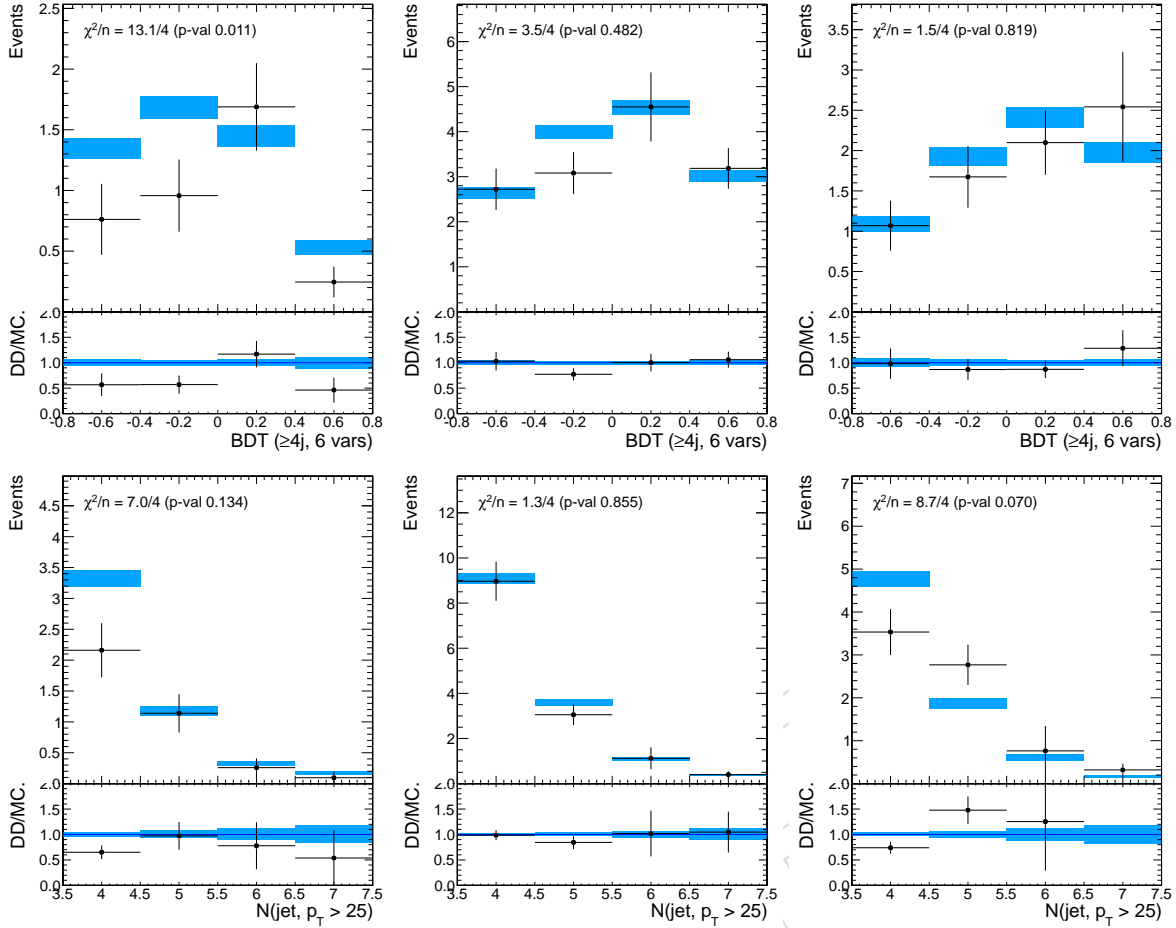


Figure 54: MC closure test in the dilepton final state: comparison between predicted background distributions using the fake rate method (filled rectangles) or applying the lepton MVA requirement on simulated events (points with error bars). From left to right, the plots are for the $\mu\mu$, ee , and $e\mu$ final states; the predictions for the BDT output are shown in the top row, the ones for the jet multiplicity in the bottom row.

1022 up to terms of order p^2 which are negligible.

1023 For electrons in the barrel, the charge misassignment probability is approximately 0.03%, with
 1024 no p_T dependence (Fig. 56, left). In the endcaps the probability increases with p_T from about
 1025 0.08% for $p_T < 20$ to about 0.28% for $p_T > 50$ GeV (Fig. 56, left). An excellent agreement
 1026 between data and simulations is observed in the barrel, while in the endcaps the simulation
 1027 appears to underestimate the charge misassignment probability by 10–20%.

1028 7.6.2 Background estimation

1029 For the same-sign dilepton analysis in the $e\mu$ and ee final states, we select a control sample of
 1030 opposite-sign dileptons satisfying the same selection requirements.

1031 The extrapolation to the same-sign signal region for the $e\mu$ final state is performed assigning
 1032 to each event a weight equal to the charge misassignment probability calculated for the p_T
 1033 and η of that lepton. For dielectron events, the weight is the sum of the probabilities for the
 1034 two electrons. Since charge misassignment probabilities are very small, we can neglect $(1 - p)$
 1035 terms in the propagation.

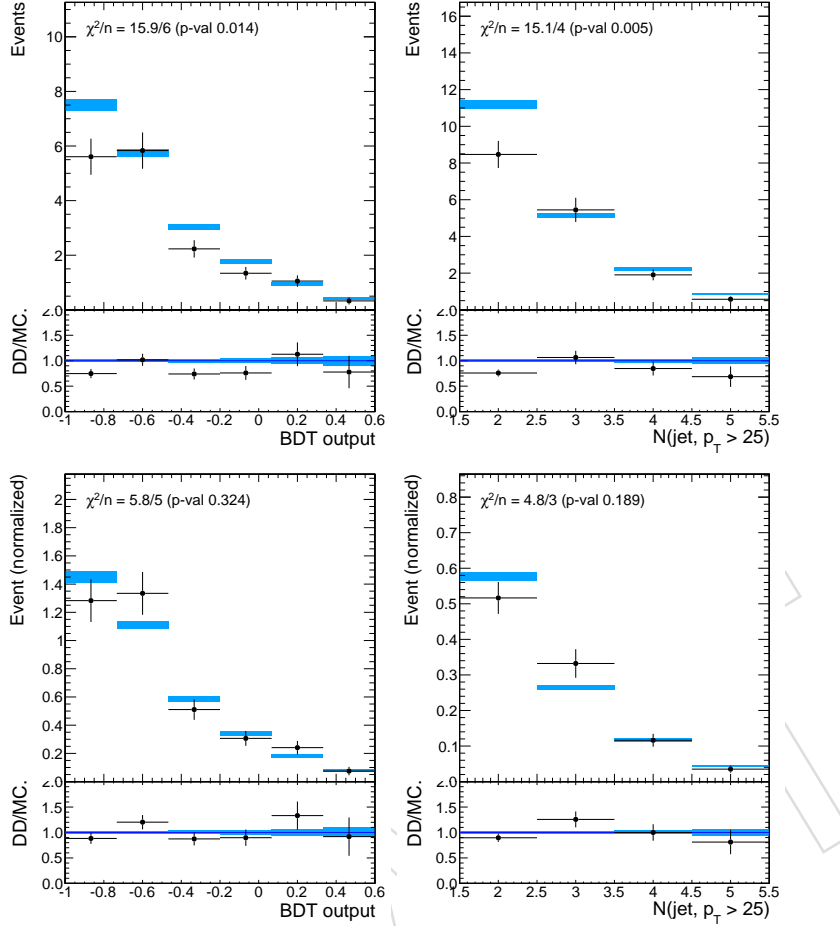


Figure 55: MC closure test in the trilepton final state: comparison between predicted background distributions using the fake rate method (filled rectangles) or applying the lepton MVA requirement on simulated events (points with error bars). The predictions for the BDT output are shown in the left plot, the ones for the jet multiplicity in the right one. In the plots in the bottom row, the two distributions are normalized to the same yield, to compare only the shapes.

1036 A closure test of the procedure was performed on simulated $t\bar{t}$ events, using the charge mis-
 1037 signment probabilities derived from simulated $Z \rightarrow ee$ events. A good agreement was found,
 1038 both in terms of the inclusive event rate and of the kinematic distributions of the events. The
 1039 corresponding plots will be added to a future revision of this analysis note.

1040 8 Summary of systematic uncertainties

1041 A summary of all the systematic uncertainties considered for the signal and the different back-
 1042 ground processes is given in Tab. 16.

1043 Experimental shape uncertainties from the fake rate and charge flip rate and shape uncertain-
 1044 ties of theoretical origin are implemented by considering up to three possible kinds of defor-
 1045 mations of the shape for a 1σ effect: (i) a constant deformation where all bins of the distribution
 1046 are shifted up or down by $\pm 1\sigma$ in a correlated way; (ii) a linear deformation where the shifts in
 1047 each bin vary linearly from $\pm 1\sigma$ at one end of the distribution to $\mp 1\sigma$ at the other end; (iii) a
 1048 quadratic deformation, where the center of the distribution varies by $\pm 1\sigma$ and both ends by

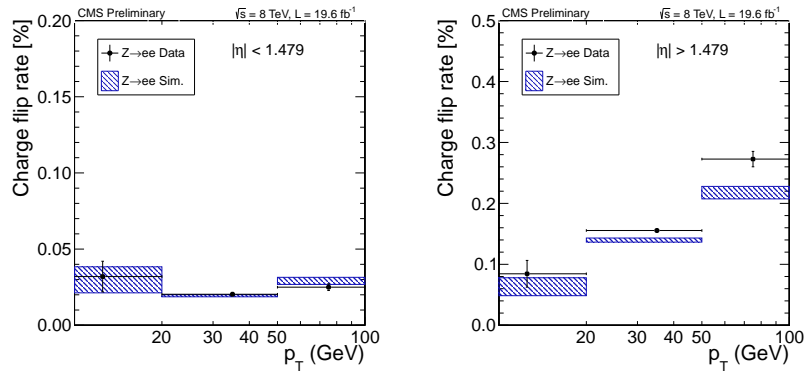


Figure 56: Measured charge misassignment probabilities in data for electrons in the barrel (left) and endcaps (right) as function of the electron p_T . The results from performing the same analysis on simulated $Z \rightarrow ee$ events is also shown.

1049 $\pm 1\sigma$. For uncertainties that affect both the shape and the normalization we consider all three
 1050 variations, while for uncertainties affecting only shapes we allow only the linear and quadratic
 1051 deformations are considered. In the statistical analysis, each of the three degrees of freedom
 1052 is associated with an independent nuisance parameter, so that the overall shape is allowed to
 vary in an almost arbitrary but smooth way within the envelope.

Syst Name	Rate or Shape	Description
tH higher orders	rate	Theoretical uncertainty on tH cross section.
tW higher orders	rate	Theoretical uncertainty on tW cross section.
tZ higher orders	rate	Theoretical uncertainty on tZ cross section.
PDF	rate	Theoretical uncertainty on cross sections for tH, tW, tZ. Correlated in all channels for all processes sharing a dominant production mechanism.
tH PDF Shape	shape only	Theoretical uncertainty from PDF on shape.
tW PDF Shape	shape only	Theoretical uncertainty from PDF on shape.
tZ PDF Shape	shape only	Theoretical uncertainty from PDF on shape.
tH PYTHIA tune	shape only	Theoretical uncertainty on MC modeling.
tW MADGRAPH scale and matching	shape only	Theoretical uncertainty on MC modeling.
tZ MADGRAPH scale and matching	shape only	Theoretical uncertainty on MC modeling.
Non-prompt Fake Rate	envelope	Applied to reducible non-prompt backgrounds.
Charge-flip	envelope	Applied to charge flip background for 2ℓ channel.
WZ	rate	Uncertainty from fit in control region.
ZZ	rate	Uncertainty from fit in control region.
Jet Energy Scale	template	Applied to WZ, ZZ, tW, tZ, tH.
b-tagging efficiency	rate	Applied to WZ, ZZ, tW, tZ, tH.
b-tagging fake rate	rate	Applied to WZ, ZZ, tW, tZ, tH.
Lepton Trigger Scale factor	rate	Applied to tW, tZ, tH.
Lepton preselection Scale factor	rate	Applied to tW, tZ, tH.
Lepton MVA discriminator scale factor	rate	Applied to tW, tZ, tH.
Luminosity	rate	Applied to tW, tZ, tH.

Table 15: Summary of systematic uncertainty treatment in the fit to extract the signal. Systematics are correlated across all channels unless otherwise stated.

1053

9 Results

1055 The results of this search are interpreted by comparing the observed event yields and distributions to the expectations from background and a SM Higgs boson of mass 125.7 GeV. A
 1056 common signal strength parameter $\mu = \sigma/\sigma_{\text{SM}}$ is introduced, scaling the expected yields from
 1057

1058 $t\bar{t}H$, without altering the branching fractions or the kinematics of the events.

1059 Results are reported both in terms of upper limits on μ at 95% confidence level (CL), and
 1060 in terms of the best fit value for μ and its associated uncertainty. The statistical procedures
 1061 adopted in this analysis are the ones that have used for the observation of the Higgs boson
 1062 candidate in CMS, and are described in detail in Ref. [43].

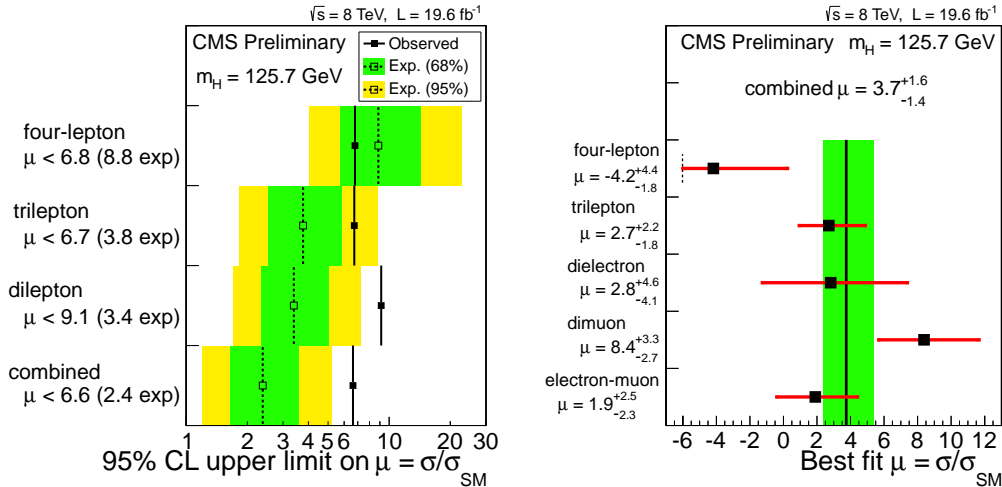


Figure 57: Results of the searches in the three final states and their combination, in terms of the signal strength parameter $\mu = \sigma/\sigma_{SM}$. Left panel: 95% CL upper limit on μ , observed (solid markers), median expected under the background-only hypothesis (hollow markers), and intervals containing 68% and 95% of the expected outcomes under that hypothesis (green and yellow bands). Right panel: best fit values of μ and $\pm 1\sigma$ uncertainties, for the five individual final states (solid markers with red error bars) and the full combination (vertical line and green band). The signal strength in the four-lepton final state is not allowed to be below approximately 6 by the requirement that the expected signal-plus-background event yield must not be negative in any of the three bins of jet multiplicity.

1063 The observed upper limits on μ are shown in Fig. 57, compared with the expectations under
 1064 the background-only hypothesis, ie assuming no $t\bar{t}H$ production. In the absence of a $t\bar{t}H$ signal,
 1065 the median expected upper limit from the combination of all the decay modes is 2.4, at 95% CL;
 1066 the corresponding median expectation under the hypothesis of SM $t\bar{t}H$ production is 3.5. The
 1067 observed upper limit is 6.6, larger than both predictions, driven by the excess of events seen
 1068 especially in the same-sign dimuon category.

1069 The best fit signal strengths from the individual channels are shown in the right hand panel
 1070 of Fig. 57. The internal consistency of the five results with a common signal strength has been
 1071 evaluated to be 16%, estimated from the asymptotic behaviour of the profile likelihood func-
 1072 tion [3]. The fit to the combination yields $\mu = 3.7^{+1.6}_{-1.4}$: the deficit in the fourlepton channel
 1073 partially compensate for the excess in the same-sign $\mu\mu$ one, bringing the combined result
 1074 closer to the results of the other three channels (trilepton, same-sign ee, and same-sign e μ).
 1075 The combined μ is compatible with the SM Higgs boson prediction $\mu = 1$ at the 3% level.

1076 The results obtained with the cross-check analysis relying on the multiplicity of hadronic jets
 1077 instead of the multivariate discriminator for the dilepton and trilepton final states are in good
 1078 agreement with the ones of the nominal analysis: the expected and observed upper limits are
 1079 3.0 and 6.9, respectively, and the best fit signal strength is $\mu = 3.9^{+1.7}_{-1.5}$.

Syst Name	Rate or Shape	Description
tH higher orders	rate	Theoretical uncertainty on tH cross section.
tW higher orders	rate	Theoretical uncertainty on tW cross section.
tZ higher orders	rate	Theoretical uncertainty on tZ cross section.
PDF	rate	Theoretical uncertainty on cross sections for tH, tW, tZ. Correlated in all channels for all processes sharing a dominant production mechanism.
tH PDF Shape	shape only	Theoretical uncertainty from PDF on shape.
tW PDF Shape	shape only	Theoretical uncertainty from PDF on shape.
tZ PDF Shape	shape only	Theoretical uncertainty from PDF on shape.
tH PYTHIA tune	shape only	Theoretical uncertainty on MC modeling.
tW MADGRAPH tune	shape only	Theoretical uncertainty on MC modeling.
tZ MADGRAPH tune	shape only	Theoretical uncertainty on MC modeling.
Non-prompt Fake Rate	envelope	Applied to reducible non-prompt backgrounds.
Charge-flip	envelope	Applied to charge flip background for 2 ℓ channel.
WZ	rate	Uncertainty from fit in control region.
ZZ	rate	Uncertainty from fit in control region.
Jet Energy Scale	template	Applied to WZ, ZZ, tW, tZ, tH.
b-tagging efficiency	rate	Applied to WZ, ZZ, tW, tZ, tH.
b-tagging fake rate	rate	Applied to WZ, ZZ, tW, tZ, tH.
Lepton Trigger Scale factor	rate	Applied to WZ, ZZ, tW, tZ, tH.
Lepton preselection Scale factor	rate	Applied to WZ, ZZ, tW, tZ, tH.
Lepton MVA discriminator scale factor	rate	Applied to W, ZZ, tW, tZ, tH.
Luminosity	rate	Applied to WZ, ZZ, tW, tZ, tH.

Table 16: Summary of systematic uncertainty treatment in the fit to extract the signal. Systematics are correlated across all channels unless otherwise stated.

A Control region plots

A.1 $t\bar{t} \rightarrow e^\pm \mu^\mp b\bar{b} \nu\bar{\nu}$

With this control region we want to validate our objects (jets, b-tagging, $E_T^{miss} LD$) in multi-jets events. To do this we select a sample of $t\bar{t}$ events with high purity. The simulated events are corrected with the scale factors for the lepton selection efficiency, the b-tagging efficiency, and reweighted to match the number of pile-up interactions in data. The MC samples are normalized to the data luminosity.

The definition of the control region is the following:

- two preselected leptons, or three with the trailing one not passing the tight working point of the lepton MVA discriminator;
- the two highest p_T leptons being an electron and a muon of opposite sign;
- tight working point of the lepton MVA discriminator and tight charge requirements applied to the two highest p_T leptons;
- the two highest p_T leptons having p_T greater than 20, 10 GeV;
- the minimum invariant mass of any $\ell\ell$ couples must be > 12 GeV;
- at least two central jets with $p_T > 25$ GeV;
- at least one central jets with $p_T > 25$ GeV satisfying the medium working point of the CSV b-tagging discriminator or two satisfying the loose one.

Some distributions are shown in Fig. 58.

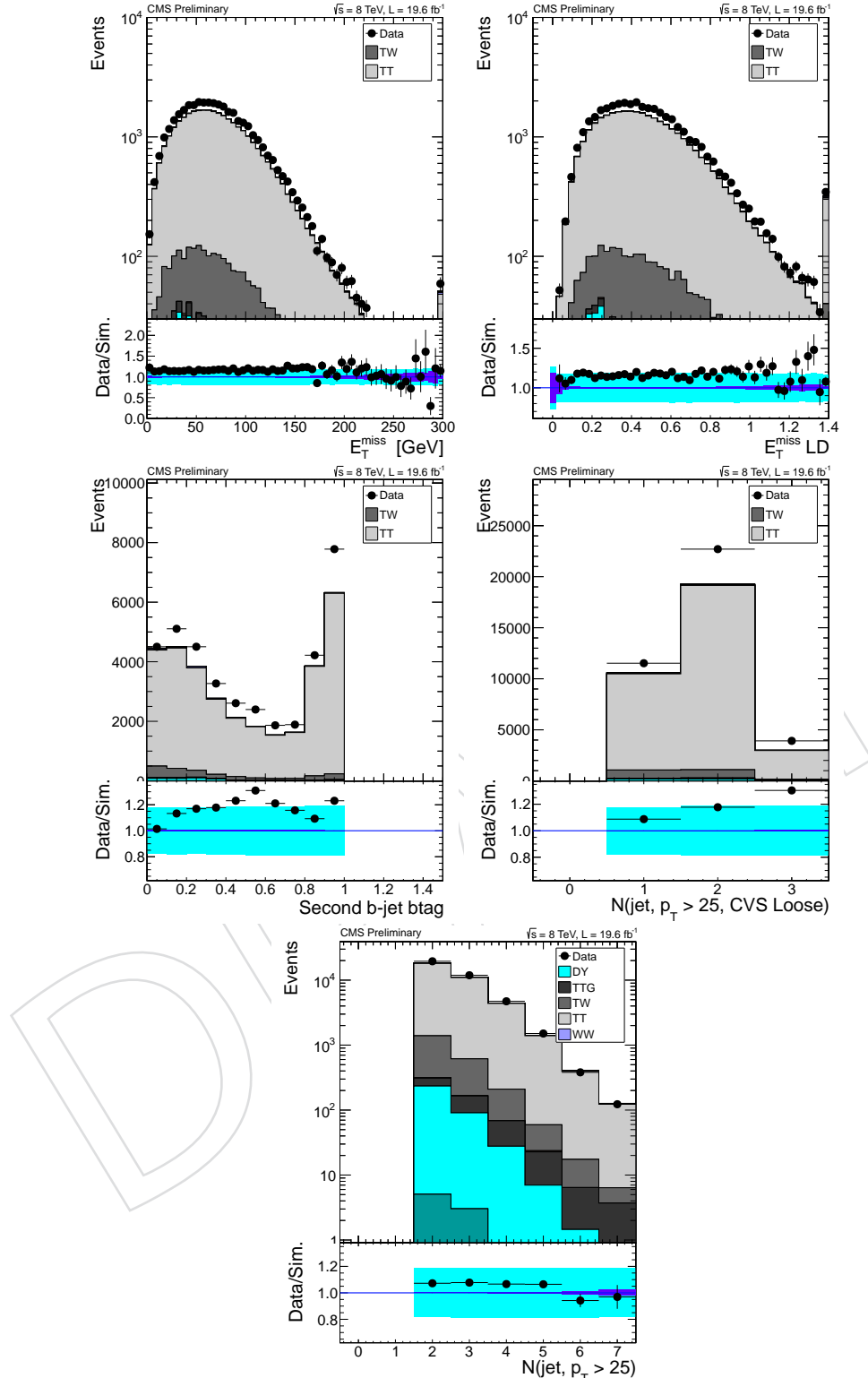


Figure 58: Data and simulation distributions in the $t\bar{t} \rightarrow e^\pm \mu^\mp b\bar{b} \nu\bar{\nu}$ control region. From top left to bottom right: the E_T^{miss} , the $E_T^{\text{miss}} \text{ LD}$, the CSV b-tagging discriminator for the second jet ordered in CSV value, the number of central jets with $p_T > 25$ satisfying the loose working point of the CSV b-tagging discriminator. The bottom panel of each plot shows the ratio between the observed events and the expectation from simulation, with statistical (violet) and systematic (cyan) uncertainties.

1099 A.2 $WZ \rightarrow 3\ell$

1100 With this control region we want to validate our objects (signal leptons, $E_T^{miss} LD$, jets) in the
 1101 three lepton final state. To do this we select a sample of $WZ \rightarrow 3\ell$ events with high purity.
 1102 The simulated events are corrected with the scale factors for the lepton selection efficiency, the
 1103 b-tagging efficiency, and reweighted to match the number of pile-up interactions in data. The
 1104 MC samples are normalized to the data luminosity.

1105 The definition of the control region is the following:

- 1106 • at least three preselected leptons;
- 1107 • tight working point of the lepton MVA discriminator applied to the three highest p_T
 1108 leptons;
- 1109 • the minimum invariant mass of any $\ell\ell$ couples must be > 12 GeV;
- 1110 • the invariant mass of the best Z ($m_{\ell^+\ell^-}$ with mass closest to the Z boson mass) must
 1111 be within 10 GeV from the nominal Z mass;
- 1112 • $E_T^{miss} LD < 0.3$;
- 1113 • no central jets with $p_T > 25$ GeV satisfying the medium working point of the CSV
 1114 b-tagging discriminator.

1115 Some distributions are shown in Fig. 59.

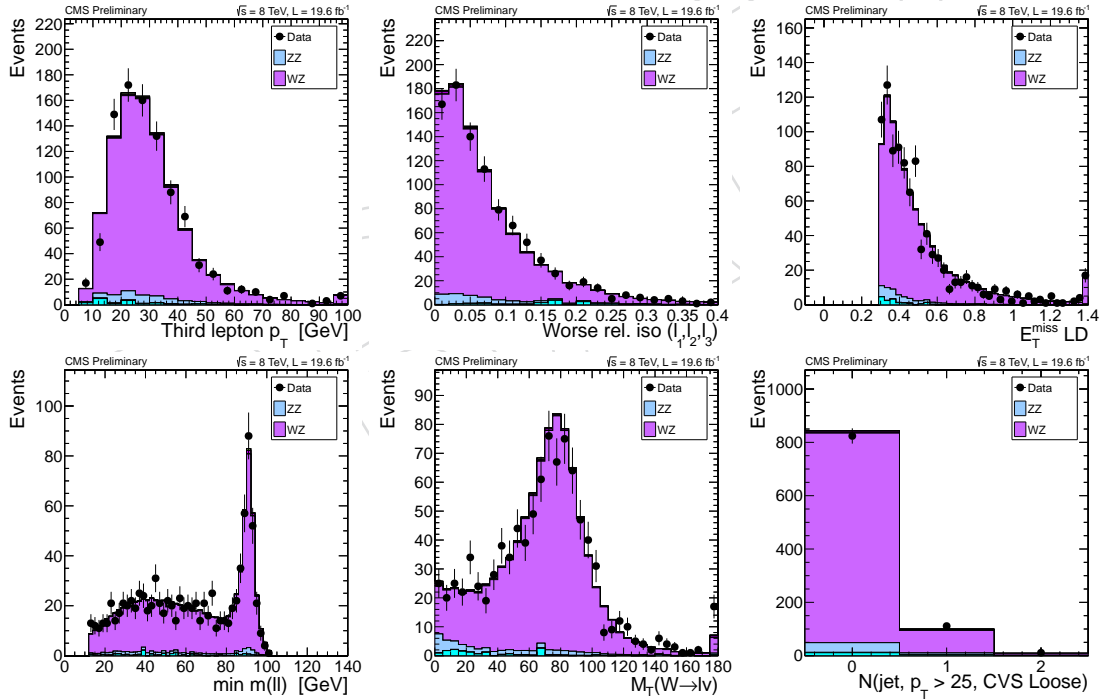


Figure 59: Data and simulation distributions in the $WZ \rightarrow 3\ell$ control region. From top left to bottom right: the p_T of the trailing lepton, the R_{ℓ}^{iso} for the worse isolated lepton, the $E_T^{miss} LD$, the minimum invariant mass of any $\ell\ell$ couples, the transverse mass of the $W \rightarrow \ell\nu$, the number of central jets with $p_T > 25$ satisfying the loose working point of the CSV b-tagging discriminator.

1116 **A.3 $t\bar{t}Z \rightarrow 3\ell$**

1117 The prediction for the $t\bar{t}Z$ process is tested directly in a trilepton control region requiring two of
 1118 the leptons to have the same flavour, opposite electrical charge and the invariant mass pair of
 1119 the pair to be within 10 GeV of the nominal Z boson mass. Good agreement is observed in this
 1120 control region, though in this case the precision of the test is dominated by the statistical uncer-
 1121 tainty of about 35%. The reducible backgrounds yields comes from the data-driven estimate,
 1122 while the other contributions come from simulated events corrected with the scale factors for
 1123 the lepton selection efficiency, the b-tagging efficiency, and reweighted to match the number of
 1124 pile-up interactions in data. The MC samples are normalized to the data luminosity.

1125 The definition of the control region is the following:

- 1126 • three preselected leptons;
- 1127 • tight working point of the lepton MVA discriminator applied to the three leptons;
- 1128 • the minimum invariant mass of any $\ell\ell$ couples must be > 12 GeV;
- 1129 • the two highest p_T leptons having p_T greater than 20, 10 GeV;
- 1130 • the invariant mass of the best Z ($m_{\ell^+\ell^-}$ with mass closest to the Z boson mass) must
 1131 be within 10 GeV from the nominal Z mass;
- 1132 • $E_T^{miss} LD > 0.2$;
- 1133 • at least two central jets with $p_T > 25$ GeV satisfying the loose working point of the
 1134 CSV b-tagging discriminator.
- 1135 • at least one central jet with $p_T > 25$ GeV satisfying the medium working point of the
 1136 CSV b-tagging discriminator.

1137 Some distributions are shown in Fig. 60.

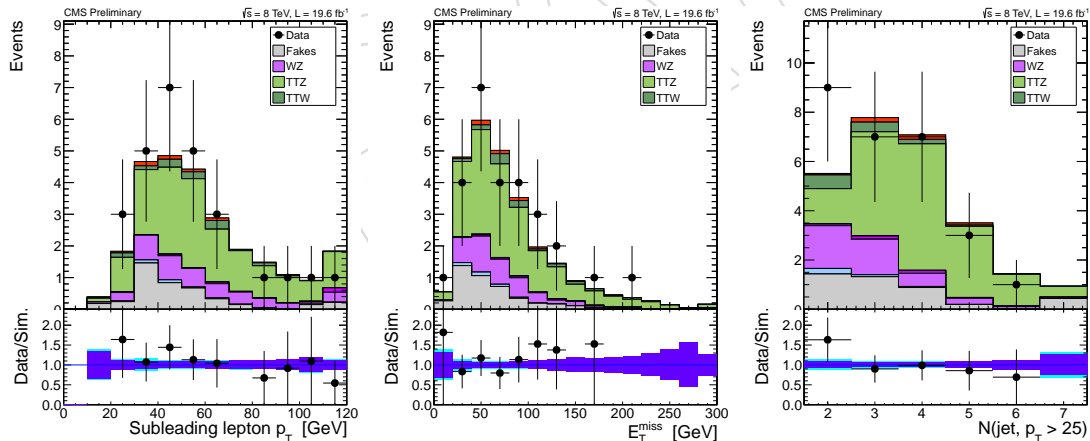


Figure 60: Data and simulation distributions in the $t\bar{t}Z \rightarrow 3\ell$ control region. From left to right: the p_T distribution of the second lepton ordered in p_T , the E_T^{miss} , the number of central jets with $p_T > 25$ GeV.

1138 When requiring also the presence of at least four central jets, as expected for a fully recon-
 1139 structed $t\bar{t}Z$ event, the control region becomes more pure in selecting $t\bar{t}Z$ events. This can
 1140 be seen in the distributions in Fig. 61.

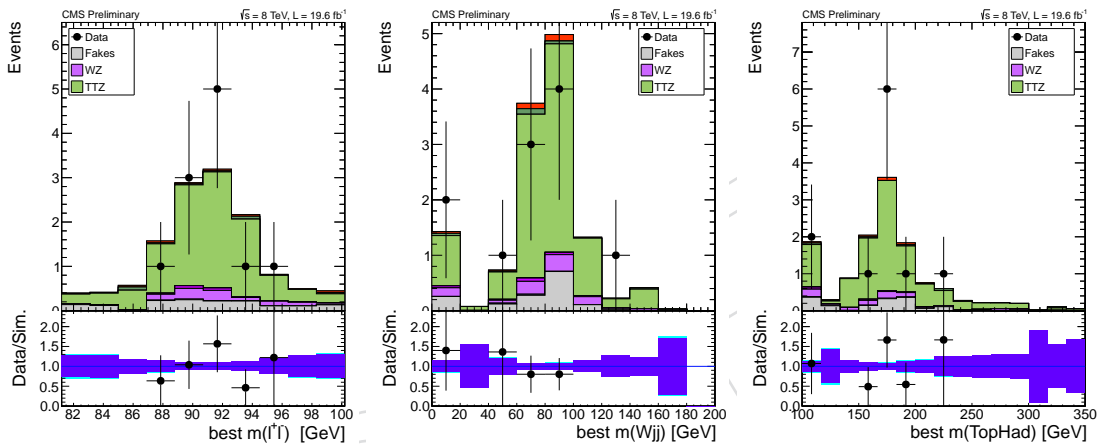


Figure 61: Data and simulation distributions in the $t\bar{t}Z \rightarrow 3\ell$ control region when the additional request of at least four central jets with $p_T > 25 \text{ GeV}$ is applied. From left to right: the invariant mass of the best Z, the mass of the best candidate hadronically-decaying W reconstructed from the central jets with $p_T > 25$ (removing those that satisfied the medium working point of the CSV b-tagging discriminator), the mass of the best candidate hadronically-decaying top quark reconstructed adding to the best W mass an additional central jet with $p_T > 25$ satisfying the loose working point of the CSV b-tagging discriminator.

1141 A.4 $ZZ \rightarrow 4\ell$

1142 With this control region we want to check the lepton efficiency in events with four leptons. We
 1143 obtain this control region from the four lepton final state selection removing the Z veto and
 1144 adding a b-jet veto. The reducible backgrounds yields comes from the data-driven estimate,
 1145 while the other contributions come from simulated events corrected with the scale factors for
 1146 the lepton selection efficiency, the b-tagging efficiency, and reweighted to match the number
 1147 of pile-up interactions in data. The MC samples are normalized to the data luminosity. The
 1148 definition of the control region is the following:

- 1149 • at least four preselected leptons;
- 1150 • the two highest p_T leptons having p_T greater than 20, 10 GeV;
- 1151 • loose working point of the lepton MVA discriminator applied to the four highest p_T
 1152 leptons;
- 1153 • the minimum invariant mass of any $\ell\ell$ couples must be > 12 GeV;
- 1154 • no central jet with $p_T > 25$ GeV satisfying the loose working point of the CSV b-
 1155 tagging discriminator.

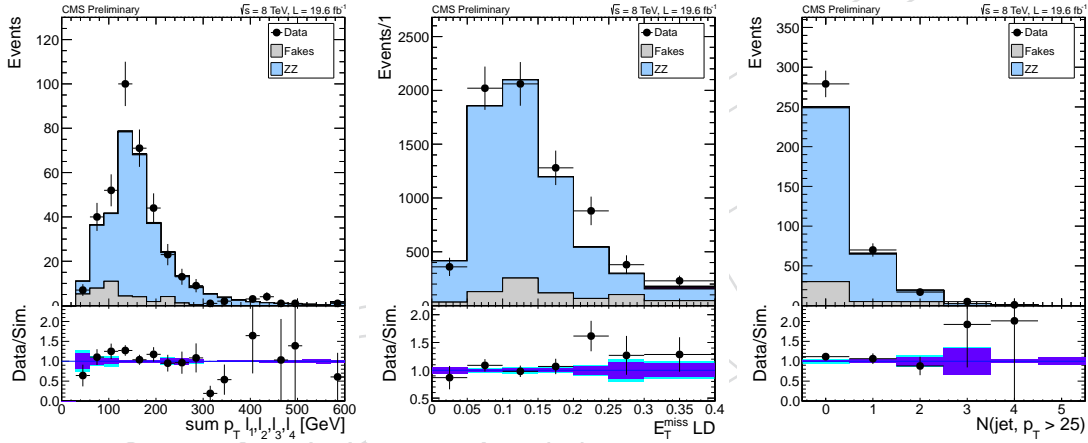


Figure 62: Data and simulation distributions in the $ZZ \rightarrow 4\ell$ control region. From left to right:
 the scalar sum of the four leptons p_T , the $E_T^{miss} LD$, the number of central jets with $p_T > 25$ GeV.

1156 **A.5 $Z \rightarrow 4\ell$**

1157 Starting from the control region described above which is dominated by on shell ZZ events,
 1158 we select only $Z \rightarrow 4\ell$ events requiring $80 < m_{4\ell} < 106$ GeV. This is done to check lower
 1159 momentum leptons. The data to simulation agreement it is still fair as shown in Fig. 63.

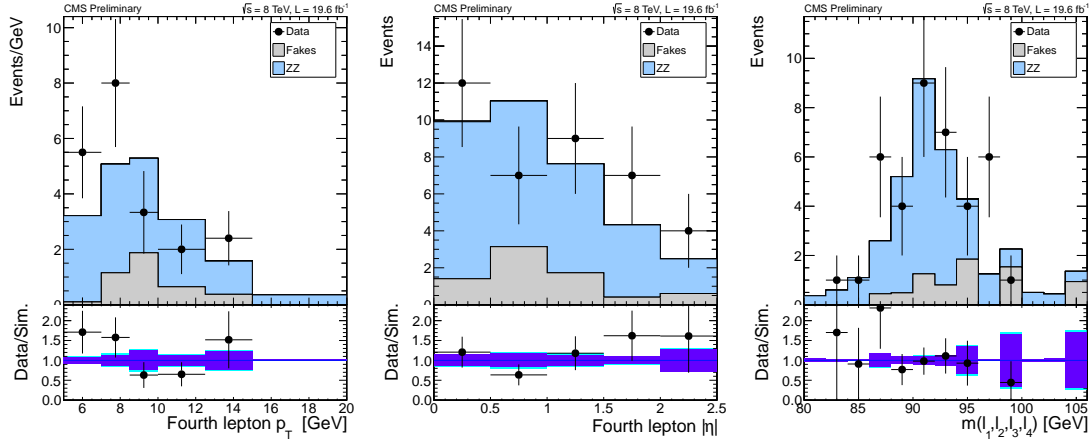


Figure 63: Data and simulation distributions in the $Z \rightarrow 4\ell$ control region. From left to right: the trailing lepton p_T , the trailing lepton η , the m_{4l} (the four highest p_T leptons are those considered).

A.6 Check for signal extraction variables in the 3-lepton selection**A.6.1 Backgrounds with fake leptons**

We select events which pass all of the cuts for the three-lepton loose-btag signal region, except that one of the three leptons is required to fail the tight lepton MVA cut. This produces a sample rich in $t\bar{t} \rightarrow \ell^\pm \ell^\mp$ but with one additional fake lepton. We check the MC modeling of this process by scaling up the $t\bar{t}$ and single top MC samples to match the data yields (a factor of 1.5 - 2) and comparing data and MC shapes for the BDT and its input variables (Fig. 64). All distributions show good agreement.

DRAFT

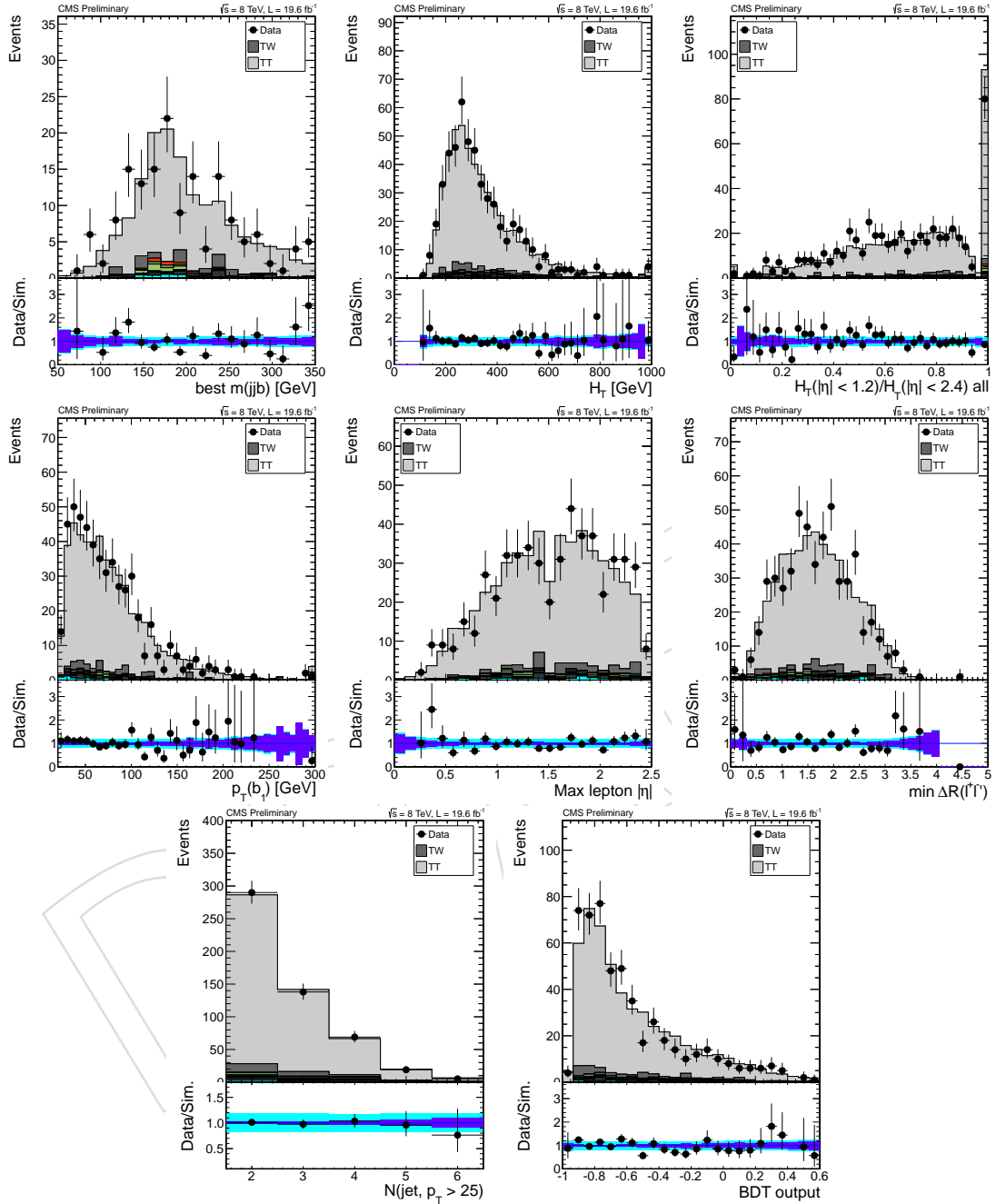


Figure 64: Data and simulation distributions in the $t\bar{t} \rightarrow \ell^\pm \ell^\mp + \ell$ control region. All events pass the inclusive loose-btag criteria. From left to right: the best hadronic reconstructed top mass (when one can be reconstructed), the scalar sum of all jet p_T , the ratio of this sum in central and inclusive jets, the highest jet p_T , η of the softest lepton, lowest separation between leptons, number of jets, and the BDT output.

A.6.2 Backgrounds with prompt leptons

The goal of this cross-check region is to verify that the variables most closely related to signal extraction are well-modeled. The selection of these events is the same as events in the $t\bar{t}Z \rightarrow 3\ell$ control region except for the $E_T^{miss} LD$ cut, which is slightly different.

- 3 leptons, all passing the tight working point of the lepton MVA, p_T cuts, and minimum invariant mass cuts.
- Either: number of jets ≥ 4 or $E_T^{miss} LD > 0.2$
- Require one pair of same-flavor, opposite charge leptons to fall within 10 GeV of the Z mass.
- Inclusive loose b-tagging selection: at least two central jets with $p_T > 25$ GeV satisfying the loose working point of the CSV b-tagging discriminator or at least one central jet with $p_T > 25$ GeV satisfying the medium working point of the CSV b-tagging discriminator.

Fig. 65 shows the data-to-simulation comparisons in this region.



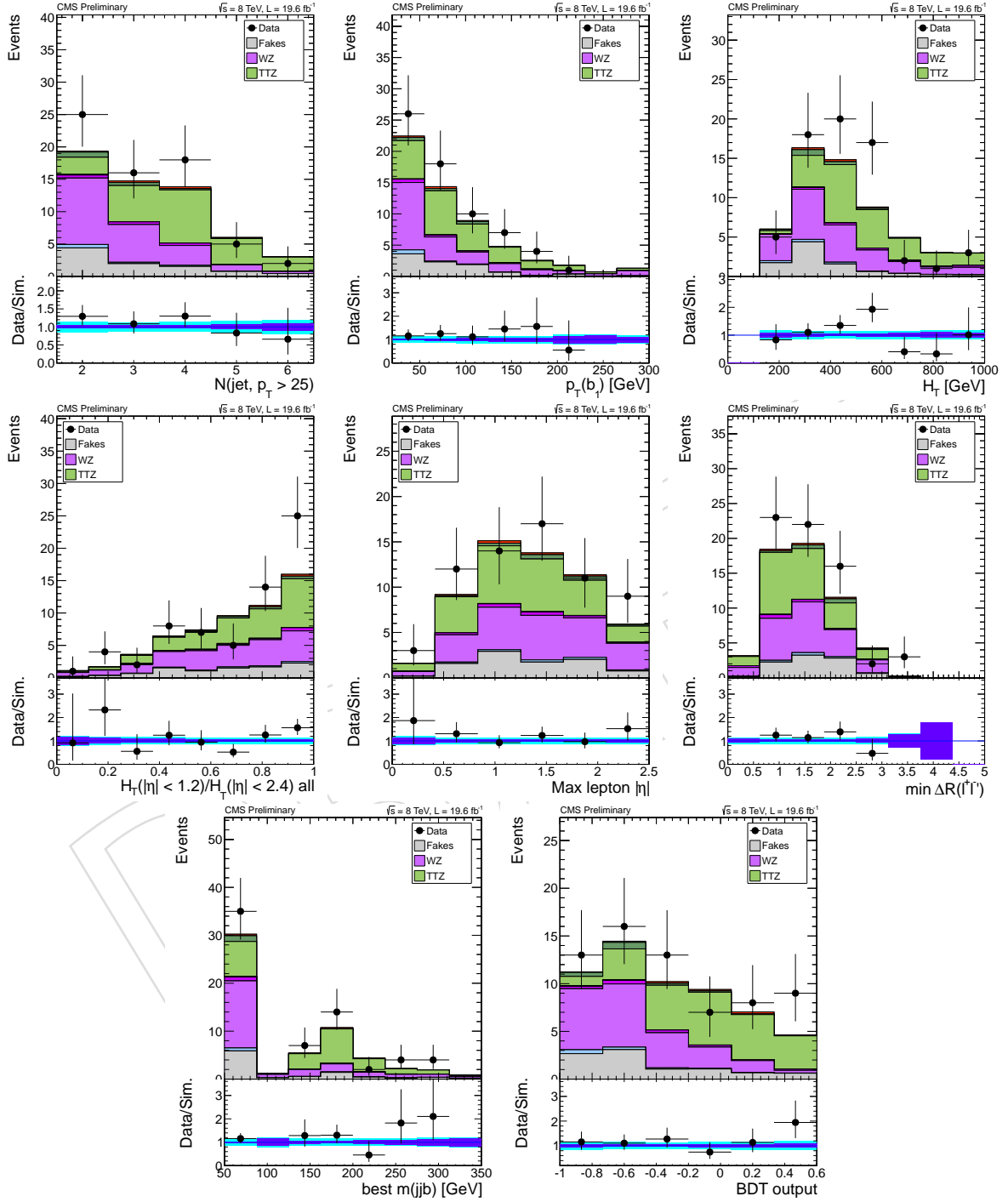


Figure 65: 3ℓ control region: Data and simulation distributions in the signal extraction control region. This region has the inclusive loose b-tagging selection applied.

A.7 Check for signal extraction variables for 2lss

We select events with a muon and electron which pass all but one of the cuts for the same-sign, inclusive loose-btag signal category. Unlike the signal region, we require that one of the two leptons to fail the tight lepton MVA cut. This produces a sample rich in $t\bar{t} \rightarrow \ell^\pm + jets$ but with one additional fake lepton. We check the MC modeling of this process by scaling up the $t\bar{t}$ and single top MC samples to match the data yields (a factor of 1.5 - 2) and comparing data and MC shapes for the BDT and its input variables (Fig. 66 through Fig. 68). All distributions show good agreement.

DRAFT

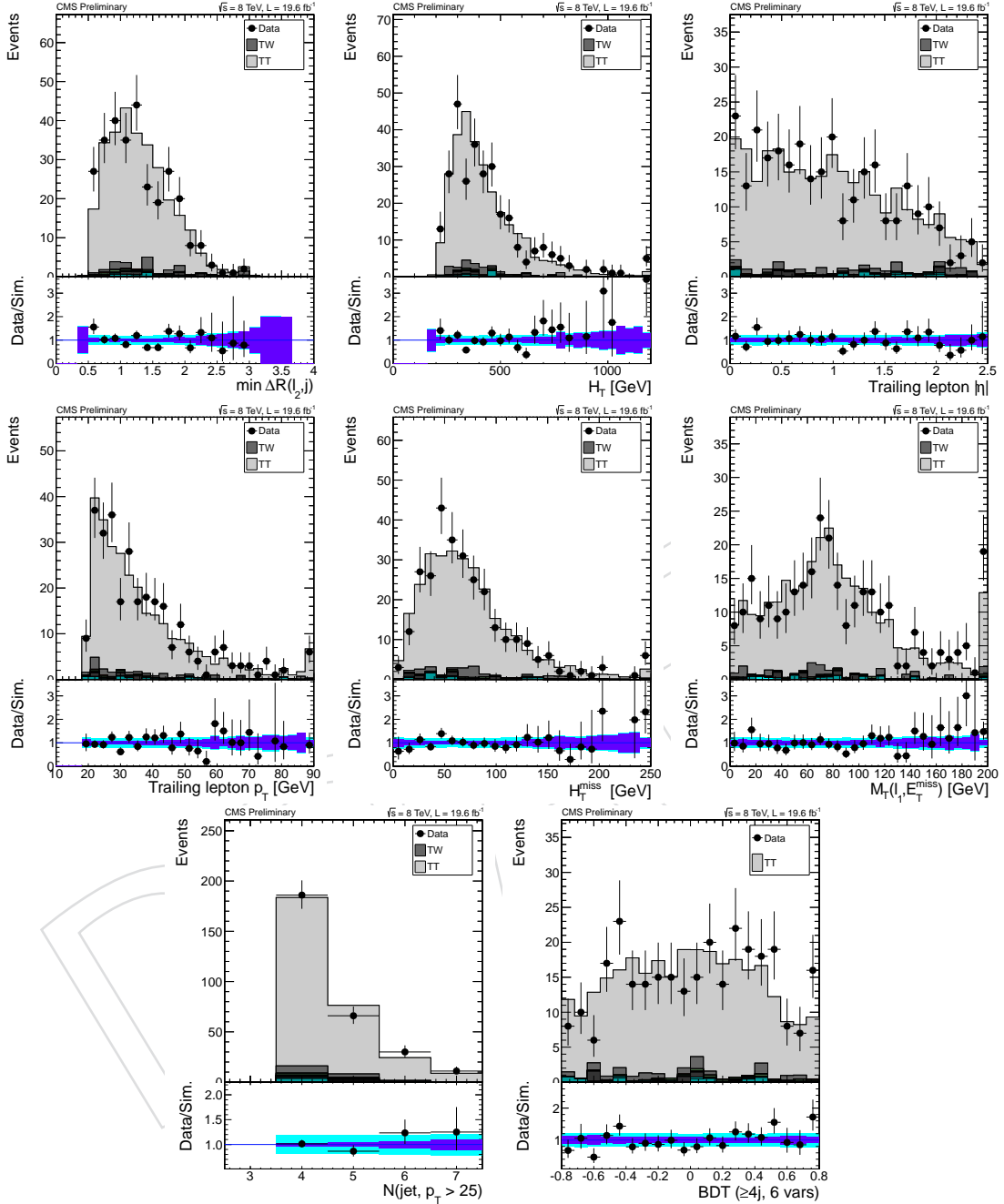


Figure 66: $2\ell e, \mu$: data and simulation distributions in the $t\bar{t} \rightarrow e^\pm \mu^\pm$ control region. All events pass the inclusive loose-btag criteria. From left to right: the minimum separation between the trailing lepton and a jet, the scalar sum of all jet p_T , η of the trailing lepton, p_T of the trailing lepton, missing transverse energy measured only with selected leptons and jets, transverse mass of the leading lepton and the missing energy vector, the number of jets, and the BDT output.

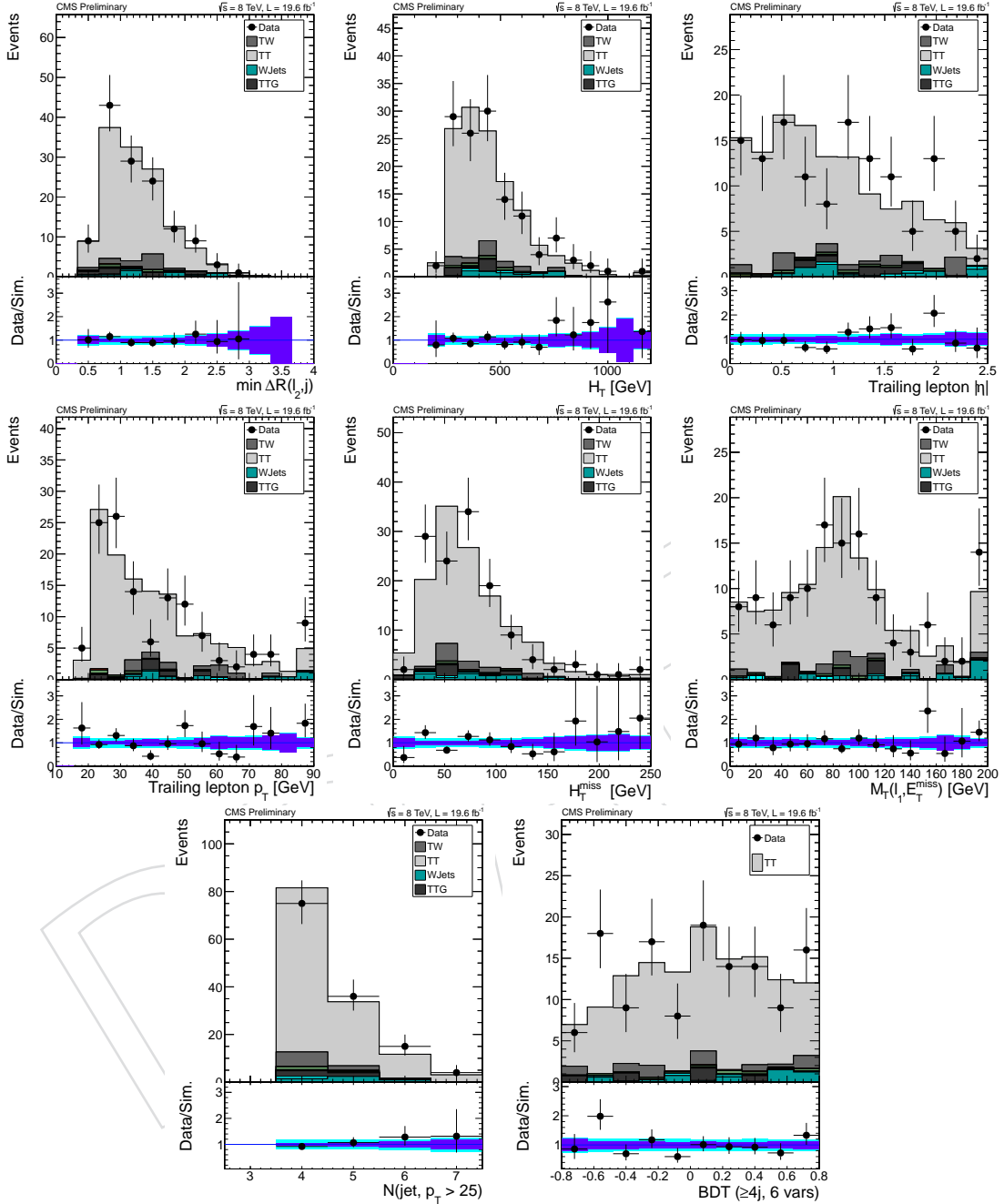


Figure 67: 2ℓ e,e : data and simulation distributions in the $t\bar{t} \rightarrow e^\pm e^\pm$ control region. All events pass the inclusive loose-btag criteria. From left to right: the minimum separation between the trailing lepton and a jet, the scalar sum of all jet p_T , η of the trailing lepton, p_T of the trailing lepton, missing transverse energy measured only with selected leptons and jets, transverse mass of the leading lepton and the missing energy vector, the number of jets, and the BDT output.

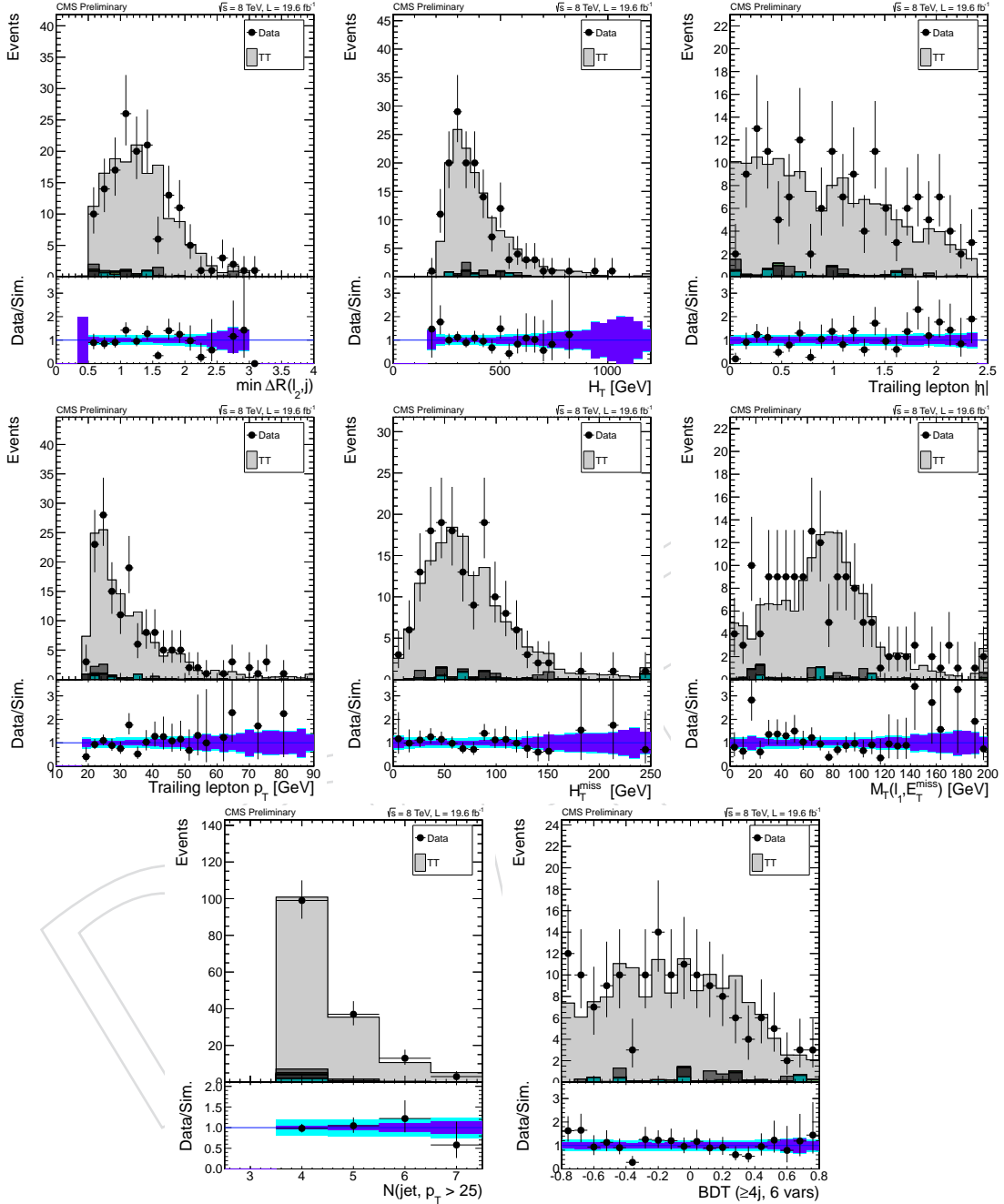


Figure 68: $2\ell \mu\mu$: Data and simulation distributions in the $t\bar{t} \rightarrow \mu^\pm \mu^\pm$ control region. All events pass the inclusive loose-btag criteria. From left to right: the minimum separation between the trailing lepton and a jet, the scalar sum of all jet p_T , η of the trailing lepton, p_T of the trailing lepton, missing transverse energy measured only with selected leptons and jets, transverse mass of the leading lepton and the missing energy vector, the number of jets, and the BDT output.

1190 B Additional plots for fake rates

1191 B.1 QCD dilepton control region

1192 Measured fake rates for the loose and tight MVA working points for the different control regions are shown in figures 71, 72, 71, 72, 73.

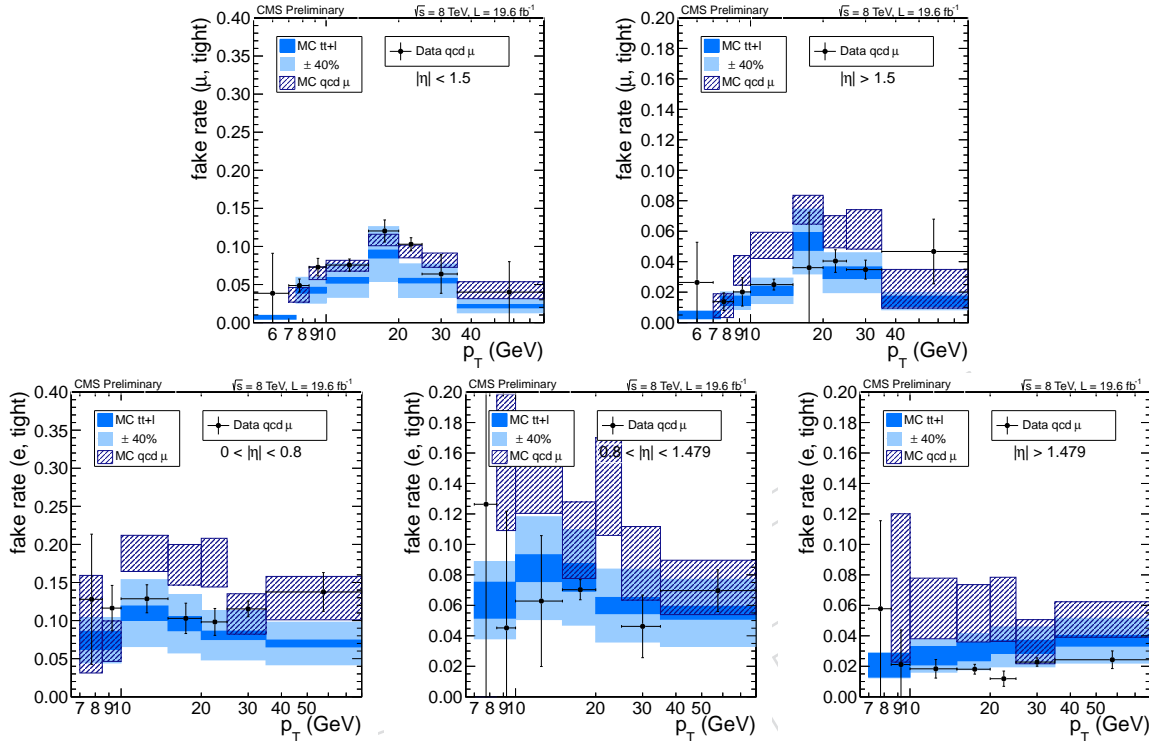


Figure 69: Measured fake rates for the tight MVA working point in the QCD dilepton control region. Data (dots) are compared with the expectations for non-prompt leptons in simulated QCD dilepton events (blue hatched boxes) and $t\bar{t}$ events (azure filled boxes). The results in the top row are for muons, the ones in the bottom for electrons; the results in the different columns corresponds to different $|\eta|$ ranges, as written in the plots.

1193

1194 B.2 QCD b-jet control region

1195 B.3 Z plus lepton control region

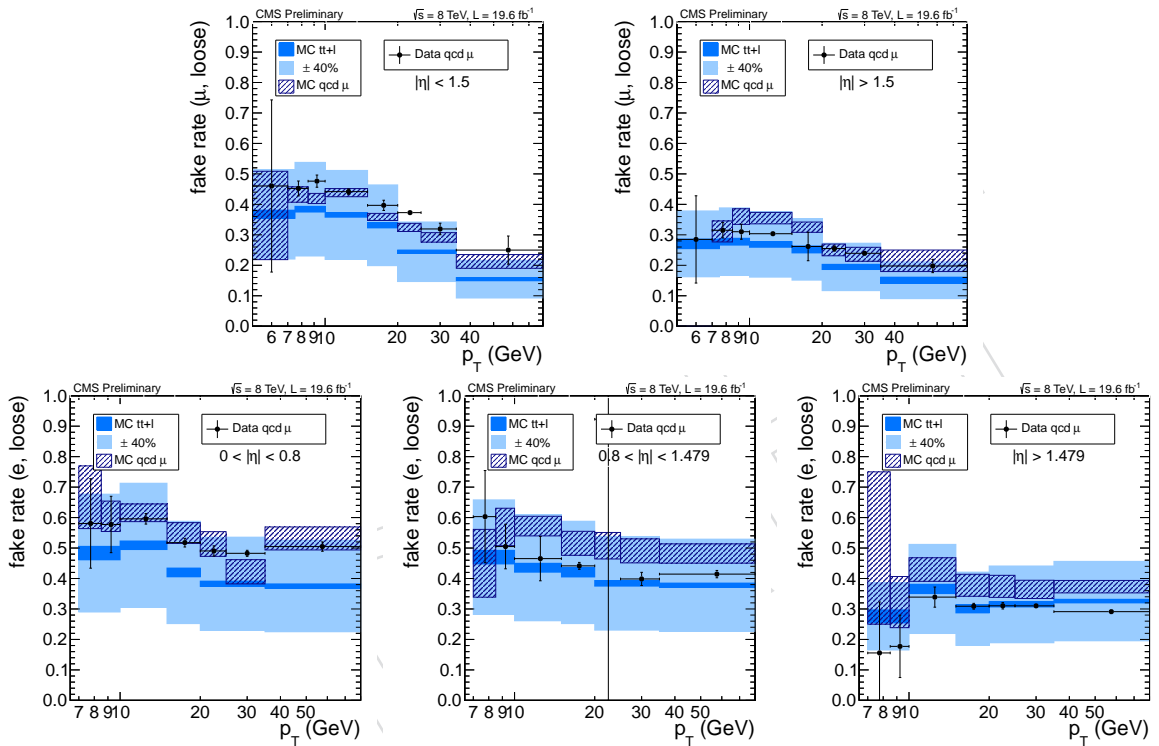


Figure 70: Measured fake rates for the tight MVA working point in the QCD dilepton control region. Data (dots) are compared with the expectations for non-prompt leptons in simulated QCD dilepton events (blue hatched boxes) and $t\bar{t}$ events (azure filled boxes). The results in the top row are for muons, the ones in the bottom for electrons; the results in the different columns corresponds to different $|\eta|$ ranges, as written in the plots.

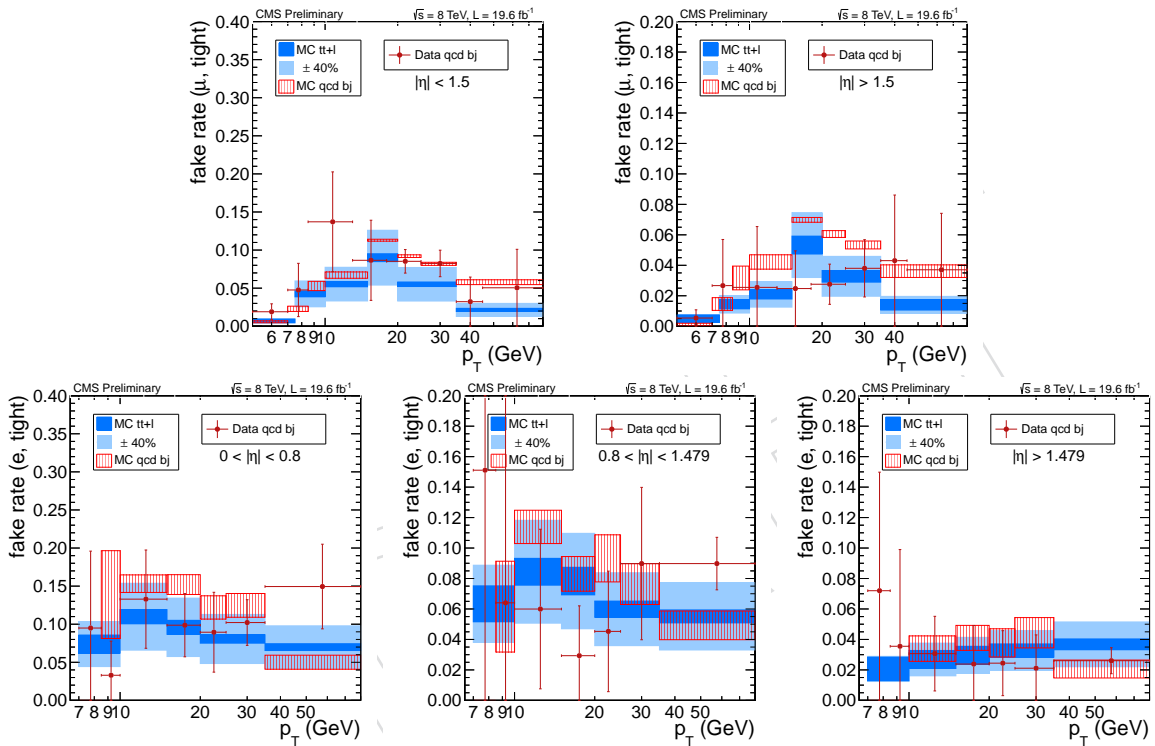


Figure 71: Measured fake rates for the tight MVA working point in the QCD b-jet control region. Data (dots) are compared with the expectations for non-prompt leptons in simulated QCD lepton plus b-jet events (red hatched boxes) and $t\bar{t}$ events (azure filled boxes). The results in the top row are for muons, the ones in the bottom for electrons; the results in the different columns corresponds to different $|\eta|$ ranges, as written in the plots.

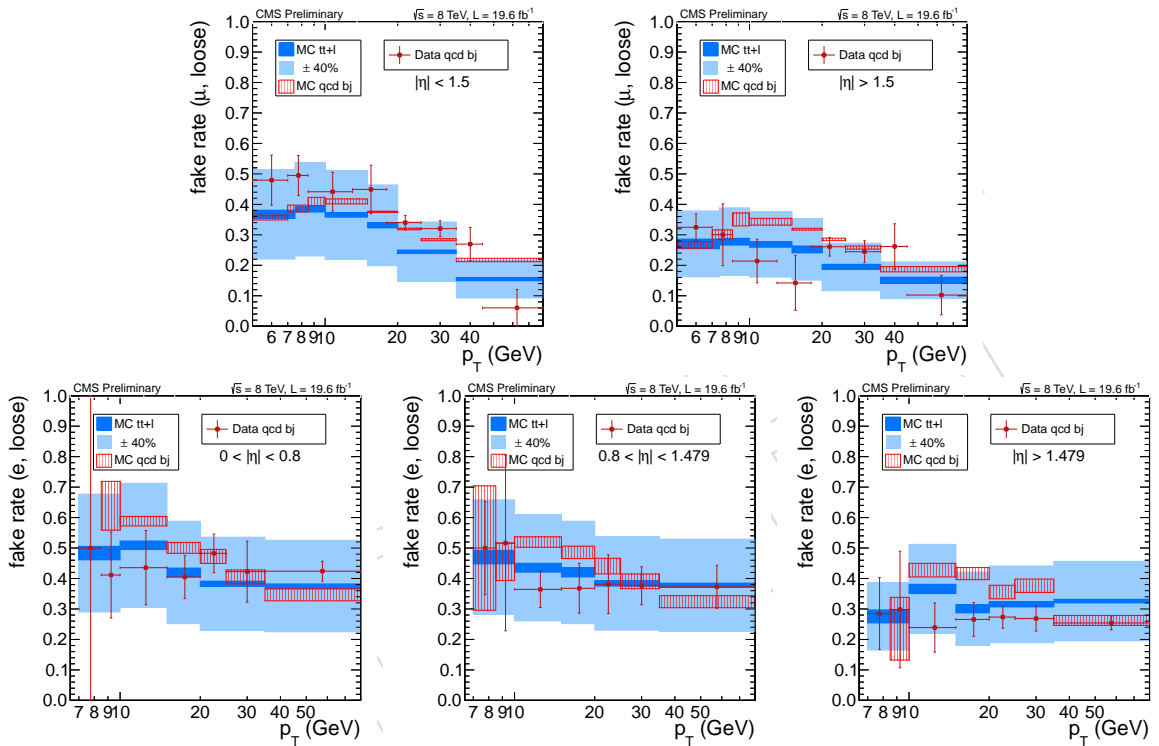


Figure 72: Measured fake rates for the tight MVA working point in the QCD b-jet control region. Data (dots) are compared with the expectations for non-prompt leptons in simulated QCD lepton plus b-jet events (red hatched boxes) and $t\bar{t}$ events (azure filled boxes). The results in the top row are for muons, the ones in the bottom for electrons; the results in the different columns corresponds to different $|\eta|$ ranges, as written in the plots.

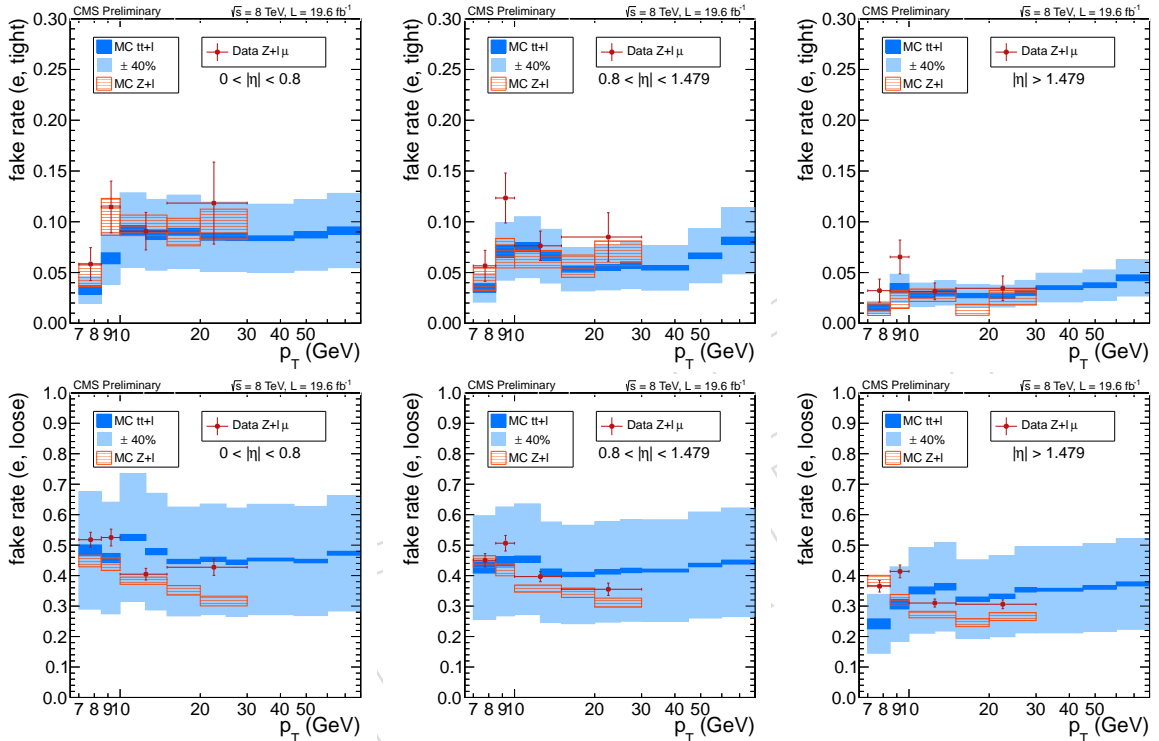


Figure 73: Measured fake rates for the two MVA working points in the Z plus electron control region. Data (dots) are compared with the expectations for non-prompt electrons in simulated Z plus lepton events (red hatched boxes) and $t\bar{t}$ events (azure filled boxes). The results in the top row are for the tight MVA working points, the ones in the bottom for the loose MVA working point; the results in the different columns corresponds to different $|\eta|$ ranges, as written in the plots.

1196 C Additional plots for lepton MVA

1197 C.1 High pile-up events

1198 The agreement between data and simulation of the input variables is shown in Fig. 74,75 for
 1199 events with high pile-up (we request at least 20 reconstructed vertices), using the $Z \rightarrow \mu^+ \mu^-$,
 1200 $Z \rightarrow e^+ e^-$ control samples.

1201 Fig. 76 shows the data and simulation comparison for the BDT output of the lepton MVA dis-
 1202 criminator for signal muons and electrons in different p_T and η regions for events with high
 1203 pile-up, using the $Z \rightarrow \mu^+ \mu^-$ and the $Z \rightarrow e^+ e^-$ control regions.

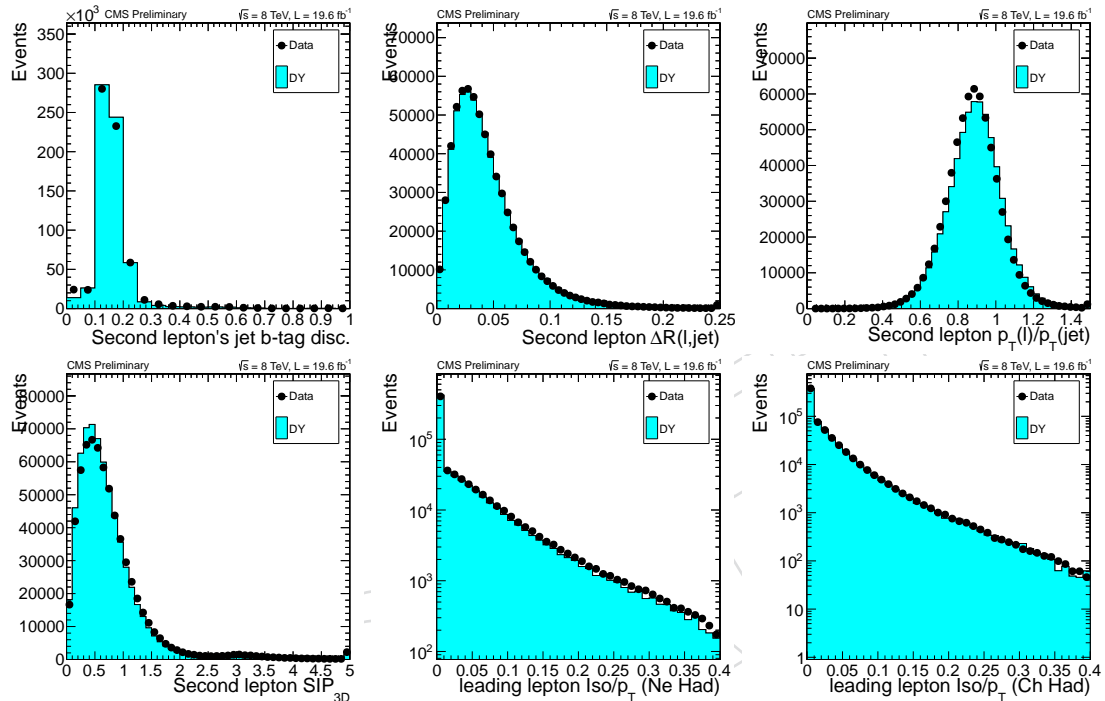


Figure 74: Data to simulation comparison for the shapes of the input variables to the lepton MVA discriminator in the $Z \rightarrow \mu^+ \mu^-$ control region requiring the events to have at least 20 reconstructed vertices. From top left to bottom right the following variables for the signal muon are shown: the CSV b-tagging discriminator value of the closest jet, ΔR distance between the lepton and the closest jet, the ratio between the p_T of the lepton and the p_T of the closest jet, SIP_{3D} of the lepton, the neutral hadrons iso deposit, and the charged hadrons iso deposit.

1204 C.2 Efficiencies

1205 The efficiencies of the loose and tight working point of the lepton MVA discriminator for pres-
 1206 selected signal leptons from $Z \rightarrow \ell^+ \ell^-$ decays, are shown in Fig. 77 and Fig. 78 as a function of
 1207 the number of central jets with $p_T > 25$ GeV, and number of reconstructed vertices in the event.

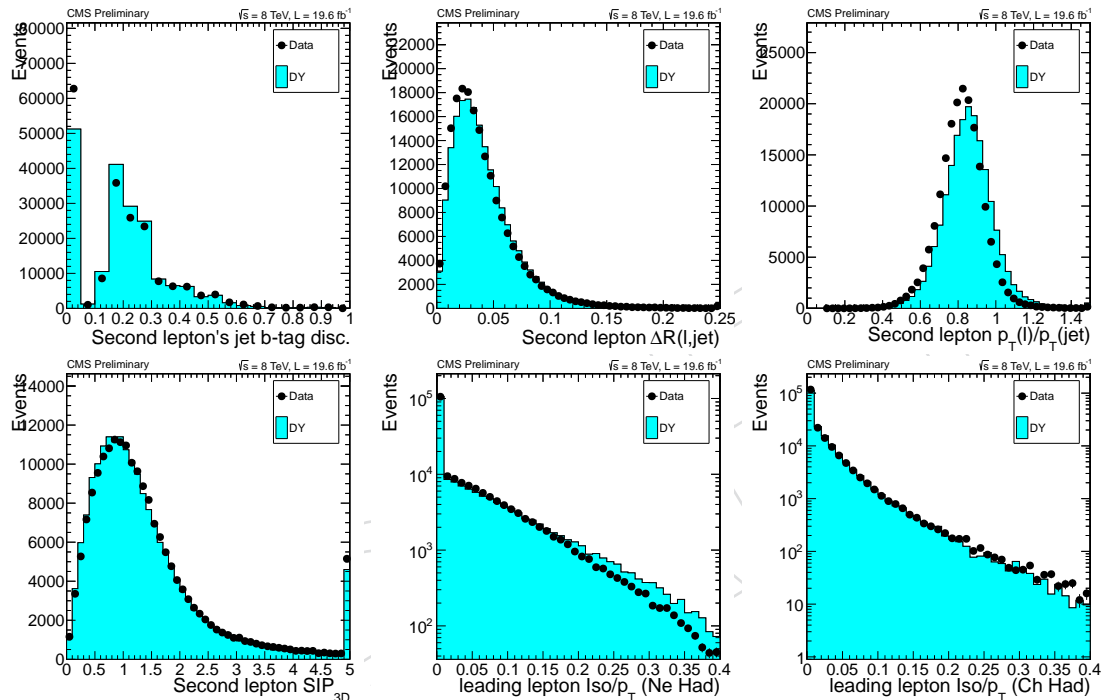


Figure 75: Data to simulation comparison for the shapes of the input variables to the lepton MVA discriminator in the $Z \rightarrow e^+e^-$ control region requiring the events to have at least 20 reconstructed vertices. From top left to bottom right the following variables for the signal electron are shown: the CSV b-tagging discriminator value of the closest jet, ΔR distance between the lepton and the closest jet, the ratio between the p_T of the lepton and the p_T of the closest jet, SIP_{3D} of the lepton, the neutral hadrons iso deposit, and the charged hadrons iso deposit.

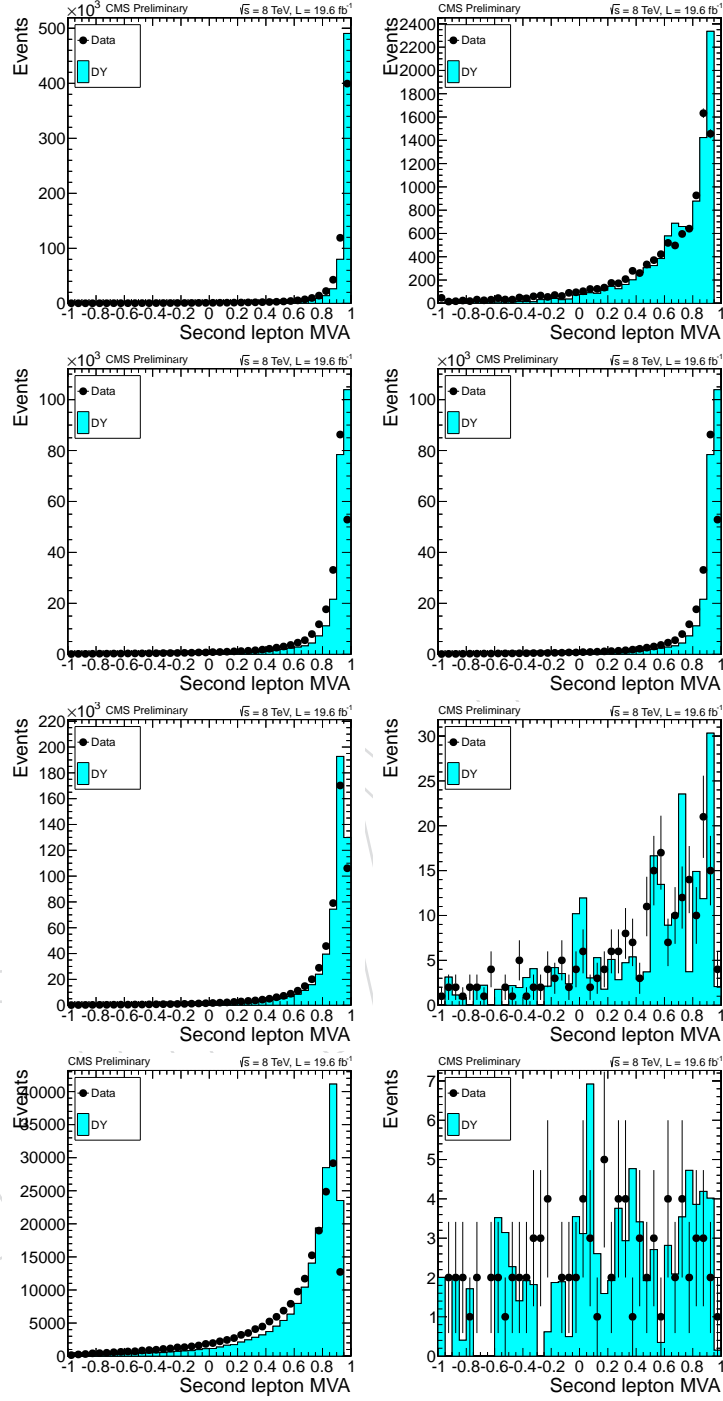


Figure 76: Data to simulation comparison for the BDT output of the lepton MVA discriminator in the $Z \rightarrow \mu^+ \mu^-$ and the $Z \rightarrow e^+ e^-$ control regions. From top left to bottom right the comparison is shown for: muons with $p_T > 15 \text{ GeV}$ and $|\eta| < 1.5$, $p_T < 15 \text{ GeV}$ and $|\eta| < 1.5$, $p_T > 15 \text{ GeV}$ and $|\eta| > 1.5$, $p_T < 15 \text{ GeV}$ and $|\eta| > 1.5$, electrons with $p_T > 10 \text{ GeV}$ and $|\eta| < 1.479$, $p_T < 10 \text{ GeV}$ and $|\eta| < 1.479$, electrons with $p_T > 10 \text{ GeV}$ and $|\eta| > 1.479$, $p_T < 10 \text{ GeV}$ and $|\eta| > 1.479$.

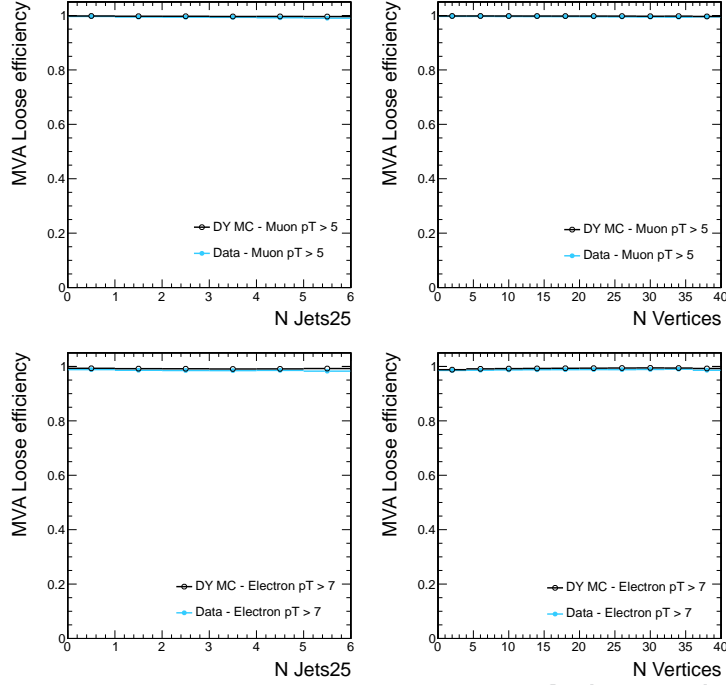


Figure 77: Efficiencies for the loose lepton MVA discriminator working point with respect to preselected muons and electrons from Z decays, extracted with the tag-and-probe technique on data and simulation. The efficiencies are shown from left to right as a function of the number of jets and vertices (in the first raw for muons, in the second raw for electrons).

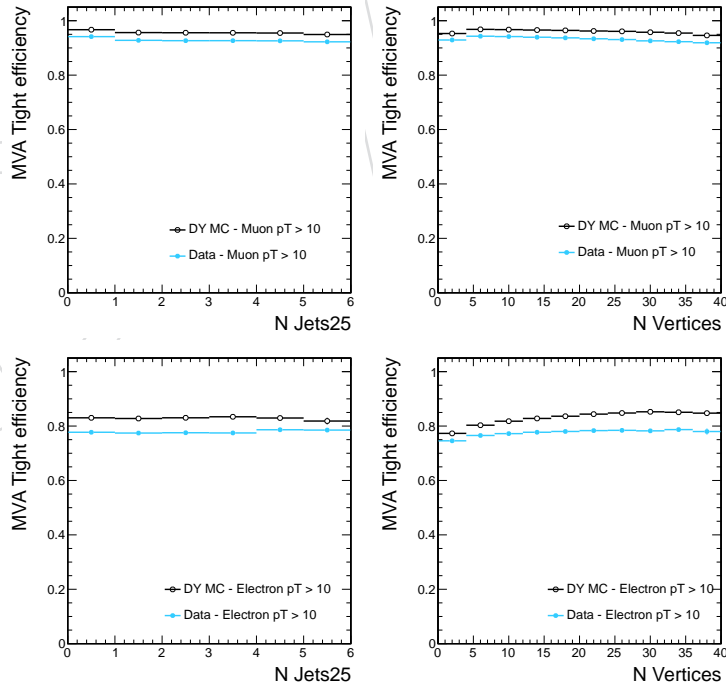


Figure 78: Efficiencies for the tight lepton MVA discriminator working point with respect to preselected muons and electrons from Z decays, extracted with the tag-and-probe technique on data and simulation. The efficiencies are shown from left to right as a function of the number of jets and vertices (in the first raw for muons, in the second raw for electrons).

D Studies of 2 same-sign muon excess

An excess of data events above the expected yield was observed in the two same-sign muons channel. There were 41 events observed compared to 26.4 ± 5.2 signal and background events expected. This is a significant excess above expectation. The following appendix contains studies examining the excess.

D.1 Kinematic distributions of two-muon events

Only the two same-sign muons channel shows a significant excess of data events over the background expectation. No such excess was observed in the other 2ℓ channels or in the 3ℓ or 4ℓ channels.

The two same-sign muons background is detailed in Table 7. According to the table, the expected amount of signal is 2.7 events and the expected amount of background is 23.7 events. Of the background events, 10.8 (45%) are from non-prompt leptons, 8.2 are from ttW (34%), 2.5 (11%) are from ttZ/ γ^* , and various other small backgrounds make up the remaining 11% of the sample. There are 15 more events observed in the data than expected.

The events in the two same-sign muons category do not have any features that are significantly different from expectations except their tri-dimensional impact parameter significance (SIP_{3D}). In particular, the events do not have kinematic properties characteristic of a particular background process, such as non-prompt leptons. Figures 22 and 25 from Sections 4 and 5 included some distributions that show that the excess is not particular to a specific kind of background. For convenience of discussion in this appendix, Figure 79 shows a selection of some of the distributions from the figures of the previous sections. It can be seen that the excess is relatively flat as a function of jet multiplicity. An excess of signal-like events would be more pronounced at higher jet multiplicity. Similarly, the H_T^{miss} distribution shows an excess that is relatively evenly distributed. Additionally, Figure 79 shows that the excess is not peaked in the lowest bin of trailing lepton p_T . If the excess events were mostly non-prompt muons, then it is more likely that they would fall in the lowest bin of trailing lepton p_T . A similar argument applies to the H_T distribution: non-prompt muons tend to appear at low H_T , but the excess does not prefer those bins. The minimum ΔR between the trailing lepton and a jet appears to have a peak in the second lowest bin, but this is not strongly suggestive of a particular class of events. Since the MVA input variables are not particularly background-like, the MVA output distribution of the data is also not especially background-like.

In addition to kinematic variables that are sensitive to sample composition, distributions that are sensitive to lepton reconstruction features were also checked. Figure 80 shows some of these variables; the leptons do not have unexpected reconstruction features, like nearly overlapping muons or muons without a sufficient number of hits.

Finally Figure 81 shows the distribution of the input variable to the lepton MVA. From this set of plots we can conclude that the excess of events is mainly dominated by well isolated muons, and that part of it is characterized by events with one muon with large SIP_{3D} . This last feature will be discussed in more detail in the next section.

In addition, lepton ID and lepton MVA variables are shown in Figure 82 for the muon failing the lepton MVA cut in the two same-sign muon final state selection. In these distributions the tt and single top MC components are scaled to the yield in data. These distributions confirm that in the application region of the fake rate, the modelling of the lepton related variables in the tt MC matches well with the data.

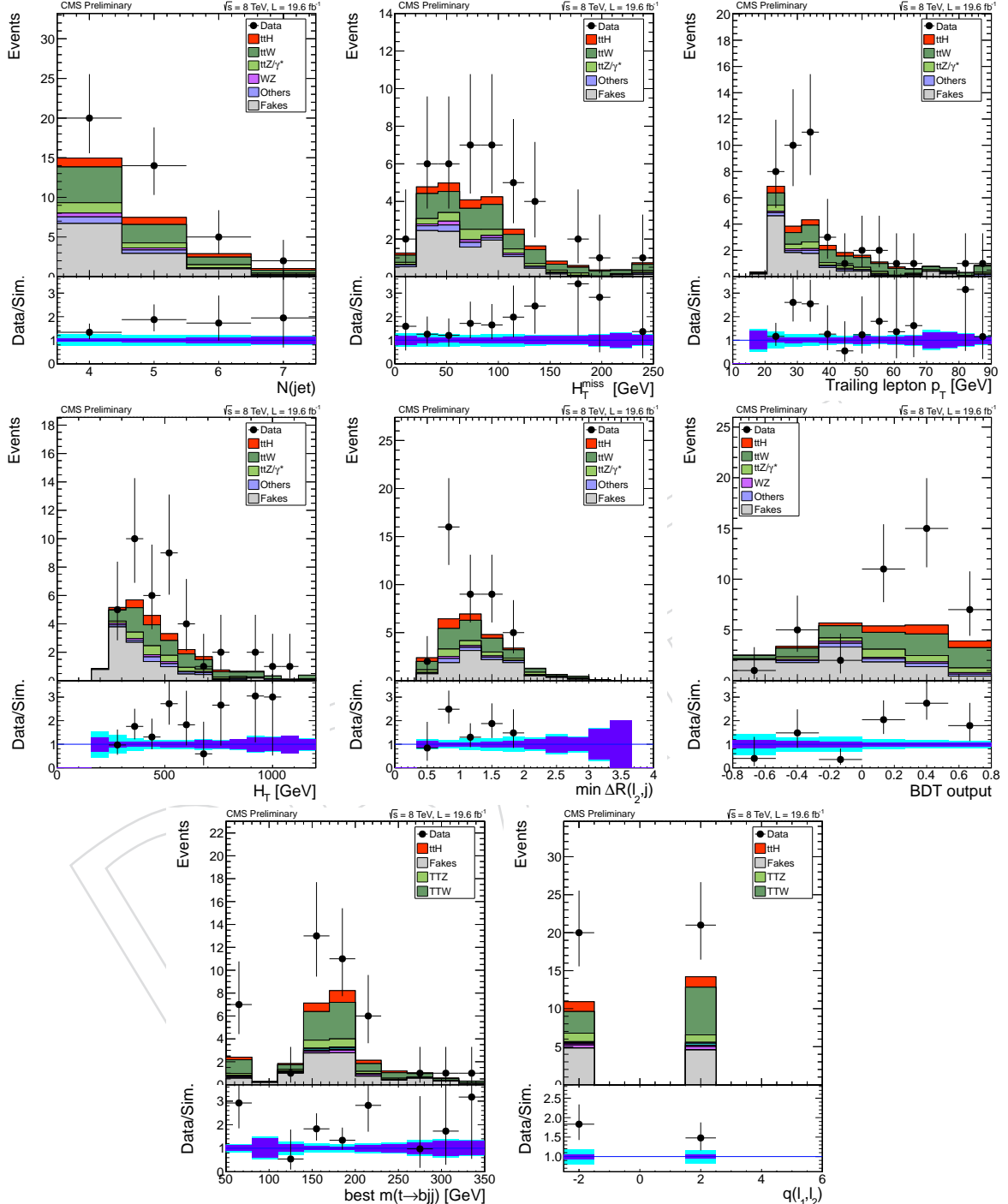


Figure 79: Distributions of kinematic variables sensitive to the composition of the sample in the two same-sign muon selection. The plots show that the excess is not especially signal-like or background-like.

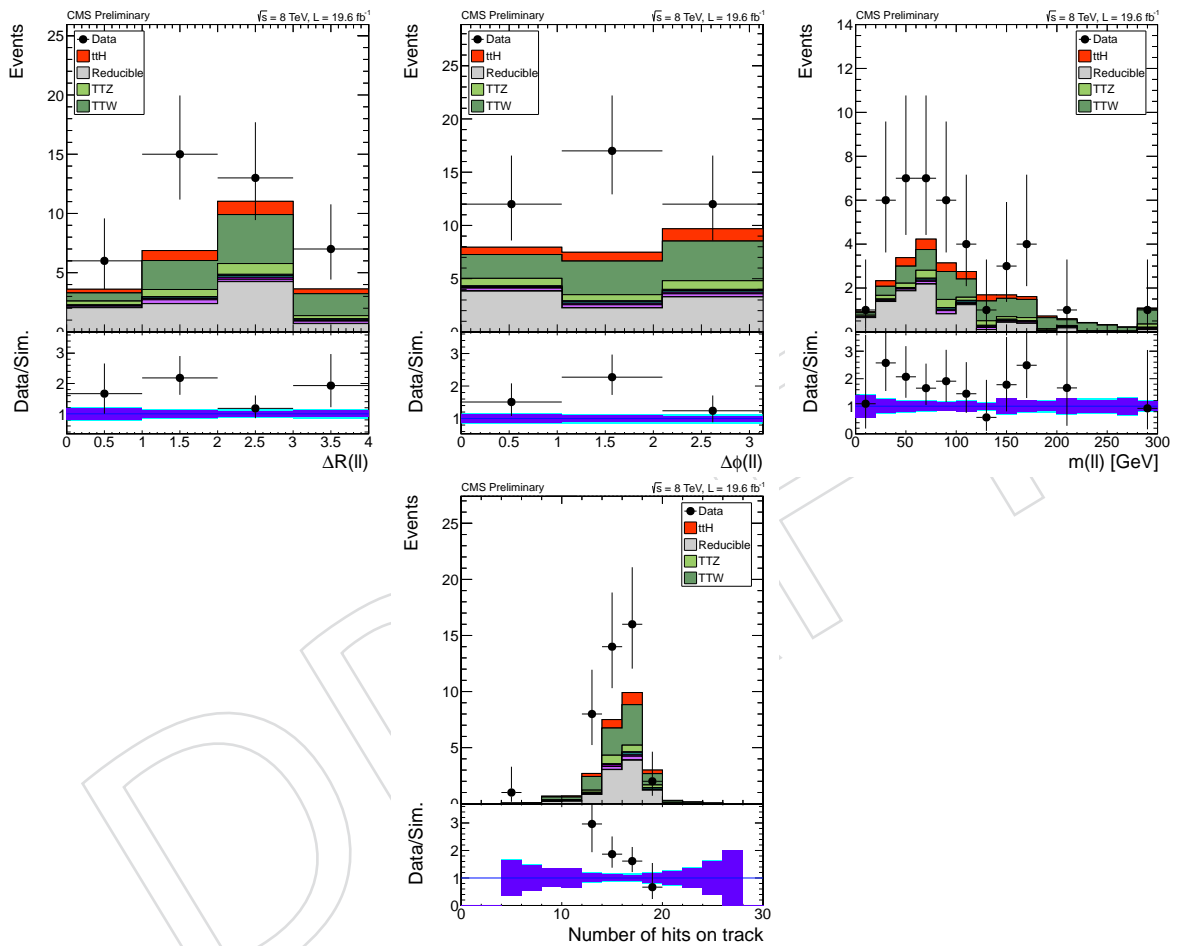


Figure 80: Distribution of variables sensible to lepton reconstruction fixtures in the two same-sign muon selection. Fake background is from $t\bar{t}$ simulation normalized to the expected number of fakes from the fake rate calculation.

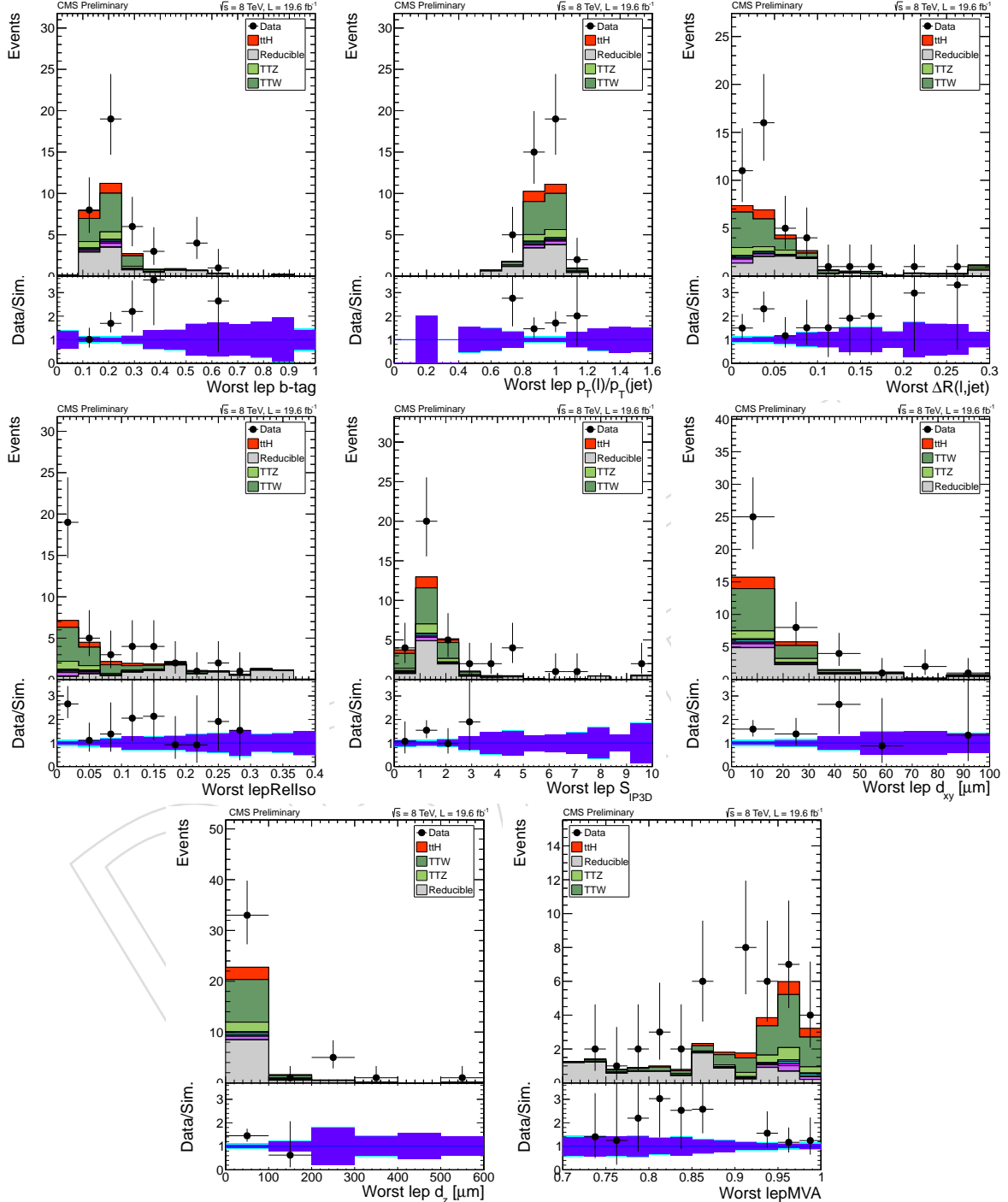


Figure 81: Lepton MVA input variables in the two same-sign muon selection. The fake background is from $t\bar{t}$ simulation normalized to the expected number of fakes from the fake rate calculation.

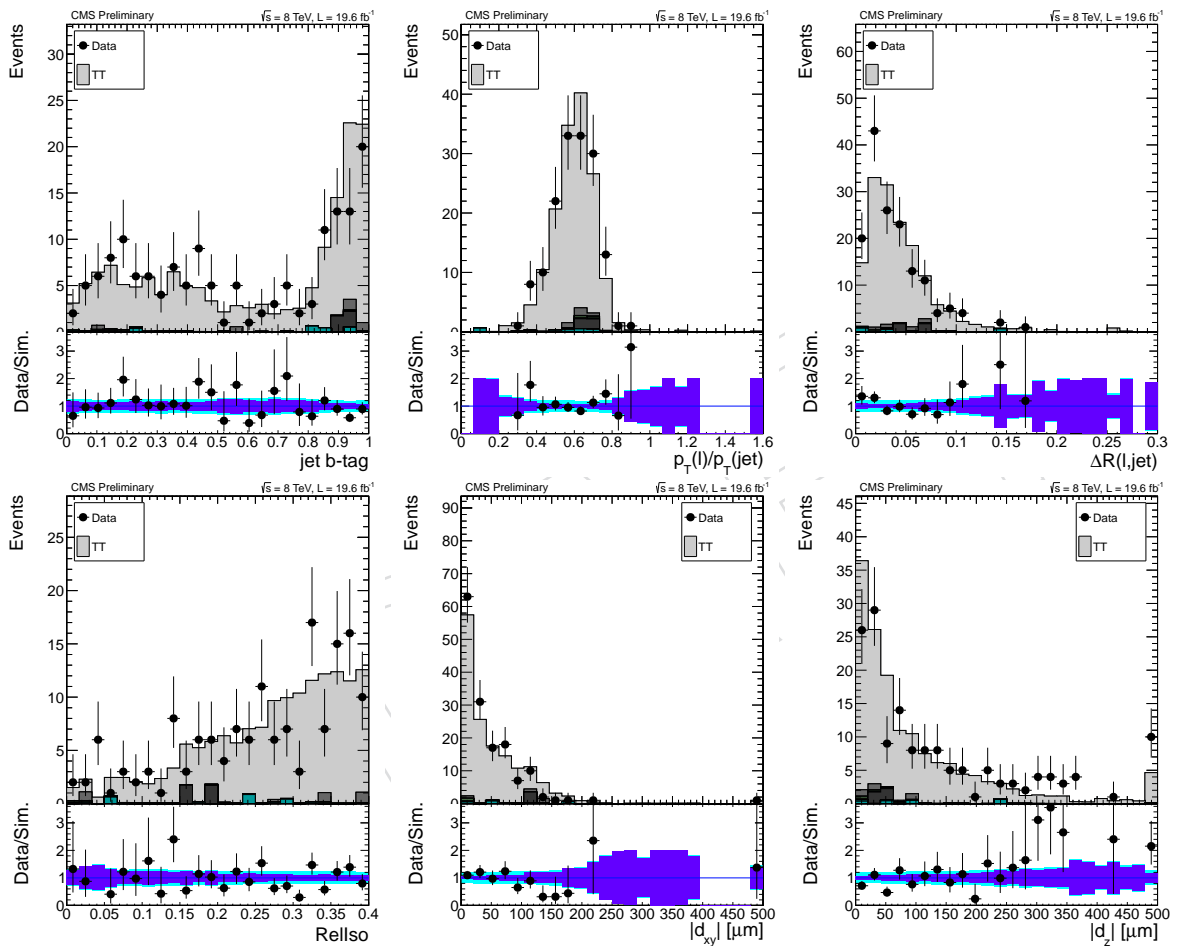


Figure 82: Lepton MVA input variables for the muon failing the lepton MVA cut. The $t\bar{t}$ and single top MC components are scaled to the yield in data.

D.1.1 Impact parameter significance checks

In this section we look in more detail at the events where one muon has $SIP_{3D} > 3.5$. The first hypothesis that we want to exclude is that this excess comes from a mismodelling of semi-leptonic $t\bar{t}$ events. For example we want to exclude that the fake rate for muons at large SIP_{3D} in data could be larger than in simulation. To do that we measured the fake rate in data and in simulation separately for muons with $SIP_{3D} > 3.5$ and $SIP_{3D} < 3.5$. The fake rate distributions are shown in Figure 83. The plots show that muons with large SIP_{3D} have smaller fake rates, as expected, and that there is good agreement between the QCD data and $t\bar{t}$ MC.

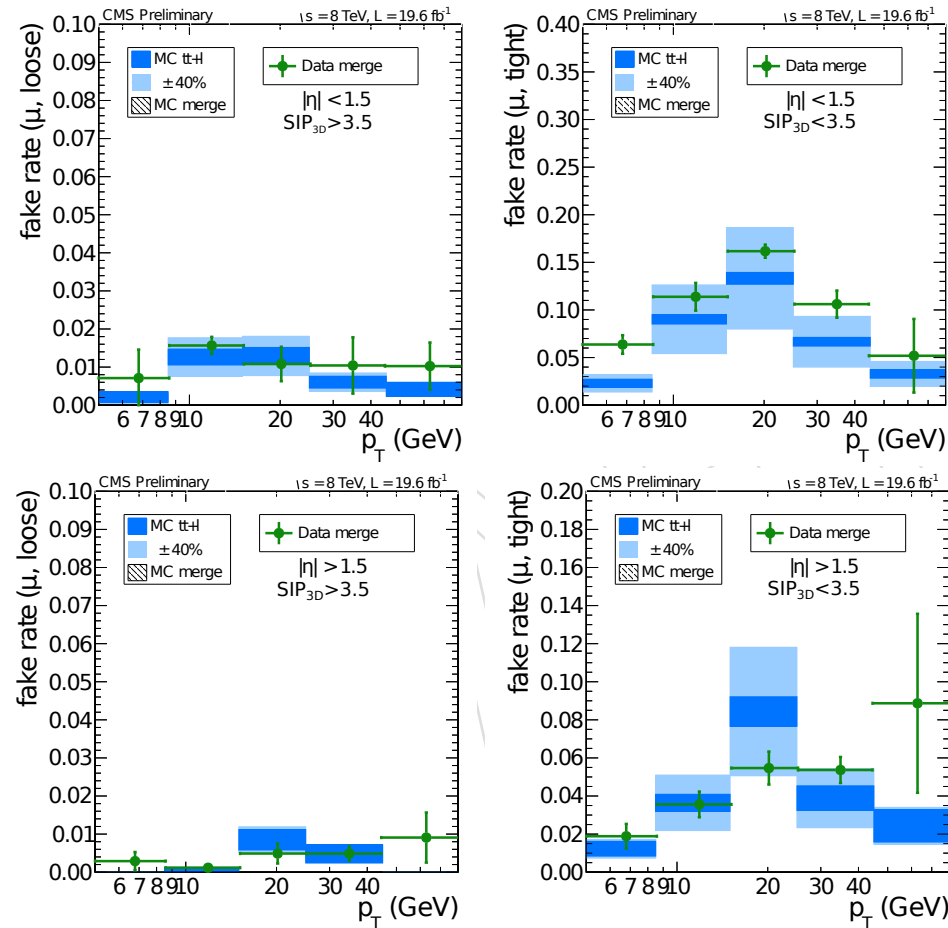


Figure 83: Measured fake rates for the tight MVA working point in the merged QCD dilepton and QCD b-jet control regions for muons in the barrel region $|\eta| < 1.5$ (top) and the end-cap region $|\eta| > 1.5$ (bottom), and with impact parameter significance ($SIP_{3D} > 3.5$) (left) and $SIP_{3D} < 3.5$ (right).

Moreover we checked if the kinematic of these high SIP_{3D} events is compatible with $t\bar{t}$ events. We looked the distributions of the missing energy, the trailing lepton p_T , the jets and b-jets multiplicity and the minimum p_T of the two jets with highest b-tag; we conclude that the events do not look very like semi-leptonic $t\bar{t}$. In addition we looked at several lepton properties distributions (some of them shown in Figure 84), and we can say that these muons are well isolated, do not appear to be part of a b-jet, most have transverse impact parameters below 100 μm and larger longitudinal impact parameter, with most muons falling between 50 and 300 μm . Figure 85 shows the BDT output for the events with at least one muon in the high SIP_{3D} region.

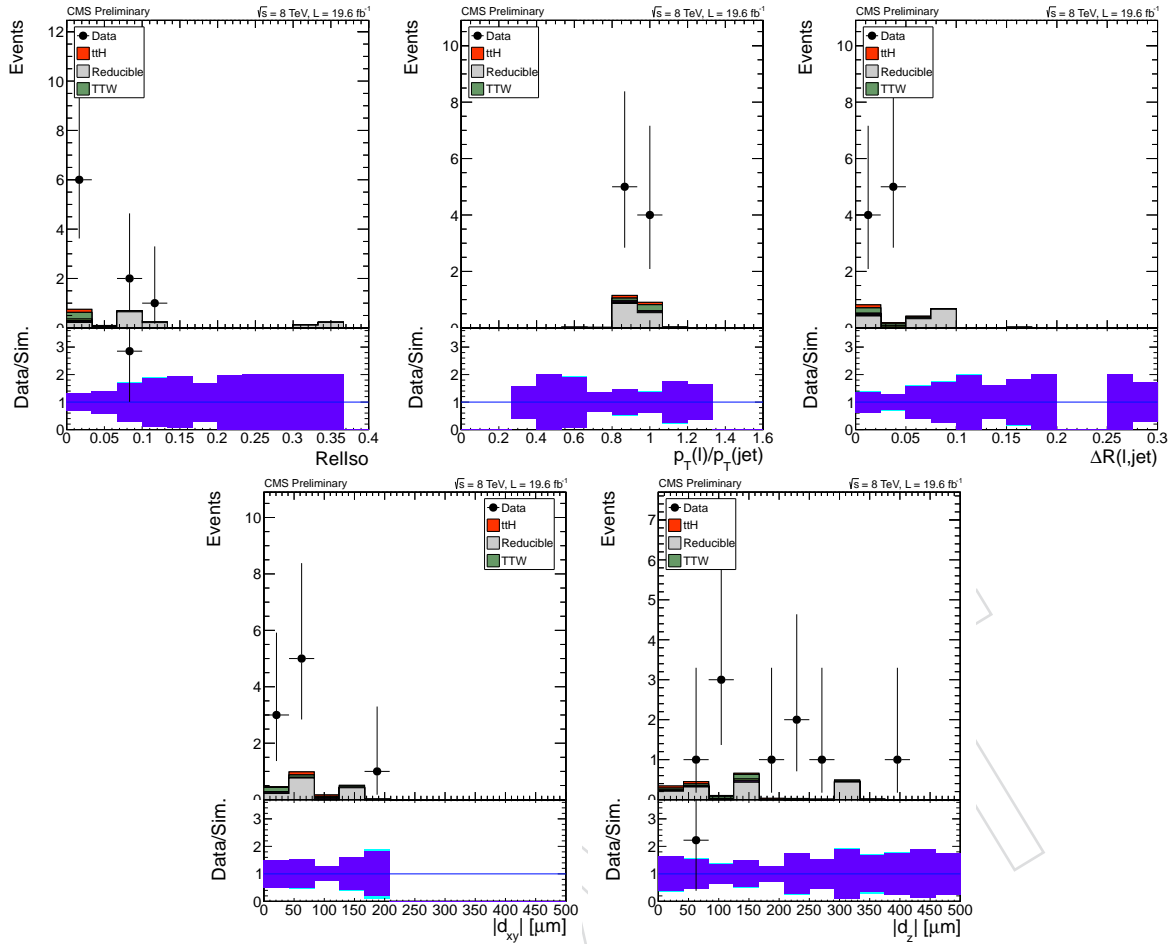


Figure 84: BDT output for muons with $SIP_{3D} > 3.5$. The fake background is from $t\bar{t}$ simulation normalized to the expected number of fakes from the fake rate calculation.

1270 The muons with $SIP_{3D} > 3.5$ were scrutinized in detail in the event display. The muons appear
 1271 to be real (good track both in the tracker and in the muon system). The inclusive vertex finder
 1272 algorithm was run on these events, and the muons are not associated to any of the found sec-
 1273 ondary vertices.

1274 Moreover we checked separately the distributions of the 3D impact parameter and its uncer-
 1275 tainty for the data, the signal MC and the $t\bar{t}$ MC for the events passing the two same-sign muon
 1276 selection, as it is shown in Figure 86.

1277 We also checked explicitly the vertex compatibility of the two same-sign leptons looking at
 1278 the difference in d_z between the two muons, absolute or relative to the uncertainty, and at the
 1279 χ^2 obtained from fitting the two tracks to a common vertex. Several other tracking variables,
 1280 like the expected inner tracker hits, have been investigated. A summary of these distributions
 1281 can be found in Figure 87 for all the two same-sign muon events, and in Figure 88 for the high
 1282 SIP_{3D} events.

1283 Additional checks were done to exclude any reconstruction issue, such as issue in data at high
 1284 occupancy that could cause prompt leptons to have mis-reconstructed SIP_{3D} . We validated
 1285 the SIP_{3D} distributions in opposite-sign dimuons events passing the full 2μ final state selection
 1286 (with a Z veto and E_T^{miss} LD cut to make the sample mostly dominated by dileptonic $t\bar{t}$ +jets
 1287 events), and we see good agreement between data and simulation in the SIP_{3D} distribution. We
 1288 also checked it in the following signal regions: the two same-sign muon signal region requiring
 1289 exactly 3 jets, the 3-lepton signal region (looking at the worst muon SIP_{3D}), and the same-sign

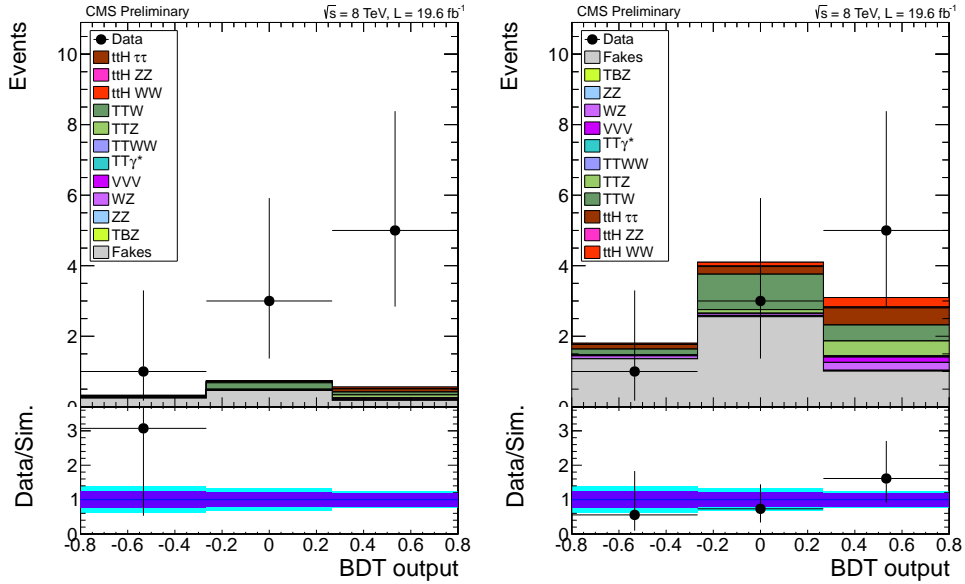


Figure 85: BDT output for the events with at least one muon in the high SIP_{3D} region in the two same-sign muon selection. In the left plot the fake background is from $t\bar{t}$ simulation normalized to the expected number of fakes from the fake rate calculation. In the right one the overall signal+background prediction is scaled to match the yields in data.

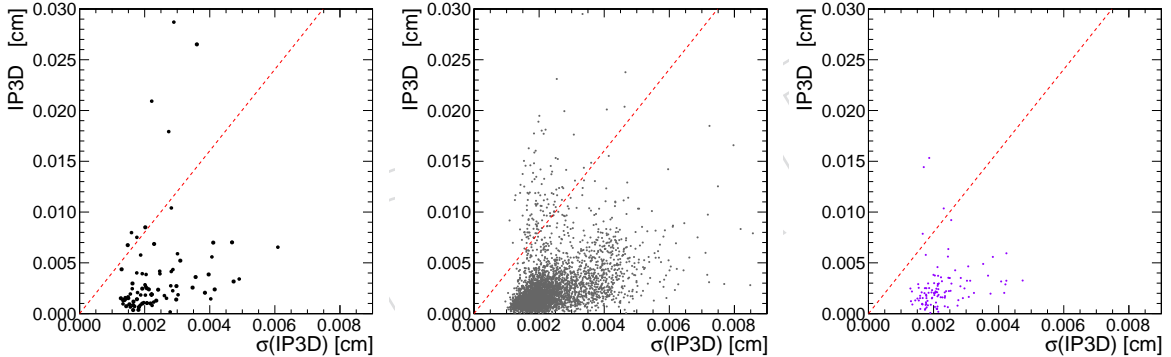


Figure 86: 3D impact parameter and its uncertainty distributions for the the data, the signal MC and the $t\bar{t}$ MC for the events passing the two same-sign muon selection.

1290 $e\mu$ signal region (looking at the muon SIP_{3D}). These latter three checks are shown in Figure 89;
1291 no excess at high SIP_{3D} is found anywhere but in the 2μ same-sign signal region with more 4
1292 jets.

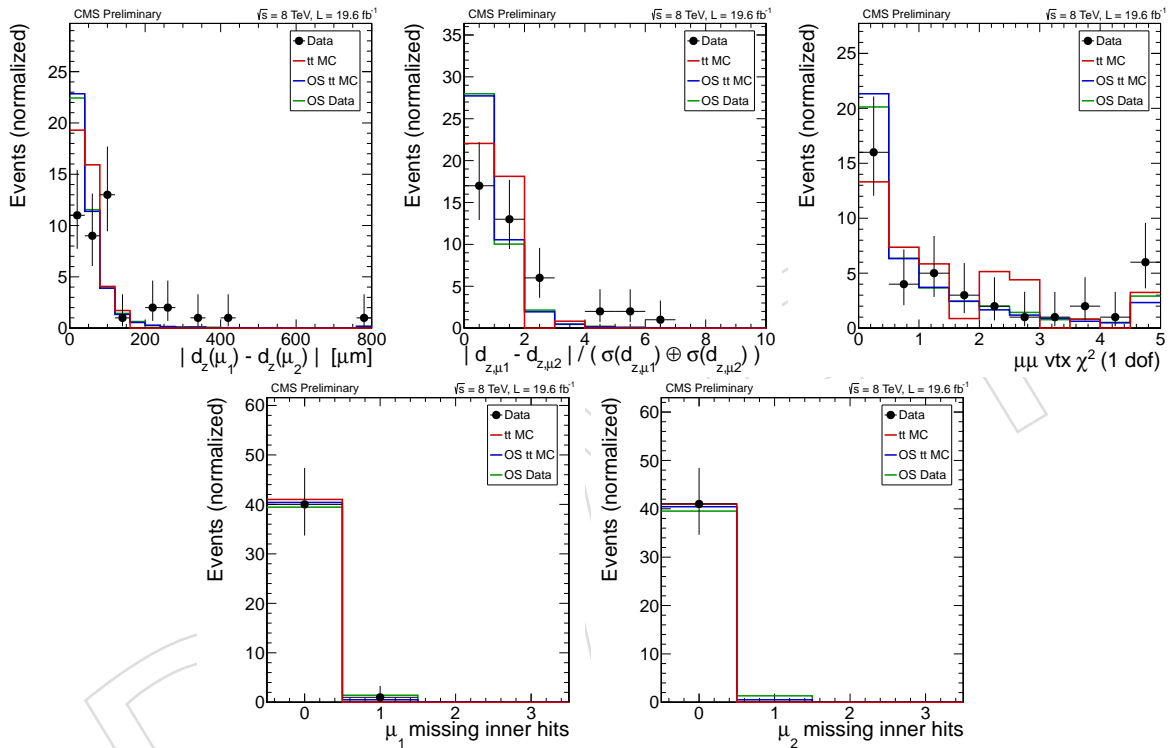


Figure 87: Tracking variables for all the events passing the two same-sign muons selection. From top right: difference in d_z between the two muons, absolute or relative to the uncertainty, the χ^2 obtained from fitting the two tracks to a common vertex, the number of expected inner tracker hits for the leading and trailing muon.

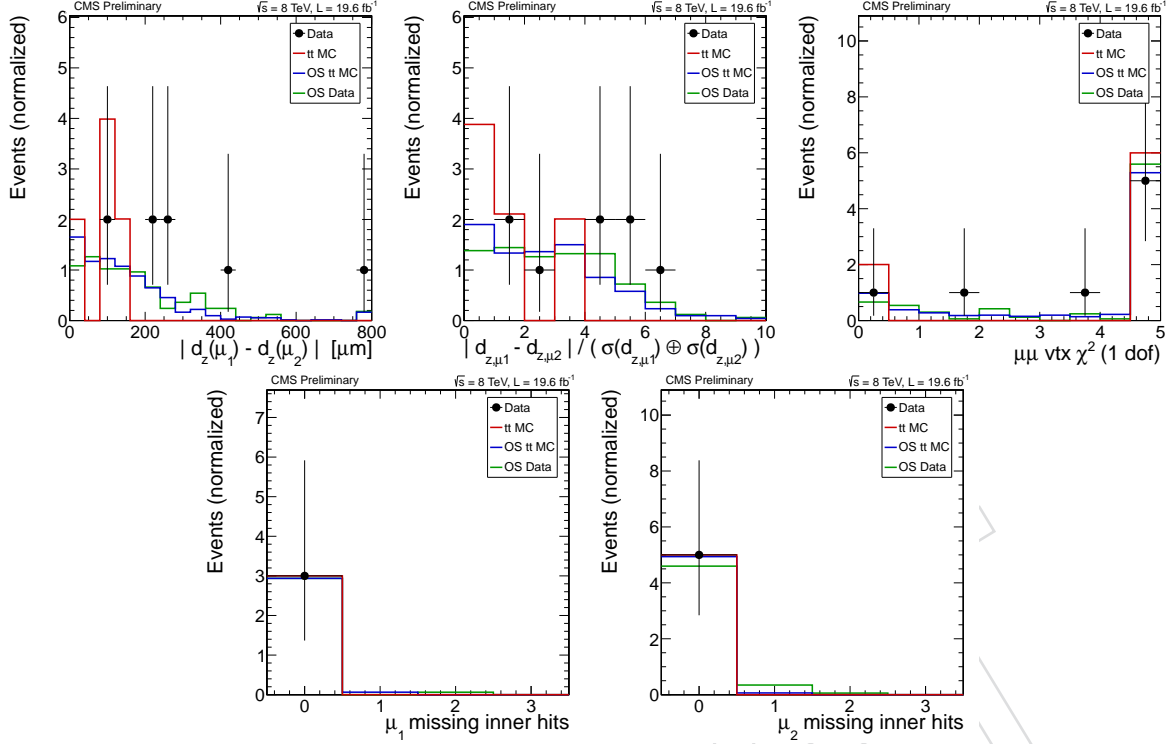


Figure 88: Tracking variables for the events passing the two same-sign muons selection and falling in the high SIP_{3D} region. From top right: difference in d_z between the two muons, absolute or relative to the uncertainty, the χ^2 obtained from fitting the two tracks to a common vertex, the number of expected inner tracker hits for the leading and trailing muon.

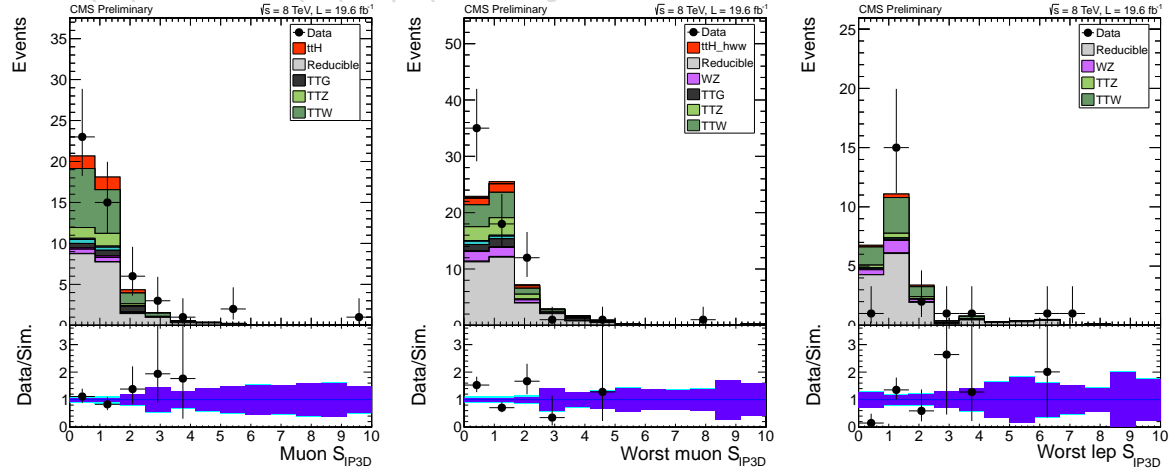


Figure 89: SIP_{3D} distributions in other signal regions: same-sign $e\mu$, 3-lepton, two same-sign muons with 3 jets.

1293 **D.2 Irreducible backgrounds: fitter studies**

1294 In the nominal fit to extract the $t\bar{t}H$ signal, all other backgrounds are constrained to their in-
 1295 put predictions. However, it is also interesting to explore fits in which the normalizations of
 1296 the main backgrounds, $t\bar{t}V$ and the reducible background from non prompt leptons, are left
 1297 unconstrained. In those cases, the normalization will be determined directly from the signal
 1298 regions relying on the difference in the shapes of the final discriminants, and on the differences
 1299 in the expected yields in the various modes. As less external information is used, the sensitivity
 1300 to $t\bar{t}H$ in these fits will however be worse than for the nominal one.

1301 **D.2.1 Fits for $t\bar{t}V$ backgrounds in control regions**

1302 First, however, we explore how to measure separately the $t\bar{t}W$ and $t\bar{t}Z$ backgrounds from con-
 1303 trol regions in data. For $t\bar{t}Z$, we can rely on the trilepton final state modifying the selection
 1304 to require a pair of same-flavour opposite-sign leptons with an invariant mass within 10 GeV
 1305 from the mass of an on-shell Z boson (these events are vetoed in the nominal $t\bar{t}H$ selection). If
 1306 we perform a fit for the $t\bar{t}Z$ yield in that final state, using as the same categorization and BDT
 1307 discriminator as for the nominal trilepton analysis, and fixing the normalization of $t\bar{t}W$ and $t\bar{t}H$
 1308 to be as in the SM, we obtain $\mu(t\bar{t}Z) = 1.3_{-0.4}^{+0.5}$; the theoretical uncertainty on the inclusive $t\bar{t}Z$
 1309 cross section from unknown higher orders in QCD is not included in these uncertainties, but
 1310 all the other systematic and statistical uncertainties are.

1311 For $t\bar{t}W$ we obtain a control region from the dilepton selection requiring exactly three jets in-
 1312 stead of at least four. For the extraction of the signal, we a BDT discriminator using the same
 1313 variables and training samples that are used in the nominal dilepton analysis, but trained on
 1314 events with ≤ 3 jets; this provides a good separation also between $t\bar{t}$ from $t\bar{t}W$ since the ex-
 1315 pected distribution of $t\bar{t}W$ and $t\bar{t}H$ in those variables are similar. Due to the large background
 1316 from $t\bar{t}$ the measurement we can obtain for $t\bar{t}W$ is less precise: $\mu(t\bar{t}W) = 1.6_{-0.7}^{+0.9}$. Similarly to
 1317 the $t\bar{t}Z$ case, the uncertainty on the theoretical prediction for the the inclusive cross is not not
 1318 included in these reported uncertainty on mu.

1319 From these two fits, we obtain estimates of the backgrounds that are compatible with the input
 1320 predictions within better than one standard deviation, but the uncertainties from the fit are
 1321 much larger than the ones from the theoretical prediction.

1322 **D.2.2 Combined fits**

1323 We explore four possible combined fits, depending on two choices: (i) whether the dilepton
 1324 events with three jets are included as a separate category or not; (ii) whether the normalization
 1325 for the reducible backgrounds are also left free in the fit or not. The control region for $t\bar{t}Z$ is
 1326 always included in these fits.

1327 Compared to the nominal analysis, there are a few changes:

- 1328 • we do not include systematic uncertainties on the theoretical predictions on inclu-
 1329 sive cross sections for the $t\bar{t}V$ backgrounds, since the overall normalization is left
 1330 free.
- 1331 • when fitting also for the normalization of the reducible background, we introduce
 1332 two parameters $\mu(\text{fake } \mu)$ and $\mu(\text{fake e})$ that scale the reducible backgrounds from
 1333 non-prompt muons and from non-prompt electrons separately; in the electron-muon
 1334 and trilepton final states this is achieved by scaling the non-prompt background
 1335 yield by $0.40 \cdot \mu(\text{fake } \mu) + 0.60 \cdot \mu(\text{fake e})$ and $0.45 \cdot \mu(\text{fake } \mu) + 0.65 \cdot \mu(\text{fake e})$,
 1336 where the coefficients correspond to the relative fractions from non-prompt muons

and electrons obtained from the control regions in data. In this case, we don't include the overall systematic uncertainty on the normalization of the reducible background, but we still include the uncertainties on its shape and on the relative normalization between the dilepton and trilepton categories.

- if the three-jet dilepton category is included, we assume an extra 20% uncertainty on the relative normalization of the reducible background in this category compared to the rest of the dilepton events (both for muons and for electrons, uncorrelated).

For each of the four possibilities, we explore compute the expected sensitivity and the observed results for the different parameters (Tab. 17 and Fig. 90). Overall, we see that the expected sensitivity for the unconstrained fit is 17% worse than the nominal fit if the 3-jet events are included, and 25% worse if not. In all the four fits, the fitted signal strength for $t\bar{t}H$ is reduced from 3.7 to about 2.8, as part of the excess is absorbed by $t\bar{t}W$ and $t\bar{t}Z$. In all fits the normalizations for the irreducible backgrounds are compatible with the input values within one standard deviation, and similarly the non-prompt backgrounds are compatible with the normalization from the fake rate within the uncertainties used in the nominal fit (approximately $\pm 50\%$ for muons and $\pm 60\%$ for electrons).

parameter	without 3-jet events		with 3-jet events	
	expected	observed	expected	observed
$\mu(t\bar{t}H)$	$1.0^{-1.4}_{+1.6}$	$2.7^{-1.7}_{+2.0}$	$1.0^{-1.3}_{+1.5}$	$2.7^{-1.6}_{+1.7}$
$\mu(t\bar{t}W)$	$1.0^{-0.6}_{+0.6}$	$1.4^{-0.6}_{+0.7}$	$1.0^{-0.5}_{+0.5}$	$1.4^{-0.5}_{+0.6}$
$\mu(t\bar{t}Z)$	$1.0^{-0.3}_{+0.4}$	$1.2^{-0.4}_{+0.4}$	$1.0^{-0.3}_{+0.4}$	$1.1^{-0.3}_{+0.4}$
without 3-jet events		with 3-jet events		
parameter	expected	observed	expected	observed
$\mu(t\bar{t}H)$	$1.0^{-1.4}_{+1.6}$	$2.9^{-1.7}_{+2.0}$	$1.0^{-1.3}_{+1.5}$	$2.8^{-1.6}_{+1.8}$
$\mu(t\bar{t}W)$	$1.0^{-0.6}_{+0.6}$	$1.6^{-0.7}_{+0.8}$	$1.0^{-0.5}_{+0.5}$	$1.4^{-0.5}_{+0.6}$
$\mu(t\bar{t}Z)$	$1.0^{-0.3}_{+0.4}$	$1.2^{-0.4}_{+0.4}$	$1.0^{-0.3}_{+0.4}$	$1.1^{-0.3}_{+0.4}$
$\mu(\text{fake } \mu)$	$1.0^{-0.4}_{+0.5}$	$0.7^{-0.5}_{+0.5}$	$1.0^{-0.3}_{+0.3}$	$0.7^{-0.3}_{+0.4}$
$\mu(\text{fake e})$	$1.0^{-0.4}_{+0.4}$	$0.5^{-0.3}_{+0.4}$	$1.0^{-0.3}_{+0.3}$	$0.9^{-0.3}_{+0.3}$

Table 17: Expected sensitivities and observed results for different unconstrained fits. The first set of results is when leaving the normalization of the reducible backgrounds constrained to the prediction from the fake rate, the second one is allowing the normalization to float freely in the fit instead. For comparison, the expected result for the nominal fit is $1.0^{+1.3}_{-1.1}$.

We select two of the four fits and study also the correlations between the fitted parameters. The results for the fit not including 3-jet events and not floating the reducible background normalization are shown in Fig. 91, while the ones for the fit including 3-jet events and floating the reducible background are shown in Fig. 92. In both fits the correlation between the $\mu(t\bar{t}H)$ and $\mu(t\bar{t}W)$ is clearly visible, while $\mu(t\bar{t}Z)$ is uncorrelated since it contributes less to the signal region and is measured accurately in the dedicated control region. Some correlation is also visible between $\mu(t\bar{t}W)$ and the normalization of the reducible backgrounds, since the two processes both contribute to the 3-jet final state; the correlation is larger for the muons since in the electron case there are additional backgrounds that contribute (e.g. $t\bar{t}\gamma$ and charge misassignment). The correlation between the normalization of the reducible backgrounds from non-prompt leptons and the $t\bar{t}H$ signal yield are smaller, since $t\bar{t}H$ does not contribute to the

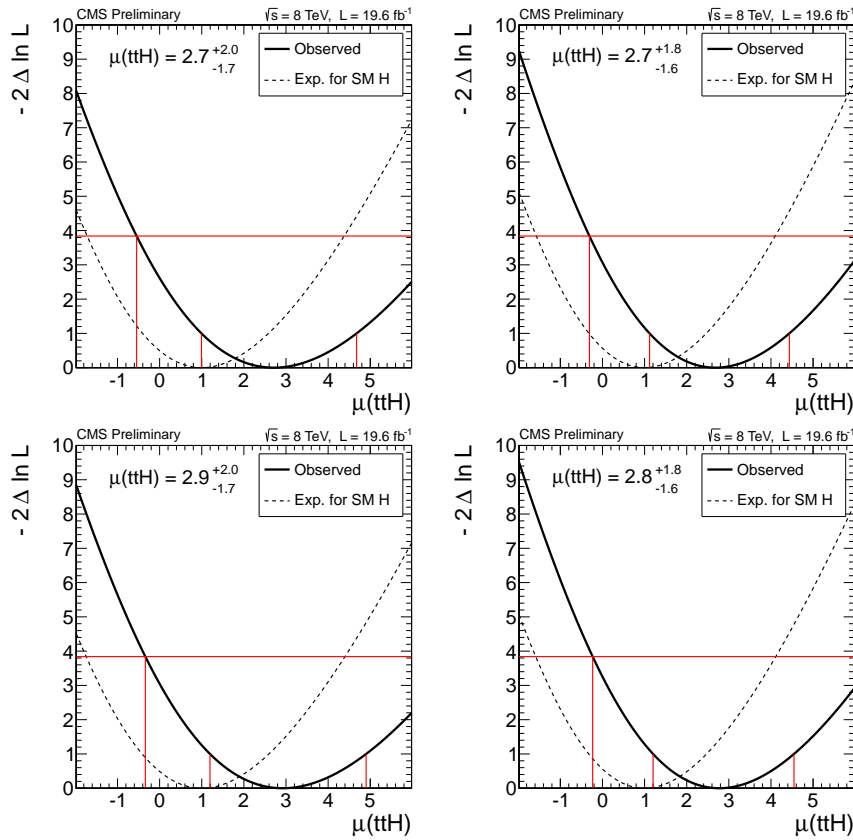


Figure 90: Scan of the profiled likelihood as function of $\mu(\text{ttH})$ for the four unconstrained fit, when not including the 3-jet category (left) and when including it (right). The plots in the top row are with the normalization of the reducible backgrounds constrained by the fake rate prediction, the ones on the bottom row have it freely floating.

3-jet final state.

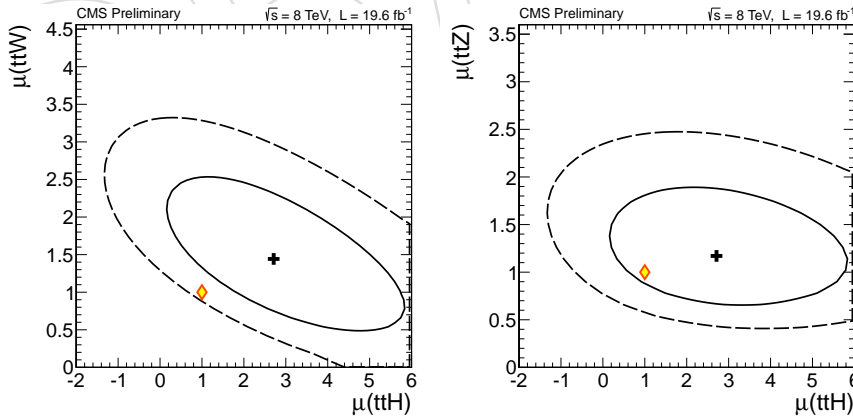


Figure 91: Best fit value, 68%, and 95% CL contours from a two-dimensional likelihood scan of $\mu(\text{ttH})$ and $\mu(\text{ttW})$ (left) or $\mu(\text{ttZ})$ (right). The diamond indicates the SM prediction (1, 1).

1364

1365 In conclusion, we observe that when releasing the constraints on the normalizations of the
 1366 different backgrounds the fitted signal strength for $\text{t}\bar{\text{t}}\text{H}$ is reduced a bit since part of the excess
 1367 is attributed to the $\text{t}\bar{\text{t}}\text{V}$ backgrounds. For all the fits we explored, the normalizations of the
 1368 backgrounds obtained from the fit are compatible with the inputs used in the nominal analysis
 1369 within the uncertainties.

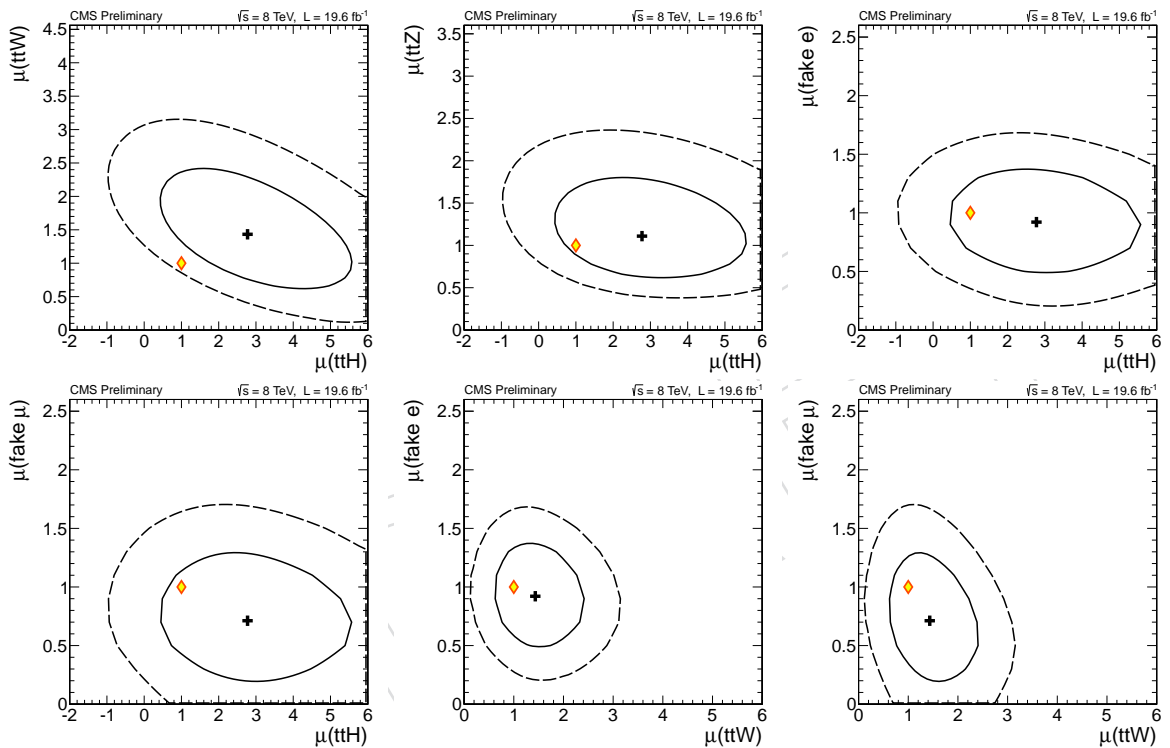


Figure 92: Best fit value (cross), 68% CL (solid), and 95% CL (dashed) contours from two-dimensional likelihood scans for the more complex fit including 3-jet events and leaving the normalization of the reducible backgrounds freely floating.

D.3 Non-prompt background studies

D.3.1 Fake rates for LF vs HF from simulation

Fake rates for muons from b-jets and muons from light-jets were checked in $t\bar{t}$ MC samples. Table 18 shows that these fake rates in MC are different by a large amount, almost an order of magnitude. It is important to confirm that the sample composition of the application region matches the expectation in MC, and that the amount of fakes from light flavor is not substantially different from expectation.

The plots in Sec. A.7 Fig. 68 show that the application region does indeed have the same kinematics as the $t\bar{t}$ sample.

Muon Source	b tag category	Fake rate in $t\bar{t}$ MC
muons from b	b-loose	0.0213
muons from b	b-tight	0.0521
muons from jets	b-loose	0.45
muons from jets	b-tight	0.39
all muons	b-loose	0.026
all muons	b-tight	0.077

Table 18: Fake rates from $t\bar{t}$ MC for muons from different sources.

D.3.2 Sample composition studies

A cut designed to remove muons from light jets can be a useful tool to understand the composition of the samples. In $t\bar{t}$ MC, a cut requiring that a muon:

- have least 2 matched muon stations
- be a tracker muon, and
- pass the “GlobalMuonPromptTight” ID cut

removes one third of the muons from punch-through or the in flight decay of kaons or pions, referred to as LF muons, while cutting less than 5% of prompt muons and muons from b-decay. This is shown in Table 19, which looks at the muon which fails the lepton MVA in the same-sign dimuon application region in MC and data. Data and MC show good agreement on the LF cut efficiency, indicating there is not a major excess of LF muons in the application region. Yields for MC are raw events, not normalized by luminosity to expectations.

Source	Events	Composition	Pass LF cut	Eff.
Prompt	6	0.6%	6	100%
b-quark	1039	96.2%	994	95.7%
c-quark	17	1.6%	16	94.1%
LF	18	1.7%	10	55.6%
Data	183		174	95.1%

Table 19: Efficiency for LF cut on data and MC in the $t\bar{t}$ application region.

A check in a data sample dominated by Z bosons decaying to opposite sign tight muons confirms the high efficiency of the LF cut on prompt muons (Table 20).

Looking at muons in the signal region, we find that 3 muons out of 82 fail the LF cut in the dimuon channel. From the 97.5% efficiency on prompt and b-decay muons, we would expect 2 out of 82 to fail. Thus we only expect that one LF muon failed the cut, from which we would

	Events	lep1 pass LF cut	lep1 eff.	lep2 pass LF cut	lep2 eff.	both leps pass	Evt. eff.
Yield	4801240	4682494	97.5%	4685403	97.6%	4568688	95.2%

Table 20: Efficiency for LF cut on muons in dimuon Z decay in data.

1396 infer three LF muons total in the final selection. This estimate comes with large uncertainties,
 1397 but is fully consistent with MC predictions for the LF composition of fakes in the final selection.

1398 Additionally, 0 muons out of 44 in the muon-electron channel fail the LF cut. This gives us
 1399 confidence that there is no major unexpected excess of LF muons in the signal region.

1400 D.3.3 LF Fake rate measurement in data

1401 From MC, we expect the fake rate for LF muons to be substantially higher than the FR for
 1402 b-decay muons. To check this in data, we selected a region where LF muons are expected to
 1403 make up a sizable portion of the fakes: W+jets events with two same-sign muons. We select
 1404 this region by requiring:

- 1405 • < 3 jets, and 0 loose tagged jets
- 1406 • MET and MHT > 30 GeV, $|\Delta\phi_{\text{MET MHT}}| > 2.5$
- 1407 • MT MET lep1 > 50 GeV
- 1408 • $|\Delta\phi_{\text{lep1 lep2}}| < 2.1$
- 1409 • lep1 pT > 20, lep1 pT > 10, lep1 passes tight lepton MVA

1410 As shown in Table 21, the efficiency for lep2 to pass the tight lepton MVA cut matches well in
 1411 data and MC. (MC yields are raw event yields, not normalized to expectation.)

Source	lep2 Fail	Composition	lep2 Pass	Eff.
Prompt	1	0.9%	4	
b-quark	61	54.0%	11	18.0%
c-quark	16	14.2%	8	50.0%
LF	35	21.0%	11	31.4%
Total	113		34	30.1%
Data	890		341	38.3%

Table 21: Efficiency for tight lepton MVA in same-sign dimuon W+jets MC and data.

D.4 Cross checks with different selection criteria, including tighter SIP

As a cross check, the analysis is reproduced using different selection criteria.

First of all a cut-based selection including a tight cut on SIP_{3D} is considered. It requires $SIP_{3D} < 4$, $I_{rel} < 0.12$, and standard POG Tight ID for muons and $SIP_{3D} < 4$, $I_{rel} < 0.12$, and standard POG MVA ID for electrons.

We also tried other cut based lepton selections. We implemented a lepton selection similar to the one used in the analysis which is searching for SUSY in same-sign dilepton final states [44]. Moreover, to test the usage of the tracker isolation instead of the full isolation, we tested a modified version of the SUSY lepton identification. In particular we modified the lepton isolation criteria to be $I_{rel}(ch) < 0.05$ instead of $I_{rel} < 0.1$, where $I_{rel}(ch)$ is the isolation computed only from the PF charged hadrons (practically equivalent to tracks). The tighter threshold is needed to keep the fake rate down to a comparable level.

For each selection, the fake rate was re-measured from data. The fake rate is computed as the probability that a lepton selected with all the identification criteria but the isolation one, is also isolated. For these tests we used the same fake rate independently on the multiplicity of the b-jets in the final state, since with this tighter denominator there are not enough events to properly measure the fake rate for the b-tight category. Moreover we expect this fake rate to be less sample-dependent with respect to the nominal one (the extrapolation is only in isolation).

Distributions of the BDT discriminator using the nominal and cut-based selections are shown in Figure 93. The picture remains qualitatively similar across the three selection criteria: some excess of events, especially in the two same-sign muons channel is observed. This excess is mostly in the signal-like BDT region. Moreover we observed that modifying the isolation definition of the SUSY cut based selection we still get quite compatible results; the excess at high value of the BDT discriminant is still there.

	$\mu\mu$	ee	$e\mu$
$t\bar{t}W$	7.38	3.64	13.00
$t\bar{t}Z/\gamma^*$	1.74	0.97	2.71
non-prompt	9.90	3.55	20.15
charge flip	-	1.92	2.38
all signals	1.8	0.96	2.85
all backgrounds	20.1	10.69	39.93
data	28	22	42

Table 22: Expected and observed yields for the cut-based selection with tight SIP cut.

	$\mu\mu$	ee	$e\mu$
$t\bar{t}W$	6.25	2.90	10.43
$t\bar{t}Z/\gamma^*$	1.86	1.16	3.11
non-prompt	8.30	3.29	11.51
charge flip	-	1.54	1.95
all signals	1.60	0.82	2.51
all backgrounds	18.11	10.54	29.63
data	29	16	28

Table 23: Expected and observed yields for the SUSY cut-based selection.

In addition we performed a test where the application region for the fake rate is defined as a sideband in the lepton MVA rather than the full inverted region. To do this we have defined as a sideband region in the lepton MVA distribution the range [-0.7,0.5], which excludes the very background-like leptons and leaves some clearance between the sideband and the signal

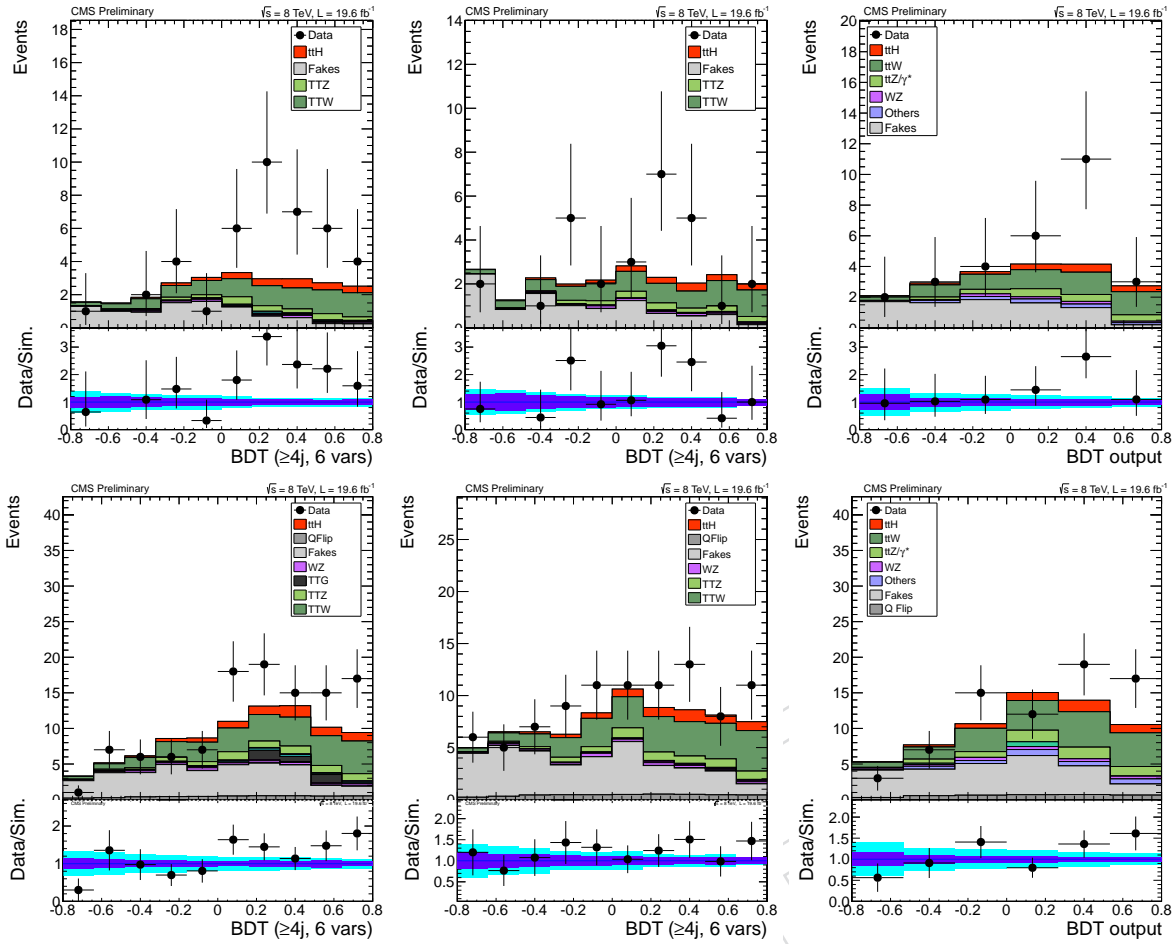


Figure 93: Distribution of the BDT discriminator for the two same-sign muons final state (top row) and all same-sign dileptons final states (bottom row) using the nominal selection (left), the cut-based selection with tight SIP cut (middle), and the SUSY cut-based selection (right).

(> 0.7). For reference, the distribution of the lepton MVA in two same-sign muons events with one failing lepton is shown in Figure 94. For this study the fake rate is defined in a given bin as $N(\text{signal leptons})/(N(\text{signal leptons})+N(\text{sideband leptons}))$; the fake rate distributions are shown in Figure 95. A comparison of the final MVA distributions for the two same-sign muon final state using the sideband fake rate and the nominal one is shown in Figure 96. The number of fake-lepton background events predicted with the sideband fake rate is 13.6 ± 2.6 (stat), while the nominal one is 10.8 ± 1.0 (stat). The difference between the two results is compatible with the difference in their statistical uncertainties. We therefore get quite compatible results even when using a sideband in lepton MVA to compute the fake rate, though that causes larger statistical uncertainty on the reducible background prediction.

D.4.1 Looser lepton MVA selections

We also changed the two same-sign muon selection loosening the lepton MVA selection, but retaining the tight cuts for conversions and charge flip from the nominal selection. We compare the results we obtained with the following working points: *inclusive tight* ($\text{mva} > 0.7$), *inclusive medium* ($\text{mva} > 0.3$), *inclusive loose* ($\text{mva} > -0.3$), *inclusive very loose* ($\text{mva} > -0.7$), *exclusive medium* ($0.3 < \text{mva} < 0.7$), *exclusive loose* ($-0.3 < \text{mva} < 0.7$), *exclusive very loose* ($-0.7 < \text{mva} < 0.7$). We can compare the performances of the looser working points looking at the ROC curve in Figure 97.

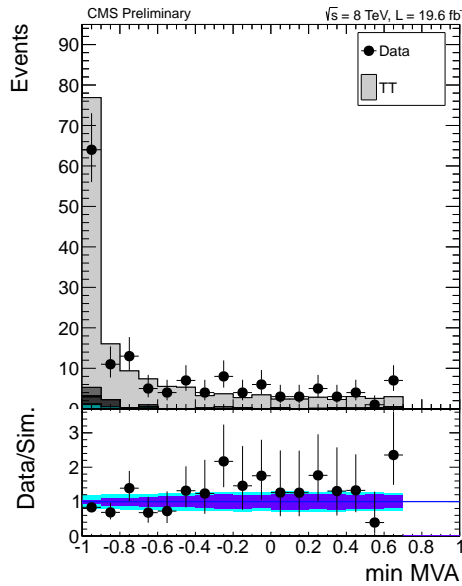


Figure 94: Distribution of the lepton MVA in two same-sign muons events with one failing lepton MVA cut.

1458 First of all we checked that even relaxing the lepton MVA working point the fake-rate mea-
 1459 surement and application regions are still working properly. Figure 98 shows the fake-rate
 1460 distributions for the different working points. Figure 99 shows the shapes agreement between
 1461 data and simulation in the fake-rate application region (obtained applying the full two muon
 1462 same-sign event selection but inverting the lepton MVA cut on one of two muons).

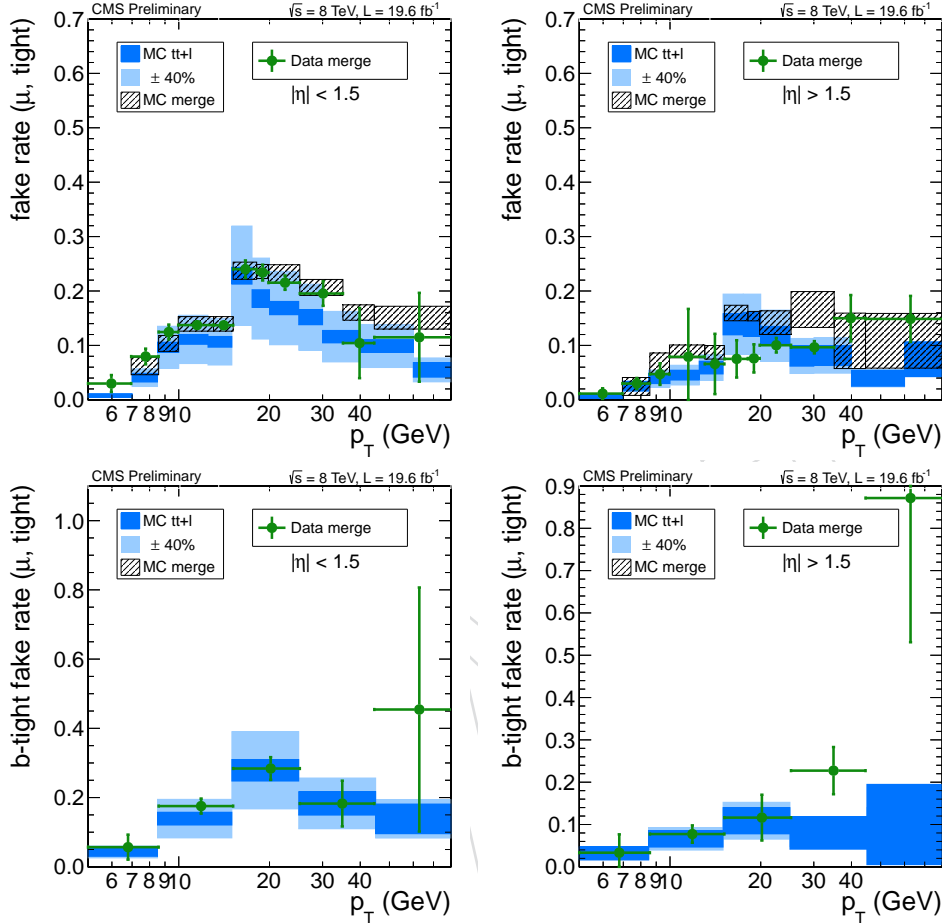


Figure 95: Measured fake rates for the tight MVA working point, combining the different control regions used for the measurement. Combined values from data (dots with error bars) are compared with the combination of the expectations simulated events in control regions (black hatched boxes) and $t\bar{t}$ events in the signal region (blue filled boxes). In the bottom raw the same distributions are presented for events with at least two jets satisfying the medium operation point of the CSV tagger. Plots on the left are for the barrel region and plots on the right for the endcap regions.

The last bin of the fake rates for events with at least two medium b-tagged jets is overestimated due to the background subtraction not working well (probably due to the very small statistics); for the purpose of this test we use it as is, but to avoid tiny numbers at denominator for endcap muons we compute the weight as $f/\max(1-f, 0.5)$ instead of $f/(1-f)$.

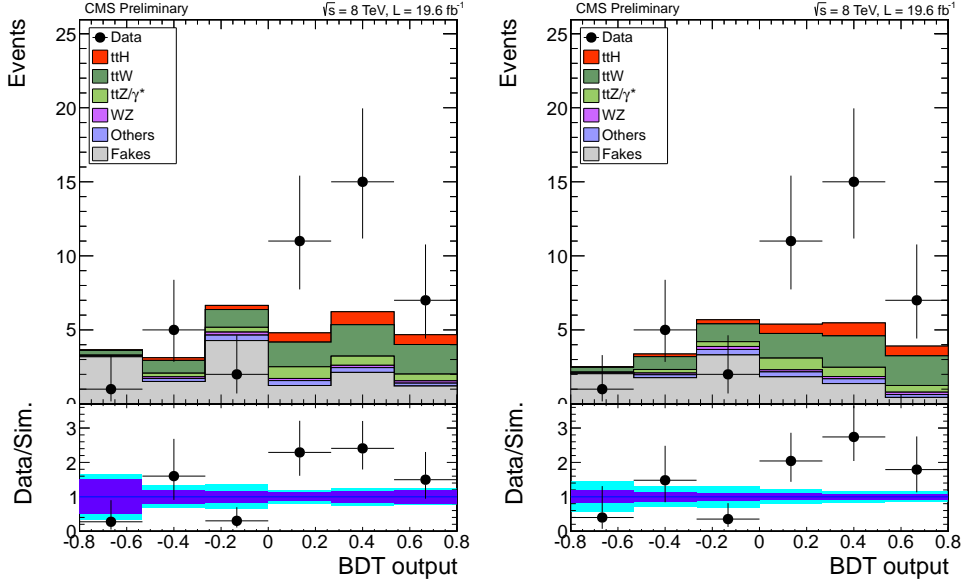


Figure 96: Distribution of the final MVA for the two same-sign muon selection with the side-band fake rate (left) and with the nominal one (right).

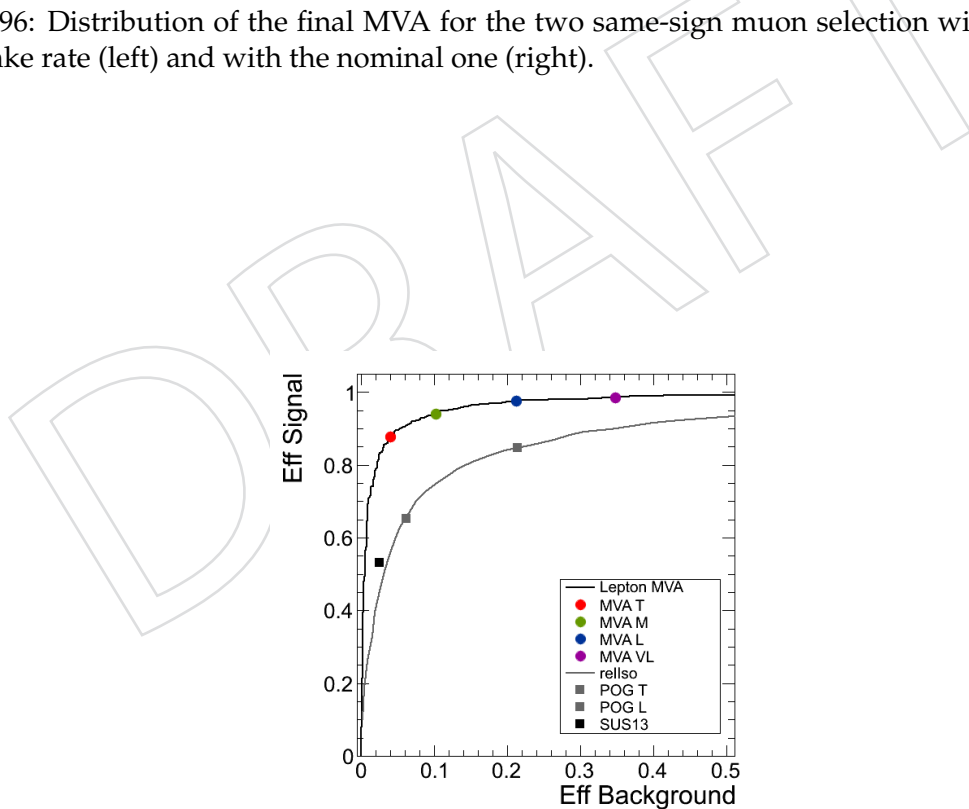


Figure 97: ROC curve for the lepton MVA: $t\bar{t}H$ signal and $t\bar{t}$ background efficiencies given events with two preselected same-sign muons after all the selection cuts. The red, green, blue and violet points show the different working points considered for this check.

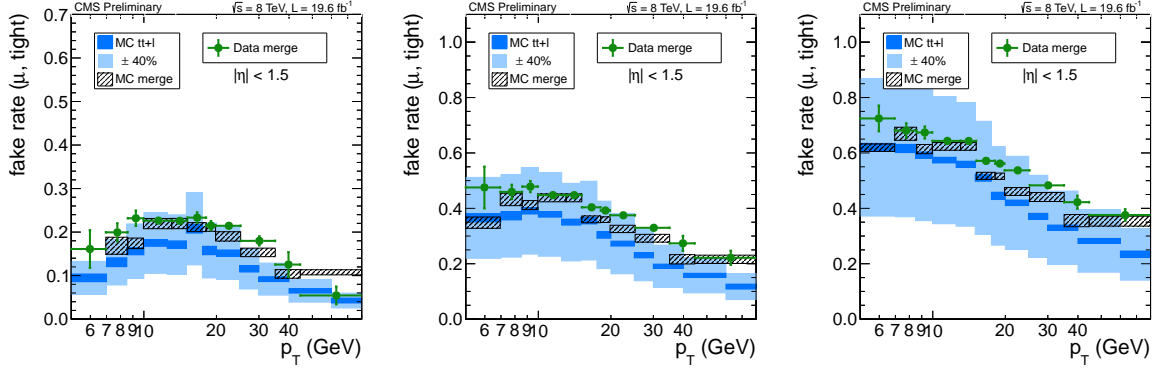


Figure 98: Fake-rate distributions in data and simulation (for muons in the barrel region and for the b-loose category). From left to right the fake-rate is measured for different working points: medium, loose and very loose.

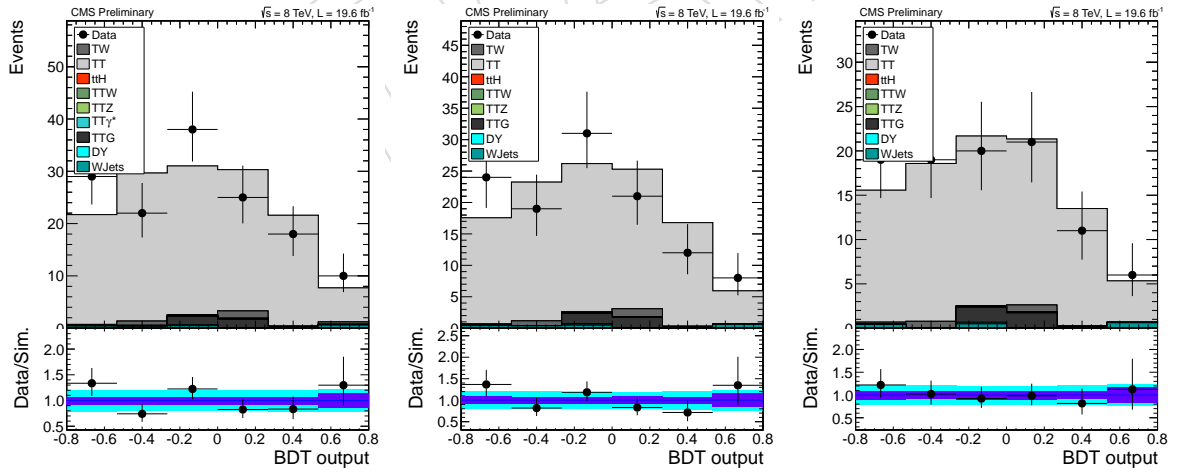


Figure 99: Distribution of the final MVA for the fake-rate application region of the two same-sign muon selection. In these distributions the $t\bar{t}$ and single top MC components are scaled to the yield in data. From left to right the lepton MVA working point used is medium, loose, and very loose.

1463 All these distributions confirm that we can still use the fake-rate method to control the back-
 1464 ground with fake leptons even relaxing the lepton MVA working point. So we run the analysis
 1465 changing the lepton MVA selection and the fake-rate for each working point. The lepton effi-
 1466 ciency scale factors for the medium and very loose working point are approximately estimated
 1467 from the measurements of the loose and tight ones. Only the two same-sign muon channel
 1468 is considered. Figure 100 shows the BDT output for the inclusive medium, loose and very
 1469 loose selections. Both the pre-fit and post-fit plots are shown, meaning that in the latter ones
 1470 the background yields are from the fit to the final discriminant fixing the signal yield to the
 1471 amount predicted by the standard model. Figure 101 shows the BDT output for the exclusive
 1472 medium, loose and very loose selections. Both the pre-fit and post-fit plots are shown.
 1473 Table 24, Table 25, Table 26, summarize numerically what we see in the distributions of the
 1474 final MVA for different lepton MVA working points.

1475 Looking at all these results we can summarize the following: going to a looser lepton MVA
 1476 working point brings in more events, dominantly at low BDT values, in an amount that is well
 1477 compatible with the prediction for the reducible background. The number of events at high
 1478 BDT value in excess with respect to the predictions remains unchanged ($\sim 11 \pm 2$ events) de-
 1479 spite the large increase of the expected reducible background yield (2.1 to 12.5 events). The
 1480 observed best fit σ for each selection are compatible. The statistical significance of the excess
 1481 decreases when going to a looser WP: from a p-value of 0.1 % (3.0 σ) with the tight WP, to 2.6
 1482 % (1.9 σ) with the very loose one.

1483 We did also look at several distributions for the lepton ID variables with the relaxed lepton
 1484 MVA selection; nothing really interesting was found. In the high BDT region, only one extra
 1485 lepton with $SIP_{3D} > 4$ is found with the loose MVA WP, in addition to the 6 already found with
 1486 the tight MVA, despite the 5-times increase in reducible background (from 2.1 to 12.5 events).

WPs	data (++)	non-prompt (++)	others (++)	excess
tight	41 (21)	10.8 ± 4.5 (5.0)	15.6 ± 2.7 (9.5)	14.7 ± 8.3
medium	56 (29)	21.3 ± 9.0 (10.1)	16.3 ± 3.3 (10.1)	18.4 ± 12.1
loose	85 (45)	42 ± 18 (20)	16.9 ± 3.5 (10.4)	26 ± 20
very loose	106 (54)	69 ± 29 (32)	17.1 ± 3.5 (10.5)	20 ± 31
exclusive medium	15 (8)	10.3 ± 3.4 (4.9)	3.0 ± 1.1 (2.2)	1.7 ± 5.9
exclusive loose	44 (24)	30.2 ± 7.3 (14)	4.3 ± 1.3 (2.8)	10 ± 14
exclusive very loose	65 (33)	53.0 ± 9.5 (25)	4.9 ± 1.7 (3.2)	7 ± 24

Table 24: Final yields for the different lepton MVA working points. The excess is in number of events, not normalized to the signal yields. The expected yields and uncertainties are pre-fit (with $\mu = 1$). Uncertainties on fakes and others are only systematical. Uncertainties on the excess include the statistical term.

WPs	data (++)	non-prompt (++)	others (++)	excess
tight	41 (21)	11.8 ± 4.5 (5.8)	18.8 ± 1.7 (11.4)	10.5 ± 8
medium	56 (29)	27.6 ± 7.6 (13)	19.7 ± 1.2 (12.2)	8.7 ± 11
loose	85 (45)	57 ± 11 (27)	20.0 ± 1.1 (12.3)	8.1 ± 14
very loose	106 (54)	82 ± 13 (38)	18.6 ± 0.8 (11.6)	5.5 ± 16
exclusive medium	15 (8)	11.9 ± 3.4 (5.7)	3.0 ± 0.6 (2.1)	0.1 ± 5.2
exclusive loose	44 (24)	38.1 ± 7.3 (18)	4.3 ± 0.8 (2.8)	1.5 ± 9.9
exclusive very loose	65 (33)	59.2 ± 9.5 (28)	4.9 ± 0.6 (3.2)	0.9 ± 13

Table 25: Final yields for the different lepton MVA working points. The excess is in number of events, not normalized to the signal yields. The expected yields and uncertainties are post-fit (with $\mu = 1$), so for the exclusive WPs the agreement is good by design. Uncertainties on fakes and others are only systematical. Uncertainties on the excess include the statistical term.

WPs	data (++)	non-prompt (++)	others (++)	excess
tight	22 (13)	2.1 ± 0.8 (1.3)	9.3 ± 0.3 (5.7)	10.7 ± 4.9
medium	23 (14)	4.8 ± 1.4 (2.7)	9.6 ± 1.2 (6.0)	8.6 ± 5.1
loose	31 (19)	8.7 ± 1.8 (5.3)	9.7 ± 1.1 (6.1)	12.6 ± 6.0
very loose	33 (21)	12.5 ± 2.8 (7.3)	9.0 ± 0.8 (5.8)	11.5 ± 6.2
exclusive medium	1 (1)	1.8 ± 0.5 (1.1)	1.4 ± 0.4 (1.1)	-2.2 ± 1.2
exclusive loose	9 (6)	5.4 ± 1.1 (3.3)	2.0 ± 0.6 (1.3)	1.6 ± 3.3
exclusive very loose	11 (8)	8.2 ± 1.5 (4.9)	2.2 ± 0.5 (1.4)	0.6 ± 3.7

Table 26: Yields in the two highest final BDT bins for the different lepton MVA working points. The excess is in number of events, not normalized to the signal yields. The expected yields and uncertainties are post-fit (with $\mu = 1$). Uncertainties on fakes and others are only systematical. Uncertainties on the excess include the statistical term. Systematics on prompt contributions in exclusive WPs are underestimated.

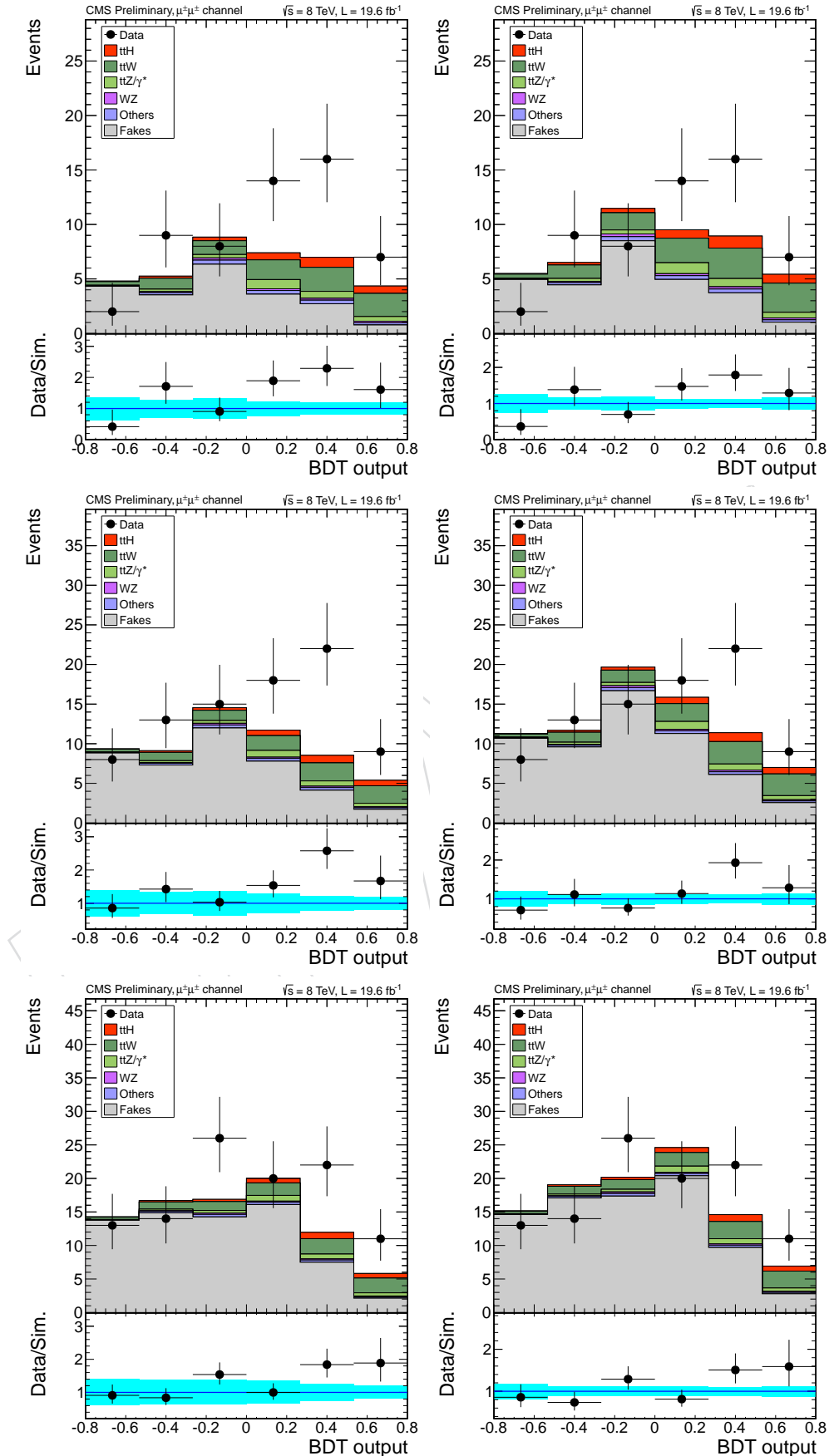


Figure 100: Distributions of the final MVA for the two same-sign muon selection. From top to bottom the lepton MVA working point used are the inclusive medium, loose, very loose. The pre-fit plots are shown on the left and the post-fit ones on the right.

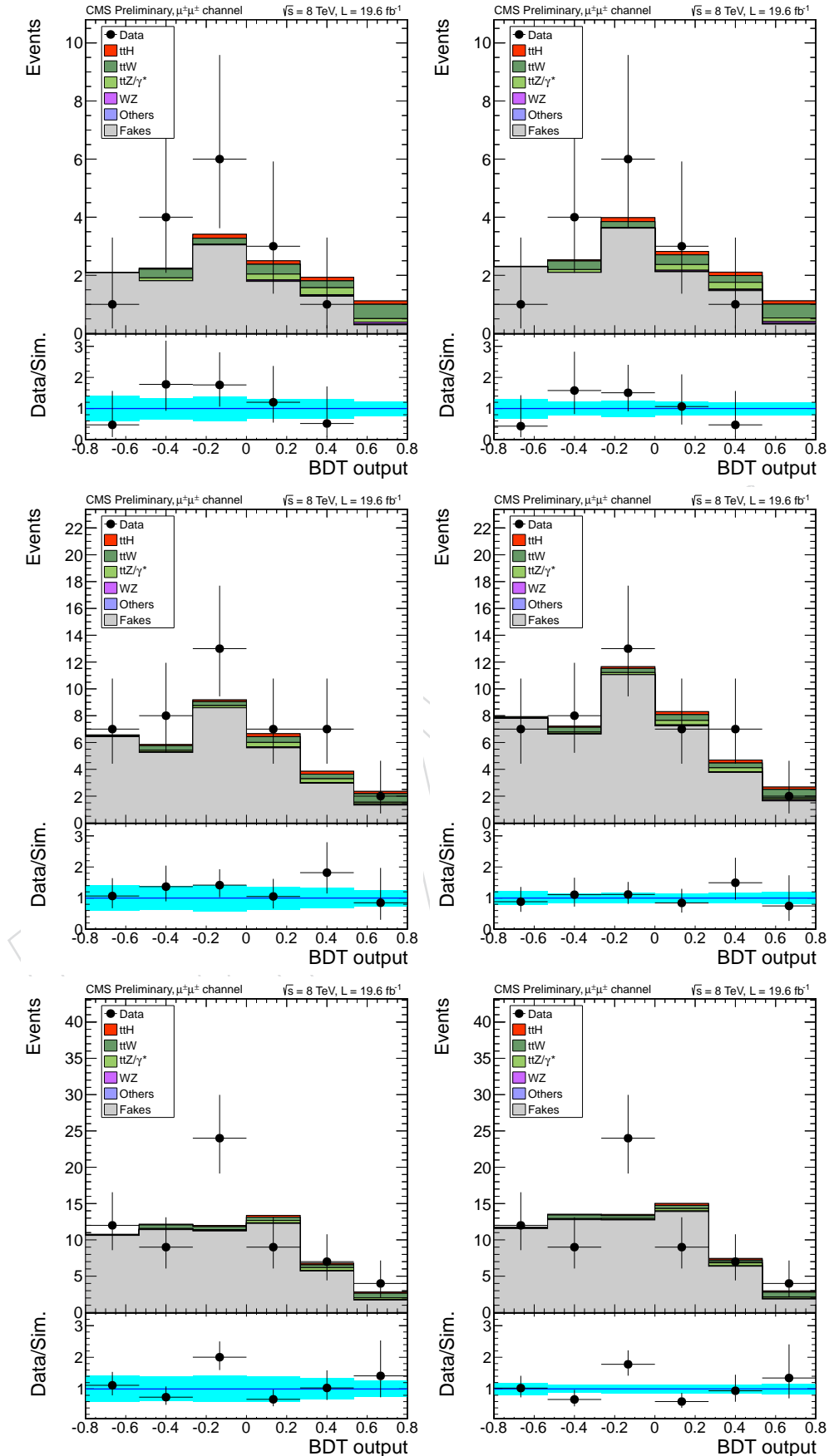


Figure 101: Distributions of the final MVA for the two same-sign muon selection. From top to bottom the lepton MVA working point used are the exclusive medium, loose, very loose. The pre-fit plots are shown on the left and the post-fit ones on the right.

D.5 Tight Charge cut

1487 As last check, we removed the tight charge cut on the muons ($\sigma(p_T)/p_T < 0.2$), which was
1488 there to reduce the charge-flip probability. We observed 3 more events in data. From MC we
1489 expect negligible contribution from signal leptons (from ttH, ttW, ttZ), and 3.3 events from
1490 the reducible background (if we normalize the reducible background MC to the data-driven
1491 prediction). The MC numbers are approximate since we did not compute tag-and-probe scale
1492 factors specifically for the events failing the cut, and the data to simulation agreement for this
1493 inefficiency might not be perfect since it is the tail of a distribution. Anyway the overall yield
1494 is well reproduce.

DRAFT

1496 References

- 1497 [1] CMS Collaboration, "Observation of a new boson at a mass of 125 GeV with the CMS
1498 experiment at the LHC", *Phys. Lett. B* **716** (2012) 30,
1499 doi:10.1016/j.physletb.2012.08.021.
- 1500 [2] ATLAS Collaboration, "Observation of a new particle in the search for the Standard
1501 Model Higgs boson with the ATLAS detector at the LHC", *Phys. Lett. B* **716** (2012) 1,
1502 doi:10.1016/j.physletb.2012.08.020.
- 1503 [3] CMS Collaboration, "Measurements of the properties of the new boson with a mass near
1504 125 GeV", CMS Physics Analysis Summary CMS-PAS-HIG-13-005, (2013).
- 1505 [4] LHC Higgs Cross Section Working Group et al., "Handbook of LHC Higgs Cross
1506 Sections: 1. Inclusive Observables", CERN-2011-002 (CERN, Geneva, 2011)
1507 arXiv:1101.0593.
- 1508 [5] DØ Collaboration, "Search for the Standard Model Higgs boson in the $t\bar{t}H \rightarrow t\bar{t}b\bar{b}$
1509 channel", *DØ Conference Note* **D0 CONF-5739** (2008).
- 1510 [6] CDF Collaboration, "Search for the Standard Model Higgs Boson Produced in
1511 Association with Top Quarks Using the Full CDF Data Set", *Phys. Rev. Lett.* **109** (Nov,
1512 2012) 181802, doi:10.1103/PhysRevLett.109.181802.
- 1513 [7] ATLAS Collaboration, "Search for the Standard Model Higgs boson produced in
1514 association with top quarks in proton-proton collisions at $\sqrt{s} = 7\text{TeV}$ using the ATLAS
1515 detector", *ATLAS Conference Report* **ATLAS-CONF-2012-135** (2012).
- 1516 [8] CMS Collaboration, "Search for the standard model Higgs boson produced in association
1517 with a top-quark pair in pp collisions at the LHC", CERN-PH-EP-2013-027 (2013)
1518 arXiv:1303.0763.
- 1519 [9] CMS Collaboration, "Search for $t\bar{t}H$ production in events with $H \rightarrow f\bar{f}l\bar{l}$ at $\sqrt{s} = 8\text{ TeV}$
1520 collisions", CMS Physics Analysis Summary CMS-PAS-HIG-13-015, (2013).
- 1521 [10] CMS Collaboration, "CMS Luminosity Based on Pixel Cluster Counting - Summer 2012
1522 Update", CMS PAS LUM-12-001, (2012).
- 1523 [11] CMS Collaboration, "Dilepton trigger and lepton identification efficiencies for the top
1524 quark pair production cross section measurement at 8 TeV in the dilepton decay
1525 channel.", CMS AN AN-12-389, (2012).
- 1526 [12] CMS Collaboration, "Search for Higgs Produced in Association with a Top Quark Pair
1527 and Decaying to Bottom Quarks or Tau Leptons", CMS AN AN-13-145, (2013).
- 1528 [13] CMS Collaboration, "Particle-Flow Event Reconstruction in CMS and Performance for
1529 Jets, Taus, and MET", CMS Physics Analysis Summary CMS-PAS-PFT-09-001, (2009).
- 1530 [14] CMS Collaboration, "Commissioning of the Particle-Flow reconstruction in
1531 Minimum-Bias and Jet Events from pp Collisions at 7 TeV", CMS Physics Analysis
1532 Summary CMS-PAS-PFT-10-002, (2010).
- 1533 [15] M. Cacciari, G. P. Salam, G. Soyez, "FastJet user manual", (2011).
1534 arXiv:hep-ph/1111.6097v1.

- [16] M. Cacciari, G. P. Salam, "Dispelling the N^3 myth for the k_t jet-finder", *Phys. Lett. B* **641** (2006) 57, doi:10.1016/j.physletb.2006.08.037, arXiv:hep-ph/0512210.
- [17] CMS Collaboration, "Determination of Jet Energy Calibration and Transverse Momentum Resolution in CMS", *JINST* **6** (2011) 11002, doi:10.1088/1748-0221/6/11/P11002.
- [18] CMS Collaboration Collaboration, "Identification of b-quark jets with the CMS experiment", *JINST* **8** (2013) P04013, doi:10.1088/1748-0221/8/04/P04013, arXiv:1211.4462.
- [19] C. Collaboration, "Results on b-tagging identification in 8 TeV pp collisions", DP 2013/005, (2013).
- [20] N. Amapane et al., "Search for the standard model Higgs boson in the decay channel $H \rightarrow ZZ \rightarrow 4\ell$ in pp collisions", *CMS AN* **2012/141** (2012).
- [21] N. Amapane et al., "Updated results on the new boson discovered in the search for the standard model Higgs boson in the $H \rightarrow ZZ \rightarrow 4\ell$ channel in pp collisions", *CMS AN* **2012/367** (2012).
- [22] CMS Collaboration, "Performance of CMS muon reconstruction in pp collision events at $\sqrt{s} = 7$ TeV", *JINST* **7** (2012) P10002, doi:10.1088/1748-0221/7/10/P10002, arXiv:1206.4071.
- [23] CMS Collaboration, "Measurement of tracking efficiency", *CMS Physics Analysis Summary CMS-PAS-TRK-10-002* (2010).
- [24] CMS Collaboration, "Commissioning of the particle-flow event reconstruction with leptons from J/Psi and W decays at 7 TeV", *CMS Physics Analysis Summary CMS-PAS-PFT-10-003* (2010).
- [25] A. Bodek and J. Han, "Improved Rochester Misalignment and Muon Scale Corrections Extracted for 2011A, 2011B CMS Data", *CMS AN* **2012/298** (2012).
- [26] S. Baffioni et al., "Electron reconstruction in CMS", *Eur. Phys. J. C* **49** (2007) 1099, doi:10.1140/epjc/s10052-006-0175-5.
- [27] CMS Collaboration, "Electron reconstruction and identification at $\sqrt{s} = 7$ TeV", CMS Physics Analysis Summary CMS-PAS-EGM-10-004, (2010).
- [28] CMS Collaboration, "Electron commissioning results at $\sqrt{s} = 7$ TeV", CMS Detector Performance Summary CMS-DP-2011-003, (2011).
- [29] CMS Collaboration, "Electron performance with 19.6 fb^{-1} of data at $\sqrt{s} = 8$ TeV with the CMS detector", CMS Detector Performance Summary CMS-DP-2013-003, (2013).
- [30] e/g POG, "Electron Selection Criteria in 2012", *CMS AN* **2012/201** (2012).
- [31] S. Baffioni et al., "Electron Reconstruction in CMS", *CMS Analysis Note* **2009/164** (2009).
- [32] CMS Collaboration, "Measurement of the Inclusive W and Z Production Cross Sections in pp Collisions at $\sqrt{s} = 7$ TeV", *JHEP* **10** (2011) 132, doi:10.1007/JHEP10(2011)132.
- [33] N. Amapane et al., "Properties of the Higgs-like boson in the decay $H \rightarrow ZZ \rightarrow 4\ell$ in pp collisions", *CMS AN* **2013/003** (2013).

- 1573 [34] CMS Collaboration, “Studies of Tracker Material”, *CDS Record* **1279138** (2010).
- 1574 [35] P. Z. Skands, “Tuning Monte Carlo Generators: The Perugia Tunes”, *Phys.Rev.* **D82**
1575 (2010) 074018, doi:10.1103/PhysRevD.82.074018, arXiv:1005.3457.
- 1576 [36] M. Botje et al., “The PDF4LHC Working Group Interim Recommendations”,
1577 arXiv:1101.0538.
- 1578 [37] P. M. Nadolsky et al., “Implications of CTEQ global analysis for collider observables”,
1579 *Phys. Rev. D* **78** (Jul, 2008) 013004, doi:10.1103/PhysRevD.78.013004.
- 1580 [38] R. D. Ball et al., “A first unbiased global NLO determination of parton distributions and
1581 their uncertainties”, *Nucl.Phys.* **B838** (2010) 136–206,
1582 doi:10.1016/j.nuclphysb.2010.05.008, arXiv:1002.4407.
- 1583 [39] A. Martin, W. Stirling, R. Thorne, and G. Watt, “Parton distributions for the LHC”,
1584 *Eur.Phys.J.* **C63** (2009) 189–285, doi:10.1140/epjc/s10052-009-1072-5,
1585 arXiv:0901.0002.
- 1586 [40] A. Collaboration, “Measurement of the inclusive $t\bar{t}\gamma$ cross section with the
1587 ATLAS detector”,
- 1588 [41] D. Peng-Fei et al., “Next-to-leading order QCD corrections to $t\bar{t}\gamma$ production at the 7 TeV
1589 LHC”, *Chin. Phys. Lett.* **28** (2011) 111401, doi:10.1088/0256-307X/28/11/111401,
1590 arXiv:1110.2315.
- 1591 [42] K. Melnikov, M. Schulze, and A. Scharf, “QCD corrections to top quark pair production in
1592 association with a photon at hadron colliders”, *Phys. Rev. D* **83** (2011) 074013,
1593 doi:10.1103/PhysRevD.83.074013, arXiv:1102.1967.
- 1594 [43] C. Collaboration, “Observation of a new boson with mass near 125 GeV in pp collisions
1595 at $\sqrt{s} = 7$ and 8 TeV”, arXiv:1303.4571. Accepted by JHEP.
- 1596 [44] CMS Collaboration, “Search for new physics in events with same-sign dileptons and jets
1597 in pp collisions at $\sqrt{s} = 8$ TeV”, CMS Physics Analysis Summary CMS-PAS-SUS-13-013,
1598 (2013).